The thermochronological evolution of the northern Gawler Craton and northern Adelaide Rift Complex

James William Hall

Department of Earth Sciences
School of Physical Sciences
The University of Adelaide

October 2018

Table of contents

Abstract

Cratons preserve information about the deformation history of the surrounding terrains and the thermal history of mineral deposits. This thesis aims to constrain the effects on the Gawler Craton of various deformation events from surrounding terrains and the thermal evolution of mineralization within the Craton. Multi-method thermochronology was applied to samples throughout the northern Gawler Craton and Willouran Ranges of the Adelaide Rift Complex to unravel the thermal evolution of the northern Gawler Craton and Willouran Ranges. The subsequent thermal histories are compared and the differences between them highlighted.

Apatite U-Pb data reveal distinct spatial patterns within the high temperature cooling history of the Gawler Craton. These spatial patterns correspond to the thermal response of a region to different magmatic and metamorphic events. The eastern Gawler Craton cooled to mid-crustal temperatures from high temperatures following magmatism of the ~1850 Ma Donington Suite and ~1590 Ma Hiltaba Suite while the central Gawler Craton cooling following the ~2500 Ma Sleaford and ~1700 Ma Kimban orogenies. The north-western Gawler Craton preserved evidence for deformation that post-dates cooling relating to magmatism with ages relating to the amalgamation of western and southern Australia at ~1300 Ma.

In addition to the apatite U-Pb data, muscovite $^{39}Ar/^{40}Ar$ preserve post magmatic cooling within the Olympic Domain of the Hiltaba Suite at ~1530 Ma within the Olympic Domain. A second hydrothermally altered muscovite $^{39}Ar/^{40}Ar$ age from the same sample is recorded at ~1380 Ma. Potassium feldspar $^{39}Ar/^{40}Ar$ data from numerous samples all preserve altered spectra during the Neoproterozoic which corresponds to the deposition of the Adelaide Rift Complex. The region first cooled to low temperatures (<200 °C) at ~1000 Ma before minor reheating during the Neoproterozoic. The main low temperature regional cooling period is preserved at ~430 – 350 Ma and is interpreted to be caused by deformation relating to the 450 – 300 Ma Alice Springs Orogeny. Younger apatite fission track ages are only preserved in close proximity to major Iron-Oxide-Copper-Gold (IOCG) deposits and form a young thermal corridor linking the IOCG deposits.

Apatite fission track data along the Karari Shear Zone of the northern Gawler Craton preserves evidence for regional Neoproterozoic cooling and a deformation event during the Carboniferous. The Nawa Domain preserves Carboniferous apatite fission track ages, whereas the Christie Domain preserves older Neoproterozoic – Cambrian ages. This is interpreted to be resultant from southward compression from the Alice Springs Orogeny and caused the Nawa Domain, to the north of the Karari Shear Zone, to thrust over the Christie Domain to the south. Additionally, this thrusting is interpreted to have ceased deposition of the Officer Basin sediments, which overlies the rocks to the north of the Karari Shear Zone. The deposition of the ~300 Ma Arckaringa Basin sediments indicates that once the compressional event stopped, deposition recommenced in the region.

East of the Torrens Hinge Zone, apatite fission track analysis from sedimentary samples within the Willouran Ranges revealed cooling ranging from 550 to 100 Ma. U-Pb data records either detrital

Proterozoic ages or ages at ~250 Ma. This younger age is interpreted to be caused by hydrothermal activity located proximally to the major fault zones in the region. Samples which preserve this younger U-Pb age also preserve apatite fission track ages of ~100 Ma that is interpreted to be cooling. This hydrothermal activity correlates well with hydrothermal activity in the Mt. Painter Inlier, a region of established high heat flow ~150 km to the east. This hints toward a broader zone of hydrothermal activity related cooling during this time.

Regional deformation events are consistently present throughout the study region, yet local thermal histories contain inconsistencies. These inconsistencies can be accounted for by differing key geological factors which are unique to each region. The thickness of any overlying sedimentary packages and the geothermal gradient are greatly important at any location as they considerably influence the local thermal histories. Major structures around the rim of the craton tend to control the thermal histories at both high and low temperatures, however, their orientation within the stress regime is important. The prior thermal history of a region can be reset and overprinted by hydrothermal activity as has been recorded in this study for regions within the Olympic Domain and the northern Adelaide Rift Complex.

List of figures

List of tables

Declaration

I certify that this work contains no material which has been accepted for the award of any other degree or diploma in my name, in any university or other tertiary institution and, to the best of my knowledge and belief, contains no material previously published or written by another person, except where due reference has been made in the text. In addition, I certify that no part of this work will, in the future, be used in a submission in my name, for any other degree or diploma in any university or other tertiary institution without the prior approval of the University of Adelaide and where applicable, any partner institution responsible for the joint-award of this degree.

I acknowledge that copyright of published works contained within this thesis resides with the copyright holder(s) of those works. I also give permission for the digital version of my thesis to be made available on the web, via the University's digital research repository, the Library Search and also through web search engines, unless permission has been granted by the University to restrict access for a period of time.

I acknowledge the support I have received for my research through the provision of an Australian Government Research Training Program Scholarship.

_____

James William Hall

Journal Articles

Hall, J.W., Glorie, S., Reid, A.J., Boone, S.C., Collins, A.S., and Gleadow, A., 2018, An Apatite U–Pb Thermal History Map for the Northern Gawler Craton, South Australia. Geoscience Frontiers.

Hall, J.W., Glorie, S., Reid, A.J., Collins, A.S., Jourdan, F., Danišík, M., and Evans, N., 2018, Thermal History of the Northern Olympic Domain, Gawler Craton; Correlations between Thermochronometric Data and Mineralising Systems. Gondwana Research 56, 90-104.

Hall, J.W., Glorie, S., Collins, A.S., Reid, A.J., Carboniferous fault reactivation at the Palaeoproterozoic northern margin of the Gawler Craton, South Australia; insights from apatite fission track thermochronology. In preparation.

Hall, J.W., Glorie, S., Collins, A.S., Reid, A., Evans, N., McInnes, B., and Foden, J., 2016, Exhumation History of the Peake and Denison Inliers: Insights from Low-Temperature Thermochronology. Australian Journal of Earth Sciences 63, 805-20.

Acknowledgements

My Ph.D. has been one of the most enjoyable experiences of my life, from the people I have met, to the things I have learned, and the places I have been. I do believe I have grown as a geologist and as a person during this time and I could not have done it without the people thanked here.

Firstly, I would like to thank my primary supervisor Dr. Stijn Glorie, who has guided me for four years and whose expertise in thermochronology has been invaluable. I would also like to extend my thanks to my co-supervisor Prof. Alan Collins whose breadth of knowledge always gave me new ideas and paths to lead my Ph.D. down. I'd like to thank my co-supervisor Dr. Anthony Reid for his extensive knowledge of South Australian geology and for the outside opinions and perspectives that he brought to my Ph.D.

To the ATLaS and Gondwana research groups, I would like to say thanks for all the help, whether it be lab based, presentation suggestions, out to fill out a particular form, or even proof reading a paragraph, there was always someone around who was happy to help out.

My lab work could not have gone so smoothly without the continued support from the team, both past and present, at Adelaide Microscopy. Dr. Ben Wade, Ms. Aoife McFadden, Dr. David Kelsey and Dr. Sarah Gilbert all patiently assisted me and answered all of my questions and for that, I am grateful to them.

To my family, I would like to say thank you for your belief in me and for pushing me to chase what I love doing. Finally, to Natalie, thank you for being there for every step, from the good times, to the bad, and for being my best friend and companion.

Introduction

Cratons are generally considered to be stable crustal blocks that are largely unaffected by tectonic processes. This stability increases their likelihood of mineral deposit preservation which makes ideal regional exploration targets. An excellent example of this is the West Australian Craton which is suggested to have been largely stable since the Mesoproterozoic (Daniels, 1975; Fairbridge and Finkl Jr, 1980) and contains numerous economic mineral deposits. The perceived longevity of cratons has recently been challenged by low temperature thermochronological studies (e.g. Belton et al., 2004; Green and Duddy, 2006; Reddy et al., 2015). In addition, many cratons are overlain by thick sedimentary packages which point toward a change in the thermal architecture and, as a consequence, the stability of a craton (e.g. Neumann et al., 2000). If cratons are not as stable as once thought, they hold the potential to preserve vast quantities of information about the deformation history of the surrounding terrains. Moreover, if they are not located proximally to a plate boundary, they may preserve information about intra-plate processes.

The Gawler Craton in South Australia is an example of a perceived 'stable' craton which has been interpreted to have seen very little tectonism since the last period of major craton building at ~1450 Ma (Webb et al., 1986; Fraser et al., 2012). It is a geologically complex craton with regions of mineral endowment, anomalously high geothermal gradients, crustal scale shear zones, large igneous provinces, and the inverted Adelaide Rift Complex outboard to the east (Houseman et al., 1989; Daly et al., 1998; Preiss, 2000; Hand et al., 2007; Ehrig et al., 2012).

There are several major tectonic events which affected regions surrounding the Gawler Craton, beginning with the collision of the West Australian Craton with the combined north and south Australian cratons at ~1300 Ma (Kirkland et al., 2017). At ~550 Ma, The Petermann Orogeny deformed central Australia, to the north of the Gawler Craton (Sandiford and Hand, 1998). At ~500 Ma, the sediments of the Adelaide Rift Complex, to the east of the Gawler Craton, were deformed during the Delamerian Orogeny (Foden et al., 2006). The subduction zone relating to the Delamerian Orogeny migrated to the east over the next ~300 Ma to form the Tasmanides of eastern Australia (Fig. 1; Glen, 2005). To the north of the Gawler Craton, the intracontinental 450 – 300 Ma Alice Springs Orogeny caused north-south compression of the Musgrave Province, and Arunta Inlier within central Australia (Bradshaw and Evans, 1988; Ballèvre et al., 2000; Klootwijk, 2013). Finally, at ~100 Ma, Australia and Antarctica began to rift apart to the south of the Gawler Craton (e.g. Russell and Gurnis, 1994) which resulted in the uplift of southern Australia.

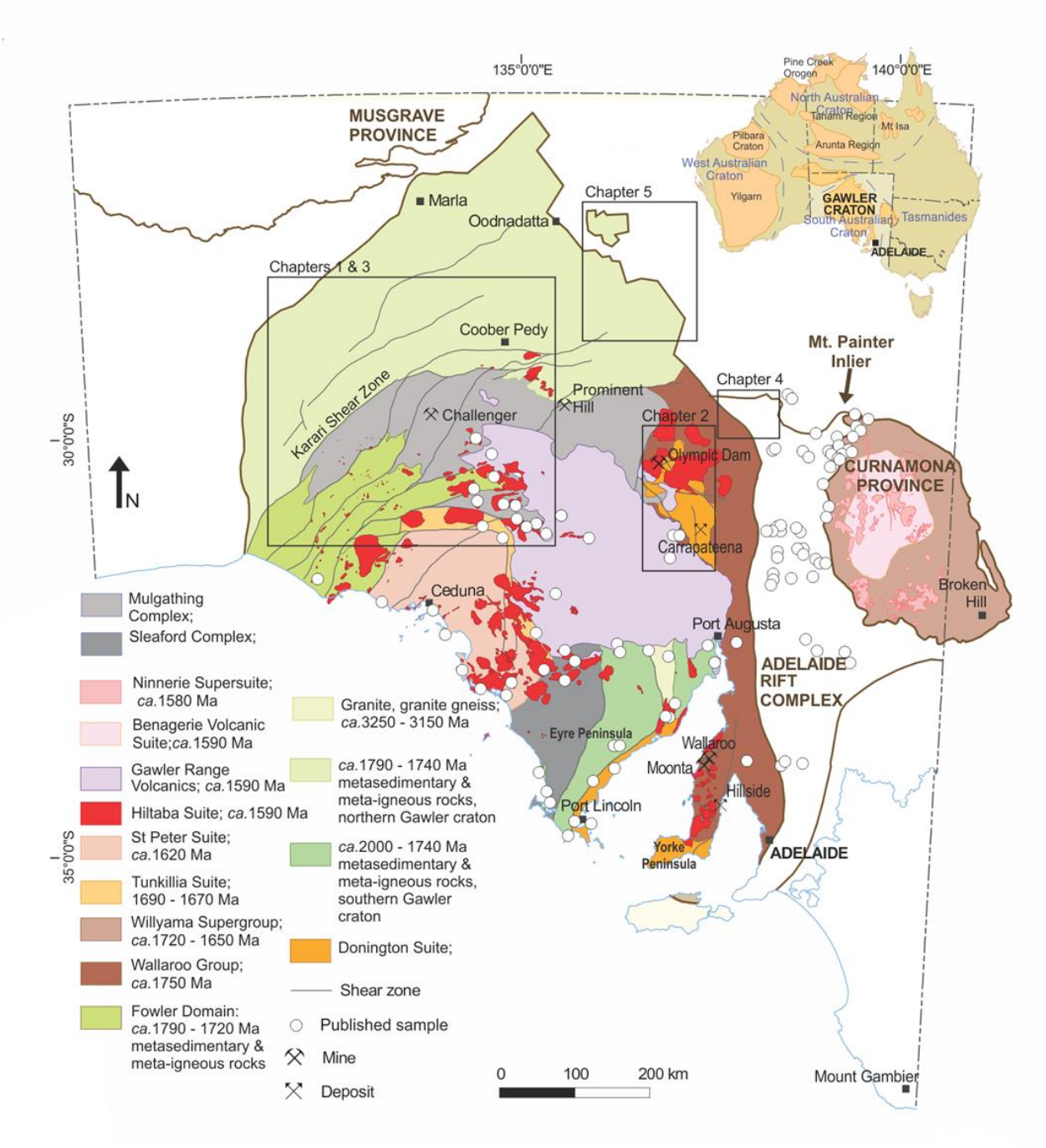

Figure 1: Simplified geological map of the Gawler Craton, indicating the locations of all chapters, major mineral deposits, and published apatite fission track samples (Foster et al., 1994; Gibson and Stüwe, 2000; Gleadow et al., 2002; Mitchell et al., 2002; Weisheit et al., 2014; Reddy et al., 2015; Boone et al., 2016). Modified from Reid et al. (2014a).

On the eastern margin of the Gawler Craton is a Neoproterozoic – Cambrian rift complex known as the Adelaide Rift Complex (Fig. 1). The Adelaide Rift Complex is a basin that, as stated above, was inverted and deformed during the ~500 Ma Delamerian Orogeny (Foden et al., 2006). In addition, the Adelaide Rift Complex underwent significant uplift during the Alice Springs Orogeny (Gibson and Stüwe, 2000; Weisheit et al., 2014). The northern Adelaide Rift Complex is a focus of this study due to the proximity to the northern Gawler Craton. The main outcropping regions within the northern Adelaide Rift Complex are the Willouran Ranges to the west and the Mt. Painter Inlier to the east. The Mt. Painter Inlier's post-depositional thermal history is well constrained (Foster et al., 1994; McLaren et al., 2002; Mitchell et al., 2002; Brugger et al., 2011; Elburg et al., 2013; Weisheit et al., 2014). However, the post-depositional thermal history of the Willouran Ranges and its relationship to both the rest of Adelaide Rift Complex and the Gawler Craton is unconstrained. As a result, the Willouran Ranges are an ideal location to compare the thermal histories of the Gawler Craton, to a younger, more mobile terrain.

Given the wealth of mineral endowment within the Gawler Craton and Adelaide Rift Complex, understanding the thermochronological history is fundamental for developing further exploration strategies. The thermal history of a region preserves information about its cooling history and preservation, which are both key factors in mineral exploration (e.g. Cao et al., 2018). Despite this, middle to low-temperature thermochronological data and thermal history models for the Gawler Craton are sparse. Numerous K-Ar and Ar-Ar studies have been conducted on the Gawler Craton (Webb et al., 1986; Foster and Ehlers, 1998; Budd and Fraser, 2004; Tomkins et al., 2004; Fraser and Lyons, 2006; Fraser et al., 2007; Forbes et al., 2012; Fraser et al., 2012; Reid et al., 2017), however, these methods offer insights into the mid-crustal thermal history and do not preserve any data for the last ~1400 Ma of thermal history of the Craton. More recently, apatite fission track studies (e.g. Gleadow et al., 2002; Reddy et al., 2015; Boone et al., 2016) have attempted to fill this gap and provide insights in local thermal histories, but they remain too sparse to conclusively determine the post-Mesoproterozoic thermal history. An aspect of the Gawler Craton, which has previously discouraged exploration and thermochronological studies, is the presence of thick sedimentary packages that cover much of the craton (e.g. Drexel, 1995). This thesis uses both outcrop and drill core samples to reveal a more comprehensive model for the thermal history of the Gawler Craton by combining mid-temperature and low-temperature data. In particular, apatite U-Pb, muscovite ^{40}Ar-^{39}Ar, and potassium feldspar ^{40}Ar-^{39}Ar analysis are used to further constrain the mid-temperature thermal history, while apatite fission track, zircon (U-Th-Sm)/He, and apatite (U-Th-Sm)/He analysis are applied to constrain the low-temperature thermal history.

Using these methods, this thesis explores two key subjects; the thermochronological evolution of the northern Gawler Craton and Adelaide Rift Complex, and their relation with the structural architecture. With the Gawler Craton as a study site, this thesis aims to observe how the different regions of the craton thermally respond to post-cratonic tectonic events and how these tectonic events are expressed in the thermochronological data.

Thesis Outline

This thesis is separated into five different chapters based on the different domains of the Northern Gawler Craton and the Willouran Ranges of the Adelaide Rift Complex. In addition to this, the high temperature data across the northern Gawler Craton has also been separated from the low temperature data due to the large difference in age data and related interpretations in the framework of the thermal history of the study area. The thesis is composed of three accepted manuscripts, and two manuscripts that are ready for submission. They are outlined below:

Chapter 1 aims to constrain the deep crustal cooling of the northern Gawler Craton using apatite U-Pb dating. Apatite U-Pb dating records the cooling from ~550 to ~330 °C (Chew and Spikings, 2015) and was applied to Proterozoic basement samples throughout the Nawa, Christie, Fowler, and Wilgena Domains, Coober Pedy Ridge and Mt Woods Inlier (Daly et al., 1998; Hand et al., 2007). The samples from the ~2500 Ma Mulgathing Complex (Cowley and Fanning, 1991; Reid et al., 2014b) preserve cooling at ~2 Ga. The ~1700 Ma Kimban Orogeny (Hand et al., 2007) is only partially preserved within the Christie Domain, while cooling relating to the ~1590 Ma Hiltaba Event (Daly et al., 1998) is dominantly preserved throughout the Gawler Craton. Samples from the western Nawa Domain preserve cooling that significantly post-date 1.5 Ga. These samples are interpreted to be recording far-field stress accommodation relating to the collision of the West Australian Craton and the combined south and north Australian cratons. All ages correlate well with published $^{40}Ar/^{39}Ar$ data and when the datasets are combined, they produced a thermal map of the Proterozoic cooling history of the northern Gawler Craton that yields a detailed view into the mid-range thermal evolution of an entire cratonic region.

Chapter 2 enquires into the thermal history of the northern Olympic Domain using multiple thermochronological methods. The Olympic Domain is home to the world class Olympic Dam Iron-Oxide-Copper-Gold (IOCG) deposit (Ehrig et al., 2012) in addition to other IOCG deposits (Skirrow et al., 2007). However, the post-Hiltaba Suite emplacement cooling history of the deposit and the region is poorly understood. Despite this, the post-Hiltaba Suite emplacement cooling history may play an important role in the exhumation and preservation potential of the deposit. Apatite U-Pb data preserve post-magmatic cooling of the ~1850 Ma Donington Suite (Reid et al., 2008) and the ~1590 Ma Hiltaba Suite/Gawler Range Volcanics. In addition, a single muscovite $^{40}Ar/^{39}Ar$ age records post-magmatic cooling of the Hiltaba Suite. A second muscovite $^{40}Ar/^{39}Ar$ age preserves a (likely) hydrothermally altered age of ~1400 Ma. Similarly, potassium feldspar samples preserve $^{40}Ar/^{39}Ar$ age that indicate thermal or mineralogical alteration during the Neoproterozoic. Apatite fission track data reveal complex cooling during the last ~1000 Ma. The region first cooled to low temperatures at ~1000 Ma, as recorded by two samples within the region. Following reheating during the deposition of the sediments that comprise the Stuart Shelf, the next major regional cooling phase was recorded at ~400 Ma, likely caused by deformation related to the Alice Springs Orogeny. Samples located in close proximity to major IOCG deposits preserve apatite fission track ages that post-date the ~400 Ma cooling ages. These samples record Mesozoic ages and are interpreted to be caused by hydrothermal activity during the ~ 500 Ma

Delamerian Orogeny that accumulated high-heat producing elements around the IOCG deposits, resulting in elevated geothermal gradients in these regions.

Chapter 3 details the low-temperature thermal history for the same samples from chapter 1. The aim of this chapter is to investigate Phanerozoic fault reactivation along the Karari Shear Zone in the northern Gawler Craton (Rankin et al., 1989). The region first reached low temperatures during the Neoproterozoic as the region cooled monotonically. The main fault movement recorded within the Nawa Domain, which cooled to low temperatures as it exhumed over the Christie Domain during the Carboniferous. This differential exhumation is interpreted to be caused by a southward propagating compressional stress field from the Alice Springs Orogeny. This event ceased deposition of the Officer Basin sediments during the Frasnian (Womer et al., 1987; Long et al., 1988; Gravestock, 1997), which coincides with the timing of exhumation observed in the thermochronological data from this study. Following the end of the Alice Springs Orogeny, deposition of the Arckaringa Basin sediments commenced at ~300 Ma over the Officer Basin (Wopfner, 1970; Hibburt, 1984, 1995). A younger Triassic thermal anomaly is preserved around Challenger deposit and is linked to an increased geothermal gradient at the time.

Chapter 4 enquires into the thermal history of the Willouran Ranges. The rocks that compose the Willouran Ranges were deposited as part of the formation of the Adelaide Rift Complex during the Neoproterozoic. This is reflected in a majority of the new apatite U-Pb data, which preserve detrital Proterozoic ages. However, samples located within close proximity to major fault zones preserve a younger ~250 Ma apatite U-Pb age. This ~250 Ma age is mimicked in the apatite fission track data, where samples that are located within close proximity to major faults, all record a younger apatite fission track age of ~100 Ma. In comparison, samples located distally to major faults preserve a mixture of apatite fission track ages from ~550 to 200 Ma. The older ages are interpreted to reflect cooling after the Delamerian Orogeny and the younger ages are interpreted to be related with the thermal event that preserved the ~250 Ma apatite U-Pb ages. This ~250 Ma event is interpreted to be caused by hydrothermal activity along the major fault zones within the region, related to concurrent hydrothermal activity within the Mt. Painter Inlier (Fig. 1). Finally, the ~100 Ma apatite fission track ages are interpreted to reflect the last cooling of the region.

Chapter 5 investigates the thermal history of the Peake and Denison Inliers, the region with the highest elevation in the northern Gawler Craton. The Peake and Denison Inliers are dominated by Proterozoic metasedimentary rocks which have been intruded by the ~1800 Ma Wirriecurrie Granite, the ~1800 Ma Tidnamurkuna Volcanics, and the ~500 Ma Bungadilina Monzonite (Ambrose et al., 1981; Hopper, 2001; Fanning et al., 2007). Thermochronological interpretations for samples from the Bungadilina Monzonite suggest rapid cooling during the Delamerian Orogeny, to temperatures of ~100 °C at ~450 Ma. Following minor reburial at ~400 Ma, the inliers cooled to surface temperatures, interpreted to be the result of compression caused by the Carboniferous pulse of the Alice Springs Orogeny coupled with deformation from orocline formation within the Benambran Orogeny (Cayley, 2011; Moresi et al., 2014). This is supported by the presence of the Early Permian Mount Margaret erosion surface. Following minor burial at

~150-100 Ma, shallow crustal cooling reinstated the inliers at surface temperatures during the late Cretaceous. It is suggested that the final cooling pulse may have some relation to the break-up of Australia and Antarctica.

References

Ambrose, G.J., Flint, R.B., Webb, A.W., 1981. Precambrian and Palaeozoic Geology of the Peake and Denison Ranges. Geological Survey of South Australia Bullitin 50.

Ballèvre, M., Möller, A., Hensen, B.J., 2000. Exhumation of the lower crust during crustal shortening: an Alice Springs (380 Ma) age for a prograde amphibolite facies shear zone in the Strangways Metamorphic Complex (central Australia). Journal of Metamorphic Geology 18, 737-747.

Belton, D.X., Brown, R.W., Kohn, B.P., Fink, D., Farley, K.A., 2004. Quantitative resolution of the debate over antiquity of the central Australian landscape: implications for the tectonic and geomorphic stability of cratonic interiors. Earth and Planetary Science Letters 219, 21-34.

Boone, S.C., Seiler, C., Reid, A.J., Kohn, B., Gleadow, A., 2016. An Upper Cretaceous paleo -aquifer system in the Eromanga Basin of the central Gawler Craton, South Australia: evidence from apatite fission track thermochronology. Australian Journal of Earth Sciences 63, 315-331.

Bradshaw, J.D., Evans, P.R., 1988. Palaeozoic tectonics, Amadeus Basin, central Australia. APEA Journal 28, 267-282.

Brugger, J., Foden, J., Wulser, P.-A., 2011. Genesis and preservation of a uranium-rich paleozoic epithermal system with a surface expression (Northern Flinders Ranges, South Australia): radiogenic heat driving regional hydrothermal circulation over geological timescales. Astrobiology 11, 499+.

Budd, A.R., Fraser, G.L., 2004. Geological relationships and 40Ar/39Ar age constraints on gold mineralisation at Tarcoola, central Gawler gold province, South Australia. Australian Journal of Earth Sciences 51, 685-699.

Cao, M.-J., Hollings, P., Cooke, D.R., Evans, N., McInnes, B., Qin, K.-Z., Li, G.-M., Sweet, G., Baker, M., 2018. Physicochemical Processes in the Magma Chamber under the Black Mountain Porphyry Cu-Au Deposit, Philippines: Insights from Mineral Chemistry and Implications for Mineralization. Economic Geology 113, 63-82.

Cayley, R.A., 2011. Exotic crustal block accretion to the eastern Gondwanaland margin in the Late Cambrian–Tasmania, the Selwyn Block, and implications for the Cambrian–Silurian evolution of the Ross, Delamerian, and Lachlan orogens. Gondwana Research 19, 628-649.

Chew, D.M., Spikings, R.A., 2015. Geochronology and Thermochronology Using Apatite: Time and Temperature, Lower Crust to Surface. Elements 11, 189-194.

Cowley, W.M., Fanning, C.M., 1991. Low-grade Archaean metavolcanics in the northern Gawler Craton. Geological Survey of South Australia, Quarterly Geological Notes 119, 2-17.

Daly, S.J., Fanning, C.M., Fairclough, M.C., 1998. Tectonic evolution and exploration potential for the Gawler Craton, South Australia. AGSO Journal of Australian Geology and Geophysics 17, 145-168.

Daniels, J., 1975. Palaeogeographic development of Western Australia - Precambrian. Geological Survey of Western Australia, Perth, WA.

Drexel, J.F.,

Preiss, W. V.,, 1995. The Geology of South Australia, The Phanerozoic. The Geological Survey of South Australia Volume 2.

Ehrig, K., McPhie, J., Kamenetsky, V.S., 2012. Geology and mineralogical zonation of the Olympic Dam iron oxide Cu-U-Au-Ag deposit, South Australia. Society of Economic Geologists Special Publication.

Elburg, M.A., Andersen, T., Bons, P.D., Simonsen, S.L., Weisheit, A., 2013. New constraints on Phanerozoic magmatic and hydrothermal events in the Mt Painter Province, South Australia. Gondwana Research 24, 700-712.

Fairbridge, R.W., Finkl Jr, C.W., 1980. Cratonic erosional unconformities and peneplains. The Journal of Geology 88, 69-86.

Fanning, C.M., Reid, A.J., Teale, G., 2007. A geochronological framework for the Gawler Craton, South Australia. . South Australia. Geological Survey. Bulletin 55.

Foden, J., Elburg, M.A., Dougherty-Page, J., Burtt, A., 2006. The Timing and Duration of the Delamerian Orogeny: Correlation with the Ross Orogen and Implications for Gondwana Assembly. The Journal of Geology 114, 189-210.

Forbes, C.J., Giles, D., Jourdan, F., Sato, K., Omori, S., Bunch, M., 2012. Cooling and exhumation history of the northeastern Gawler Craton, South Australia. Precambrian Research 200–203, 209-238.

Foster, D.A., Ehlers, K., 1998. 40Ar-39Ar thermochronology of the southern Gawler Craton, Australia: Implications for Mesoproterozoic and Neoproterozoic tectonics of East Gondwana and Rodinia. Journal of Geophysical Research 103, 10,177-110,193.

Foster, D.A., Murphy, J.M., Gleadow, A.J.W., 1994. Middle tertiary hydrothermal activity and uplift of the northern flinders ranges, South Australia: Insights from apatite fission-track thermochronology. Australian Journal of Earth Sciences 41, 11-17.

Fraser, G., Reid, A., Stern, R., 2012. Timing of deformation and exhumation across the Karari Shear Zone, north-western Gawler Craton, South Australia. Australian Journal of Earth Sciences 59, 547-570.

Fraser, G.L., Lyons, P., 2006. Timing of Mesoproterozoic tectonic activity in the northwestern Gawler Craton constrained by 40Ar/39Ar geochronology. Precambrian Research 151, 160-184.

Fraser, G.L., Skirrow, R.G., Schmidt-Mumm, A., Holm, O., 2007. Mesoproterozoic Gold in the Central Gawler Craton, South Australia: Geology, Alteration, Fluids, and Timing. Economic Geology 102, 1511-1539.

Gibson, H.J., Stüwe, K., 2000. Multiphase cooling and exhumation of the southern Adelaide Fold Belt: constraints from apatite fission track data. Basin Research 12, 31-45.

Gleadow, A.J.W., Kohn, B.P., Brown, R.W., O'Sullivan, P.B., Raza, A., 2002. Fission track thermotectonic imaging of the Australian continent. Tectonophysics 349, 5-21.

Glen, R.A., 2005. The Tasmanides of eastern Australia. Geological Society, London, Special Publications 246, 23-96.

Gravestock, D.I., 1997. Geological setting and structural history., In: Morton, J., Drexel, J.F. (Eds.), Petroleum Geology of South Australia, vol. 3. Officer Basin. South Australian Department of Mines and Energy Resources (SADME) Report Book 97/19., pp. 5-44.

Green, P.F., Duddy, I.R., 2006. Interpretation of apatite (U–Th)/He ages and fission track ages from cratons. Earth and Planetary Science Letters 244, 541-547.

Hand, M., Reid, A., Jagodzinski, L., 2007. Tectonic Framework and Evolution of the Gawler Craton, Southern Australia. Economic Geology 102, 1377-1395.

Hibburt, J.E., 1984. Review of exploration activity in the Arckaringa Basin region 1858 to 1983. Report Book 84/1. Department of Mines and Energy. South Australia.

Hibburt, J.E., 1995. Arckaringa Basin, In: Drexel, J.F., Preiss, W.V. (Eds.), The geology of South Australia. Vol. 2, The Phanerozoic. South Australia. Geological Survey. Bulletin, pp. 73 - 76.

Hopper, D.J., 2001. Crustal evolution of paleo- to mesoproterozoic rocks in the Peake and Denison Ranges, South Australia, School of Physical Sciences. The University of Queensland, Brisbane (unpubl.), p. 216.

Houseman, G.A., Cull, J.P., Muir, P.M., Paterson, H.L., 1989. Geothermal signatures and uranium ore deposits on the Stuart Shelf of South Australia. Geophysics 54, 158-170.

Kirkland, C.L., Smithies, R.H., Spaggiari, C.V., Wingate, M.T.D., Quentin de Gromard, R., Clark, C., Gardiner, N.J., Belousova, E.A., 2017. Proterozoic crustal evolution of the Eucla basement, Australia: Implications for destruction of oceanic crust during emergence of Nuna. Lithos 278–281, 427-444.

Klootwijk, C., 2013. Middle–Late Paleozoic Australia–Asia convergence and tectonic extrusion of Australia. Gondwana Research 24, 5-54.

Long, J.A., Turner, S., Young, G.C., 1988. A Devonian fish fauna from subsurface sediments in the eastern Officer Basin, South Australia. Alcheringa: An Australasian Journal of Palaeontology 12, 61-78.

McLaren, S., Dunlap, W.J., Sandiford, M., McDougall, I., 2002. Thermochronology of high heat-producing crust at Mount Painter, South Australia: Implications for tectonic reactivation of continental interiors. Tectonics 21, 2-1-2-18.

Mitchell, M.M., Kohn, B.P., O'Sullivan, P.B., Hartley, M.J., Foster, D.A., 2002. Low-temperature thermochronology of the Mt Painter Province, South Australia. Australian Journal of Earth Sciences 49, 551-563.

Moresi, L., Betts, P.G., Miller, M.S., Cayley, R.A., 2014. Dynamics of continental accretion. Nature 508, 245-248.

Neumann, N., Sandiford, M., Foden, J., 2000. Regional geochemistry and continental heat flow: implications for the origin of the South Australian heat flow anomaly. Earth and Planetary Science Letters 183, 107-120.

Preiss, W.V., 2000. The Adelaide Geosyncline of South Australia and its significance in Neoproterozoic continental reconstruction. Precambrian Research 100, 21-63.

Rankin, L.R., Martin, A.R., Parker, A.J., 1989. Early Proterozoic history of the Karari Fault Zone, northwest Gawler Craton, South Australia. Australian Journal of Earth Sciences 36, 123-133.

Reddy, M., Glorie, S., Reid, A.J., Collins, A.S., 2015. Phanerozoic cooling history of the central Gawler Craton: implications of new low-temperature thermochronological data. MESA Journal 75, 56-60.

Reid, A., Hand, M., Jagodzinski, E., Kelsey, D., Pearson, N., 2008. Paleoproterozoic orogenesis in the southeastern Gawler Craton, South Australia. Australian Journal of Earth Sciences 55, 449-471.

Reid, A.J., Jagodzinski, E.A., Armit, R.J., Dutch, R.A., Kirkland, C.L., Betts, P.G., Schaefer, B.F., 2014a. U-Pb and Hf isotopic evidence for Neoarchean and Paleoproterozoic basement in the buried northern Gawler Craton, South Australia. Precambrian Research 250, 127-142.

Reid, A.J., Jagodzinski, E.A., Fraser, G.L., Pawley, M.J., 2014b. SHRIMP U–Pb zircon age constraints on the tectonics of the Neoarchean to early Paleoproterozoic transition within the Mulgathing Complex, Gawler Craton, South Australia. Precambrian Research 250, 27-49.

Reid, A.J., Jourdan, F., Jagodzinski, E.A., 2017. Mesoproterozoic fluid events affecting Archean crust in the northern Olympic Cu–Au Province, Gawler Craton: insights from 40Ar/39Ar thermochronology. Australian Journal of Earth Sciences 64, 103-119.

Russell, M., Gurnis, M., 1994. The planform of epeirogeny: vertical motions of Australia during the Cretaceous. Basin Research 6, 63-76.

Sandiford, M., Hand, M., 1998. Controls on the locus of intraplate deformation in central Australia. Earth and Planetary Science Letters 162, 97-110.

Skirrow, R.G., Bastrakov, E.N., Barovich, K., Fraser, G.L., Creaser, R.A., Fanning, C.M., Raymond, O.L., Davidson, G.J., 2007. Timing of Iron Oxide Cu-Au-(U) Hydrothermal Activity and Nd Isotope Constraints on Metal Sources in the Gawler Craton, South Australia. Economic Geology 102, 1441-1470.

Tomkins, A.G., Dunlap, W.J., Mavrogenes, J.A., 2004. Geochronological constraints on the polymetamorphic evolution of the granulite-hosted Challenger gold deposit: implications for assembly of the northwest Gawler Craton*. Australian Journal of Earth Sciences 51, 1-14.

Webb, A.W., Thomson, B.P., Blissett, A.H., Daly, S.J., Flint, R.B., Parker, A.J., 1986. Geochronology of the Gawler Craton, South Australia. Australian Journal of Earth Sciences 33, 119-143.

Weisheit, A., Bons, P.D., Danisík, M., Elburg, M.A., 2014. Crustal-scale folding: Palaeozoic deformation of the Mt Painter Inlier, South Australia. Geological Society, London, Special Publications 394, 53-77.

Womer, M.B., Baker, R.N., J., N.E., van Nieuwenhuise, R., 1987. Technical evaluation of PEL 29, east Officer Basin, South Australia, for Amoco Australia Petroleum Co. South Australia. Department of Mines and Energy. Open File Envelope.

Wopfner, H., 1970. Permian paleogeography and depositional environment of the Arckaringa Basin, South Australia. , Second Gondwana symposium, Council for Scientific and Industrial Research, Scientia, South Africa, pp. 273-291.

Chapter 1

Apatite U-Pb map for the northern Gawler Craton

Published as:

Hall, J.W., Glorie, S., Reid, A.J., Boone, S.C., Collins, A.S., and Gleadow, A., 2018, An Apatite U–Pb Thermal History Map for the Northern Gawler Craton, South Australia. Geoscience Frontiers.

Statement of Authorship

Title of Paper	An apatite U–Pb thermal history map for the northern Gawler Craton, South Australia
Publication Status	☐ Published ☑ Accepted for Publication ☐ Submitted for Publication ☐ Unpublished and Unsubmitted work written in manuscript style
Publication Details	Hall, J.W., Glorie, S., Reid, A.J., Boone, S.C., Collins, A.S., and Gleadow, A., 2018, An Apatite U–Pb Thermal History Map for the Northern Gawler Craton, South Australia. Geoscience Frontiers.

Principal Author

Name of Principal Author (Candidate)	James Hall		
Contribution to the Paper	Sample collection, data collection, data interpretation, manuscript and figure composition.		
Overall percentage (%)	70 %		
Certification:	This paper reports on original research I conducted during the period of my Higher Degree by Research candidature and is not subject to any obligations or contractual agreements with a third party that would constrain its inclusion in this thesis. I am the primary author of this paper.		
Signature		Date	1/05/18

Co-Author Contributions

By signing the Statement of Authorship, each author certifies that:

i. the candidate's stated contribution to the publication is accurate (as detailed above);

ii. permission is granted for the candidate in include the publication in the thesis; and

iii. the sum of all co-author contributions is equal to 100% less the candidate's stated contribution.

Name of Co-Author	Stijn Glorie		
Contribution to the Paper	Assistance in data collection, assistance in data interpretation, manuscript review. 10% contribution.		
Signature		Date	1/05/18

Name of Co-Author	Anthony Reid		
Contribution to the Paper	Sample collection, assistance in data interpretation, manuscript review . 5% contribution.		
Signature		Date	11/05/18
Name of Co-Author	Samuel Boone		
Contribution to the Paper	Sample collection, manuscript review . 5% contribution.		
Signature		Date	10/4/18
Name of Co-Author	Alan Collins		
Contribution to the Paper	Assistance in data interpretation, manuscript review . 5% contribution.		
Signature		Date	27/6/18
Name of Co-Author	Andrew Gleadow		
Contribution to the Paper	Assistance in data interpretation, manuscript review . 5% contribution.		
Signature		Date	26/4/18

Abstract

Apatite U–Pb thermochronology was applied to granitoid basement samples across the northern Gawler Craton to unravel the Proterozoic, post-orogenic, cooling history and to examine the role of major fault zones during cooling. Our observations indicate that cooling following the ~2500 Ma Sleaford Orogeny and ~1700 Ma Kimban Orogeny is restricted to the Christie and Wilgena Domains of the central northern Gawler Craton. The northern Gawler Craton mainly records post-Hiltaba Event (~1590 Ma) U–Pb cooling ages. Cooling following the ~1560 Ma Kararan Orogeny is preserved within the Coober Pedy Ridge, Nawa Domain and along major shear zones within the south-western Fowler Domain. The Nawa Domain samples preserve U–Pb cooling ages that are >150 Ma younger than the samples within the Coober Pedy Ridge and Fowler Domain, indicating that later (~1300 Ma) fault movement within the Nawa Domain facilitated cooling of these samples, caused by arc collision in the Madura Province of eastern Western Australia. When compared to $^{40}Ar/^{39}Ar$ from muscovite, biotite and hornblende, our new apatite U–Pb ages correlate well, particularly in regions of higher data density. Our data also preserve a progressive younging of U–Pb ages from the nucleus of the craton to the periphery with a stark contrast in U–Pb ages across major structures such as the Karari Shear Zone and the Southern Overthrust, which indicates the timing of reactivation of these major crustal structures. Although this interpolation was based solely on thermochronological data and did not take into account structural or other geological data, these maps are consistent with the structural architecture of the Gawler Craton and reveal the thermal footprint of known tectonic and magmatic events in the Gawler Craton.

1.1 Introduction

The duration and extent of tectonic events within a long-lived craton can be difficult to determine (Daly et al., 1998; Hand et al., 2007). The difficulty is increased when major crustal structures are reactivated in different stress regimes by different tectonic events (e.g. Butler et al., 1997; Shaw et al., 2001; Williams and Betts, 2009), subsequently erasing evidence of older tectonic events. However, these structures play a key role in the longevity and stability of cratonic crust and influence their thermal histories. The chronology of these structures are often difficult to determine due to factors such as outcrop availability, or difficulty in dating the timing of movement (Reddy and Potts, 1999; Müller, 2003). Australia contains many examples of reworking of major crustal structures in long-lived cratons (e.g. Direen et al., 2005; Dutch et al., 2008; Williams and Betts, 2009; Stewart and Betts, 2010; Fraser et al., 2012; Glorie et al., 2017), such as those in the Gawler Craton of South Australia (Fig. 1.1). Shear zones in the Gawler Craton underwent extensive reworking in response to intracontinental stresses (e.g. Betts and Giles, 2006; Hand et al., 2007). Chronological data within the Gawler Craton related to tectonism and movement of major structures is dominated by monazite U–Pb (Dutch et al., 2008; Payne et al., 2008; Dutch et al., 2010), muscovite and biotite $^{40}Ar/^{39}Ar$ (Swain et al., 2005; Fraser and Lyons, 2006; Forbes et al., 2012; Fraser et al., 2012), and apatite fission track studies (Gleadow et al., 2002; Hall et al., 2016).

However, recent advancements in the U–Pb dating of apatite (Chew et al., 2011; Chew et al., 2014), allow the use of a new radiometric clock to calculate cooling ages through a closure temperature of ~350 – 550 °C (Chew and Spikings, 2015). This is an emerging method which can be applied to many different settings, such as the thermochronology of mineral deposits (e.g. Liu et al., 2014), or constraints on rift formation (e.g. Zhang et al., 2017) or to date mafic rocks (e.g. Pochon et al., 2016). Here, we have applied the apatite U–Pb radiometric clock to enhance our understanding of the buried Gawler Craton terranes and their Proterozoic thermal evolution.

We present the first apatite U–Pb dataset from within the Gawler Craton, to uncover the spatial distribution of cooling events in relation to various tectonic events throughout the Palaeo-Mesoproterozoic. This dataset reveals post-orogenic cooling from at least four different orogenic events, over a ~1 Ga time span from ~2.3 Ga to 1.3 Ga. The apatite U–Pb data are subsequently compared to pre-existing muscovite, biotite and hornblende $^{40}Ar/^{39}Ar$ data from the Gawler Craton (Foster and Ehlers, 1998; Tomkins and Mavrogenes, 2002; Budd and Fraser, 2004; Tomkins et al., 2004; Fraser and Lyons, 2006; Forbes et al., 2012; Fraser et al., 2012; Reid et al., 2017). These two datasets reveal ages that are well correlated, and therefore have been combined to produce a Mesoproterozoic middle crustal cooling map that illustrates the spatial extent for the timing of the ~550 – 350 °C cooling history across the northern Gawler Craton at the present-day surface. In addition, they provide valuable information concerning the timing of reactivation of major crustal structures as both datasets preserve differential cooling across these major structures.

1.2 Geological setting

The Gawler Craton is an Archaean – Mesoproterozoic craton that occupies most of South Australia. There are two major periods of craton growth, firstly, during the late Archaean (~2500 – 2400 Ma) and then from ~2000 Ma to 1550 Ma (Daly et al., 1998; Hand et al., 2007). These two periods of craton growth are separated by an interval of quiescence with no recorded geological activity (Fig. 1.2). The Gawler Craton can be subdivided into a number of different domains based on magnetic surveys (Fairclough et al., 2003). The northern Gawler Craton consists of the Coober Pedy Ridge, Mount Woods Inlier, Nawa, Christie, Fowler, Wilgena, Coulta, Nuyts, and Olympic domains (Fig. 1.1). The rocks that make up these domains are discussed below and the associated periods of craton development are summarised in Fig. 1.2.

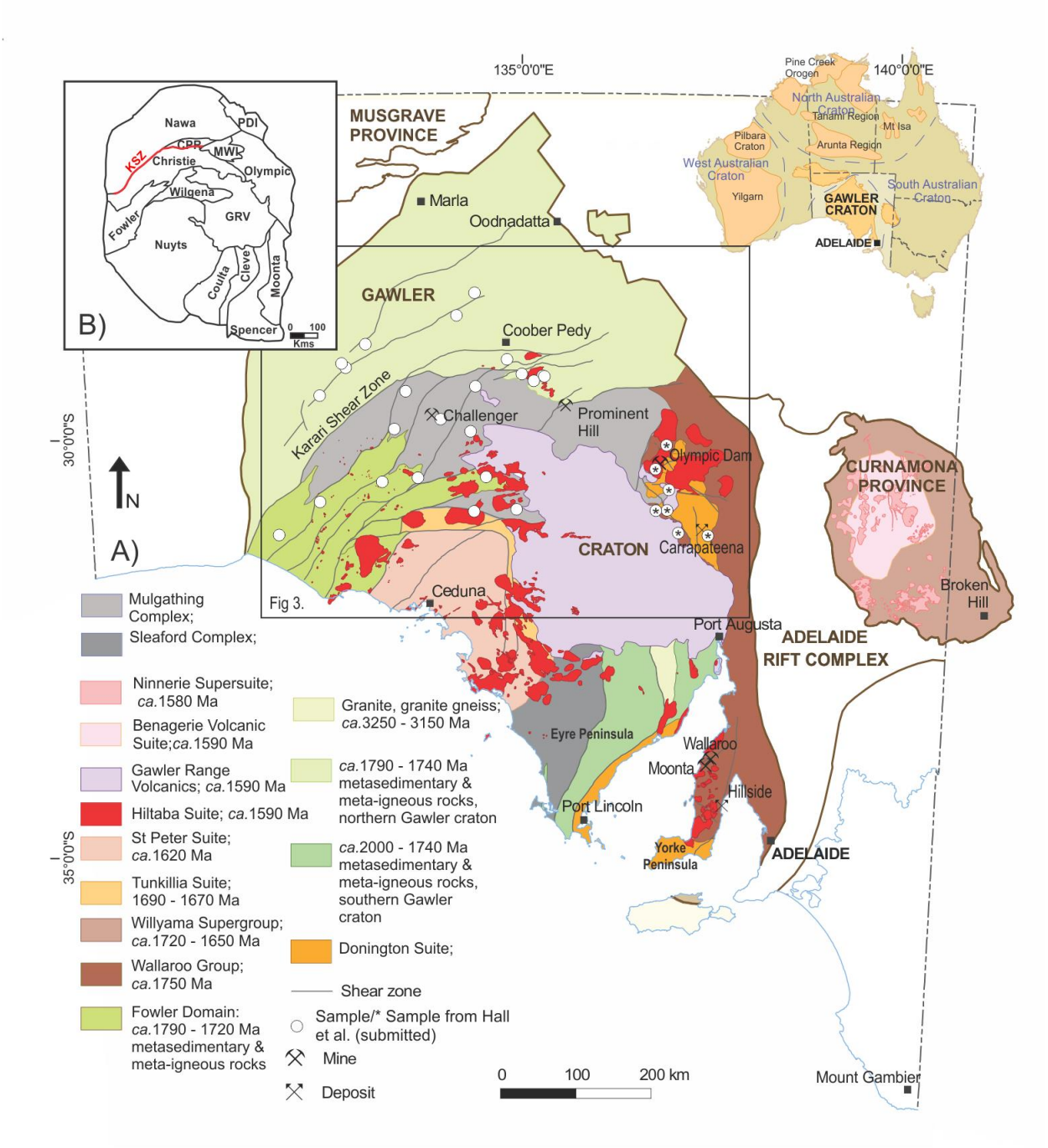

Figure 1.1: (A) Simplified geological map of the Gawler Craton, indicating the locations of all apatite U–Pb samples (including samples from Hall et al., submitted), and major mineral deposits. Inset (B) illustrating the boundaries of all the domains within the Gawler Craton. Abbreviations are: PDI–Peake and Denison Inliers; CPR–Coober Pedy Ridge; MWI–Mt. Woods Inlier; KSZ–Karari Shear Zone; GRV–Gawler Range Volcanics. Modified from Reid et al. (2014).

The Sleaford and Mulgathing complexes form the Archaean nucleus of the Gawler Craton (Fig. 1.1). They both include ~2560 – 2480 Ma volcanosedimentary rocks and felsic to intermediate intrusions (Cowley and Fanning, 1991; Jagodzinski et al., 2009; Reid et al., 2009; Reid et al., 2010; Reid et al., 2014), these complexes are located in the north-west Christie Domain (Mulgathing Complex) and central south Coulta Domain (Sleaford Complex) of the craton. They were subsequently deformed and metamorphosed during the Sleafordian Orogeny at ~2470 – 2410 Ma (Daly et al., 1998; Fanning et al., 2007; Reid et al., 2014). The Sleafordian Orogeny reached granulite facies and metamorphic conditions of ~850 °C and 5 – 7 kbar in the central Mulgathing Complex (Halpin and Reid, 2016). The end of the orogeny ushered in a ~400 Ma tectonic hiatus within the Gawler Craton and signalled the end of the first phase of craton growth (Hand et al., 2007).

The second phase of craton growth can be further divided into rift-basin development from ~2000 – 1690 Ma and magmatism from 1690 – 1500 Ma (Hand et al., 2007). To the east, deposition of the Hutchison Group (Parker and Lemon, 1982; Fanning et al., 2007; Szpunar et al., 2011), and the emplacement of the Donington Suite at ~1850 Ma (both located within the Olympic Domain; Fig. 1.1) initiated the second phase (Fig. 1.1; Jagodzinski, 2005). Reid et al. (2008) suggested that the Donington Suite was emplaced in an intracontinental back arc basin setting, and was associated with the ~1850 – 1840 Ma Cornian Orogeny. Further rifting along the eastern margin accommodated the deposition of the Wallaroo Group and its associated magmatism from 1770 – 1740 Ma, while widespread coeval deposition across the Gawler Craton is represented by the formation of the Price Metasediments, Moonabie Formation, Mount Woods Inlier Sediments, Peake Metamorphics, and metasediments within the Fowler and Nawa domains (Fig. 1.1; Fanning et al., 1988; Parker et al., 1993; Oliver and Fanning, 1997; Daly et al., 1998; Cowley et al., 2003; Jagodzinski, 2005; Hand et al., 2007).

The craton-wide 1730 – 1690 Ma, high temperature, deformation event known as the Kimban Orogeny, caused magmatism and transpressional deformation, particularly in the southern Gawler Craton (Hand et al., 2007). The peak metamorphic conditions ranged from 800 – 900 °C and 7 – 10 kbar (Parker et al., 1993; Payne et al., 2008), with the highest metamorphic conditions recorded in the far west of the craton, in the Fowler Domain. Stresses related to the Kimban Orogeny were accommodated by movement along the Karari Shear Zone and Tallacootra Shear Zone at ~1680 ± 37 Ma in the Fowler Domain (Swain et al., 2005; Stewart et al., 2009).

Following the start of the Kimban Orogeny, the 1690 – 1670 Ma I-type Tunkillia Suite was emplaced in the central Gawler Craton (Ferris and Schwarz, 2004). In the southwest Gawler Craton,

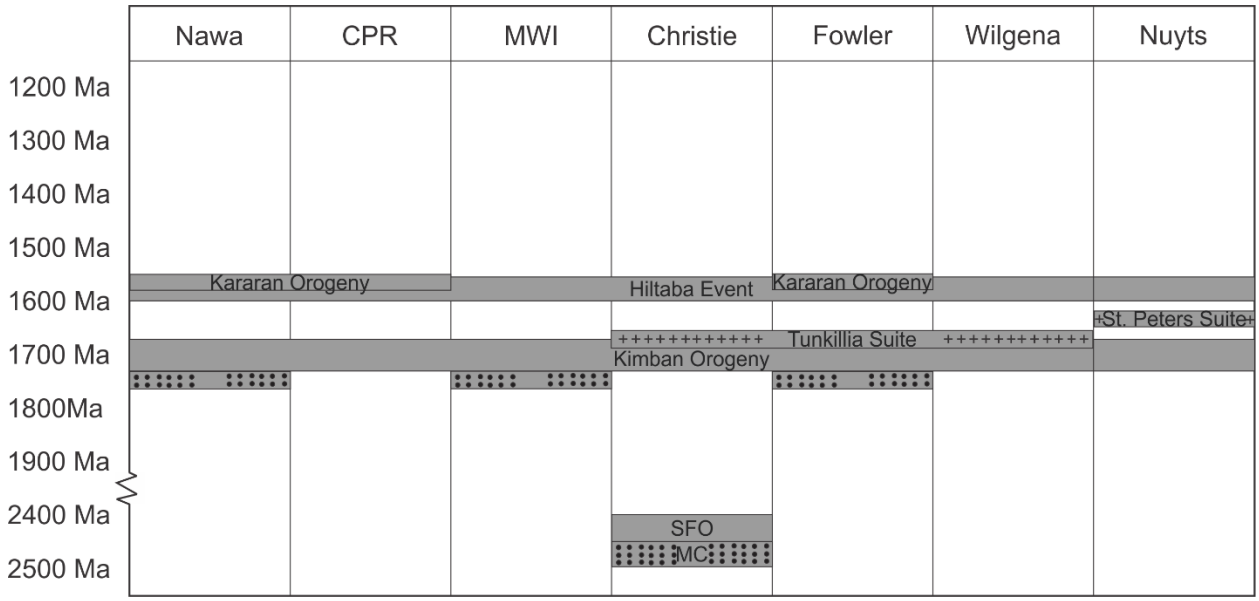

Figure 1.2: Simplified time-space plot illustrating the different geological events within the different domains of the Gawler Craton through time. The domains are ordered from north, on the left, to south, on the right. Abbreviations are: CPR–Coober Pedy Ridge; MWI–Mt. Woods Inlier; SFO–Sleaford Orogeny; MC–Mulgathing Complex.

the St. Peter Suite and co-magmatic Nuyts volcanics were emplaced at ~1620 Ma forming the Nuyts Domain (Flint et al., 1990; Rankin et al., 1990; Budd et al., 2001; Hand et al., 2007). This was followed by the ~1590 – 1570 Ma Hiltaba event that emplaced the Hiltaba Granite and co-magmatic Gawler Range Volcanics (Fig. 1.1; Giles, 1988; Creaser and White, 1991; Creaser, 1996; Daly et al., 1998; Budd et al., 2001; Skirrow et al., 2002). This event represents one of the largest felsic volcanic systems in the world (Allen et al., 2008) and is associated with the formation of the world class Olympic Dam Cu-Au-U deposit (e.g. McPhie et al., 2011; Ehrig et al., 2012). In addition, the Hiltaba event was associated with deformation around the Gawler Craton, with northwest-southeast compression and metamorphism in the Mount Woods Inlier. The metamorphic conditions reached temperatures of 750 °C at ~4.7 kbar during peak metamorphism (Forbes et al., 2011). Immediately following this metamorphism, the Mt. Woods Inlier underwent exhumation that has been interpreted to be caused by arrival of a mantle plume at the nearby subduction zone which resulted in compression along the Southern Overthrust in the Mount Woods Inlier (Fig. 1.1; Betts et al., 2009; Forbes et al., 2012).

The ~1590 – 1560 Ma Kararan Orogeny is the youngest Proterozoic orogenic event recorded within the Gawler Craton, which deformed and metamorphosed the northeast of the craton, including the Karari Shear Zone (Fig. 1.3; Rankin et al., 1989; Hand et al., 2007; Fraser et al., 2012). The south western Fowler Domain records peak metamorphic conditions of 800 °C and 10 kbar resulting from this orogeny (Teasdale, 1997; Fanning et al., 2007), while Fraser et al. (2012)

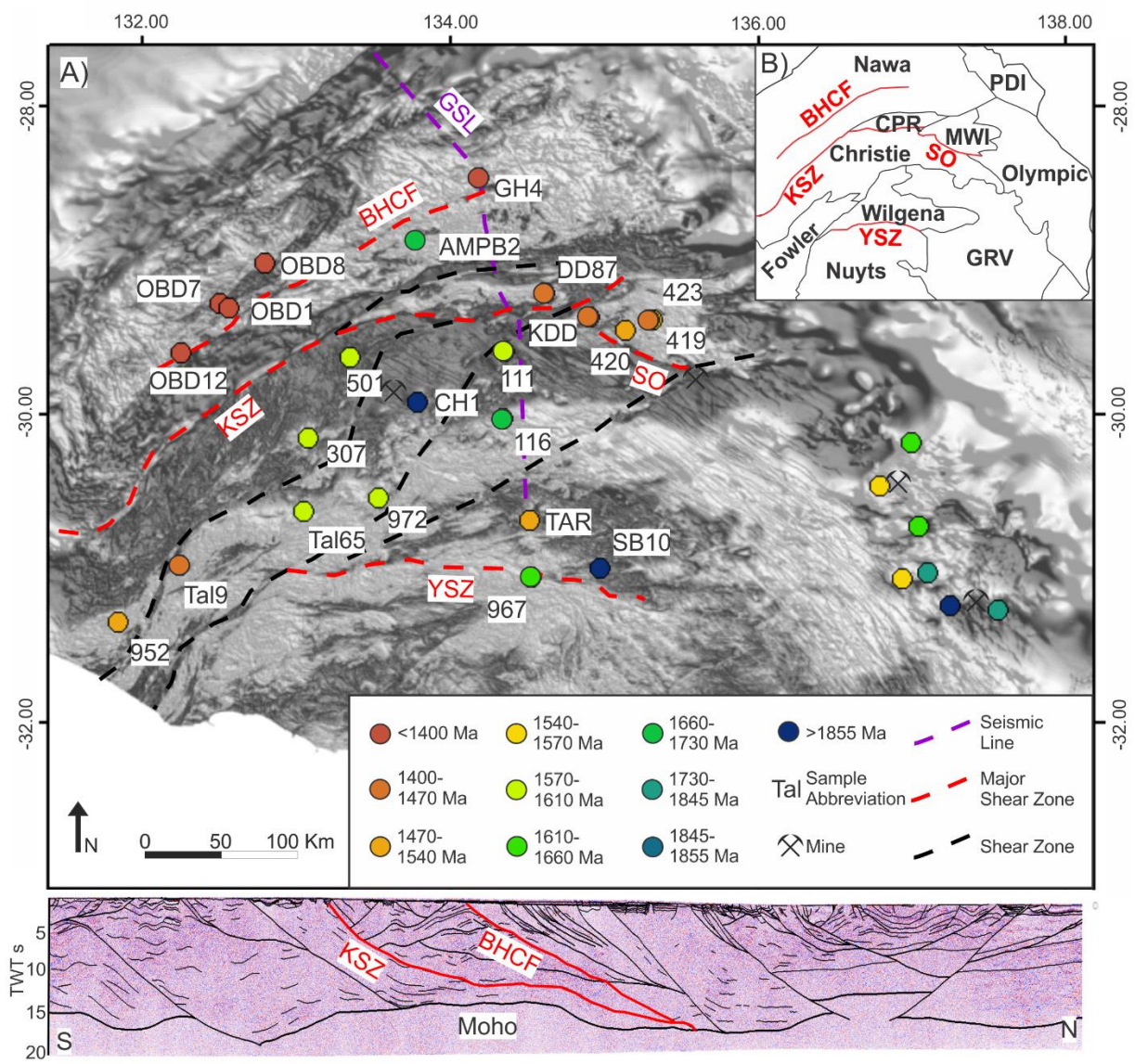

Figure 1.3: Total Magnetic Intensity (TMI) map of the northern Gawler Craton which reveals shear zones, major mineral mines, the GOMA seismic line, and sample locations (including samples from Hall et al., submitted) and weighted mean ages. GOMA seismic line adapted from Korsch et al. (2010). Abbreviations are: GSL–GOMA seismic line; BHCF–Box Hole Creek Fault; KSZ–Karari Shear Zone; SO–Southern Overthrust; YSZ–Yerda Shear Zone. OBD12– 2131385 from drill hole OBD 12; OBD7– 2131379 from drill hole OBD 7; OBD1– 2131386 from drill hole OBD 01; OBD8– 2131380 from drill hole OBD 8; AMPB2– 2131373 from drill hole AM/PB 2; GH4– 2131374 from drill hole GOMA DH4; DD87– 2131367 from drill hole DD87LR 3; KDD– 2131371 from drill hole KDD 005; 420– 1039420; 423– 1039423; 419– 1039419; 307– 0307; 501– 0501; CH1– 2131395 from drill hole CH 1; Wall1– 650666 from drill hole Wallira 1; 111– 2016111; 952– 2017952; Tal9– 1472758 from drill hole Tal 9; Tal65– 1472763 from drill hole Tal 65; 972– 2017972; 116– 2016116; 967– 2017967; SB10– SB12-10. Inset (B) shows the boundaries of the domains within the northern Gawler Craton. Abbreviations are: PDI– Peake and Denison Inliers; BHCF– Box Hole Creek Fault; CPR– Coober Pedy Ridge; MWI– Mt. Woods Inlier; KSZ– Karari Shear Zone; SO– Southern Overthrust; GRV– Gawler Range Volcanics; YSZ– Yerda Shear Zone.

suggested that up to 10 km of exhumation of the Nawa Domain occurred along the Karari Shear Zone during this orogenic event. Both the Yerda Shear Zone and the Coorabie Shear Zone, in the Wilgena and Fowler Domains (Fig. 1.1), recorded movement at ~1500 Ma following the Kararan Orogeny (McLean and Betts, 2003; Swain et al., 2005). A final period of movement along the Karari Shear zone is recorded at ~1450 Ma and is interpreted to be sinistral strike-slip movement (Fraser and Lyons, 2006; Fraser et al., 2012), whereas coeval deformation on the Tallacootra Shear Zone is interpreted as forming a large dextral positive flower structure (Stewart et al., 2009).

1.3 Methodology

All samples were collected from granitiods, either drill core (where the basement was buried), or from exposed rock outcrop. Samples were collected with the intention of an even coverage across major structures (such as the Karari Shear Zone) throughout the major domains that constitute the northern Gawler Craton. The sampling strategy was therefore aimed at observing the cooling history of the northern Gawler Craton within each domain and across the major structures (Table 1.1).

Because all sampled rocks were either igneous rocks, or metamorphic rocks that experienced temperatures above ~550 °C, apatite U–Pb dating preserves the timing that apatite cooled below its closure temperature of ~550 – 350 °C (Chew and Spikings, 2015). Samples were crushed and separated using conventional crushing and separating techniques. Apatites were handpicked, mounted in epoxy resin, and then ground and polished to reveal internal crystal surfaces. Uranium and lead data collection on the Laser-Ablation Inductively-Coupled-Plasma Mass-Spectrometer (LA-ICP-MS) was performed at Adelaide Microscopy, The University of Adelaide. Measured masses were: ^{238}U, ^{232}Th, ^{208}Pb, ^{207}Pb, ^{206}Pb, ^{204}Pb, ^{91}Zr, ^{44}Ca, ^{43}Ca, ^{35}Cl, and ^{29}Si. All samples were ablated for 30 s on a 30 µm spot at ~ 5 J/cm^2, after a 30 s laser warm up period and a 20 s dwell in between samples. All samples were ablated with a *New Wave 213* laser. Samples SB12 – 10, 12, 13 and TAR were analysed on an *Agilent 7900* quadrupole mass-spectrometer, while all remaining samples analysed on the previously used *Agilent 7500* quadrupole mass-spectrometer. Madagascar apatite (474.25 ± 0.41 Ma, *n* = 9, MSWD = 1.5; Thomson et al., 2012) was used as the primary standard, with Durango apatite (31.44 ± 0.18 Ma; McDowell et al., 2005) and Mt. McClure apatite (518 ± 11 Ma; Thomson et al., 2012) used as secondary standards. We obtained a weighted mean ^{206}Pb–^{238}U age of 473.4 ± 2.0 Ma (*n* = 227, MSWD = 0.76) for Madagascar apatite, and ^{207}Pb corrected weighted mean ^{206}Pb–^{238}U ages of 32.08 ± 0.74 Ma (*n* = 90, MSWD = 0.79) for Durango and 529.1 ± 7.2 Ma (*n* = 57, MSWD = 1.6) for Mt. McClure (Fig. 1.4). All data reduction was completed on *Iolite* software (Paton et al., 2011) using the data reduction scheme *VizualAge_UcomPbine*, following the method outlined by Chew et al. (2011, 2014). Common Pb was corrected for using the ^{207}Pb correction (Chew et al., 2014) based on the initial measured ^{207}Pb/^{206}Pb ratio for individual samples. This is calculated using a Concordia line (referred to as a common Pb line) through the individual analyses on a Tera-Wasserburg plot. Analyses that

contained strongly zoned elemental signals or large uncertainties, often due to low ^{238}U (<2 ppm), were removed during data reduction. Few additional individual outliers, which plotted away from the corresponding common Pb line in Tera-Wasserburg plots, were also removed. Similar methods for data treatment based on the same criteria are outlined in Zattin et al. (2012) and Mark et al. (2016). Concordia and weighted mean plots were created using *Isoplot 4.15* (Ludwig, 1999; Ludwig, 2012).

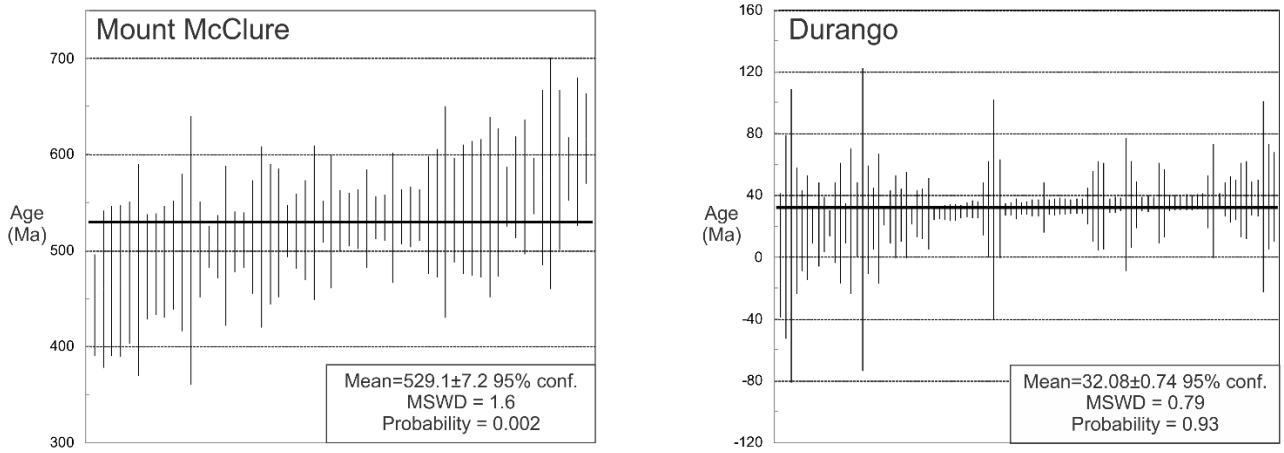

Figure 1.4: ^{207}Pb corrected weighted mean ^{206}Pb–^{238}U age for secondary standards Mount McClure (518±11 Ma; Thomson et al., 2012) and Durango (31.44±0.18 Ma; McDowell et al., 2005). Weighted mean is ordered by age.

1.4 Results

All apatite U–Pb data are reported in Table 1.2 and Fig. 1.5.

1.4.1 Nawa Domain

Sample 2131385 is a paragneiss that was collected from drill hole OBD 12. It displays a ^{207}Pb corrected weighted mean ^{206}Pb–^{238}U age of 1289 ± 32 Ma with a MSWD of 1.3 from an average common Pb line with a lower intercept of 1284 ± 93 Ma (MSWD =3.2; Fig. 1.5A).

A ^{207}Pb corrected weighted mean ^{206}Pb–^{238}U age of 1382 ± 13 Ma was recorded for sample 2131379 (a granite collected down drill hole OBD 7), with a MSWD of 1.3. The accompanying Tera-Wasserburg plot revealed a common Pb line lower intercept of 1382 ± 30 Ma with an MSWD of 1.6 (Fig. 1.5B).

Sample 2131386 is a paragneiss that was collected from drill hole OBD 01 and is located within 7 km of 2131379. The ^{207}Pb corrected weighted mean ^{206}Pb–^{238}U age is recorded as 1385 ± 19 Ma

(MSWD of 1.02). The lower intercept of the common Pb line was recorded at 1384 ± 25 Ma (MSWD = 1.2; Fig. 1.5C).

A ^{207}Pb corrected weighted mean ^{206}Pb–^{238}U age of 1276 ± 31 Ma was obtained for sample 2131380 (a granite from drill hole OBD 8), with a MSWD of 1.5. The accompanying Tera-Wasserburg plot displays a common Pb line lower intercept of 1282 ± 76 Ma (MSWD of 1.9; Fig. 1.5D).

Sample 2131373 was collected from a paragneiss within drill hole AM/PB 2. This sample failed to produce a reliable common Pb line. The best common-Pb line estimate reveals a lower intercept of 1661 ± 57 Ma (MSWD=3.3), controlled by three grains outside of a cluster of U–Pb ages (Fig. 1.5E). The ^{207}Pb corrected weighted mean ^{206}Pb–^{238}U age 1661 ± 27 Ma produced a MSWD of 2.8. A biotite ^{40}Ar/^{39}Ar plateau age of 1554 ± 5 Ma from the same drill hole (Fraser et al., 2012) suggests that the sample had cooled to temperatures of ~300 °C by this time.

Only five grains were analysed from sample 2131374 (a paragneiss from drill hole GOMA DH4), however, an adequate common Pb line was produced, with a lower intercept of 1334 ± 160 Ma with an MSWD of 0.48. An associated ^{207}Pb corrected weighted mean ^{206}Pb–^{238}U age of 1331 ± 50 Ma was produced from this common Pb line, with an MSWD of 0.17 (Fig. 1.5F).

In summary, the five reliable samples within the Nawa Domain preserve U–Pb ages between 1276 ± 31 Ma and 1385 ± 19 Ma, which suggests cooling through ~550 – 350 °C across the terrane at ~1400 – 1300 Ma. The final sample preserves a poorly constrained older age of 1661 ± 57 Ma which, when combined with a biotite ^{40}Ar/^{39}Ar from Fraser et al. (2012) indicates that this sample cooled below ~300 °C over 150 Ma before the other five samples within the Nawa Domain.

1.4.2 Coober Pedy Ridge & Mt. Woods Inlier

Sample 2131367, which was collected from a gabbro down drill hole DD87LR 3, produced a reliable common Pb line with a lower intercept of 1402 ± 33 and a MSWD of 1.4. This common-Pb line was used in the calculation of the ^{207}Pb corrected weighted mean ^{206}Pb–^{238}U age of 1413 ± 17 Ma (MSWD=1.03; Fig. 1.5G). This age is slightly younger than the recorded biotite ^{40}Ar/^{39}Ar pseudo-plateau age of 1476 ± 5 Ma from the same drill hole (Fraser et al., 2012), which indicates this sample underwent cooling at ~1.4 Ga.

A ^{207}Pb corrected weighted mean ^{206}Pb–^{238}U age of 1429 ± 29 Ma (MSWD of 1.15) was obtained from sample 2131371 (a paragneiss collected from KDD 005). A common Pb line with a lower intercept of 1449 ± 91 Ma (MSWD = 1.8; Fig. 1.5H) was also calculated from these data.

Sample	Drill hole number	Latitude	Longitude	Depth (m)	Region	Rock type	Formation age	Metamorphic Age (mineral)
2131385	*OBD 12*	*-29.6008065*	*132.2554548*	*470-471*	*Nawa Domain*	*paragneiss*	~1740 Ma	~1550 Ma (zircon)
2131379	*OBD 7*	*-29.2831073*	*132.5062594*	*261-262*	*Nawa Domain*	*granite*	1752±9 Ma	1715±17 Ma (zircon)
2131386	*OBD 01*	*-29.310519*	*132.568165*	*139-140*	*Nawa Domain*	*paragneiss*	1752±9 Ma	1715±17 Ma (zircon)
2131380	*OBD 8*	*-29.017528*	*132.8058533*	*183-184*	*Nawa Domain*	*granite*	~1740 Ma	1458±9 Ma (monazite)
2131373	*AM/PB 2*	*-28.8199561*	*133.8273135*	*344-345*	*Nawa Domain*	*paragneiss*	~1740 Ma	1555±11 Ma (Monazite)
2131374	*GOMA DH4*	*-28.4687532*	*134.1938652*	*512-514*	*Nawa Domain*	*paragneiss*	2462±17 Ma	1523±10 Ma (zircon)
2131367	*DD87LR 3*	*-29.2146561*	*134.619117*	*93-95*	*Coober Pedy Ridge*	gabbro	~1740 Ma	-
2131371	*KDD 005*	*-29.3758388*	134.9082905	*333-336*	*Coober Pedy Ridge*	*paragneiss*	~1740 Ma	1590±10 Ma (monazite)
1039420	-	*-29.389993*	*135.295242*	-	*Mt. Woods Inlier*	granite	1584±18 Ma	-
1039423	-	-29.4616	*135.145611*	-	*Mt. Woods Inlier*	granite	1584±18 Ma	-
1039419	-	*-29.396233*	*135.313564*	-	*Mt. Woods Inlier*	granite	1584±18 Ma	-
0307	-	*-30.15667473*	*133.088121117*	-	*Christie Domain*	granite	1695±6 Ma	-
0501	-	*-29.63513888*	*133.3580277*	-	*Christie Domain*	*tonalite*	2493±6 Ma	2565 Ma (Zircon)
2131395	*CH 1*	*-29.9253457*	*133.7903421*	*68-80*	*Christie Domain*	*granite*	2440±20 Ma	-
2016111	-	*-29.5934*	*134.355*	-	*Christie Domain*	granite	1578±7 Ma	-
2017952	-	*-31.3528*	*131.8547*	-	*Fowler Domain*	gabbro	1739±6 Ma	1718±15 Ma (zircon)
1472758	*Tal 9*	*-30.9871284*	*132.2473098*	*21.8-22.5*	*Fowler Domain*	*paragneiss*	1698±7 Ma	-
1472763	*Tal 65*	*-30.6371679*	*133.0589695*	*56-59.5*	*Fowler Domain*	gabbronorite	1583±5 Ma	-
2017972	-	*-30.5509*	*133.5415*	-	*Fowler Domain*	granite	1692±15 Ma	-
2016116	-	*-30.0318*	*134.3451*	-	*Wilgena Domain*	granite	~1730 Ma	-
TAR	-	*-30.689*	*134.517*	-	*Wilgena Domain*	granite	1587±20 Ma	-
2017967	-	*-31.0582*	*134.5313*	-	*Wilgena Domain*	granite	1732±15 Ma	-
SB12-10	-	*-31.008*	*134.976*	-	*Wilgena Domain*	granite	2507±3 Ma	-

Table 1.1: Sample details. Formation ages from Finlay (1993) Daly et al. (1998), Cowley (2005), Payne et al. (2006), Hand et al. (2007), Jagodzinski et al. (2009), Jagodzinski and Reid (2010), Howard et al. (2011a), Howard et al. (2011b), Reid et al. (2014), Reid and Fabris (2015), and Dawson (2016).

Figure 1.5 (next page): Tera-Wasserburg concordia plots and associated ^{207}Pb corrected weighted mean plots for all samples. Data points with dashed lines were included in ^{207}Pb correction but were later excluded from the weighted mean plots. Tera-Wasserburg plots that contain dashed data-symbols indicate these analyses were used in the ^{207}Pb correction but have been removed from the ^{207}Pb corrected ^{206}Pb–^{238}U weighted mean plot as they were found to only hold information on the common Pb line but little accurate information in the weighted mean plots.

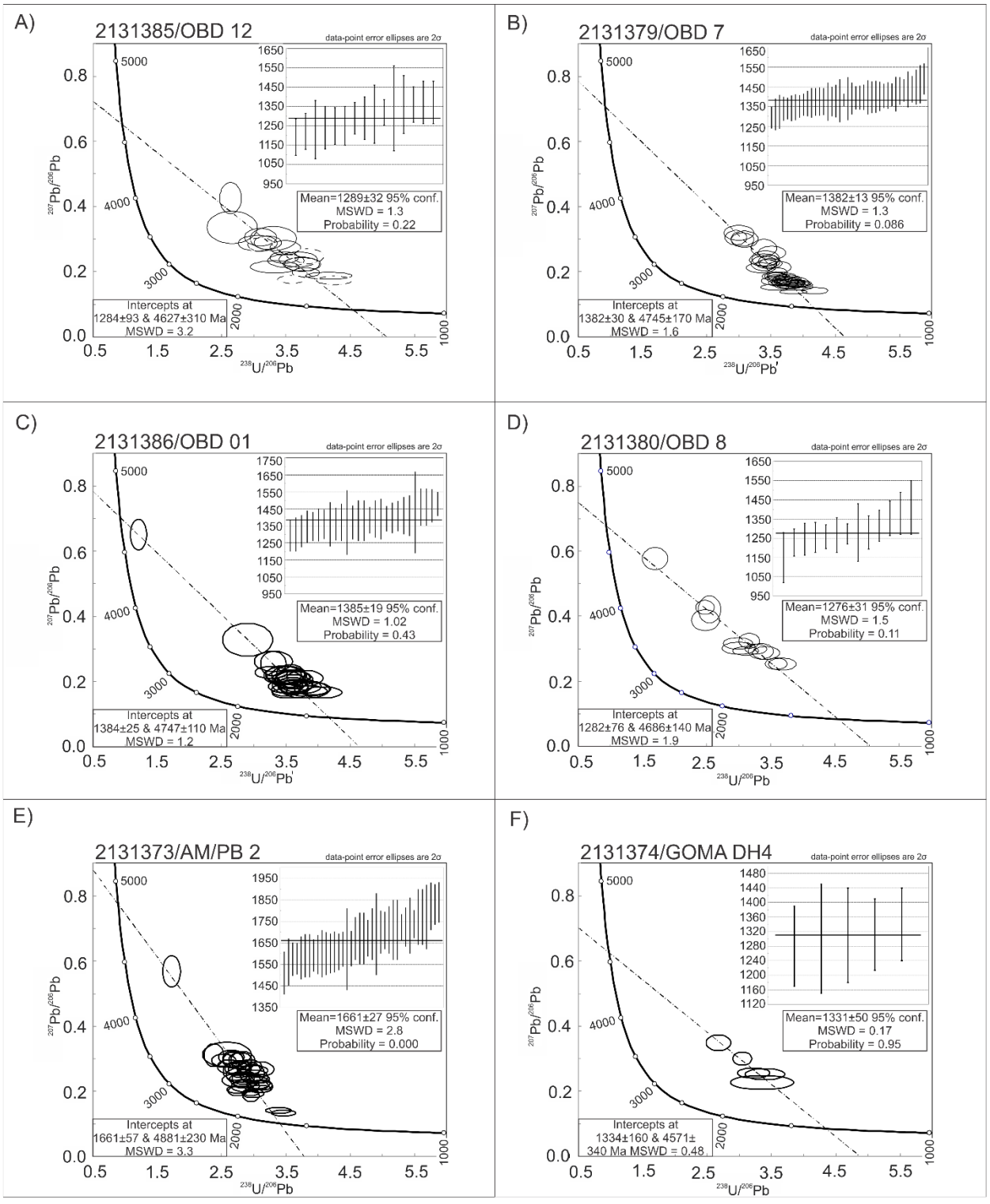
A)
2131385/OBD 12
data-point error ellipses are 2σ
Mean=1289±32 95% conf.
MSWD = 1.3
Probability = 0.22
Intercepts at
1284±93 & 4627±310 Ma
MSWD = 3.2
B)
2131379/OBD 7
data-point error ellipses are 2σ
Mean=1382±13 95% conf.
MSWD = 1.3
Probability = 0.086
Intercepts at
1382±30 & 4745±170 Ma
MSWD = 1.6
C)
2131386/OBD 01
data-point error ellipses are 2σ
Mean=1385±19 95% conf.
MSWD = 1.02
Probability = 0.43
Intercepts at
1384±25 & 4747±110 Ma
MSWD = 1.2
D)
2131380/OBD 8
data-point error ellipses are 2σ
Mean=1276±31 95% conf.
MSWD = 1.5
Probability = 0.11
Intercepts at
1282±76 & 4686±140 Ma
MSWD = 1.9
E)
2131373/AM/PB 2
data-point error ellipses are 2σ
Mean=1661±27 95% conf.
MSWD = 2.8
Probability = 0.000
Intercepts at
1661±57 & 4881±230 Ma
MSWD = 3.3
F)
2131374/GOMA DH4
data-point error ellipses are 2σ
Mean=1331±50 95% conf.
MSWD = 0.17
Probability = 0.95
Intercepts at
1334±160 & 4571±
340 Ma MSWD = 0.48
207Pb/206Pb
238U/206Pb
238U/206Pb'

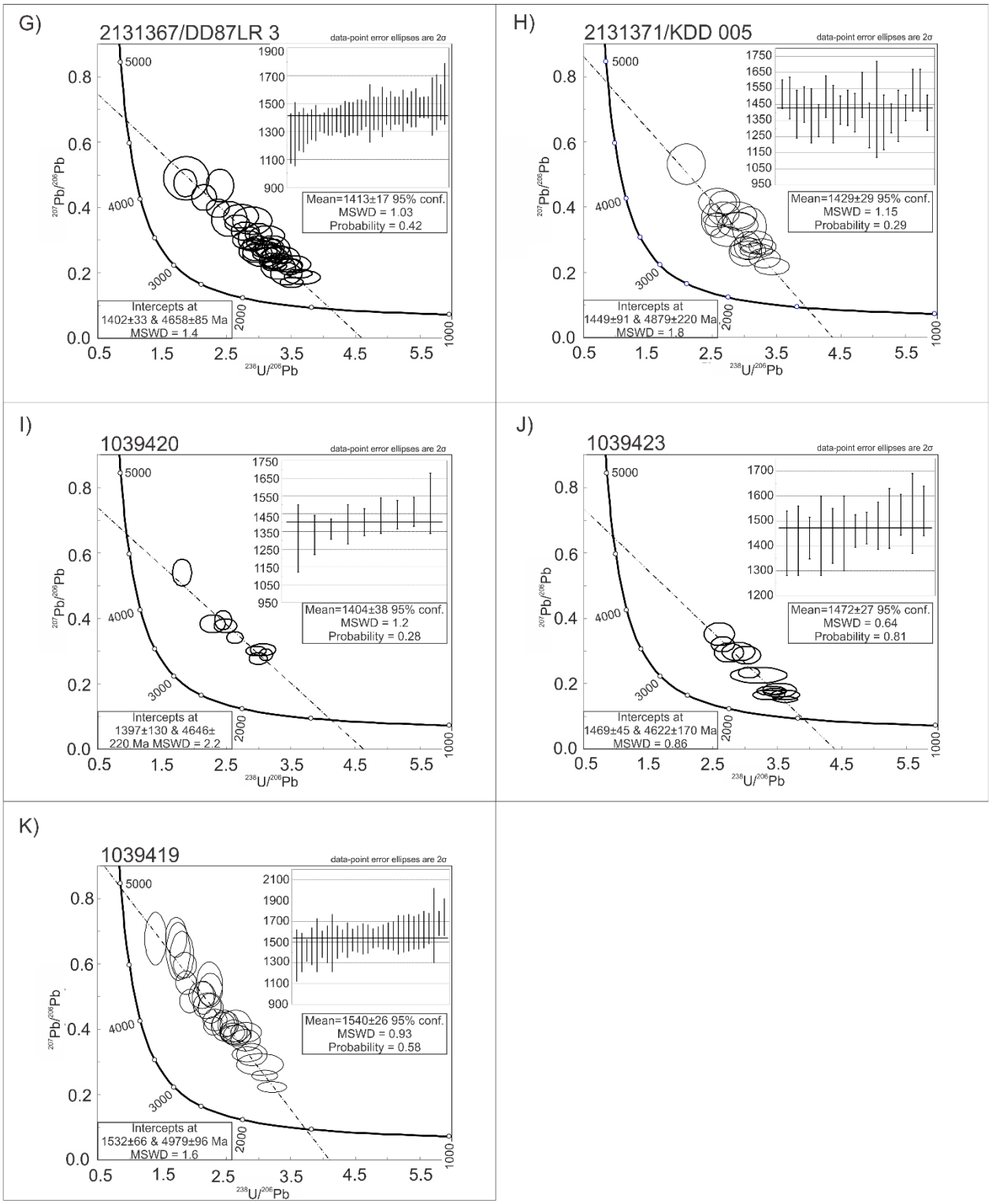

Figure 1.5: continued.

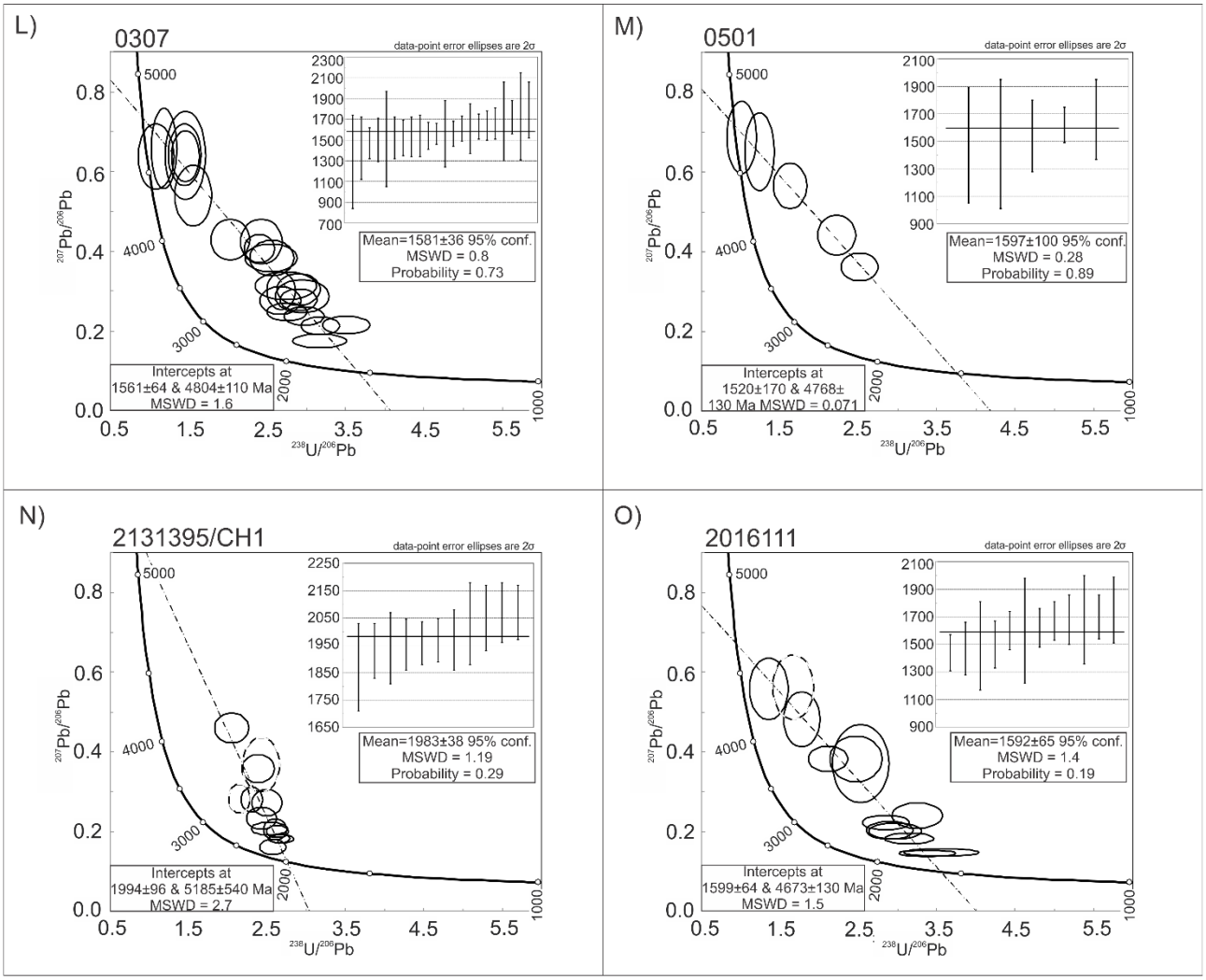

Figure 1.5: continued.

Sample 1039420 is a granite outcrop sample that recorded a common Pb line lower intercept of 1397 ± 130 Ma with a MSWD of 2.2. The associated ^{207}Pb corrected ^{206}Pb–^{238}U weighted mean produced an age of 1404 ± 38 Ma with an MSWD of 1.2 (Fig. 1.5I).

Sample 1039423 is another granite outcrop sample. A ^{207}Pb corrected weighted mean ^{206}Pb–^{238}U age of 1472 ± 27 Ma (MSWD = 0.64) was observed for this sample. The associated common Pb line yields a lower intercept age of 1469 ± 45 Ma with an MSWD of 0.86 (Fig. 1.5J). A nearby biotite ^{40}Ar/^{39}Ar plateau age of 1529 ± 10 Ma (Forbes et al., 2012) is in relatively good agreement with this sample and indicates this region underwent cooling at around 1.5 Ga.

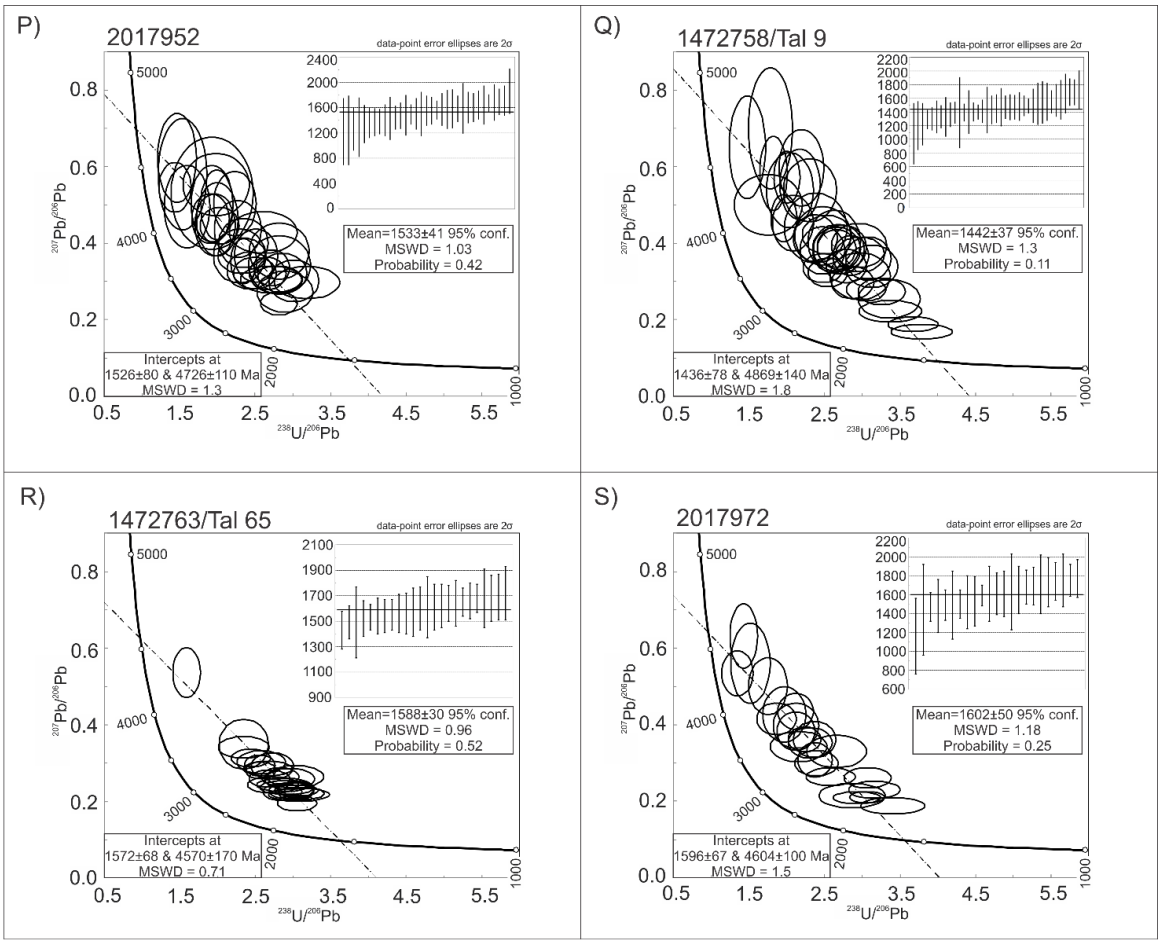

Figure 1.5: continued.

Sample 1039419 was taken from a granite. It produced a ^{207}Pb corrected weighted mean ^{206}Pb–^{238}U age of 1540 ± 26 Ma (MSWD of 0.93) from a reliable common Pb line, which produced a lower intercept of 1532 ± 66 Ma (MSWD of 1.6; Fig. 1.5K).

These two domains preserve very similar U–Pb ages which range between 1404 ± 38 Ma and 1540 ± 26 Ma from 5 samples.

1.4.3 Christie Domain

Sample 0307 was taken from a granite outcrop. A reliable common Pb line lower intercept age of 1561 ± 54 Ma (MSWD of 1.6) was recorded in this sample, with a ^{207}Pb corrected weighted mean ^{206}Pb–^{238}U age of 1581 ± 36 Ma (MSWD of 0.8) produced from the common Pb line (Fig. 1.5L).

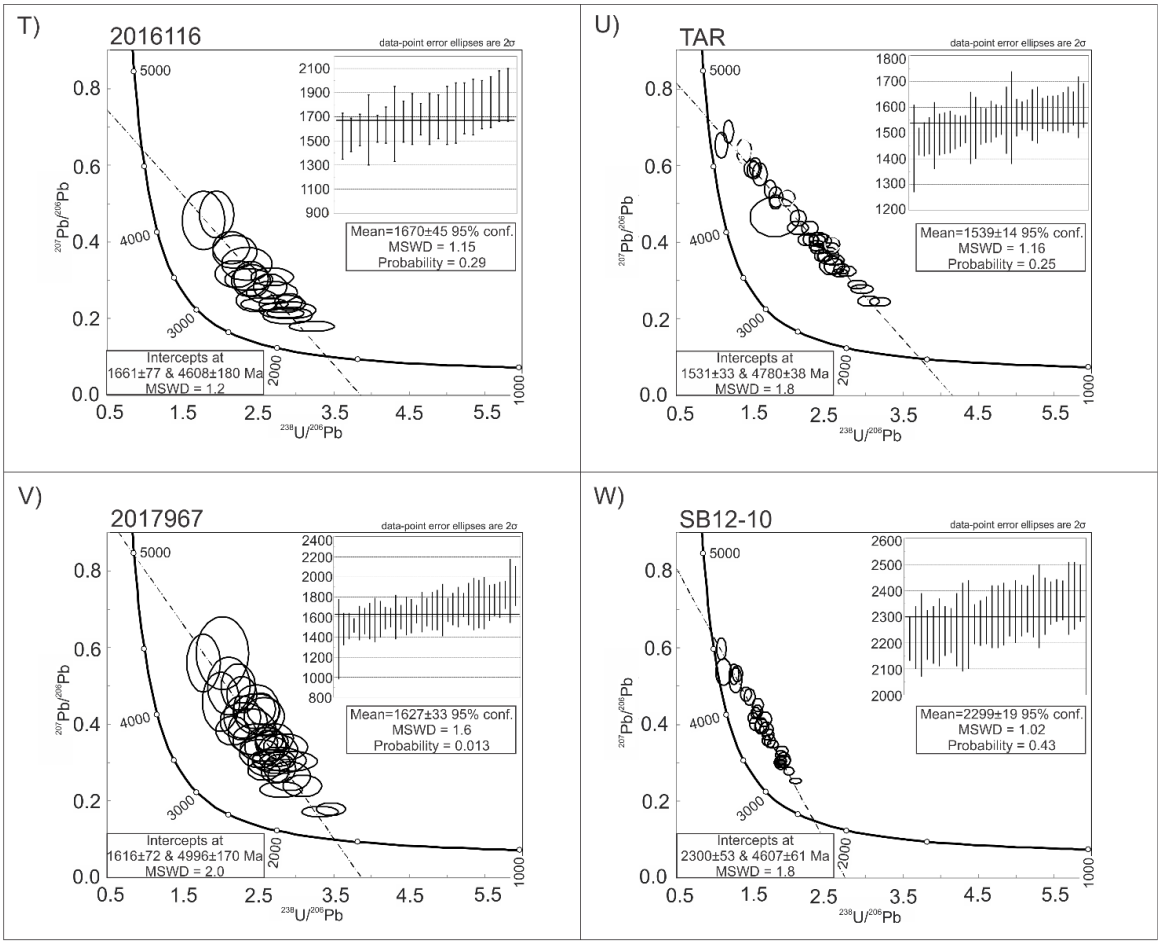

Figure 1.5: continued.

Sample 0501 is an outcropping tonalite. It only produced five reliable dates, yet these dates form a good common Pb line, with a lower intercept of 1520 ± 170 Ma and a MSWD of 0.071. The resultant ^{207}Pb corrected weighted mean revealed a ^{206}Pb–^{238}U age of 1597 ± 100 Ma with a MSWD of 0.28 (Fig. 1.5M).

Sample 2131395 was a granite collected from drill hole CH 1. It recorded a ^{207}Pb corrected weighted mean ^{206}Pb–^{238}U age of 1983 ± 38 Ma (MSWD = 1.19) from a common Pb line with a lower intercept of 1994 ± 96 Ma (MSWD = 2.7; Fig. 1.5N).

Sample 2016111 is a Hiltaba granite. It preserved a common Pb line with a lower intercept of 1599 ± 64 Ma (MSWD of 1.5). The calculated ^{207}Pb corrected weighted mean produced a ^{206}Pb–^{238}U age of 1592 ± 65 Ma with a MSWD of 1.4 (Fig. 1.5O).

Sample	Drill hole number	n	Concordia Intercept	MSWD	$^{207}Pb/^{206}Pb$ intercept	^{207}Pb corrected ^{206}Pb–^{238}U age	MSWD	Probability	$^{39}Ar/^{40}Ar$ age (mineral)
2131385	*OBD 12*	*15*	*1284±93 Ma*	*3.2*	*0.7232*	*1289±32 Ma*	*1.3*	0.22	-
2131379	*OBD 7*	*39*	*1382±30*	*1.6*	*0.7867*	*1382±13 Ma*	*1.3*	0.086	-
2131386	*OBD 01*	*27*	*1384±25 Ma*	*1.2*	*0.7829*	*1385±19 Ma*	*1.02*	0.43	-
2131380	*OBD 8*	*13*	*1282±76 Ma*	*1.9*	*0.7506*	*1276±31 Ma*	*1.5*	0.11	-
2131373	*AM/PB 2*	*38*	*1661±67 Ma*	3.3	*0.8801*	*1661±27 Ma*	*2.8*	0.00	1554*±5 Ma (Biotite)*
2131374	*GOMA DH4*	*5*	*1334±160 Ma*	0.48	*0.7017*	*1331±50 Ma*	*0.17*	0.95	-
2131367	*DD87LR 3*	38	1402*±33 Ma*	*1.4*	*0.7461*	*1413±17 Ma*	*1.03*	0.42	1476*±5 Ma (Biotite)*
2131371	*KDD 005*	*21*	*1449±91 Ma*	*1.8*	*0.8617*	*1429±29 Ma*	*1.15*	0.29	-
1039420	-	*9*	*1397±130 Ma*	*2.2*	*0.401*	*1404±38 Ma*	*1.2*	0.28	-
1039423	-	*13*	*1469±45 Ma*	*0.86*	*0.7349*	*1472±27 Ma*	*0.64*	0.81	1529*±10 Ma (Biotite)*
1039419	-	*30*	*1532±66*	*1.6*	*1.0681*	*1540±26 Ma*	*0.93*	0.58	-
0307	-	*22*	*1561±64 Ma*	*1.6*	*0.8306*	*1581±36 Ma*	*0.8*	0.73	-
0501	-	*5*	*1520±170 Ma*	*0.071*	*0.8088*	*1597±100 Ma*	*0.28*	0.89	-
2131395	*CH 1*	11	1994*±96 Ma*	*2.7*	*1.3369*	*1983±38 Ma*	*1.19*	0.29	-
2016111	-	*12*	*1599±64 Ma*	*1.5*	*0.7689*	*1592±65 Ma*	*1.4*	0.19	-
2017952	-	*33*	*1526±80 Ma*	*1.3*	*0.7887*	*1533±41 Ma*	*1.03*	0.42	-
1472758	*Tal 9*	*37*	*1436±78 Ma*	*1.8*	*0.8552*	*1442±37 Ma*	*1.3*	0.11	1441*±10 Ma (Biotite)*
1472763	*Tal 65*	*24*	*1572±68 Ma*	*0.71*	*0.7199*	*1588±30 Ma*	*0.96*	0.52	-
2017972	-	*23*	*1596±67 Ma*	*1.5*	*0.7368*	*1602±50 Ma*	*1.18*	0.25	-
2016116	-	*20*	*1661±77 Ma*	*1.2*	*0.7441*	*1670±45 Ma*	*1.15*	0.29	-
TAR	-	*34*	*1531±33 Ma*	*1.8*	*0.8158*	*1539±14 Ma*	*1.16*	0.25	1582*±5 Ma (Hornblende)*
2017967	-	*35*	*1616±72 Ma*	*2.0*	*1.1463*	*1627±33 Ma*	*1.6*	0.013	1586*±11 Ma (Biotite)*
SB12-10	-	*30*	*2300±53 Ma*	*1.8*	*0.8077*	*2299±19 Ma*	*1.02*	0.43	-

Table 1.2: Apatite U/Pb data, where; n = number of analyses, and $^{39}Ar/^{40}Ar$ age = $^{39}Ar/^{40}Ar$ age of a sample nearby or within the same drill hole from Budd and Fraser (2004), Fraser and Lyons (2006), Forbes et al. (2012), and Fraser et al. (2012).

Three of the four samples preserve cooling at ~1600 – 1500 Ma, with the other recording cooling at 1983 ± 38 Ma. The ~1600–1500 Ma samples were from rocks that are thought to have crystallised at around the same time, suggesting that they represent rapid post-crystallisation cooling.

1.4.4 Fowler Domain

A ^{207}Pb corrected weighted mean ^{206}Pb–^{238}U age of 1533 ± 41 Ma (MSWD = 1.03) was recorded in sample 2017952. This sample also records a common Pb line lower intercept of 1526 ± 80 Ma (MSWD = 1.3; Fig. 1.5P).

Sample 1472758 (from drill hole Tal 9) produced a reliable common Pb line with a lower intercept of 1436 ± 78 Ma and a MSWD of 1.8. This common Pb line was used to produce the ^{207}Pb corrected weighted mean ^{206}Pb–^{238}U age of 1442 ± 37 Ma, with a MSWD of 1.3 (Fig. 1.5Q). A biotite ^{40}Ar/^{39}Ar sample located 7 km to the south west is in very good agreement with this sample as it records a plateau age of 1441 ± 10 Ma (Fraser and Lyons, 2006).

Sample 1472763 is a gabbronorite collected from drill hole Tal 65. It recorded a ^{207}Pb corrected weighted mean ^{206}Pb–^{238}U age of 1588 ± 30 Ma with a MSWD of 0.96. The associated common Pb line recorded a lower intercept age of 1572 ± 68 Ma with a MSWD of 0.71 (Fig. 1.5R).

Sample 2017972 is an outcrop of granite. It records a reliable common Pb line with a lower intercept of 1596 ± 67 Ma (MSWD of 1.5). The ^{207}Pb corrected weighted mean records a ^{206}Pb–^{238}U age of 1602 ± 50 Ma with a MSWD of 1.18 (Fig. 1.5S).

The four samples within the Fowler Domain preserve U–Pb ages between 1442 ± 37 Ma and 1602 ± 50 Ma.

1.4.5 Wilgena & Nuyts domains

Sample 2016116 preserved a ^{207}Pb corrected weighted mean ^{206}Pb–^{238}U age of 1670 ± 45 Ma with a MSWD of 1.15. The ^{207}Pb correction was calculated on a common Pb line with a lower intercept of 1661 ± 77 Ma (MSWD of 1.2; Fig. 1.5T).

TAR was collected from a Hiltaba granite. A reliable common Pb line was produced for this sample, with a lower intercept of 1531 ± 33 (MSWD = 1.8). The ^{207}Pb corrected weighted mean plot produced a ^{206}Pb–^{238}U age of 1539 ± 14 Ma with a MSWD of 1.16 (Fig. 1.5U). A hornblende ^{40}Ar/^{39}Ar sample located 2 km to the south east of TAR preserves a plateau age of 1582 ± 5 Ma (Budd and Fraser, 2004). Given the difference in closure temperatures between ^{40}Ar/^{39}Ar in hornblende (~450 °C; McDougall and Harrison, 1999) and U–Pb in apatite (350 °C), it is considered these two ages are part of the same cooling event.

Sample 2017967 is a granite sample. It yielded a ^{207}Pb corrected weighted mean ^{206}Pb–^{238}U age of 1627 ± 33 Ma (MSWD of 1.6). When plotted on a Tera-Wasserburg plot a common Pb line with a lower intercept of 1616 ± 72 Ma (MSWD of 2.0) was produced (Fig. 1.5V).

A ^{207}Pb corrected weighted mean ^{206}Pb–^{238}U age of 2299 ± 19 Ma (MSWD of 1.02) was preserved in sample SB12–10 (a Glenloth Granite sample). The common Pb line lower intercept preserved an age of 2300 ± 53 Ma with a MSWD of 1.8 (Fig. 1.5W).

In summary, all four samples produced reliable U–Pb ages between 1539 ± 14 Ma and 2299 ± 19 Ma. They preserve three periods of cooling, at 2.3 Ga, 1.6 Ga, and 1.5 Ga, the latter probably reflecting post-magmatic cooling of the Hiltaba granite.

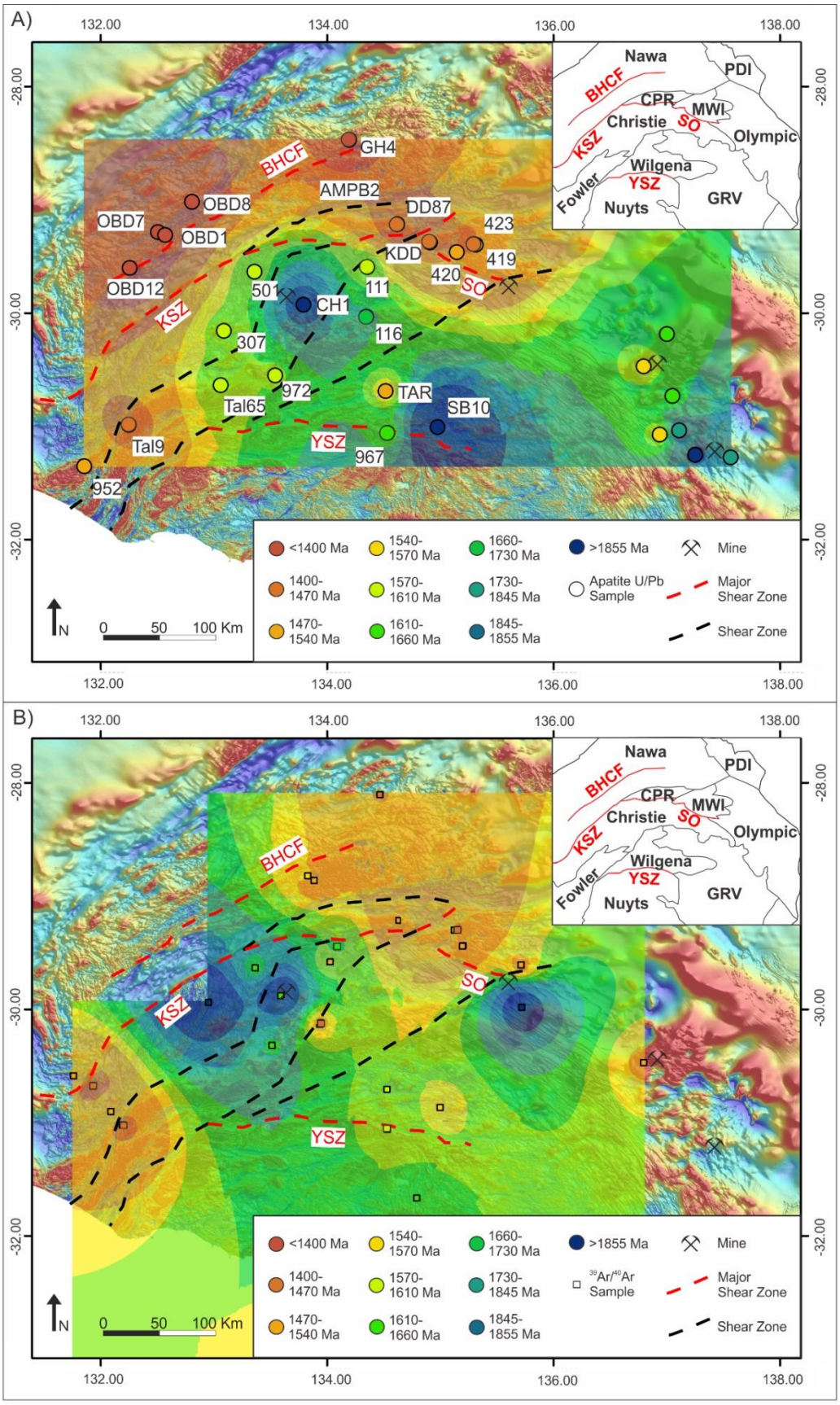
A)
B)
132.00
134.00
136.00
138.00
-28.00
-30.00
-32.00
Nawa
PDI
BHCF
CPR
MWI
Christie
SO
Olympic
KSZ
Wilgena
YSZ
Fowler
Nuyts
GRV
GH4
AMPB2
OBD8
DD87
OBD7
OBD1
423
KDD
419
420
OBD12
501
111
CH1
116
307
972
TAR
SB10
Tal65
Tal9
967
952
<1400 Ma
1400-1470 Ma
1470-1540 Ma
1540-1570 Ma
1570-1610 Ma
1610-1660 Ma
1660-1730 Ma
1730-1845 Ma
1845-1855 Ma
>1855 Ma
Mine
Apatite U/Pb Sample
39Ar/40Ar Sample
Major Shear Zone
Shear Zone
N
0 50 100 Km

Figure 1.6 (previous page): (A) A gridded Inverse Distance Weighting model based on the apatite U–Pb ages overlain on a total magnetic intensity map of the northern Gawler Craton with the same extent as Fig. 1.3, showing the locations of apatite U–Pb samples, $^{40}Ar/^{39}Ar$ samples, shear zones, and major mineral deposits. This map models the ages of cooling in the northern Gawler Craton through the closure temperature of Pb in apatite of ~550– 350 °C (Chew and Spikings, 2015). Additional U–Pb apatite data from the Olympic Domain from Hall et al. (submitted). (B) A gridded Inverse Distance Weighting model of mica and hornblende $^{40}Ar/^{39}Ar$ ages overlain on the total magnetic intensity map of the northern Gawler Craton with the same extent and contents as Fig. 1.6. This map models the ages of cooling through mid-crustal temperatures represented by the closure temperature of Ar in these minerals (~550-300 °C; McDougall and Harrison, 1999; Harrison et al., 2009). $^{40}Ar–^{39}Ar$ data from Foster and Ehlers (1998), Tomkins and Mavrogenes (2002), Budd and Fraser (2004), Tomkins et al. (2004), Fraser and Lyons (2006), Fraser et al. (2007), Forbes et al. (2012), Fraser et al. (2012), and Reid et al. (2017). The insets of (A) and (B) show the boundaries of the domains within the northern Gawler Craton. Abbreviations are: PDI–Peake and Denison Inliers; BHCF– Box Hole Creek Fault; CPR– Coober Pedy Ridge; MWI– Mt. Woods Inlier; KSZ– Karari Shear Zone; SO– Southern Overthrust; GRV– Gawler Range Volcanics; YSZ– Yerda Shear Zone.

1.5 Discussion

1.5.1 Palaeoproterozoic cooling

The oldest recorded apatite U–Pb ages within the northern Gawler Craton occur in the Mulgathing Complex of the Christie and Wilgena domains (Figs. 3 and 6). These >1950 Ma U–Pb ages are interpreted to record cooling of the Mulgathing Complex following the end of the Sleaford Orogeny at ~2410 Ma (Hand et al., 2007; Jagodzinski et al., 2009; Reid et al., 2010). Moreover, these U–Pb ages indicate that later orogenic events such as the Kimban Orogeny did not homogeneously reheat the Christie and Wilgena domains to temperatures in excess of ~550 °C (Parker et al., 1993; Payne et al., 2008). Similarly, ~1.6 – 1.7 Ga U–Pb ages that might reflect cooling after the Kimban Orogeny are only preserved in two samples (SB12–10 and 2131395), from the Christie and Wilgena domains. Despite the widespread deformation of both the Sleaford and Kimban orogenies, they are poorly recorded by the apatite U–Pb data, and are also only sparsely recorded in $^{40}Ar/^{39}Ar$ data (Fig. 1.7; Fig. 1.8; Tomkins and Mavrogenes, 2002; Budd and Fraser, 2004; Tomkins et al., 2004; Fraser et al., 2007) as they are restricted to the Christie Domain. This distribution suggests that the remainder of the Gawler Craton was heated to at least greenschist-facies conditions after the Kimban Orogeny.

To the east, within the Olympic Domain, apatite U–Pb data records cooling following emplacement of the ca. 1850 Ma Donington Suite (Hall et al., submitted). This supports observation that the Kimban Orogeny had minimal effect on the Olympic Domain (Reid and Fabris, 2015) and suggests cooling within the central west and east of the craton were not linked during the Palaeoproterozoic.

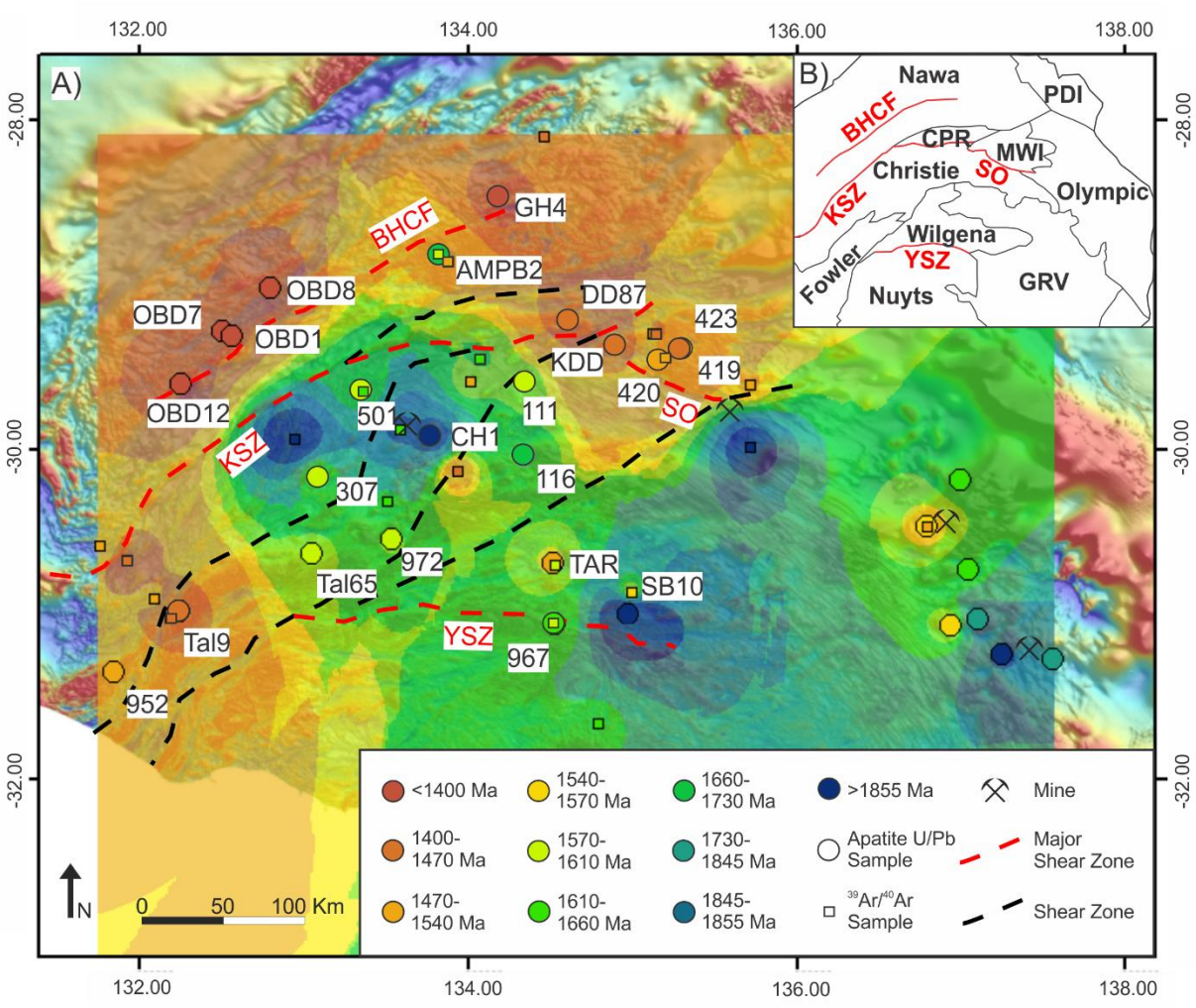

Figure 1.7: (A) A gridded Inverse Distance Weighting model of the northern Gawler combining all U–Pb apatite ages and mica and hornblende $^{40}Ar/^{39}Ar$ ages. Inset (B) reveals the boundaries of the domains within the northern Gawler Craton. Abbreviations are: PDI–Peake and Denison Inliers; BHCF–Box Hole Creek Fault; CPR–Coober Pedy Ridge; MWI– Mt. Woods Inlier; KSZ–Karari Shear Zone; SO– Southern Overthrust; GRV– Gawler Range Volcanics; YSZ– Yerda Shear Zone.

1.5.2 Mesoproterozoic cooling

The dominant period of cooling recorded by apatite U–Pb analysis is interpreted to be cooling following the ~1590 – 1580 Ma Hiltaba Event. This period of cooling is preserved in samples from the Mt. Woods Inlier, Christie Domain, Fowler Domain, and Wilgena Domain, in addition to data from the Olympic Domain. Data from Fraser et al. (2012) also preserve post-Hiltaba ages in $^{40}Ar/^{39}Ar$ samples from the central Nawa Domain. Samples from the Mt. Woods Inlier (1039419 at 1540 ± 26 Ma, 1039420 at 1404 ± 38 Ma, and 1039423 at 1472 ± 27 Ma), Christie Domain

(2016111 at 1592 ± 65 Ma), and Wilgena Domain (TAR at 1539 ± 14 Ma) are from Hiltaba Granites (Daly et al., 1998; Reddy et al., 2015; Boone et al., 2016). Therefore, their apatite U–Pb ages (Table 1.2) are interpreted to be post-magmatic cooling following the Hiltaba Event. Samples from the Christie (0501, and 0307) and Fowler Domains (1472763, and 2017972), which formed over 100 Ma prior to the Hiltaba Event (Howard et al., 2011a; Dawson, 2016) record Hiltaba apatite U–Pb ages, indicating these samples were reheated to over ~550 – 350 °C during this event.

Most samples in the Nawa Domain, to the north of the Karari Shear Zone, and all samples north of the poorly known Box Hole Creek Fault (Fig. 1.3), preserve U–Pb ages that considerably post-date the ~1590 – 1560 Ma Kararan Orogeny. These U–Pb ages are consistently around ~1400 – 1300 Ma, and are therefore considered to have shared a similar cooling history, following their deposition and subsequent metamorphism during the Kimban Orogeny (Payne et al., 2006; Howard et al., 2011b). In the central Nawa Domain, to the south of the Box Hole Creek Fault, Fraser et al. (2012) obtained U–Pb monazite secondary ion mass-spectrometry (SIMS) ages of 1575 ± 5 Ma. Biotite $^{40}Ar/^{39}Ar$ data from the same area yielded ages between ~1465 Ma and 1500 Ma (Fraser et al., 2012) and both biotite and muscovite $^{40}Ar/^{39}Ar$ data from within the Karari Shear Zone preserved ages of ~1440 – 1430 Ma (Fraser and Lyons, 2006; Fraser et al., 2012). These data suggest that the Nawa Domain experienced temperatures of over 550 – 350 °C until ~1400 – 1300 Ma, over 150 Ma after the Kararan orogeny. The samples within the central Nawa Domain, north of the Box Hill Creek Fault, preserve U–Pb ages of ~1400 – 1300 Ma, whereas the rocks between the Box Hill Creek Fault and the Karari Shear Zone preserve biotite $^{40}Ar/^{39}Ar$ ages of ~1440 – 1430 Ma. Due to the lack of apatite U–Pb data between the Box Hill Creek Fault and the Karari Shear Zone it is difficult to conclude if there is any differential cooling across the Box Hill Creek Fault. However, a potential hypothesis on the ~100 Ma difference in ages is that, either the north and western Nawa domain underwent greater exhumation and cooling over an extremely protracted time period after the Kararan Orogeny, or the region north of the Box Hill Creek Fault was reheated after the Kararan orogeny, possibly at ~1440 – 1430 Ma as strike-slip shear zone reactivation was proposed on the Karari Shear Zone by Fraser et al. (2012).

Recently, considerable middle Mesoproterozoic magmatism has been recorded in the covered basement of the far west of Gawler craton. The ~1490 Ma Undawidgi Supersuite in the Coompana Block (Kirkland et al., 2017) and the ~1415 – 1389 Ma Haig Cave Supersuite of the Madura Province, in Western Australia, record juvenile magmatism, which is thought to be a destructive plate margin on the edge of the South Australian Craton during the middle Mesoproterozoic. Similar-aged arc-magmatism and broadly coeval orogenesis also occur in the ~1345 – 1295 Ma Mount West Orogeny of the western Musgraves (Howard et al., 2015). This orogeny is thought to reflect the amalgamation of the previously combined South Australian and North Australian Cratons with the Western Australian Craton (Howard et al., 2015). An interpretation supported by new ages for the peak Yapunku metamorphism in the Rudall province of the far eastern Pilbara

(Anderson et al., 2016) and changing provenance in the northern Australian basins at this time (Cox et al., 2016; Yang et al., submitted). We suggest that ~1440 – 1430 Ma reactivation of the Karari Shear Zone (Fraser et al., 2012) along with the significant heating recorded by apatite U–Pb data between this time and ~1300 Ma in the northern Nawa Domain reflect the foreland effects of arc-formation on the western margin of the Gawler Craton, and the subsequent collision with the Western Australian Craton.

Samples in the west of the craton, within the Fowler Domain, preserve Kararan Orogeny (~1530 Ma) and post-Kararan Orogeny (~1440 Ma) cooling. These U–Pb ages correlate well with $^{40}Ar/^{39}Ar$ from the Fowler Domain (Fraser and Lyons, 2006; Fraser et al., 2012) which are interpreted to be cooling related to movement along the Karari Shear Zone. Furthermore, Fraser et al. (2012) suggested this movement resulted in up to 10 km of exhumation in the region from the Kararan Orogeny ages. In comparison, samples along strike of the shear zones in the north-eastern Fowler Domain and Christie Domain record cooling following the Hiltaba Event. Therefore, the western Fowler Domain underwent greater exhumation from higher temperatures during the Kararan Orogeny than the centre of the craton. The younger ~1450 Ma ages are restricted to the Karari and Tallacootra shear zones and are interpreted to be a phase of strike-slip movement along these shear zones (Fraser and Lyons, 2006; Fraser et al., 2012). As previously suggested, the cause of this shear zone movement is interpreted to be foreland effect of arc-formation within the far western Gawler Craton and the ensuing collision of the Western Australian Craton with the South and North Australian Cratons.

1.5.3 Comparisons to pre-existing ^{40}Ar-^{39}Ar datasets and interpolation maps

When compared to sixty $^{40}Ar/^{39}Ar$ ages from muscovite, biotite, and hornblende (~350 - 550 °C; McDougall and Harrison, 1999; Harrison et al., 2009) data from the northern Gawler, apatite U–Pb data preserve similar ages overall. In order to visually represent the similarities and differences in these ages and to reveal the timing and extent of tectonic events, Inverse Distance Weighted (IDW; Bartier and Keller, 1996) interpolated maps were created (Fig. 1.6 A,B). In regions with higher data density, such as the Mt. Woods Inlier, and south-western Fowler Domain, the apatite U–Pb IDW map and $^{40}Ar/^{39}Ar$ IDW map preserve very similar ages. The two maps differ more extensively in regions where data are lacking, such as in the Nawa Domain which, due to the lack of $^{40}Ar/^{39}Ar$ data, results in a large discrepancy between the two maps. The Christie and Wilgena domains display some similarities. However, the contrasting ages of the older Mulgathing Complex and younger Hiltaba Suite coupled with the differing sampled locations between the thermochronometers ($^{40}Ar/^{39}Ar$ data and apatite U–Pb) result in the disparity between the two maps. Figure 1.6B represents a more accurate temperature contour for the gap in data between the samples of the Wilgena Domain and the samples of the Olympic Domain, as this region is

covered by the ~1590 Ma Gawler Range Volcanics (Giles, 1988; Creaser and White, 1991; Hand et al., 2007).

Overall, the $^{40}Ar/^{39}Ar$ and apatite U–Pb data correlate well, therefore, both datasets were combined into an IDW interpolated map (Fig. 1.7). This map identifies the rough location of major structures which played a role in the preservation of the $^{40}Ar/^{39}Ar$ and apatite U–Pb ages. For example, the rough location of the Karari Shear Zone is highlighted by younger ages (orange – red colours) curving around the north and west of the map, which is in stark contrast to the older ages (green – blue colours) within the Christie Domain, to the south. The younger fault movement within the Fowler Domain is also highlighted. To the east, the Olympic Domain is separated into cooling at ~1.6 Ga (green – yellow colours) and 1.7 – 1.8 Ga (blue – dark blue colours) which correlates to the locations of the ~1.6 Ga Hiltaba Suite and GRV to the north, and the ~1.8 Ga Donington Suite to the south (Fig. 1.1). It is important to note that in regions where the data is lacking, the IDW assumes the data is homogenous. As a result, the interpolation in these regions contain large uncertainties. More data is needed to better constrain these regions.

1.6 Conclusions

Apatite U–Pb data from the northern Gawler Craton preserve cooling following multiple Palaeo-Mesoproterozoic tectonic and igneous events:

(1) Ages older than 2000 Ma record cooling of Mulgathing complex following the Sleaford Orogeny.

(2) Central Gawler cooling is dominated by post-Kimban cooling ages of 1620 – 1670 Ma and post-Hiltaba Event cooling ages of 1600 – 1530 Ma.

(3) Ages in the Mt. Woods Inlier are the result of post-peak metamorphism cooling and thrusting along the Southern Overthrust at around 1590 Ma during the Kararan Orogeny.

(4) Ages within the Nawa Domain are interpreted to reflect cooling following poorly documented heating that is thought to result from the forelandward effects of arc formation on the margin of the Gawler Craton and the subsequent collision between the combined South and North Australian cratons and the Western Australia Craton at ~1450 – 1300 Ma.

(5) Data from the southwestern Fowler Domain record shear zone movement at around 1440 Ma, which indicates that this region underwent greater amount of cooling and exhumation than samples along strike of the shear zones in the centre of the Gawler Craton.

1.7 Acknowledgements This study is funded by the Geological Survey of South Australia and was made possible through an Australian Research Council grant (ARC LE150100145). Ben Wade (Adelaide Microscopy) is thanked for his assistance with the use of the LA-ICP-MS. AR publishes with permission of the director of the Geological Survey of South Australia. This paper forms TRaX #395 and is a contribution to IGCP projects 628 (Gondwana Map) and 648 (Supercontinents).

1.8 References

Allen, S.R., McPhie, J., Ferris, G., Simpson, C., 2008. Evolution and architecture of a large felsic Igneous Province in western Laurentia: The 1.6 Ga Gawler Range Volcanics, South Australia. Journal of Volcanology and Geothermal Research 172, 132-147.

Anderson, J.R., Kelsey, D.E., Hand, M., Collins, W.J., 2016. Mesoproterozoic metamorphism in the Rudall Province: revising the timeline of the Yapungku Orogeny and implications for cratonic Australia assembly, Australian Earth Sciences Convention. Geological Society of Australia, Adelaide, p. 227.

Bartier, P.M., Keller, C.P., 1996. Multivariate interpolation to incorporate thematic surface data using inverse distance weighting (IDW). Computers & Geosciences 22, 795-799.

Betts, P.G., Giles, D., 2006. The 1800–1100 Ma tectonic evolution of Australia. Precambrian Research 144, 92-125.

Betts, P.G., Giles, D., Foden, J., Schaefer, B.F., Mark, G., Pankhurst, M.J., Forbes, C.J., Williams, H.A., Chalmers, N.C., Hills, Q., 2009. Mesoproterozoic plume-modified orogenesis in eastern Precambrian Australia. Tectonics 28, n/a-n/a.

Boone, S.C., Seiler, C., Reid, A.J., Kohn, B., Gleadow, A., 2016. An Upper Cretaceous paleo-aquifer system in the Eromanga Basin of the central Gawler Craton, South Australia: evidence from apatite fission track thermochronology. Australian Journal of Earth Sciences 63, 315-331.

Budd, A.R., Fraser, G.L., 2004. Geological relationships and 40Ar/39Ar age constraints on gold mineralisation at Tarcoola, central Gawler gold province, South Australia. Australian Journal of Earth Sciences 51, 685-699.

Budd, A.R., Wyborn, L.A., Bastrakova, I.V., 2001. The metallogenic potential of Australian Proterozoic granites. Geoscience Australia, Record 2001/12.

Butler, R.W.H., Holdsworth, R.E., Lloyd, G.E., 1997. The role of basement reactivation in continental deformation. Journal of the Geological Society 154, 69-71.

Chew, D.M., Petrus, J.A., Kamber, B.S., 2014. U–Pb LA–ICPMS dating using accessory mineral standards with variable common Pb. Chemical Geology 363, 185-199.

Chew, D.M., Spikings, R.A., 2015. Geochronology and Thermochronology Using Apatite: Time and Temperature, Lower Crust to Surface. Elements 11, 189-194.

Chew, D.M., Sylvester, P.J., Tubrett, M.N., 2011. U–Pb and Th–Pb dating of apatite by LA-ICPMS. Chemical Geology 280, 200-216.

Cowley, W.M., Conor, C.H.H., Zang, W., 2003. New and revised Proterozoic stratigraphic units on northern Yorke Peninsula. Minerals and Energy South Australia Journal 29, 46-58.

Cowley, W.M., Fanning, C.M., 1991. Low-grade Archaean metavolcanics in the northern Gawler Craton. Geological Survey of South Australia, Quarterly Geological Notes 119, 2-17.

Cox, G.M., Jarrett, A., Edwards, D., Crockford, P.W., Halverson, G.P., Collins, A.S., Poirier, A., Li, Z.-X., 2016. Basin redox and primary productivity within the Mesoproterozoic Roper Seaway. Chemical Geology 440, 101-114.

Creaser, R.A., 1996. Petrogenesis of a Mesoproterozoic quartz latite-granitoid suite from the Roxby Downs area, South Australia. Precambrian Research 79, 371-394.

Creaser, R.A., White, A.J.R., 1991. Yardea Dacite; large-volume, high temperature felsic volcanism from the middle Proterozoic of South Australia. Geology 19, 48-51.

Daly, S.J., Fanning, C.M., Fairclough, M.C., 1998. Tectonic evolution and exploration potential for the Gawler Craton, South Australia. AGSO Journal of Australian Geology and Geophysics 17, 145-168.

Dawson, J., 2016. Characterising Magmatic Suites in the Western Gawler Craton: Geochemical and Geochronological Constraints, Earth Sciences. University of Adelaide, Unpublished, p. 45.

Direen, N.G., Cadd, A.G., Lyons, P., Teasdale, J.P., 2005. Architecture of Proterozoic shear zones in the Christie Domain, western Gawler Craton, Australia: Geophysical appraisal of a poorly exposed orogenic terrane. Precambrian Research 142, 28-44.

Dutch, R., Hand, M., Kinny, P.D., 2008. High-grade Paleoproterozoic reworking in the southeastern Gawler Craton, South Australia. Australian Journal of Earth Sciences 55, 1063-1081.

Dutch, R.A., Hand, M., Kelsey, D.E., 2010. Unravelling the tectonothermal evolution of reworked Archean granulite facies metapelites using in situ geochronology: an example from the Gawler Craton, Australia. Journal of Metamorphic Geology 28, 293-316.

Ehrig, K., McPhie, J., Kamenetsky, V.S., 2012. Geology and mineralogical zonation of the Olympic Dam iron oxide Cu-U-Au-Ag deposit, South Australia. Society of Economic Geologists Special Publication.

Fairclough, M.C., Schwarz, M.P., Ferris, G.M., 2003. Interpreted crystalline basement geology of the Gawler Craton. South Australia, Geological Survey, Special Map, 1:1,000,000.

Fanning, C.M., Flint, R.B., Parker, A.J., Ludwig, K.R., Blissett, A.H., 1988. Refined Proterozoic evolution of the Gawler Craton, South Australia, through U-Pb zircon geochronology. Precambrian Research 40–41, 363-386.

Fanning, C.M., Reid, A.J., Teale, G., 2007. A geochronological framework for the Gawler Craton, South Australia. . South Australia. Geological Survey. Bulletin 55.

Ferris, G., Schwarz, M., 2004. Definition of the Tunkillia Suite, western Gawler craton. Minerals and Energy South Australia Journal 34, 32-41.

Flint, R.B., Rankin, L.R., Fanning, C.M., 1990. Definition; the Palaeoproterozoic St. Peter Suite of the western Gawler craton. Geological Survey of South Australia, Quarterly Geological Notes 114, 2-8.

Forbes, C.J., Giles, D., Hand, M., Betts, P.G., Suzuki, K., Chalmers, N., Dutch, R., 2011. Using P–T paths to interpret the tectonothermal setting of prograde metamorphism: An example from the northeastern Gawler Craton, South Australia. Precambrian Research 185, 65-85.

Forbes, C.J., Giles, D., Jourdan, F., Sato, K., Omori, S., Bunch, M., 2012. Cooling and exhumation history of the northeastern Gawler Craton, South Australia. Precambrian Research 200–203, 209-238.

Foster, D.A., Ehlers, K., 1998. 40Ar-39Ar thermochronology of the southern Gawler Craton, Australia: Implications for Mesoproterozoic and Neoproterozoic tectonics of East Gondwana and Rodinia. Journal of Geophysical Research 103, 10,177-110,193.

Fraser, G., Reid, A., Stern, R., 2012. Timing of deformation and exhumation across the Karari Shear Zone, north-western Gawler Craton, South Australia. Australian Journal of Earth Sciences 59, 547-570.

Fraser, G.L., Lyons, P., 2006. Timing of Mesoproterozoic tectonic activity in the northwestern Gawler Craton constrained by 40Ar/39Ar geochronology. Precambrian Research 151, 160-184.

Fraser, G.L., Skirrow, R.G., Schmidt-Mumm, A., Holm, O., 2007. Mesoproterozoic Gold in the Central Gawler Craton, South Australia: Geology, Alteration, Fluids, and Timing. Economic Geology 102, 1511-1539.

Giles, C.W., 1988. Petrogenesis of the Proterozoic Gawler Range Volcanics, South Australia. Precambrian Research 40–41, 407-427.

Gleadow, A.J.W., Kohn, B.P., Brown, R.W., O'Sullivan, P.B., Raza, A., 2002. Fission track thermotectonic imaging of the Australian continent. Tectonophysics 349, 5-21.

Glorie, S., Agostino, K., Dutch, R., Pawley, M., Hall, J., Danišík, M., Evans, N.J., Collins, A.S., 2017. Thermal history and differential exhumation across the Eastern Musgrave Province, South Australia: Insights from low-temperature thermochronology. Tectonophysics 703–704, 23-41.

Hall, J.W., Glorie, S., Collins, A.S., Reid, A., Evans, N., McInnes, B., Foden, J., 2016. Exhumation history of the Peake and Denison Inliers: insights from low-temperature thermochronology. Australian Journal of Earth Sciences 63, 805-820.

Hall, J.W., Glorie, S., Reid, A.J., Collins, A.S., Jourdan, F., Evans, N., submitted. Regional thermal history of the northern Olympic Domain, Gawler Craton. Gondwana Research.

Halpin, J.A., Reid, A.J., 2016. Earliest Paleoproterozoic high-grade metamorphism and orogenesis in the Gawler Craton, South Australia: The southern cousin in the Rae family? Precambrian Research 276, 123-144.

Hand, M., Reid, A., Jagodzinski, L., 2007. Tectonic Framework and Evolution of the Gawler Craton, Southern Australia. Economic Geology 102, 1377-1395.

Harrison, T.M., Célérier, J., Aikman, A.B., Hermann, J., Heizler, M.T., 2009. Diffusion of 40Ar in muscovite. Geochimica et Cosmochimica Acta 73, 1039-1051.

Howard, H.M., Smithies, R.H., Kirkland, C.L., Kelsey, D.E., Aitken, A., Wingate, M.T.D., Quentin de Gromard, R., Spaggiari, C.V., Maier, W.D., 2015. The burning heart — The Proterozoic geology and geological evolution of the west Musgrave Region, central Australia. Gondwana Research 27, 64-94.

Howard, K.E., Hand, M., Barovich, K.M., Payne, J.L., Belousova, E.A., 2011a. U–Pb, Lu–Hf and Sm–Nd isotopic constraints on provenance and depositional timing of metasedimentary rocks in the western Gawler Craton: Implications for Proterozoic reconstruction models. Precambrian Research 184, 43-62.

Howard, K.E., Hand, M., Barovich, K.M., Payne, J.L., Cutts, K.A., Belousova, E.A., 2011b. U–Pb zircon, zircon Hf and whole-rock Sm–Nd isotopic constraints on the evolution of Paleoproterozoic rocks in the northern Gawler Craton. Australian Journal of Earth Sciences 58, 615-638.

Jagodzinski, E., 2005. Compilation of SHRIMP U-Pb geochronological data, Olympic Domain, Gawler Craton, South Australia, 2001-2003. Geoscience Australia Record 20, 197.

Jagodzinski, E.A., Reid, A.J., Fraser, G., 2009. Compilation of SHRIMP U-Pb geochronological data for the Mulgathing Complex, Gawler Craton, South Australia, 2007-09. South Australia. Department of Primary Industries and Resources. Report Book 2009/00016. .

Kirkland, C.L., Smithies, R.H., Spaggiari, C.V., Wingate, M.T.D., Quentin de Gromard, R., Clark, C., Gardiner, N.J., Belousova, E.A., 2017. Proterozoic crustal evolution of the Eucla basement, Australia: Implications for destruction of oceanic crust during emergence of Nuna. Lithos 278–281, 427-444.

Liu, W., Zhang, J., Sun, T., Wang, J., 2014. Application of apatite U–Pb and fission-track double dating to determine the preservation potential of magnetite–apatite deposits in the Luzong and Ningwu volcanic basins, eastern China. Journal of Geochemical Exploration 138, 22-32.

Ludwig, K.R., 1999. Using Isoplot/Ex, Version 2.01: a geochronological toolkit for Microsoft Excel. Berkeley Geochronology Center Special Publication No. 1a: 47.

Ludwig, K.R., 2012. User's manual for Isoplot 3.75, A Geochronological Toolkit for Microsoft Excel. Berkeley Geochronology Center Special Publication No. 5

Mark, C., Cogné, N., Chew, D., 2016. Tracking exhumation and drainage divide migration of the Western Alps: A test of the apatite U-Pb thermochronometer as a detrital provenance tool. Geological Society of America Bulletin 128, 1439-1460.

McDougall, I., Harrison, M., 1999. Geochronology and Thermochronology by the 40Ar/39Ar Method. Oxford University Press, New York.

McDowell, F.W., McIntosh, W.C., Farley, K.A., 2005. A precise 40Ar–39Ar reference age for the Durango apatite (U–Th)/He and fission-track dating standard. Chemical Geology 214, 249-263.

McLean, M.A., Betts, P.G., 2003. Geophysical constraints of shear zones and geometry of the Hiltaba Suite granites in the western Gawler Craton, Australia. Australian Journal of Earth Sciences 50, 525-541.

McPhie, J., Kamenetsky, V.S., Chambefort, I., Ehrig, K., Green, N., 2011. Origin of the supergiant Olympic Dam Cu-U-Au-Ag deposit, South Australia: Was a sedimentary basin involved? Geology 39, 795-798.

Müller, W., 2003. Strengthening the link between geochronology, textures and petrology. Earth and Planetary Science Letters 206, 237-251.

Oliver, R.L., Fanning, C.M., 1997. Australia and Antarctica; precise correlation of Palaeoproterozoic terrains, In: Ricci Carlo, A. (Ed.), The Antarctic region; Geological evolution and processes: Proceedings of the VII International Symposium on Antarctic Earth Sciences. Terra Antarctica Publication, Siena, Italy, pp. 163-172.

Parker, A.J., Daly, S.J., Flint, D.J., Flint, R.B., Preiss, W.V., Teale, G., 1993. Palaeoproterozoic, In: Drexel, J.F., Preiss, W.V., Parker, A.J. (Eds.), The geology of South Australia; Volume 1, The Precambrian: South Australia Geological Survey, Bulletin 54.

Parker, A.J., Lemon, N.M., 1982. Reconstruction of the early Proterozoic stratigraphy of the Gawler craton, South Australia. Journal of the Geological Society of Australia 29, 221-238.

Paton, C., Hellstrom, J., Paul, B., Woodhead, J., Hergt, J., 2011. Iolite: Freeware for the visualisation and processing of mass spectrometric data. Journal of Analytical Atomic Spectrometry 26, 2508-2518.

Payne, J.L., Barovich, K.M., Hand, M., 2006. Provenance of metasedimentary rocks in the northern Gawler Craton, Australia: Implications for Palaeoproterozoic reconstructions. Precambrian Research 148, 275-291.

Payne, J.L., Hand, M., Barovich, K.M., Wade, B.P., 2008. Temporal constraints on the timing of high-grade metamorphism in the northern Gawler Craton: implications for assembly of the Australian Proterozoic. Australian Journal of Earth Sciences 55, 623-640.

Pochon, A., Poujol, M., Gloaguen, E., Branquet, Y., Cagnard, F., Gumiaux, C., Gapais, D., 2016. U-Pb LA-ICP-MS dating of apatite in mafic rocks: Evidence for a major magmatic event at the Devonian-Carboniferous boundary in the Armorican Massif (France), American Mineralogist, p. 2430.

Rankin, L.R., Flint, R.B., Fanning, C.M., 1990. Palaeoproterozoic Nuyts Volcanics of the western Gawler craton, South Australia. Department of Primary Industries and Resources, Report Book 90/60, 17.

Rankin, L.R., Martin, A.R., Parker, A.J., 1989. Early Proterozoic history of the Karari Fault Zone, northwest Gawler Craton, South Australia. Australian Journal of Earth Sciences 36, 123-133.

Reddy, M., Glorie, S., Reid, A.J., Collins, A.S., 2015. Phanerozoic cooling history of the central Gawler Craton: implications of new low-temperature thermochronological data. MESA Journal 75, 56-60.

Reddy, S.M., Potts, G.J., 1999. Constraining absolute deformation ages: the relationship between deformation mechanisms and isotope systematics. Journal of Structural Geology 21, 1255-1265.

Reid, A., Hand, M., Jagodzinski, E., Kelsey, D., Pearson, N., 2008. Paleoproterozoic orogenesis in the southeastern Gawler Craton, South Australia. Australian Journal of Earth Sciences 55, 449-471.

Reid, A.J., Fabris, A., 2015. Influence of Preexisting Low Metamorphic Grade Sedimentary Successions on the Distribution of Iron Oxide Copper-Gold Mineralization in the Olympic Cu-Au Province, Gawler Craton. Economic Geology 110, 2147-2157.

Reid, A.J., Fricke, C.E., Cowley, W.M., 2009. Extent of low-grade Archaean metavolcanics in the northeastern Gawler Craton: new evidence and definition of the Devils Playground Volcanics. MESA Journal 054, 009-019.

Reid, A.J., Jagodzinski, E.A., Fraser, G.L., 2010. New constraints on the tectonics of the Archaean–Paleoproterozoic transition from the Gawler Craton, South Australia., In: M., T.I., M., K.-R.C. (Eds.), Fifth International Archean Symposium Abstracts. Geological Survey of Western Australia, Record 2010/18,, p. 203.

Reid, A.J., Jagodzinski, E.A., Fraser, G.L., Pawley, M.J., 2014. SHRIMP U–Pb zircon age constraints on the tectonics of the Neoarchean to early Paleoproterozoic transition within the Mulgathing Complex, Gawler Craton, South Australia. Precambrian Research 250, 27-49.

Reid, A.J., Jourdan, F., Jagodzinski, E.A., 2017. Mesoproterozoic fluid events affecting Archean crust in the northern Olympic Cu–Au Province, Gawler Craton: insights from 40Ar/39Ar thermochronology. Australian Journal of Earth Sciences 64, 103-119.

Shaw, C.A., Karlstrom, K.E., Williams, M.L., Jercinovic, M.J., McCoy, A.M., 2001. Electron-microprobe monazite dating of ca. 1.71–1.63 Ga and ca. 1.45–1.38 Ga deformation in the Homestake shear zone, Colorado: Origin and early evolution of a persistent intracontinental tectonic zone. Geology 29, 739-742.

Skirrow, R.G., Bastrakov, E.N., Davidson, G.J., Raymond, O.L., Heithersay, P., 2002. The geological framework, distribution and controls of Fe-oxide and related alteration, and Cu-Au mineralisation in the Gawler craton, South Australia. Part II: Alteration and mineralisation, In: Porter, T.M. (Ed.), Hydrothermal iron oxide copper-gold and related deposits: A global perspective, 2. Porter GeoConsultancy Publishing, Adelaide, pp. 33-47.

Stewart, A.J., Betts, P.G., Collins, A.S., Schaefer, B.F., 2009. Multi-scale analysis of Proterozoic shear zones: an integrated structural and geophysical study. Journal of Structural Geology 31, 1238-1254.

Stewart, J.R., Betts, P.G., 2010. Implications for Proterozoic plate margin evolution from geophysical analysis and crustal-scale modeling within the western Gawler Craton, Australia. Tectonophysics 483, 151-177.

Swain, G.M., Hand, M., Teasdale, J., Rutherford, L., Clark, C., 2005. Age constraints on terrane-scale shear zones in the Gawler Craton, southern Australia. Precambrian Research 139, 164-180.

Szpunar, M., Hand, M., Barovich, K., Jagodzinski, E., Belousova, E., 2011. Isotopic and geochemical constraints on the Paleoproterozoic Hutchison Group, southern Australia: Implications for Paleoproterozoic continental reconstructions. Precambrian Research 187, 99-126.

Teasdale, J., 1997. The interpretive geology and tectonothermal evolution of the western Gawler Craton, Ph.D. thesis, University of Adelaide. (Unpublished). 1–142.

Thomson, S.N., Gehrels, G.E., Ruiz, J., Buchwaldt, R., 2012. Routine low-damage apatite U-Pb dating using laser ablation–multicollector–ICPMS. Geochemistry, Geophysics, Geosystems 13.

Tomkins, A.G., Dunlap, W.J., Mavrogenes, J.A., 2004. Geochronological constraints on the polymetamorphic evolution of the granulite-hosted Challenger gold deposit: implications for assembly of the northwest Gawler Craton*. Australian Journal of Earth Sciences 51, 1-14.

Tomkins, A.G., Mavrogenes, J.A., 2002. Mobilization of Gold as a Polymetallic Melt during Pelite Anatexis at the Challenger Deposit, South Australia: A Metamorphosed Archean Gold Deposit. Economic Geology 97, 1249-1271.

Williams, H.A., Betts, P.G., 2009. The Benagerie Shear Zone: 1100 Myr of reactivation history and control over continental lithospheric deformation. Gondwana Research 15, 1-13.

Yang, B., Smith, T., Collins, A.S., Munson, T.J., Schoemaker, B., Nicholls, D., Cox, G., Farkas, J., Glorie, S., submitted. Spatial and temporal detrital zircon U-Pb provenance of the hydrocarbon-bearing upper Roper Group, Beetaloo Sub-basin, Northern Territory, Australia. Precambrian Research.

Zattin, M., Andreucci, B., Thomson, S.N., Reiners, P.W., Talarico, F.M., 2012. New constraints on the provenance of the ANDRILL AND-2A succession (western Ross Sea, Antarctica) from apatite triple dating. Geochemistry, Geophysics, Geosystems 13, n/a-n/a.

Zhang, F., Wang, X., Sun, Z., Chen, X., Zhou, X., Yang, T., 2017. Geochemistry and zircon-apatite U-Pb geochronology of mafic dykes in the Shuangxiwu area: Constraints on the initiation of Neoproterozoic rifting in South China. Precambrian Research.

Chapter 2

Thermal history of the northern Olympic Domain

Published as:

Hall, J.W., Glorie, S., Reid, A.J., Collins, A.S., Jourdan, F., Danišík, M., and Evans, N., 2018, Thermal History of the Northern Olympic Domain, Gawler Craton; Correlations between Thermochronometric Data and Mineralising Systems. Gondwana Research 56, 90-104.

Statement of Authorship

Title of Paper	Thermal history of the northern Olympic Domain, Gawler Craton; correlations between thermochronometric data and mineralising systems
Publication Status	☑ Published ☐ Accepted for Publication ☐ Submitted for Publication ☐ Unpublished and Unsubmitted work written in manuscript style
Publication Details	Hall, J.W., Glorie, S., Reid, A.J., Collins, A.S., Jourdan, F., Danišík, M., and Evans, N., 2018, Thermal History of the Northern Olympic Domain, Gawler Craton; Correlations between Thermochronometric Data and Mineralising Systems. Gondwana Research 56, 90-104.

Principal Author

Name of Principal Author (Candidate)	James Hall		
Contribution to the Paper	Sample collection, data collection, data interpretation, manuscript and figure composition.		
Overall percentage (%)	70 %		
Certification:	This paper reports on original research I conducted during the period of my Higher Degree by Research candidature and is not subject to any obligations or contractual agreements with a third party that would constrain its inclusion in this thesis. I am the primary author of this paper.		
Signature		Date	1/05/18

Co-Author Contributions

By signing the Statement of Authorship, each author certifies that:

i. the candidate's stated contribution to the publication is accurate (as detailed above);

ii. permission is granted for the candidate in include the publication in the thesis; and

iii. the sum of all co-author contributions is equal to 100% less the candidate's stated contribution.

Name of Co-Author	Stijn Glorie		
Contribution to the Paper	Assistance in data collection, assistance in data interpretation, manuscript review. 10% contribution.		
Signature		Date	1/05/18

Name of Co-Author	Anthony Reid		
Contribution to the Paper	Sample collection, assistance in data interpretation, manuscript review . 4% contribution.		
Signature		Date	11/05/18
Name of Co-Author	Alan Collins		
Contribution to the Paper	Assistance in data interpretation, manuscript review . 4% contribution.		
Signature		Date	27/6/18
Name of Co-Author	Fred Jourdan		
Contribution to the Paper	data collection, manuscript review . 4% contribution.		
Signature		Date	26/04/18
Name of Co-Author	Martin Danišik		
Contribution to the Paper	data collection, manuscript review . 4% contribution.		
Signature		Date	3/05/18
Name of Co-Author	Noreen Evans		
Contribution to the Paper	data collection, manuscript review . 4% contribution.		
Signature		Date	10/04/18

Abstract

Multi-method thermochronology applied to the northern Olympic Domain of South Australia reveals a complex thermal evolution with multiple thermal events. Apatite U-Pb (closure temperature ~550 – 350 °C) and muscovite $^{40}Ar/^{39}Ar$ ages (~400 – 350 °C) record post magmatic cooling from 1850 – 750 Ma for the ~1850 Ma Donington Suite, and from ~1560 – 1500 Ma for the ~1590 Ma Hiltaba Suite and the Gawler Range Volcanics. Potassium feldspar $^{40}Ar/^{39}Ar$ ages (~350 – 150 °C) record disturbed spectra that are likely related to hydrothermal alteration at ~1000 – 650 Ma in the Neoproterozoic Adelaide Rift Complex. Apatite fission track (~60 – 120 °C), zircon (U-Th-Sm)/He (~180 – 200 °C), and apatite (U-Th-Sm)/He (~45 – 75 °C) ages reveal regional low temperature thermal events at ~1000 Ma, ~430 – 400 Ma, 350 – 330 Ma, and ~200 Ma, in addition to localised thermal events during the Cretaceous. The ~1000 Ma apatite fission track ages are amongst the oldest recorded for South Australia and are only preserved near the margins of the Olympic Domain. The ~430 – 400 Ma and ~350 – 330 Ma cooling events are interpreted to be driven by the Alice Springs Orogeny. The Mesozoic thermochronometric ages are interpreted to record localised thermal perturbations, possibly related with hydrothermal activity within the northern Olympic Domain. The presence of abundant IOCG deposits near these young thermal anomalies may indicate that these zones record more favourable thermal conditions and/or exposure levels for IOCG discoveries in the study area.

2.1 Introduction

The Olympic Domain is home to the world class Olympic Dam Iron Oxide Copper Gold (IOCG) mineral deposit, in addition to numerous other IOCG mineral deposits such as Prominent Hill, Carrapateena, Khamsin, and Emmie Bluff (Fig 2.1). The Olympic Domain is the most deposit-rich domain within the Gawler Craton of South Australia (in particular, the northern Olympic Domain; Fig. 2.1) and preserves a complex geological history that began in the Palaeoproterozoic (Hand et al., 2007). After initial formation of the Gawler Craton, the most notable thermo-tectonic event within the Olympic Domain was the ca. 1590 Ma Hiltaba Event (e.g. Daly et al., 1998; Budd et al., 2001; Skirrow et al., 2002; Fanning et al., 2007; Hand et al., 2007), which was associated with emplacement of the Hiltaba Suite granites and extensive IOCG mineralisation. Published work conducted on these IOCG deposits have inquired into various aspects of their formation (Belperio et al., 2007; Davidson et al., 2007; Direen and Lyons, 2007; Skirrow et al., 2007; McPhie et al., 2011; Ismail et al., 2014; Jagodzinski, 2014; Kamenetsky et al., 2016; Kirchenbaur et al., 2016; Macmillan et al., 2016). However, only few studies have ventured into investigating the post-Hiltaba thermal history of the Olympic Domain (Reid et al., 2017). Recent studies have highlighted that early Phanerozoic hydrothermal activity affected the Olympic Dam deposits (Maas et al., 2011; McPhie et al., 2011; Kamenetsky et al., 2016), and this activity appears to have remobilised and concentrated the uranium (Kamenetsky et al., 2016). Consequently, a better understanding of the thermal history of the Olympic Domain is becoming increasingly relevant to understand its

regional complexity in relation to the occurrence of IOCG deposits, and, perhaps, inform future exploration.

This study applies multi-method thermochronology by combining apatite U-Pb, muscovite and potassium feldspar $^{40}Ar/^{39}Ar$, zircon and apatite (U-Th-Sm)/He, and apatite fission track (AFT) dating on selected drill cores from the top of Palaeoproterozoic basement to provide insights into the thermal history of the northern Olympic Domain between ~550 °C and surface temperatures (Wagner and van den Haute, 1992; McDougall and Harrison, 1999; Ehlers and Farley, 2003; Reiners et al., 2004; Schoene and Bowring, 2007). Where possible and relevant, thermal history models are presented. Associated thermal events that affected the northern Olympic Domain are linked to the tectonic events that affected the Gawler Craton and/or with thermal perturbations that are likely related with elevated geothermal gradients and hydrothermal activity.

2.2 Geological setting

2.2.1 Gawler Craton

The Gawler Craton is a Mesoarchaean – Mesoproterozoic craton that occupies most of South Australia (Daly et al., 1998; Fraser et al., 2010). The nucleus of the Gawler Craton is comprised of relatively small outcrops of Mesoarchaean rocks of the Cleve Domain that are surrounded by the ~2500 – 2400 Ma metasedimentary rocks of the Sleaford Complex in the southern Gawler Craton (Daly et al., 1998; Fanning et al., 2007; Hand et al., 2007) and the ~2500 – 2400 Ma metasedimentary rocks of the Mulgathing Complex in the western Gawler Craton (Fig. 2.1; Hand et al., 2007; Reid et al., 2014). Following tectonic quiescence from ~2400 – 2000 Ma, the remaining rocks of the Gawler Craton, including the units of the Olympic Domain, formed during the late Palaeoproterozoic – early Mesoproterozoic (Fig. 2.2; Hand et al., 2007). In the western and southern Gawler Craton, metasedimentary rocks of the Fowler, Nuyts, Coulta, and Cleve domains were deformed at about the same time as metasedimentary rocks of the Nawa Domain, at around 1730 – 1690 Ma in response to the Kimban Orogeny (Hand et al., 2007). The final stages of craton building were dominated by igneous activity, including the emplacement of the Tunkillia Suite within the central Gawler Craton (1690 – 1670 Ma; Fanning et al., 2007; Payne et al., 2010), the Nuyts Volcanics (1630 Ma; Rankin et al., 1990), the St. Peter Suite (1620 – 1610 Ma; Flint et al., 1990) in the southwestern Gawler Craton (Fig. 2.1), and the ~1590 Ma Hiltaba Event.

2.2.2 Olympic Domain

The Olympic Domain is located on the eastern margin of the Gawler Craton (Fig. 2.1). It is characterised by the occurrences of copper and gold mineralisation stretching from Prominent Hill and Olympic Dam in the north (Belperio et al., 2007; McPhie et al., 2011), to Hillside on the Yorke Peninsula (Ismail et al., 2014). The oldest unit within the Olympic Domain is the 1866 ± 10 Ma Hutchison Group, which is a deformed sedimentary sequence (Fig. 2.2; Parker and Lemon,

1982; Fanning et al., 2007; Szpunar et al., 2011). The Donington Suite was emplaced at ~1850 Ma along the eastern margin on the Gawler Craton, likely in an intracontinental back arc basin setting (Reid et al., 2008). The Donington Suite is a granite-granodiorite dominated magmatic suite associated with the Cornian Orogeny (Jagodzinski, 2005; Reid et al., 2008). Back-arc rifting along the eastern Gawler Craton from 1770 to 1740 Ma resulted in deposition of the Wallaroo Group and associated magmatism in the Olympic Domain (Fig. 2.2; Cowley et al., 2003; Hand et al., 2007). Sedimentation ceased by the onset of the Kimban Orogeny (1730–1690 Ma; Hoek and Schaefer, 1998), which deformed the central Gawler Craton, yet only had a minimal effect within the Olympic Domain (Reid and Fabris, 2015).

The ~1590 Ma Hiltaba Event is the most volumetrically significant magmatic event within the Olympic Domain and resulted in the formation of the co-magmatic Hiltaba Suite granitoids and the Gawler Range Volcanics (GRV; Fig. 2.2; e.g. Giles, 1988; Creaser and White, 1991; Creaser, 1996; Hand et al., 2007). The Hiltaba Event is associated with regional alteration and mineralisation including iron oxide-copper-gold (IOCG) deposits such as Olympic Dam, Prominent Hill and Carrapateena within the Olympic Domain (Fig. 2.1; Skirrow et al., 2002; Skirrow et al., 2007). Skirrow et al. (2007) suggested that major fault zones within the northern Olympic Domain were active at ~1590 Ma, which likely facilitated fluid flow and regional alteration systems. This fault system has been interpreted to be part of an inverted northeast directed graben system (Hayward and Skirrow, 2010).

2.2.3 Pandurra Formation, Stuart Shelf and Delamerian Orogeny

The basement geology of the Olympic Domain is largely overlain by the ~1560 – 1420 Ma Pandurra Formation of the Cariewerloo Basin (Fig. 2.1), indicating the region underwent extension and sedimentary burial after emplacement of the GRV and Hiltaba Suite granitiods (Fanning et al., 1983; Cowley, 1993; Schmidt and Williams, 2011; Rollison, 2016; Cherry et al., 2017). The next major phase of deposition occurred during the Neoproterozoic, with the formation of Adelaide Rift Complex (Fig. 2.1; Preiss, 1993, 2000; Mahan et al., 2010). The Adelaide Rift Complex preserves at least five phases of rifting, and three associated sedimentary supergroups: the Warrina (840 – 710 Ma), Heysen (700 – 500 Ma), and Moralana (530 – 515 Ma) supergroups (Preiss, 2000; Mahan et al., 2010). The Heysen, and Moralana supergroups blanket the entire northern Olympic Domain that lay on the western flank of the Adelaide Rift Complex within the Stuart Shelf (Fig. 2.1). However, the thicker rift sequences were deposited to the east in the Flinders Ranges (Gow et al., 1993; Preiss, 1993). A regional unconformity is recorded between the Warrina and Heyson supergroups. Glacial unconformities are recorded within the ~650 Ma Whyalla Sandstone and Marinoan glacials within the Heysen supergroup (Preiss, 1993; Preiss et al., 1998; Williams, 1998; Preiss, 2000; Le Heron et al., 2011; Le Heron, 2012).

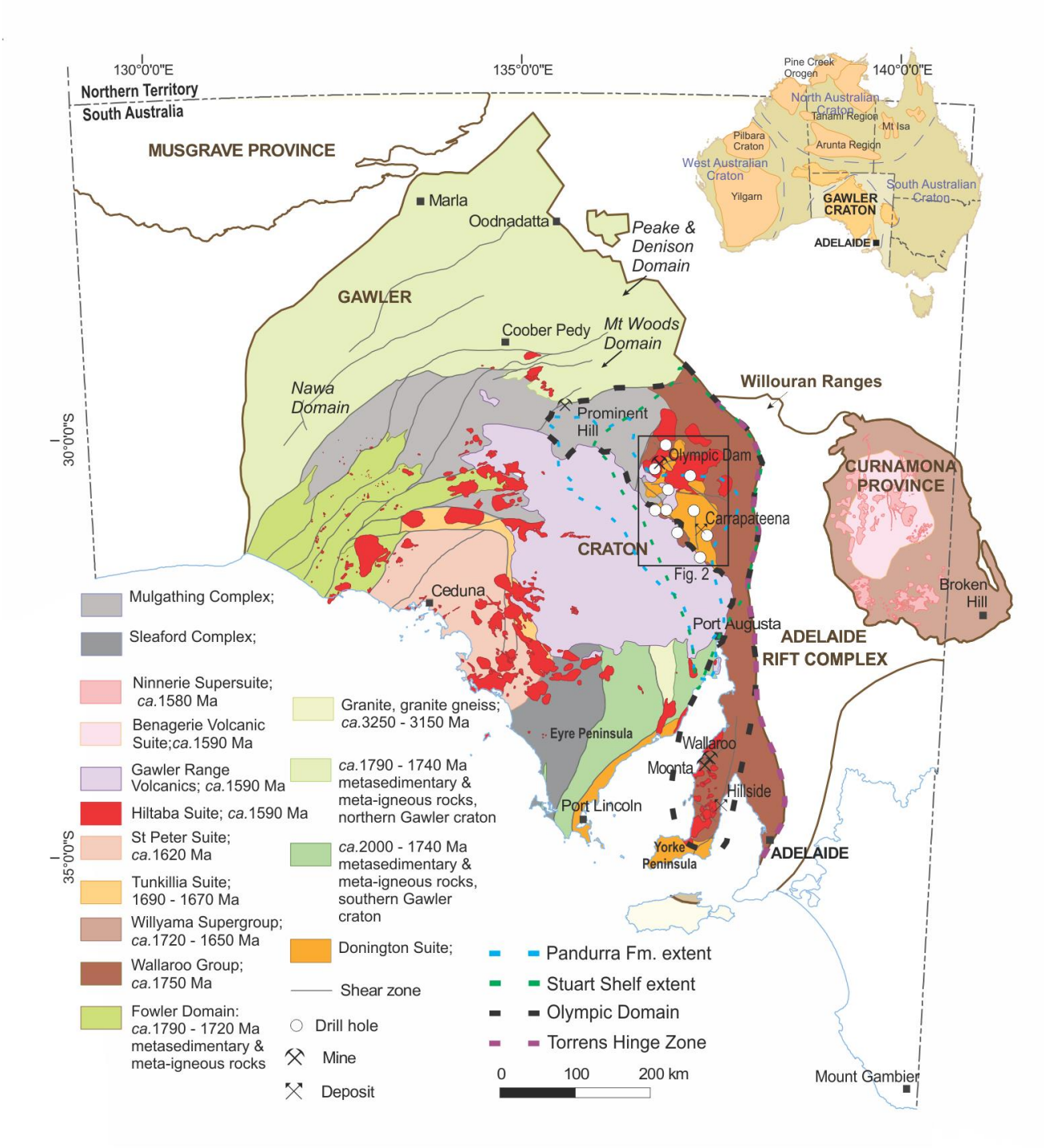

Figure 2.1: Simplified geological map of the Gawler Craton and adjacent geological domains, showing the locations of sampled drill holes, major IOCG deposits, the Torrens Hinge Zone, and the extent of the Pandurra Formation and Stuart Shelf. Adapted from Reid and Fabris (2015).

Deposition of the Adelaide Rift Complex was terminated by the onset of the Delamerian Orogeny at c. 515 Ma (Foden et al., 2006). Foden et al. (2006) described the Delamerian Orogeny as diachronous with onset of the orogeny being marked by the commencement of felsic magmatism. The northernmost part of the orogen, the Peake and Denison Ranges (located north west of the Olympic Domain), records emplacement of monzonite at 513 ± 8 Ma (Foden et al., 2006). Localised strain within the Torrens Hinge Zone caused late orogenic deformation that ceased between 496 ± 2 Ma and 480 ± 4 Ma within the Adelaide Rift Complex. Preiss (1995) relates the occurrence of folding and faulting within the Stuart Shelf to the Delamerian Orogeny, however, the exact timing of this deformation within the orogeny is unconstrained.

2.2.4 Post-Delamerian tectonics

Although there is little documentation of tectonism that post-dates the Delamerian Orogeny within the Olympic Domain, thermochronological studies have suggested deformation and/or denudation to the east within the northern Flinders Ranges (e.g. Mt. Painter region; Foster et al., 1994; McLaren et al., 2002; Mitchell et al., 2002; Elburg et al., 2013; Weisheit et al., 2014), to the north within the Peake and Denison Inliers (Hall et al., 2016), and to the west within the central Gawler Craton (Reddy et al., 2015; Boone et al., 2016) (Fig. 2.1). All of these regions underwent cooling caused by exhumation during the Carboniferous, which has been suggested to be related to the far-field effects of the intracontinental Alice Springs Orogeny (~450 - 300 Ma; Hand et al., 1999; Ballèvre et al., 2000; Haines et al., 2001) and the Lachlan Orogen at the eastern plate margin (namely the Benambran, Tabberabberan, and Kanimblan Orogenies; Glen, 2005). Younger, more localised thermal events are also recorded within the northern Flinders Ranges, the central Gawler Craton, and Peake and Denison Inliers. Within the Mt. Painter Inlier, Late Cretaceous – Early Palaeogene and Miocene thermal resetting caused by hydrothermal activity is attributed to the presence of high uranium granites (Foster et al., 1994). Late Cretaceous – Early Palaeogene resetting of apatite fission tracks have also been documented within the Gawler Craton and this is thought to be related with hot fluid movement in a palaeo-aquifer system in overlying Mesozoic sandstones (Boone et al., 2016).

2.2.5 Current regional geothermal gradient

The elevated geothermal gradient within the Gawler Craton is well documented (Houseman et al., 1989; Neumann et al., 2000; Matthews, 2009) The geothermal is particularly elevated within the Olympic Domain and Stuart Shelf, with an average geothermal gradient of ~51 °C/km that increases to ~83 °C/km near the Olympic Dam deposit (Houseman et al., 1989). This is significantly higher than the global average of ~33 °C/km (Polak and Horsfall, 1979). The elevated geothermal gradients are caused by enrichment of heat-producing elements, such as U, Th and K, within the basement rocks of the Olympic Domain (Wyborn et al., 1992; Creaser, 1996; Neumann et al., 2000; Mclaren et al., 2003; Hand et al., 2007). Neumann et al. (2000) showed that the Hiltaba Suite of

the Stuart Shelf contains double the concentration of U, Th, and K ppm compared to the Hutchison Group.

2.3 Methodology

2.3.1 Rock sampling strategy

When low temperature thermochronology is generally applied to drill hole samples, it is to provide insights into the sedimentary burial history of a basin (e.g. Arne et al., 1989; Osadetz et al., 2002; Tingate and Duddy, 2002; Sahu et al., 2013). In this study we used drill core, but instead of targeting the sedimentary sequences, we sampled the buried basement to investigate the thermal history of the Proterozoic basement rocks. This approach has the advantage that, unlike sedimentary basins, the drill hole samples don`t record provenance information, making data interpretations generally more straight-forward. However, the geothermal gradient and heat flow of the region must be accounted for in a similar way to sedimentary basin studies in order to ensure that samples record meaningful cooling ages instead of ages related with the present-day geothermal gradient. The Olympic Domain preserves an elevated geothermal gradient caused by an enrichment in U, Th and K within the basement granites (Houseman et al., 1989; Wyborn et al., 1992; Creaser, 1996; Neumann et al., 2000; Mclaren et al., 2003; Matthews, 2009). As a result, only samples currently shallower than ~1 km were considered. Assuming an average geothermal gradient within the Olympic Domain of ~51 °C/km (Houseman et al., 1989), these are the only samples that may preserve information on the low-temperature thermal history for the region. The effect of modern partial reset related with elevated thermal gradients adds a complexity to the data that will be discussed further below.

The northernmost sample, 2131358, was collected from a gneiss within the Hutchison Group. Samples 2111462 and 2131362 were collected from granites of the Hiltaba Suite, while samples 2131363, 2131364, 2131355, and 1709141 were collected from rhyolites of the Gawler Range Volcanics. All remaining samples were collected from magmatic rocks within the Donington Suite. Samples 2117350, 2131357, 1831646, and 1831650, were collected from granites. Sample 2131356 was collected from a gabbro and sample 2131360 was collected from a gneiss.

2.3.2 Apatite thermochronology methods

Both apatite thermochronological methods were conducted simultaneously on the same samples. Drill core samples were crushed and the apatites were separated using conventional separation methods. The separated apatite concentrates were picked by hand, mounted in epoxy resin, ground and polished to expose internal surfaces. More details on the applied data reduction can be found in Chew et al. (2014), Gillespie et al. (2017), Glorie et al. (2017a), and Glorie et al. (2017b).

Sample	Drill hole number	Latitude	Longitude	Depth (m)	Lithology	Rock type	Formation age	Apatite U-Pb age	Ar/Ar	Zircon (U-Th-Sm)/He	AFT age population 1:	AFT age population 2:	Apatite (U-Th-Sm)/He
2131358	SHD 1	-30.185769°	137.002091°	857 – 858	Hutchison Group	Granitic Gneiss	1964 – 1850 Ma	1648±16 Ma	1250 – 950 Ma (K-spar)	-	328 ±17 Ma	-	-
2111462	Blanche 1	-30.470106°	136.797087°	1005 – 1006	Hiltaba Suite	Granite	1590 Ma	1559±20 Ma	1533±8 Ma (Mus) 900 – 600 Ma (K-spar)	250.9±15.4 Ma	347 ± 19 Ma	136.5 ± 5.7 Ma	-
2131362	BRD 1	-30.398105°	137.3016727°	804 - 805	Hiltaba Suite	Granite	1590 Ma	-	601 ± 61 Ma (K-spar)	-	-	-	-
2131363 + 2131364	RED 2	-30.575543°	137.367642°	334 – 335 445 – 446	Gawler Range Volcanics	Rhyolite	1590 Ma	-	-	-	1047±59 Ma	425±25 Ma	234.5±22.8 Ma
2117350	ASD10D04	-30.731497°	137.049772°	668 – 669	Donington Suite	Granite	1845 – 1855 Ma	1633±48 Ma	-	291±9.8 Ma	244±17 Ma	-	-
2131356	ASD 1	-31.03649°	137.108857°	961 – 962	Donington Suite	Gabbro	1845 – 1855 Ma	1811±26 Ma	-	-	401 ± 33 Ma	204 ± 8.3 Ma	-
2131355	SAE 11	-31.073198°	136.937901°	1000 – 1001	Gawler Range Volcanics	Rhyolite	1590 Ma	1508±30 Ma	-	-	962 ± 89 Ma	458 ± 21 Ma	-
2131357	PSC 7 SASC 3	-31.081659°	137.447937°	688 – 689	Donington Suite	Granite	1845 – 1855 Ma	-	-	-	406±18 Ma	-	-
1831646 + 1831650	MGD 45	-31.251144°	137.252149°	667 738	Donington Suite	Granite	1845 – 1855 Ma	1878±21 Ma	-	181.3±6.6 Ma	359±13 Ma	-	-
2131360	NHD1	-31.274311°	137.565152°	535 – 536	Donington Suite	Gneiss	1845 – 1855 Ma	1768±28 Ma	-	-	413 ± 26 Ma	201 ± 9.5 Ma	-
1709141	GHDD 1	-31.5663185°	137.4898619°	967 – 968	Gawler Range Volcanics	Altered Rhyolite	1590 Ma	-	-	258.7±11.2 Ma	-	-	-

Table 2.1: Sample details. Formation ages are from Jagodzinski (2005), Daly et al. (1998), Budd et al. (2001) and Skirrow et al. (2002).

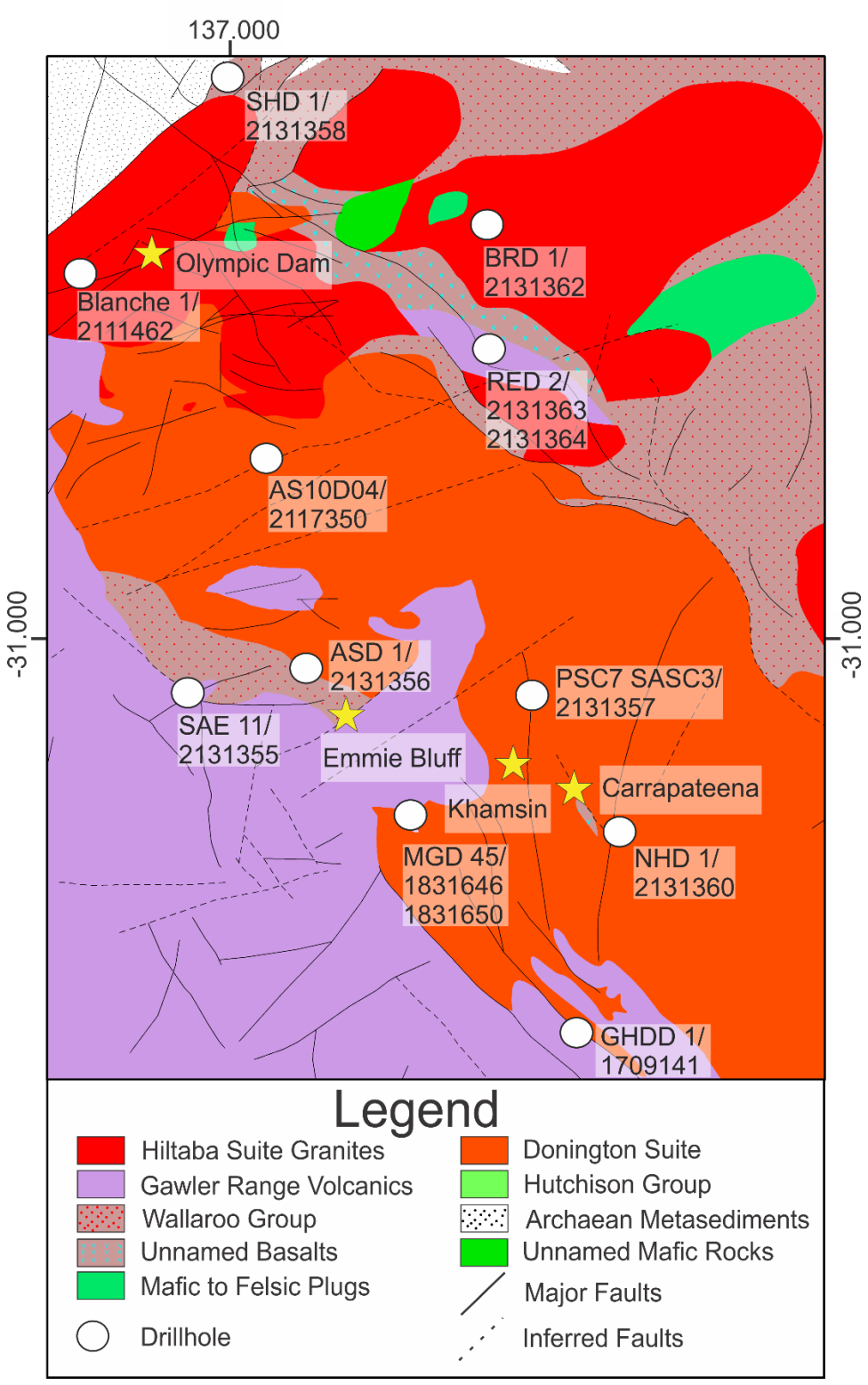

Figure 2.2: Interpreted solid geology map of the northern Olympic Domain showing the locations of major IOCG deposits, and sampled drill holes/sample numbers. Adapted from Wise et al. (2015). Note that the solid geology map only shows the units of the Gawler Craton, Adelaidean rocks of the Stuart Shelf are not presented.

2.3.2.1 Apatite fission track method

Apatite fission track (AFT) analysis was applied to constrain the timing of cooling through the apatite partial annealing zone (APAZ) at ~120 – 60 °C (Wagner and van den Haute, 1992). The apatite mounts were etched in a 5M HNO_3 solution for 20 seconds at 20 ºC to reveal the spontaneous fission tracks (Donelick et al., 1999). Determination of spontaneous fission track densities was carried by using digital imaging on a Zeiss AX10 microscope and utilizing an automatic counting routine in *Track Works* and *Fast Tracks* software packages (Gleadow et al., 2009). Uranium, lead, thorium, and chlorine, concentrations were collected using a *New Wave* Laser-Ablation system connected to an *Agilent* 7500 quadrupole Inductively-Coupled-Plasma Mass-Spectrometer (LA-ICP-MS) at Adelaide Microscopy. Data reduction was conducted using *Iolite* (Paton et al., 2011) by applying the data reduction scheme *X_trace elements_IS*. AFT data reduction for samples 2131358, 2131363, 2131364, 1831646, and 1831650 was carried out following Glorie et al. (2017a). For these samples, a suite of NIST glasses were used as primary standards and Durango apatite was used as secondary standard, producing an age of 33.5 ± 4 Ma, which is within error of the published age of 31.44 ± 0.18 Ma (McDowell et al., 2005). All other samples (2111462, 2117350, 2131356, 2131355, 2131357, and 2131360) were analysed against Madagascar apatite as primary standard (Thomson et al., 2012), following Chew et al. (2014). Durango (30.7 ± 3.9 Ma analysed compared to 31.44 ± 0.18 Ma; McDowell et al., 2005) was analysed as a secondary standard. A Zeta calibration was performed using repeated analysis on Durango apatite standards and the age equations presented in Vermeesch (2017).

2.3.2.2 Apatite U-Pb method

Apatite U-Pb records the timing of cooling of the sample through ~550 – 350 °C (Chew and Spikings, 2015). U and Pb ratios were collected on the LA-ICP-MS simultaneously along with the U, Pb, Th, and Cl concentrations for the AFT method. The same standards (NIST glass standards, Madagascar, and Durango apatite standards) analysed in the AFT method were also analysed for apatite U-Pb following Chew et al. (2014). An additional standard, Mount McClure (518 ± 11 Ma, which is within error of the published age of 523.51 ± 2.07 Ma; Thomson et al., 2012) apatite was used as a secondary standard for the U-Pb method. Data reduction was conducted using *Iolite* (Paton et al., 2011) by applying the data reduction scheme *VisualAge_UcomPbine* (Chew et al., 2014). Concordia and weighted mean plots were created using *Isoplot 4.15* (Ludwig, 2012). The initial measured $^{207}Pb/^{206}Pb$ ratios were used to correct for common Pb using the ^{207}Pb correction (Chew et al., 2014). The initial $^{207}Pb/^{206}Pb$ ratio is calculated using a Concordia line (referred to as a common Pb line) through the individual analyses on a Tera-Wasserburg plot.

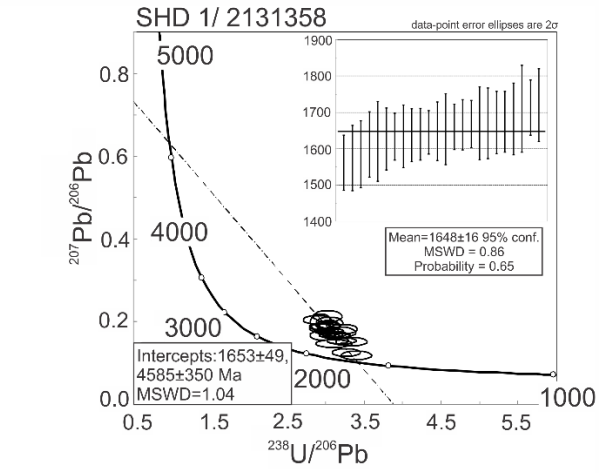
SHD 1/ 2131358
data-point error ellipses are 2σ
Mean=1648±16 95% conf.
MSWD = 0.86
Probability = 0.65
Intercepts:1653±49,
4585±350 Ma
MSWD=1.04
$^{207}Pb/^{206}Pb$
$^{238}U/^{206}Pb$

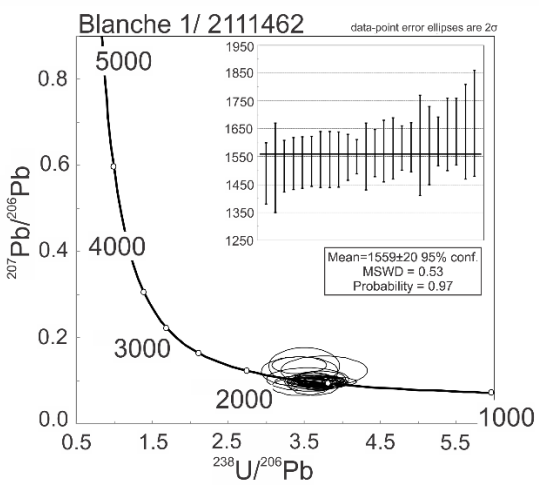
Blanche 1/ 2111462
data-point error ellipses are 2σ
Mean=1559±20 95% conf.
MSWD = 0.53
Probability = 0.97
$^{207}Pb/^{206}Pb$
$^{238}U/^{206}Pb$

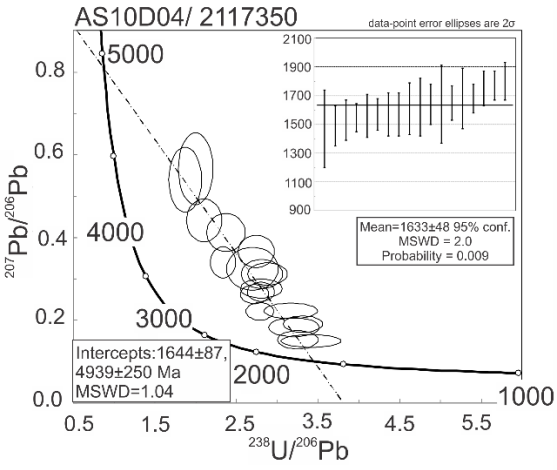
AS10D04/ 2117350
data-point error ellipses are 2σ
Mean=1633±48 95% conf.
MSWD = 2.0
Probability = 0.009
Intercepts:1644±87,
4939±250 Ma
MSWD=1.04
$^{207}Pb/^{206}Pb$
$^{238}U/^{206}Pb$

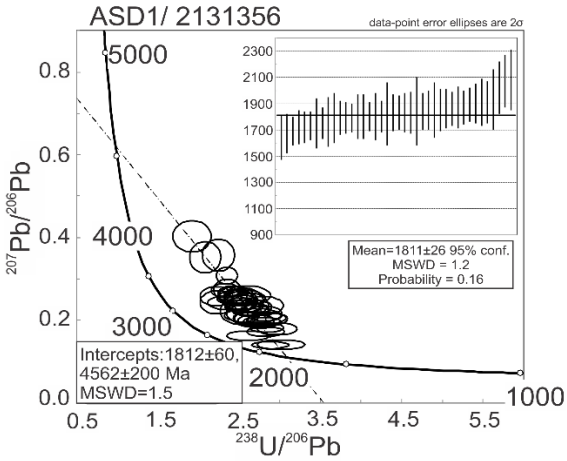
ASD1/ 2131356
data-point error ellipses are 2σ
Mean=1811±26 95% conf.
MSWD = 1.2
Probability = 0.16
Intercepts:1812±60,
4562±200 Ma
MSWD=1.5
$^{207}Pb/^{206}Pb$
$^{238}U/^{206}Pb$

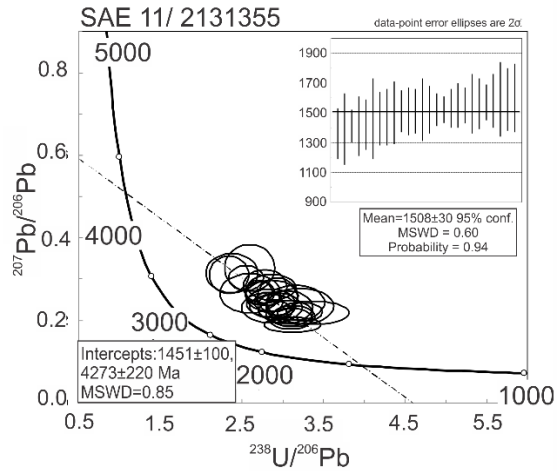
SAE 11/ 2131355
data-point error ellipses are 2σ
Mean=1508±30 95% conf.
MSWD = 0.60
Probability = 0.94
Intercepts:1451±100,
4273±220 Ma
MSWD=0.85
$^{207}Pb/^{206}Pb$
$^{238}U/^{206}Pb$

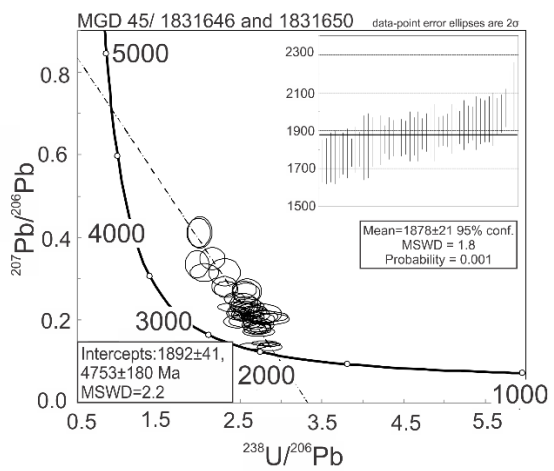
MGD 45/ 1831646 and 1831650
data-point error ellipses are 2σ
Mean=1878±21 95% conf.
MSWD = 1.8
Probability = 0.001
Intercepts:1892±41,
4753±180 Ma
MSWD=2.2
$^{207}Pb/^{206}Pb$
$^{238}U/^{206}Pb$

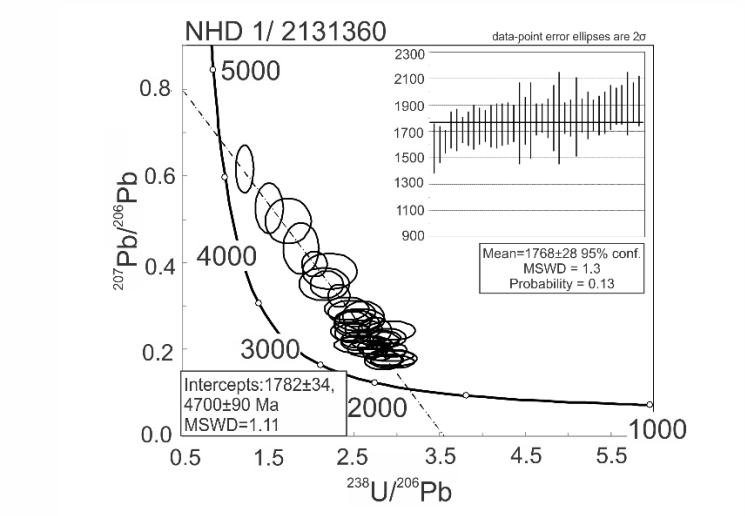

Figure 2.3: Terra-Wasserburg and associated weighted mean plots for apatite U-Pb from samples 2131358, 2111462, 2131363 + 2131364, 2117350, 2131356, 2131355, 2131357, 1831646 + 1831650, and 2131360. All ages produced are in Ma. Sample locations are shown in Figure 2.2.

Sample	Drill hole number	n	Concordia Intercept	MSWD	$^{207}Pb/^{206}Pb$ intercept	^{207}Pb corrected ^{206}Pb-^{238}U age	MSWD	Probability
2131358	SHD 1	*24*	*1653±49 Ma*	*1.04*	*0.733*	1648±16 Ma	*0.86*	0.65
2111462	Blanche 1	*28*	*1559±20 Ma*	*0.53*	-	-	-	0.97
2117350	ASD10D04	*18*	*1644±87 Ma*	1.04	*0.911*	*1633±48 Ma*	*2.0*	0.009
2131356	ASD 1	*40*	*1812±60 Ma*	1.5	*0.737*	*1811±26 Ma*	*1.2*	0.16
2131355	SAE 11	26	1451*±100 Ma*	*0.85*	*0.5926*	*1508±30 Ma*	*0.60*	0.94
1831646 + 1831650	MGD 45	*47*	*1892±41 Ma*	*2.2*	*0.8344*	*1878±21 Ma*	*1.8*	0.001
2131360	NHD1	*37*	*1782±34 Ma*	*1.11*	*0.7976*	*1768±28 Ma*	*1.3*	0.13

Table 2.2: Apatite U-Pb data.

2.3.3 Potassium feldspar and muscovite $^{40}Ar/^{39}Ar$ dating

One fresh, optically transparent muscovite sample and two fresh potassium feldspar samples for $^{40}Ar/^{39}Ar$ dating were separated using a Frantz magnetic separator, and then carefully hand-picked under a binocular microscope. The selected minerals were further leached in diluted HF for one minute and then thoroughly rinsed with distilled water in an ultrasonic cleaner (e.g. Jourdan et al., 2012).

The samples were loaded into large wells, bracketed by small wells that included Fish Canyon sanidine and were irradiated for 40 hours in the US Geological Survey nuclear reactor (Denver, USA). The $^{40}Ar/^{39}Ar$ analyses were performed at the Western Australian Argon Isotope Facility at Curtin University. The samples were step-heated using a 110 W Spectron Laser System, with a continuous Nd-YAG (IR; 1064 nm) laser rastered over the sample during 1 minute to ensure a homogenously distributed temperature. The gas was purified in a stainless-steel extraction line

using two *SAES* AP10 getters, a GP50 getter and a liquid nitrogen condensation trap. Ar isotopes were measured in static mode using a *MAP* 215-50 mass spectrometer (resolution of ~450; sensitivity of $4x10^{-14}$ mol/V) with a *Balzers* SEV 217 electron multiplier using 9 to 10 cycles of peak-hopping. The data acquisition was performed with the *Argus* program and the raw data was processed using the *ArArCALC* software (Koppers, 2002) and the ages have been calculated using the decay constants recommended by Renne et al. (2011).

2.3.4 (U-Th-Sm)/He analysis

Zircon (U-Th-Sm)/He (ZHe) and apatite (U-Th-Sm)/He (AHe) analysis were combined with AFT analysis to constrain the thermal history of the samples from 200 °C to sub-surface temperatures (Ehlers and Farley, 2003; Reiners et al., 2004). Four zircon separates and one apatite separate were selected for analysis based on grain quality, and analysed at the John de Laeter Centre at Curtin University. The full analytical procedure is outlined in Danišík et al. (2012). Individual grains were placed in Pt and Nb tubes (for apatite and zircon, respectively), and degassed at ~960°C and ~1250 °C (for apatite and zircon, respectively) in ultra-high vacuum using a diode laser. ^{4}He content was analysed by isotope dilution using ^{3}He spike on a *Pfeiffer Prisma* QMS 200 mass spectrometer. Each sample was then spiked by ^{230}Th and ^{235}U, digested in acid and analysed for U, Th and Sm by isotope dilution (U, Th) or external calibration (Sm) on an *Agilent* 7500CS mass spectrometer.

2.3.5 Radial plots and modelling

Radial Plotter (Vermeesch, 2009) was used to calculate AFT central ages (Galbraith and Laslett, 1993; Galbraith et al., 1999). Samples that fail the Pearson`s $\chi 2$ (P-Chi^{2}) test (Galbraith, 1981) and displayed large single-grain age dispersion (generally >25%) were decomposed into multiple age populations using the automatic mixing model in *Radial Plotter*. A potential relation between uranium concentrations and age populations was visually evaluated for each radial plot (Carpena et al., 1988; Hendriks and Redfield, 2005; Hall et al., 2016; Glorie et al., 2017a). Variations in Cl were found to be negligible and were therefore not included in age population discriminations.

Where available, AFT confined track lengths, and AFT ages results were compiled into *QT-qt* (Gallagher, 2012) to produce time-temperature models by utilising transdimensional Markov chain Monte Carlo statistics. The models were produced using the annealing model of Ketcham et al. (2007), with D_{par} (Burtner et al., 1994; Donelick et al., 1999; Donelick et al., 2005) used as a compositional constraint.

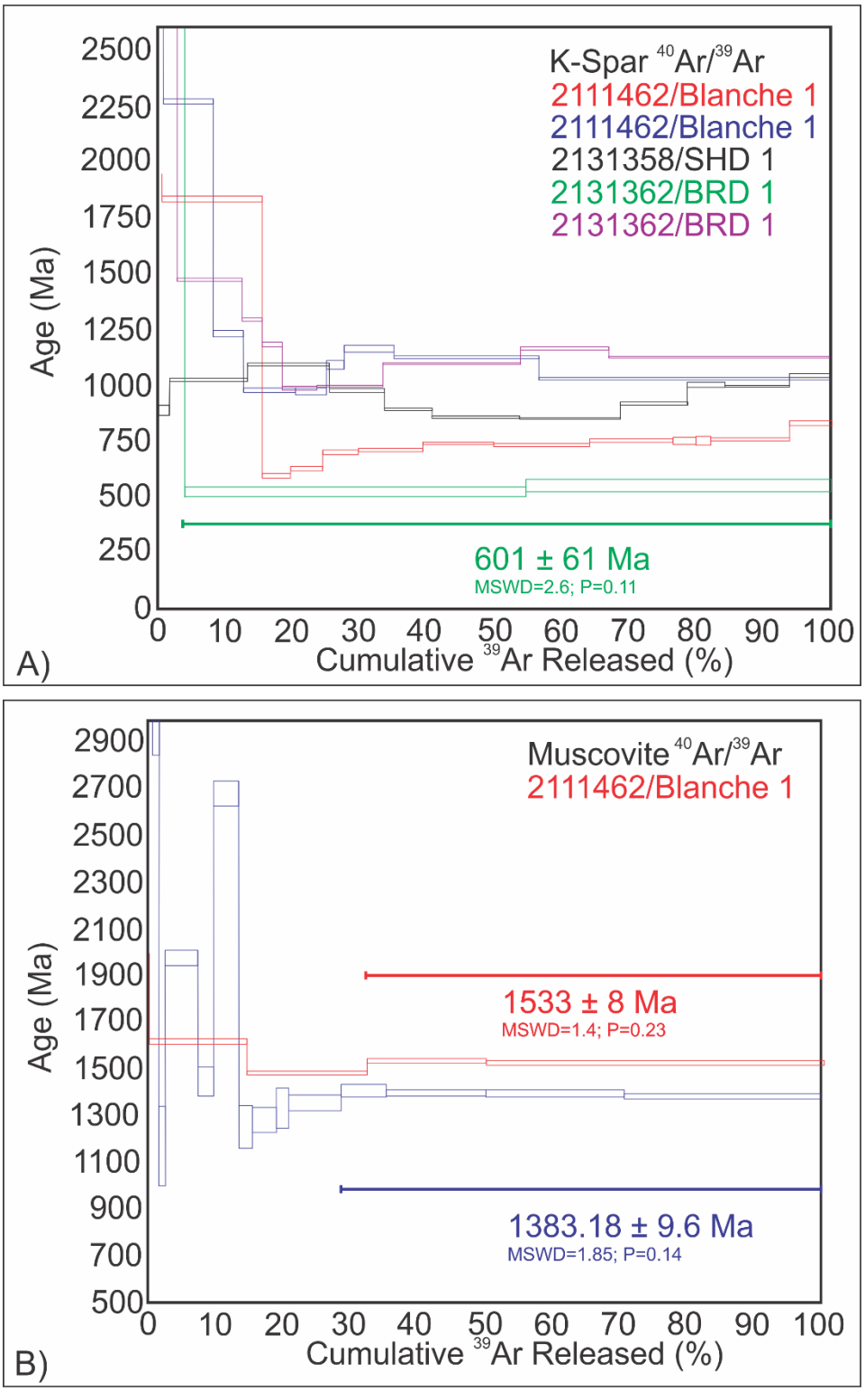

Figure 2.4: $^{40}Ar/^{39}Ar$ analysis for samples 2131358, 2111462, and 2131362. Potassium feldspar age spectra are indicated by A while B illustrates the muscovite age spectra. Sample locations are shown in Figure 2.2.

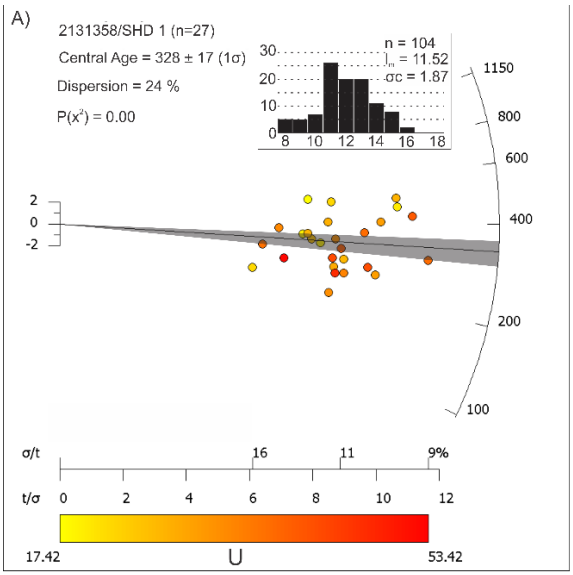
A)
2131358/SHD 1 (n=27)
Central Age = 328 ± 17 (1σ)
Dispersion = 24 %
P(χ²) = 0.00
n = 104
l_m = 11.52
σc = 1.87
σ/t
t/σ
17.42
U
53.42

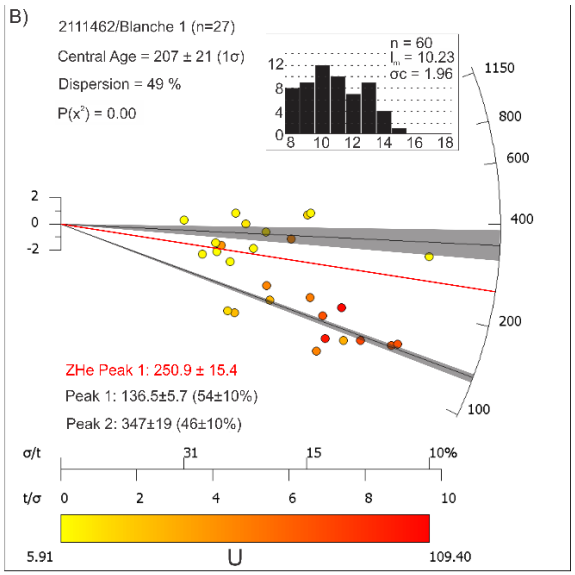
B)
2111462/Blanche 1 (n=27)
Central Age = 207 ± 21 (1σ)
Dispersion = 49 %
P(χ²) = 0.00
n = 60
l_m = 10.23
σc = 1.96
ZHe Peak 1: 250.9 ± 15.4
Peak 1: 136.5±5.7 (54±10%)
Peak 2: 347±19 (46±10%)
σ/t
t/σ
5.91
U
109.40

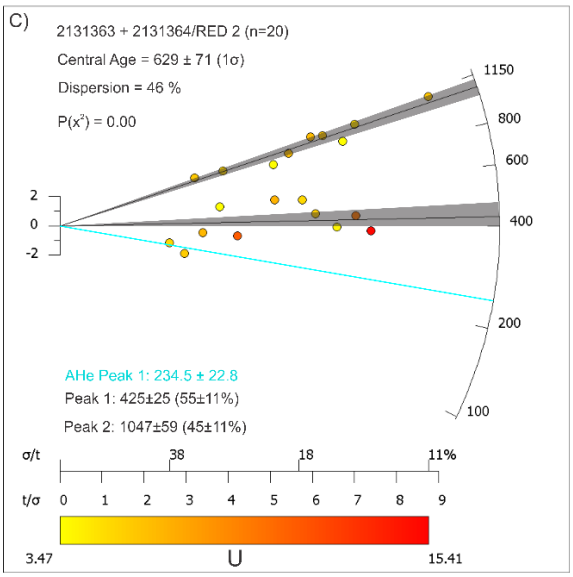
C)
2131363 + 2131364/RED 2 (n=20)
Central Age = 629 ± 71 (1σ)
Dispersion = 46 %
P(χ²) = 0.00
AHe Peak 1: 234.5 ± 22.8
Peak 1: 425±25 (55±11%)
Peak 2: 1047±59 (45±11%)
σ/t
t/σ
3.47
U
15.41

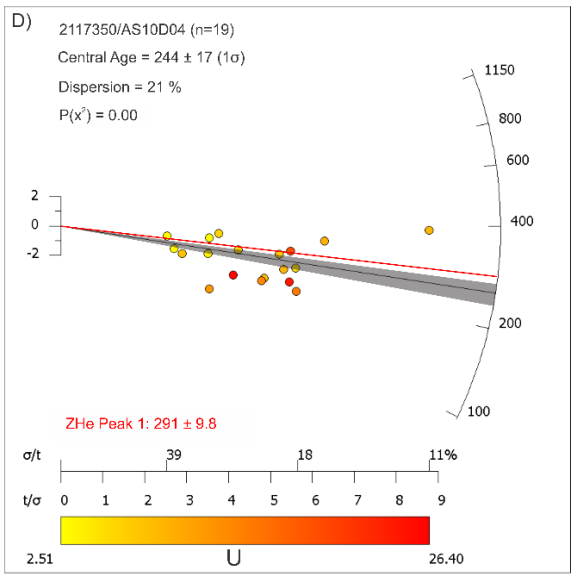
D)
2117350/AS10D04 (n=19)
Central Age = 244 ± 17 (1σ)
Dispersion = 21 %
P(χ²) = 0.00
ZHe Peak 1: 291 ± 9.8
σ/t
t/σ
2.51
U
26.40

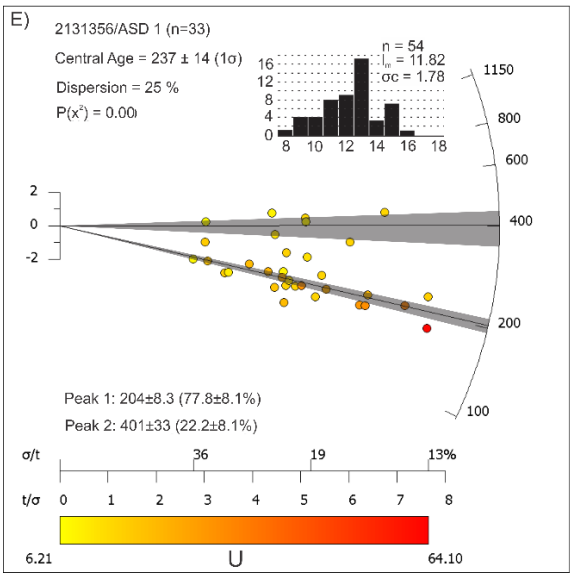
E)
2131356/ASD 1 (n=33)
Central Age = 237 ± 14 (1σ)
Dispersion = 25 %
P(χ²) = 0.00
n = 54
l_m = 11.82
σc = 1.78
Peak 1: 204±8.3 (77.8±8.1%)
Peak 2: 401±33 (22.2±8.1%)
σ/t
t/σ
6.21
U
64.10

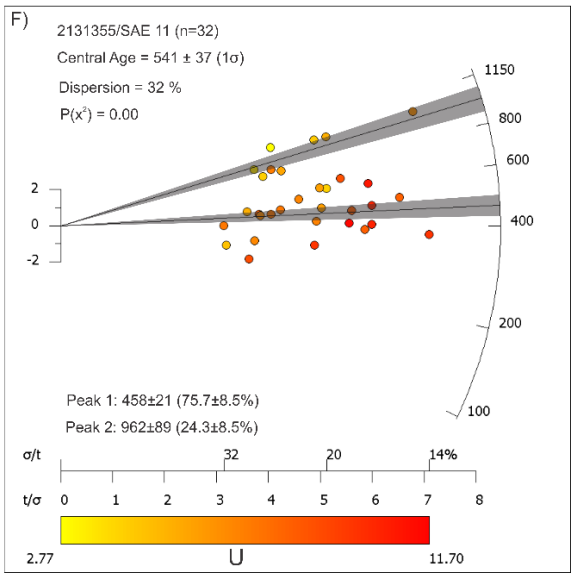
F)
2131355/SAE 11 (n=32)
Central Age = 541 ± 37 (1σ)
Dispersion = 32 %
P(χ²) = 0.00
Peak 1: 458±21 (75.7±8.5%)
Peak 2: 962±89 (24.3±8.5%)
σ/t
t/σ
2.77
U
11.70

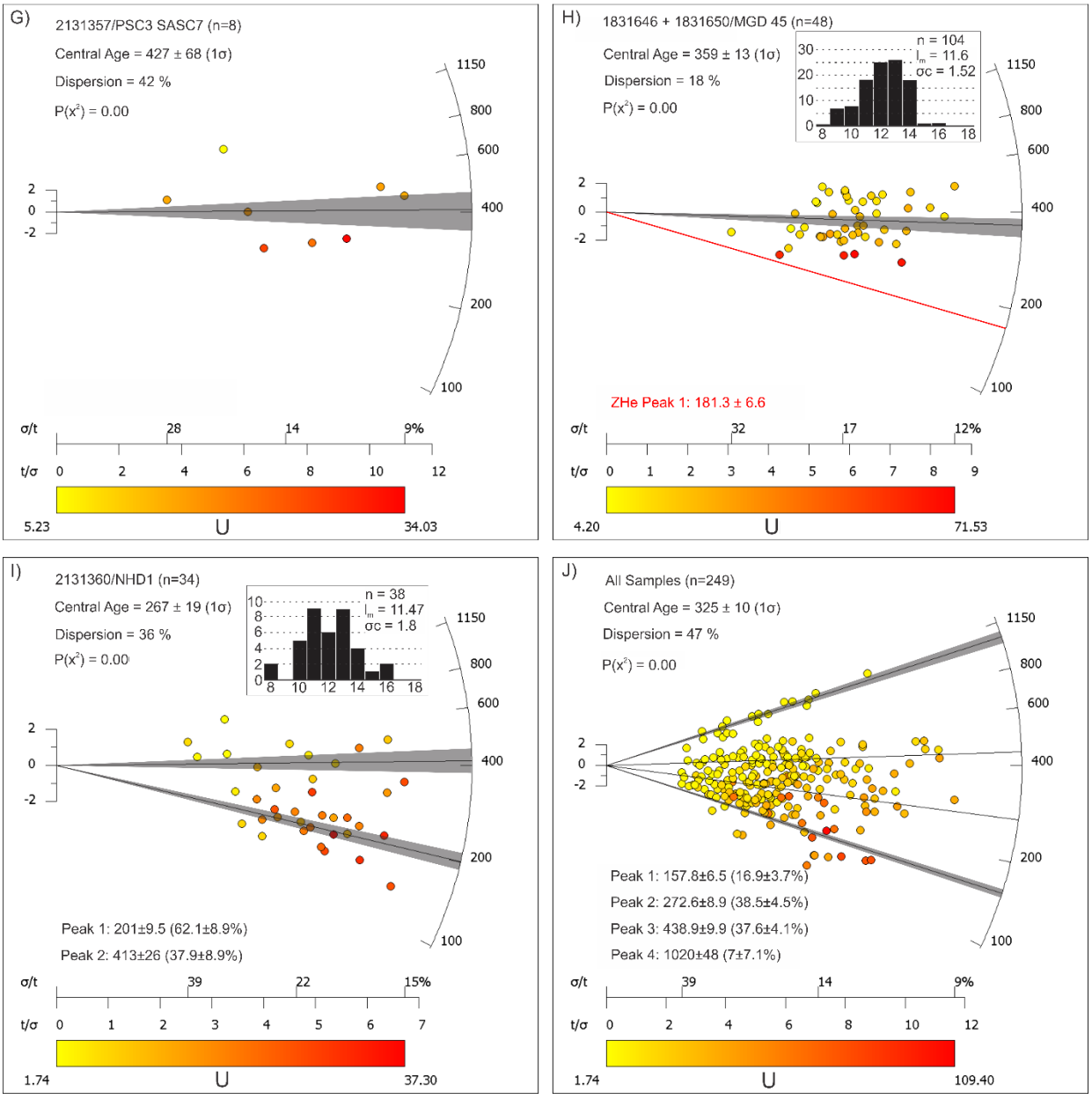

Figure 2.5: Radial plots of apatite fission track (AFT) data from samples (A) 2131358, (B) 2111462, (C) 2131363 + 2131364, (D) 2117350, (E) 2131356, (F) 2131355, (G) 2131357, (H) 1831646 + 1831650, and (I) 2131360, in addition to a radial plot containing all samples (J). 'n' indicates the number of grains measured, the central age indicates the calculated central age, 'dispersion' indicates the percentage of age dispersion within the sample, the colour difference illustrates the different measured ^{238}U concentrations in ppm. When multiple populations of ages are present, the Automatic Mixture model of Radial Plotter splits the central age into age populations. Coloured peaks indicate the accompanying zircon or apatite (U-Th-Sm)/He ages. All ages acquired from radial plots are presented in Table 2.3. Within each applicable radial plot is the associated AFT length frequency histogram (samples with not enough data are excluded). On each histogram, the x-axis is AFT length in µm while the y-axis is frequency, n is the number of tracks measured, l_m indicates average track length, while σ is the standard deviation of the sample. All radial plots were constructed using *Radial Plotter* (Vermeesch, 2009). Sample locations are shown in Figure 2.2.

Sample	Drillhole No.	ρ_s	Ns	N	^{238}U	Central age	Lower age	Upper Age	l_m	n	σc	D_{par} (µm)
2131358	SHD 1	5.84 (1.6)	3343	27	32.62 (2.06)	328 ± 17 Ma	-	-	11.52	104	1.87	1.3 (0.47)
2111462	Blanche 1	3.98 (0.53)	1653	29	37.46 (3.07)	207 ± 21 Ma	136.5 ± 5.7 Ma	347 ± 19 Ma	10.23	60	1.96	1.49 (0.4)
2131363 + 2131364	RED 2	2.42 (1.2)	1233	20	6.53 (0.72)	629 ± 71 Ma	425 ± 25 Ma	1047 ± 59 Ma	-	-	-	-
2117350	ASD1 ODO 4	1.29 (0.86)	798	19	10.45 (1.01)	244 ± 17 Ma	-	-	-	-	-	1.65 (0.53)
2131356	ASD 1	2.46 (0.97)	1233	33	20 (1.59)	237 ± 14 Ma	204 ± 8.3 Ma	401 ± 33 Ma	11.82	54	1.78	1.88 (0.38)
2131355	SAE 11	2.4 (0.87)	1105	31	7.41 (0.64)	541 ± 37 Ma	458 ± 21 Ma	962 ± 89 Ma	-	-	-	1.84 (0.52)
2131357	PSC 7 SASC 3	4.16 (0.8)	935	8	18.89 (1.47)	427 ± 68 Ma	-	-	-	-	-	2 (0.33)
1831646 + 1831650	MGD 45	3.83 (1.88)	3521	48	21.09 (2.36)	359 ± 13 Ma	-	-	11.6	104	1.52	1.35 (0.53)
2131360	NHD1	2.33 (1.37)	1350	34	16.59 (1.58)	267 ± 19 Ma	201 ± 9.5 Ma	413 ± 26 Ma	11.47	38	1.8	1.68 (0.41)

Table 2.3: Apatite fission track (AFT) details for each sample. Length measurements are also shown. ρs is counted AFT density in 10^5 tracks/cm^2, with the standard deviation in brackets, Ns is number of fission tracks counted, N is number of counted grains, ^{238}U is concentration of ^{238}U with the standard deviation indicated by the brackets, Central age is the apatite fission track central age in Ma (lower and upper age are all AFT age populations of their respected samples), l_m is average confined AFT length, n is number of confined tracks counted, σc is standard deviation of the confined tracks, D_{par} is the average D_{par} for each sample with the standard deviation in brackets.

2.4 Results

2.4.1 Apatite U-Pb age data

All apatite U-Pb data are reported in Table 2.2 and Figure 2.3.

Apatite U-Pb analysis from sample 2131358 (a granitic gneiss collected from drill hole SHD 1 at a depth of 857 m) yielded a ^{207}Pb corrected weighted mean ^{206}Pb-^{238}U age of 1648 ± 16 Ma with a MSWD of 0.86.

Sample 2111462 is a Hiltaba Suite Granite collected from Blanche 1 (at a depth of 1005 m) about 10 km to the southwest of Olympic Dam and recorded a weighted mean ^{206}Pb-^{238}U age of 1559 ± 20 Ma (MSWD = 0.53) from 24 apatite U-Pb analyses. All the grains analysed were within 10% concordance, therefore no common Pb correction was applied to this sample.

Apatite grains from sample 2117350 (collected from a Donington Suite granite at a depth of 668 m from drill hole AS10D04) produced a well-defined common Pb line, which resulted in a ^{207}Pb corrected weighted mean ^{206}Pb-^{238}U age of 1633 ± 48 Ma with an MSWD of 2.0.

Sample 2131356 is a gabbro from the Donington Suite and was collected from drill hole ASD 1 at a depth of 961 m. A ^{207}Pb corrected weighted mean ^{206}Pb-^{238}U age of 1811 ± 26 Ma (MSWD = 1.2) was obtained from 40 apatite grains, which (although clustered) preserved a reasonable spread that defined a common Pb line.

Sample 2131355 is a rhyolite from the GRV and was collected from drill hole SAE 11 at a depth of 1000 m. A ^{207}Pb corrected weighted mean ^{206}Pb-^{238}U age of 1508 ± 30 Ma (MSWD = 0.60) was collected from 26 grains. However, due to the lack of spread of data along the common Pb line (Fig. 2.3) this age is not considered to be robust. This is further supported by the large difference between the intercept age of 1451 ± 100 Ma and the ^{207}Pb corrected weighted mean ^{206}Pb-^{238}U age of 1508 ± 30 Ma.

Samples 1831646 and 1831650 (both Donington Suite granites) were collected from the same drill core, MGD 45, at depths of 667 m and 738 m (Table 2.1). Thus, they have been combined to produce a relatively well defined common Pb line with minor clustering. This common Pb line was used to produce a ^{207}Pb corrected weighted mean ^{206}Pb-^{238}U age of 1878 ± 21 Ma (MSWD = 1.8) from 47 grains.

The southernmost apatite-bearing sample, 2131360, is a Donington Suite Granite and was collected from drill hole NHD 1 at a depth of 535 m. This sample preserves a well-defined common Pb line, which was used to produce a ^{207}Pb corrected weighted mean ^{206}Pb-^{238}U age of 1768 ± 28 Ma (MSWD = 1.3) from 37 grains.

Overall, the apatite U-Pb ages record cooling of the analysed samples from two igneous suites, the older ~1850 Ma Donington Suite and the younger ~1590 Ma Hiltaba Suite and GRV, to ~550 – 350 °C. Samples from the Donington Suite record two different times for cooling, at around 1850 – 1800 Ma (samples 2131356, 1831646, 1831650, and 2131360) and ~1640 Ma (samples 2131358 and 2117350). The Hiltaba Suite/GRV samples record cooling at ~1560 – 1520 Ma (samples 2111462 and 2131355).

2.4.2 ^{40}Ar/^{39}Ar data

The ^{40}Ar/^{39}Ar data for this study are summarised in figure 2.4.

A single potassium feldspar analysis from sample 2131358 failed to produce an ^{40}Ar/^{39}Ar plateau age. The heating step at ~20 % Ar release produced a maximum apparent age of ~1200 Ma. The lowest Ar age of ~950 Ma was obtained at ~40 – 60 % Ar release (Fig. 2.4a). The sigma-shape of the age spectrum suggests that the crystal was affected by alteration and recrystallization (cf. discussion by Verati and Jourdan, 2014).

A muscovite ^{40}Ar/^{39}Ar mini-plateau age of 1533 ± 8 Ma including 65 % of ^{39}Ar released (Fig. 2.4b) was obtained for sample 2111462. This age is slightly younger than the apatite U-Pb age recorded

for this sample. A second muscovite $^{40}Ar/^{39}Ar$ age plateau from a different fraction within the same sample records an age of 1384 ± 10 Ma (Fig. 2.4b). Two potassium feldspar samples failed to record a plateau age, and yielded strongly perturbed age spectra, showing signs of excess Ar released at low heating temperatures. Individual steps yield an upper apparent age of around 1250 Ma and a lower apparent age of around 650 Ma (Fig. 2.4a).

A single potassium feldspar yielded a pseudo-plateau age of 601 ± 61 Ma but was produced by only two large heating steps in sample 2131362 (from drill hole BRD 1, at a depth of 804 m). A second potassium feldspar age failed to produce an age plateau with an upper age of ~1250 Ma and a lower age of ~1000 Ma.

Sample	*n*	*^{238}U*	*^{232}Th*	*^{147}Sm*	*$^{232}Th/^{238}U$*	*^{4}He*	*Ft*	*He Age*	*Avg He Age*	*AFT age*
2111462 (ZHe)	*5*	*3.364*	*3.222*	*0.002*	*0.95*	*97.4*	*0.77*	*249.3 ± 15.6*	*250.9 ± 15.4*	*381 ± 20 Ma*
		2.603	*3.893*	*0.010*	*1.48*	*80.2*	*0.76*	*244.2 ± 14.9*	-	*147.6 ± 5.9 Ma*
		3.384	*2.532*	*0.005*	*0.74*	*97.3*	*0.76*	*259.1 ± 15.7*	-	-
		4.768	*3.893*	*0.010*	*0.81*	*69.4*	*0.75*	*132.5 ± 9.2*	-	-
		1.358	*0.644*	*0.001*	*0.47*	*84.6*	*0.69*	*639.2 ± 36*	-	-
2131364 (AHe)	*4*	0.019	0.079	0.023	4.15	0.628	*0.64*	*211.9 ± 43.5*	*234.5 ± 22.8*	*1047 ± 59 Ma*
		0.013	*0.039*	*0.012*	*2.92*	*0.386*	*0.54*	*257.1 ± 21*	-	*425 ± 25 Ma*
		0.009	*0.023*	*0.006*	*2.41*	*0.150*	*0.59*	*139.8 ± 13*	-	-
		0.017	*0.061*	*0.017*	*3.57*	*1.130*	*0.58*	*503.5 ± 54.7*	-	-
2117350 (ZHe)	*5*	*1.757*	*2.485*	*0.013*	*1.40*	*63.6*	*0.78*	*282.5 ± 16.4*	*291 ± 9.8*	*244 ± 17 Ma*
		1.654	*0.880*	*0.005*	*0.53*	*50.0*	*0.76*	*287.1 ± 16.5*	-	-
		1.419	*0.603*	*0.006*	*0.42*	*44.8*	*0.76*	*303.4 ± 17.8*	-	-
		2.853	*2.585*	*0.022*	*0.90*	*59.5*	*0.76*	*183.9 ± 10.5*	-	-
		8.113	*5.234*	*0.029*	*0.64*	*137.4*	*0.77*	*155.3 ± 9.1*	-	-
183650 (ZHe)	*5*	*2.536*	*3.734*	*0.009*	*1.46*	*54.8*	*0.68*	*192.1 ± 16.4*	*181.3 ± 6.6*	*359 ± 13 Ma*
		1.595	*1.567*	*0.005*	*0.98*	*27.9*	*0.68*	*170.4 ± 8.8*	-	-
		5.978	*1.921*	*0.014*	*0.32*	*46.2*	*0.70*	*84.4 ± 4.5*	-	-
		5.922	*5.851*	*0.018*	*0.98*	*41.0*	*0.71*	*64.7 ± 6.7*	-	-
		3.151	*4.141*	*0.009*	*1.30*	*25.5*	*0.67*	*75.1 ± 3.8*	-	-
1709141 (ZHe)	*4*	3.053	1.280	*20.47*	0.006	0.42	89.1	*266.3 ± 31.8*	*258.7 ± 11.2*	-
		1.650	1.141	*26.61*	0.003	0.69	40.0	*250.6 ± 24.9*	-	-
		0.844	0.387	*15.98*	0.002	0.46	26.3	*310.3 ± 20.5*	-	-
		1.327	1.602	*23.90*	0.004	1.20	30.9	*207.6 ± 12.6*	-	-

Table 2.4: (U–Th–Sm)/He results indicating the helium (He) age, number of grains within each age population (n), ^{238}U concentration (ncc per µg), ^{232}Th concentration (ncc per µg), ^{147}Sm concentration (ncc per µg), $^{232}Th/^{238}U$, concentration of ^{4}He (ncc per µg), Ft (Farley et al., 1996), and apatite fission track (AFT) age (in Ma).

2.4.3 Apatite fission track, zircon (U-Th-Sm)/He and apatite (U-Th-Sm)/He data

The apatite fission track (AFT), zircon (U-Th-Sm)/He (ZHe) and apatite (U-Th-Sm)/He (AHe) data are presented in Fig. 2.5 and tables 2.3 and 4.

AFT data from sample 2131358 (a granitic gneiss) records significant scatter (24% dispersion, P-Chi^2 = 0.000) in AFT single-grain ages, clustering around a central age of 328 ± 17 Ma (Fig. 2.5a). No clear trends of AFT ages with U concentrations could be observed. A total of 104 confined fission track lengths were measured, exhibiting a broad distribution with a slight positive skew. The average track length obtained was 11.52 µm with a standard deviation of 1.87 µm. The highly scattered AFT ages and broad length distribution with relatively short mean value are indicative of a prolonged residence in the APAZ.

Five zircon separates were analysed for ZHe analysis from sample 2111462 (a Hiltaba granite), however two separates were discounted, due to low U and Th, or due to high effective uranium (eU; Guenthner et al., 2013; Murray et al., 2014). The three remaining separates record an average ZHe age of 250.9 ± 15.4 Ma (Table 2.4) with relatively little dispersion. Sample 2111462 recorded an AFT central age of 207 ± 21 Ma. Given the large dispersion (49 % with P-Chi^2 = 0.000) within the sample, this age has been separated into two age populations using *Radial Plotter* (Vermeesch, 2009). The older age population is defined by low U (generally <50 ppm) grains and yields a peak age of 347 ± 19 Ma, which is within error to the central AFT age of sample 2131358 (328 ± 17 Ma). The younger age population is defined by high U (generally >50 ppm) grains and yields a well-defined AFT peak age of 136.5 ± 5.7 Ma. A total of 60 confined track lengths were obtained, producing a broad, negatively skewed, distribution with an average track length of 10.23 µm and a standard deviation of 1.96 µm. The bimodality in AFT ages and broad length distribution suggest a complex thermal history with significant residence within the APAZ.

Two GRV rhyolite samples from the drill core RED 2 (2131363 at 334 m, and 2131364 at 445 m) were combined into one radial plot due to the lack of variance between the samples (Fig. 2.5c), yielding highly dispersed (46 % with P-Chi^2 = 0.000) single-grain AFT ages with a central AFT age of 629 ± 71. The results show a typical open-jaw display (O'Sullivan and Parrish, 1995) and, therefore, peak discrimination with the automatic mixture model in *Radial Plotter* differentiated two age populations of 1047 ± 59 Ma and 425 ± 25 Ma. No clear age-correlation with U could be observed. There was an insufficient amount of confined track lengths to produce a reliable length-frequency distribution for this sample, however, the strong AFT age bimodality suggests a complex thermal history record. Furthermore, this sample yielded two single–grain AHe ages for an average of 234.5 ± 22.8 Ma, which is significantly younger than the youngest AFT age population.

Five zircons from Sample 2117350 were analysed, producing 3 reliable ages with an average ZHe age of 291 ± 9.8 Ma (yielding only minor dispersion between the single-grain ages). The other

two separates contained high eU levels and were therefore removed from the average age. The central AFT age recorded for this sample is 244 ± 17 Ma with 21 % single-grain age dispersion (Fig. 2.5d). The sample does not pass the P-Chi^2 test, which is likely due to the presence of a few older (~400 Ma) grains. The ZHe age corresponds well with this AFT central age, suggesting relatively rapid cooling at that time. There were not enough AFT length data collected for this sample to obtain a reliable length-frequency distribution.

Sample 2131356 records an AFT central age of 237 ± 14 Ma with a dispersion of 25 % and P-Chi^2 = 0.000. The data can be subdivided into two age populations using the automatic mixture model in *Radial Plotter.* The older age population is defined by relatively low U concentrations (<17 ppm) and records an age of 401 ± 33 Ma, while the younger age population is defined by higher U concentrations (>17 ppm) and records an age of 204 ± 8.3 Ma. A total of 54 confined AFT lengths were measured, revealing a broad and slightly bimodal distribution with an average length of 11.82 µm and a standard deviation of 1.78 µm, suggesting significant residence in the APAZ.

Sample 2131355 returned an AFT central age of 541 ± 37 Ma with a large dispersion of 32 % and a P-Chi^2 of 0.000. The AFT data for this sample have been statistically separated into two age populations. The older age population is reasonably well constrained at 962 ± 89 Ma, which is in good agreement with the older age (1047 ± 59 Ma) obtained for the RED 2 drill core samples. The younger age population of 458 ± 21 Ma is quite scattered and likely indicates protracted cooling through the APAZ at that time (Fig. 2.5f, Table 2.3). Although there is relatively little variation in U concentrations, the low U (< 6 ppm) grains are exclusively constrained to the older peak. Insufficient AFT length data was gathered to produce an accurate length-frequency distribution.

Sample 2131357 is a Donington Suite granite collected at a depth of 688 m from drill hole PSC 7 SASC 3. Only 8 grains were dated for this sample, returning a scattered (42 % dispersion and P-Chi^2 = 0.000) central age of 427 ± 68 Ma. As a consequence of the limited usability of this sample, an insufficient amount of confined track lengths were collected to produce a length-frequency distribution.

The samples from MGD 45 (1831646 and 1831650) revealed an AFT central age of 359 ± 13 Ma with relatively little dispersion (18 %). The sample failed the P-Chi^2 test (P-Chi^2 = 0.000), which is likely due to the presence of few relatively high U, young grains (Fig. 2.5h). The younger ages were marginally older than the ZHe age of 181.3 ± 6.6 Ma, obtained from two different grains from this sample. A combined total of 104 confined fission track length measurements were collected with a mean track length of 11.6 µm and a standard deviation of 1.52 µm. The length-frequency distribution exhibits a unimodal distribution with minor negative skew (Fig. 2.5h), indicating prolonged APAZ residence.

Sample 2131360 recorded an AFT central age of 267 ± 19 Ma with a large dispersion of 36 % and a P-Chi^2 of 0.000. Given the large scatter, the sample was statistically subdivided into two age

populations of 413 ± 26 Ma and 201 ± 9.5 Ma. No clear age correlation with U was observed. The average confined track length of 11.47 µm from 38 confined tracks, with a standard deviation of 1.8 µm.

Sample 1709141 (from drill hole GHDD 1 at a depth of 967 m) yielded five ZHe ages for an average of 258.7 ± 11.2 Ma. No apatites were retrieved from this sample.

In order to summarise the low-temperature thermal history of the region, all collected AFT analyses were combined into a single radial plot (Fig. 2.5j). This pooled plot omits the complexity of individual sample datasets but highlights the dominant regional age trends in the data (e.g. Glorie et al., 2017a). Four age populations were calculated in this radial plot using the automatic mixture model in *Radial Plotter* at 1020 ± 48 Ma, 438.9 ± 9.8 Ma, 272.6 ± 8.9 Ma, and 157.8 ± 6.5 Ma. These age populations appear to match reasonably with those identified for individual samples. The 1020 ± 48 Ma population is only recorded in 7 % of the data (Fig. 2.5j) and is only (partially) preserved in samples 2131363, 2131364, and 2131355. All samples preserve Palaeozoic single grain AFT ages with 76 % of the data falling within the two Palaeozoic age populations of 438.9 ± 9.8 Ma and 272.6 ± 8.9 Ma (Fig. 2.5j). The ~439 Ma population is the oldest recorded age population within all samples except those that record the 1020 ± 48 Ma age (Figs. 2.5c & 2.5f). The large scatter within the 438.9 ± 9.8 Ma and 272.6 ± 8.9 Ma populations is a result of prolonged residence within the APAZ, as indicated by the broad AFT track length distributions, with mean track lengths of less than 12 µm. The absolute ages of these two peaks may therefore not be that meaningful. The youngest age population is recorded at 157.8 ± 6.5 Ma and is dominated by high U analyses from samples 2131356 and 2131360 and analyses from sample 2111462. Sample 2111462 was taken in closest proximity to Olympic Dam (Fig. 2.2).

2.4.4 Low-temperature thermochronological modelling

Samples 2131358 and 2111462 which contained sufficient AFT length data were modelled using *QT-qt* (Fig. 2.6; Gallagher, 2012), using the annealing model of Ketcham et al. (2007). Other samples either had insufficient confined fission tracks or too high single-grain dispersion to be modelled. Where additional, ZHe age data were used in the models following the Guenthner et al. (2013) ZHe diffusion model.

The modelled samples were constrained to present day temperatures of 51 ± 10 °C, which is the average geothermal gradient (51 °C/km) of the Olympic Domain (Houseman et al., 1989). This temperature was chosen as both samples are within 800 – 1000m depth and no individual geothermal gradients have been reported. The modelled samples were also constrained by the unconformities recorded within the Adelaide Rift Complex at around 700 – 650 Ma (Preiss, 1993; Preiss et al., 1998; Williams, 1998; Preiss, 2000; Le Heron et al., 2011; Le Heron, 2012), by forcing the models to cooler temperatures at this time (Fig. 2.6).

The thermal history for sample 2131358 begins at ~650 Ma, while 2111462 is modelled from 850 Ma to include the feldspar $^{40}Ar/^{39}Ar$ data recorded during the Neoproterozoic. Two different time-temperature histories are identified throughout the Olympic Domain region (Fig. 2.6). Both models preserve heating following the unconformities of the Neoproterozoic, with prolonged residence in the APAZ from ~500 Ma – 200 Ma. From 200 Ma, sample 2131358 cooled slowly to present day temperatures, while sample 2111462 reheated to ~100 °C during the Cretaceous before more recent cooling brought the sample to present-day temperatures. This Cretaceous reheating can be accounted for by the young AFT age population in sample 2111462.

2.5 Discussion

2.5.1 Proterozoic

Post-magmatic cooling is recorded in the apatite U-Pb ages for the samples within the Donington Suite (2131358, 2117350, 2131356, 1831646, 1831650, and 2131360; Fig. 2.3). Most of the remaining apatite U-Pb ages record post magmatic cooling after Hiltaba Suite emplacement at ~1590 – 1580 Ma (2111462 and 2131355; Fig. 2.3). In addition, the solitary muscovite $^{40}Ar/^{39}Ar$ age is within error of the apatite U-Pb from the same sample (sample 2111462), indicating rapid post-magmatic cooling of the Hiltaba Suite from emplacement temperatures to ~300°C at ~1530 Ma. These data strengthen previous suggestions that the Hiltaba Suite was emplaced at shallow crustal levels (Creaser, 1996; Daly et al., 1998; Hand et al., 2007).

Following Hiltaba emplacement, the deposition of the Pandurra formation shallowly (>1 km) buried the previously exposed basement at around 1560 – 1420 Ma (Fanning et al., 1983; Rollison, 2016). A second muscovite $^{40}Ar/^{39}Ar$ age spectrum from sample 2111462 shows evidence for alteration after ~1500 Ma, possibly by hydrothermal activity. Rb-Sr data collected by Rollison (2016) indicates the Pandurra formation underwent hydrothermal alteration at ~1200 Ma while Rb-Sr data from Olympic Dam (Kamenetsky et al., 2016) records a similar age for hydrothermal activity at ca. 1128 Ma. These ages are supported by illite crystallisation throughout the Pandurra formation at ~1200 Ma (Keeling et al., 2016). Collectively, these ages indicate the region underwent repeated periods of hydrothermal activity from ~1300 – 1100 Ma. The oldest AFT ages and potassium feldspar $^{40}Ar/^{39}Ar$ spectra obtained for this study (~1050 – 1000 Ma) correspond with the end of the hydrothermal activity at Olympic Dam. We therefore suggest that thermal and/or chemical alteration signals related with these events are partially preserved in the low-temperature thermochronological record of the Olympic Domain study area (samples 2131355, 2131363, and 2131364). Due to the presence of the old AFT age populations in samples 2131355, 2131363, and 2131364, these samples must have remained within, or cooler than, the APAZ from ~1000 Ma to the present in order to preserve these ages. All other samples were subsequently heated above APAZ temperatures.

Subsequently, subsidence and rifting along the eastern margin of proto-Australia resulted in the formation of the Adelaide Rift Complex throughout the Neoproterozoic. This event is reflected by hydrothermal alteration preserved in potassium feldspar $^{40}Ar/^{39}Ar$ ages from samples 2111462 and 2131362, which records a mixed step-heating age during the Neoproterozoic. The late Neoproterozoic unconformities preserved within the Adelaide Rift Complex (Preiss, 1993; Preiss et al., 1998; Williams, 1998; Preiss, 2000; Le Heron et al., 2011; Le Heron, 2012) indicates the underlying basement rocks of the Olympic Domain were at near surface temperatures during this time.

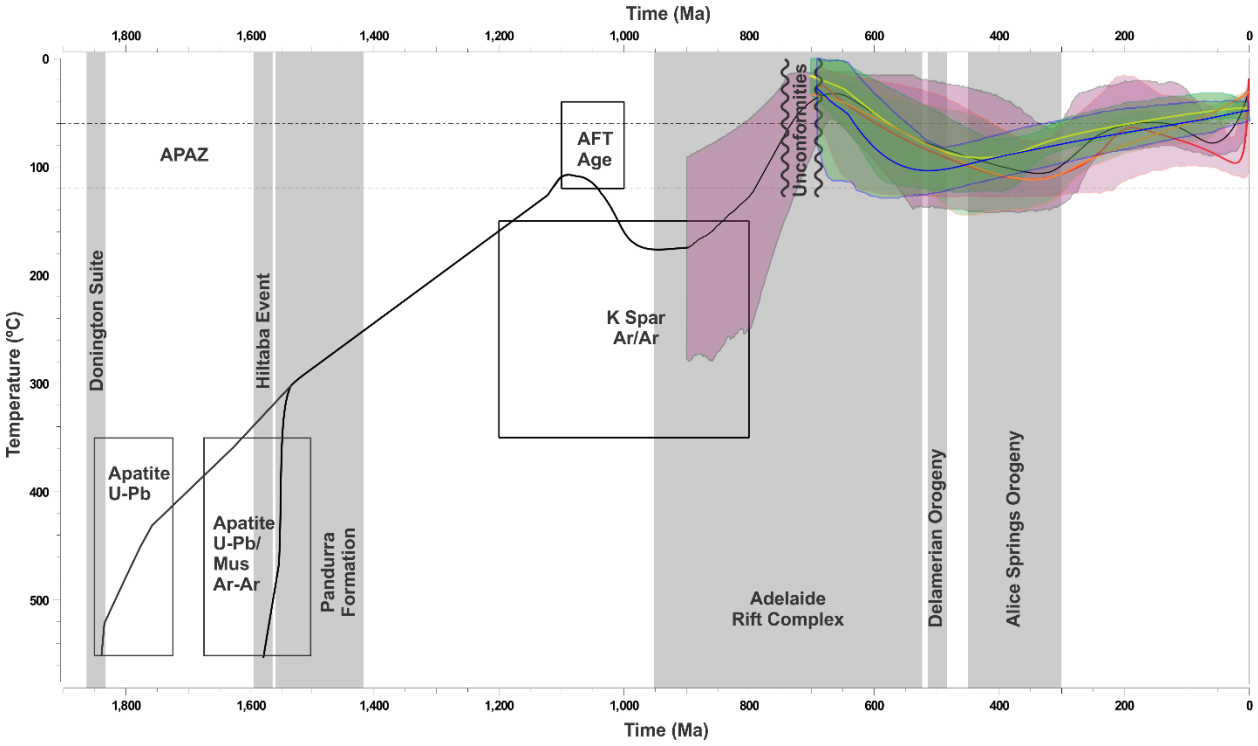

Figure 2.6: Time-temperature models for samples 2131358 (blue), and 2111462 (black), 2131356 (orange), 1831646 + 1831650 (red), and 2131360 (yellow). Apatite fission track age and length data, geological constraints, and, where applicable $^{40}Ar/^{39}Ar$ and (U-Th-Sm)/He ages were modelled using QT-qt (Gallagher, 2012). The shading indicates error of the modelled histories. The gray shaded zones indicates periods of tectonic and igneous activity.

2.5.2 Palaeozoic

The onset of the Delamerian Orogeny at ca. 515 Ma halted sedimentation in the region (Preiss, 2000; Foden et al., 2006). However, there are no Delamerian AFT ages preserved in the Olympic Domain (Fig. 2.5). Given the abundance of younger low-temperature thermochronological ages, any Delamerian ages were likely subsequently reset.

Almost all samples preserve AFT ages during the multi-pulse (~450 – 300 Ma) Alice Springs Orogeny (Hand et al., 1999; Mawby et al., 1999; Haines et al., 2001) and the Ordovician –

Carboniferous Lachlan Orogeny (Glen, 2005). The AFT age populations related to the oldest Alice Springs Orogeny pulse (~450 – 420 Ma) and/or the Benambran Orogeny of the Lachlan Orogen are preserved as the young AFT age populations of samples 2131355, 2131363, and 2131364 (and poorly constrained for sample 2131357). Samples 2131356 and 2131360 preserve a slightly younger age population of ~400 Ma, which is likely influenced by the presence of a younger AFT age populations in these samples (Fig 5e & 5i). The AFT age population (~360 – 330 Ma) related with the younger Alice Spring Orogeny pulse and/or the Carboniferous Kanimblan Orogeny of the Lachlan Orogen, and is preserved in the single age populations of samples 2131358, 1831646 and 1831650. Sample 2111462 also preserves an AFT age population during the Carboniferous, however, this age could also be influenced by the younger age population of this sample.

Ordovician hydrothermal and authigenic apatite U-Pb ages from Olympic Dam (Kamenetsky et al., 2016) indicate that Olympic Dam was reheated by hydrothermal activity following the Delamerian Orogeny. Our AFT results and thermochronological modelling within the Olympic Domain support this suggestion (Figs. 5 & 6). However, as Palaeozoic post-Delamerian AFT ages are preserved regionally throughout the study area, hydrothermal activity alone is unlikely to have reheated the entire region. We interpret that southward directed deformation from the two pulses of the Alice Springs Orogeny at 450 – 420 and 350 – 330 Ma (Ballèvre et al., 2000), potentially coalescing with deformation relating to the Benambran and Kanimblan Orogenies in the east, as the cause of this cooling activity. The Peake and Denison Inliers to the north also preserve these orogenic events at similar times (Hall et al., 2016). Samples 2131355, and 2131363 and 2131364, which are located on the outskirts of the region, do not preserve AFT ages younger than ~420 Ma, indicating that these regions stayed cooler than APAZ temperatures (<~60°C) after this time.

2.5.3 Mesozoic

A single sample, 2117350, records a Triassic age population of ~250 Ma from both ZHe and AFT data. However, this age population is interpreted to be a mixing age between the Alice Springs Orogeny related thermal activity and younger thermal activity. This interpretation is supported by the remnant older AFT ages preserved within the sample (Fig. 2.5d).

The youngest regional age population is recorded at ~200 Ma during the Jurassic. This thermal period is recorded in AFT ages in samples 2131356 and 2131360, as well as in the ZHe age in samples 1831646 and 1831650, and AHe age of samples 2131363 and 2131364. We interpret these Jurassic ages to be a result of a relaxing geothermal gradient within the region where temperatures dropped below the APAZ, at that time. This interpretation is supported by the presence of broad AFT track length distributions with a rather short mean length values (Gleadow et al., 1986), as well as the increase in temperature during the Triassic – early Jurassic in the thermal history models for these samples. The breakup of Antarctica from Australia (Veevers, 2012) could

have also played a role in these thermal events by transporting stresses related to the breakup on the plate margin into the study area.

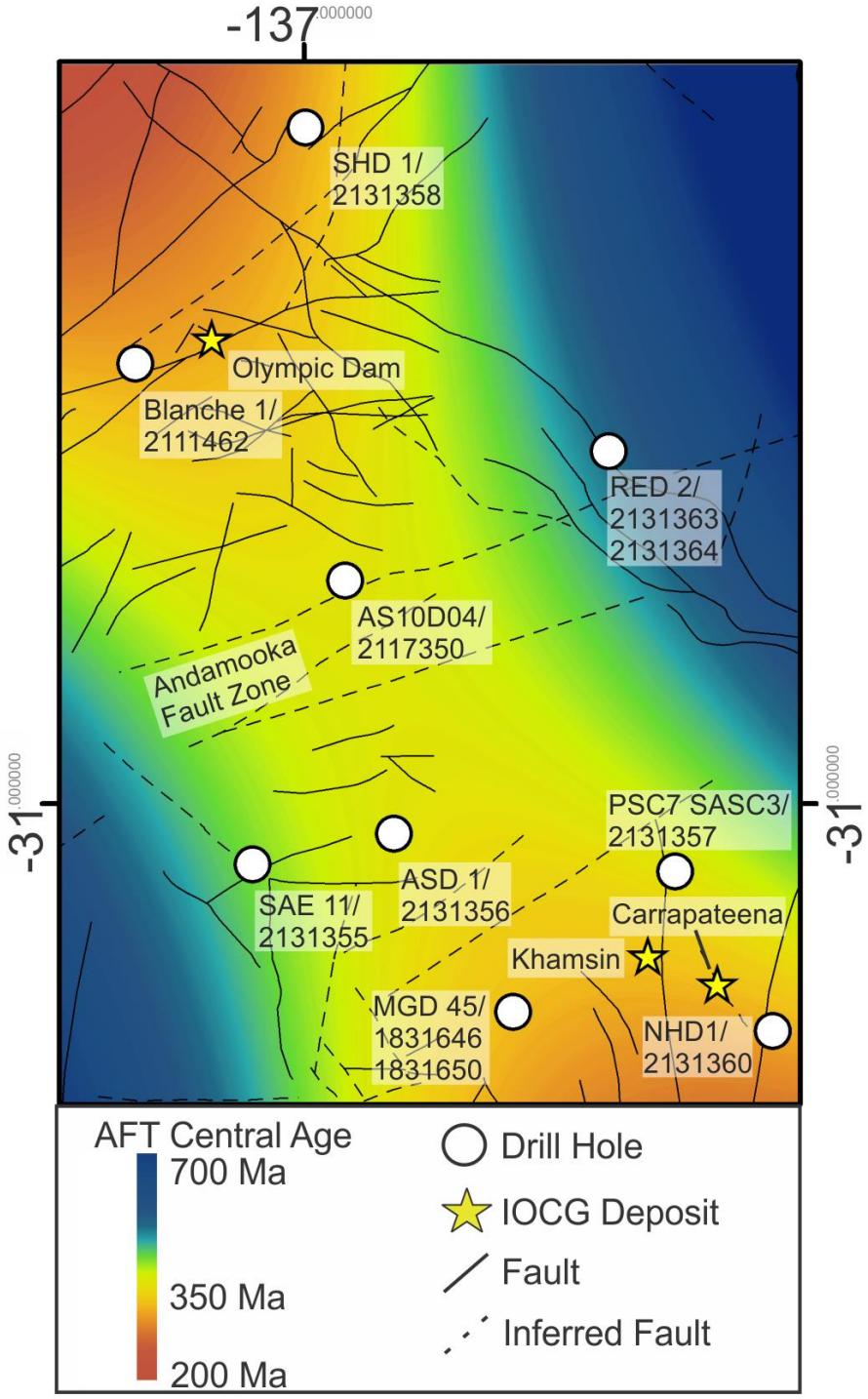

Figure 2.7: Modelled interpretation of apatite fission track central ages from this study. Blue indicates older ages and red indicates younger ages. Drill holes/sample names, IOCG deposit locations and major interpreted faults are shown. Fault interpretations are taken from (Wise et al., 2015).

The youngest AFT age population within the region is Cretaceous (~137 Ma) and is from sample 2111462, located near Olympic Dam (Fig. 2.2). The thermal history model for this sample gives evidence for a Meso-Cenozoic thermal event. Given that the young thermal event is localised to this sample, it is likely linked to a local thermal perturbation (Houseman et al., 1989; Neumann et al., 2000). This thermal perturbation could be a result of hydrothermal activity localised to Olympic Dam. In this regard, Clarke et al. (2016) and Macmillan et al. (2016) suggested that late Delamerian uraninite formation indicates continued hydrothermal activity at Olympic Dam. This hydrothermal activity concentrated high heat producing elements (i.e. uranium) during the Cambrian – Ordovcian, which may in turn have increased the local geothermal gradient into the Meso-Cenozoic.

2.5.4 Thermal anomalies within the Olympic Domain

In order to spatially visualise the AFT age data and to speculate on thermal anomalies within the study area, the AFT central ages (Fig. 2.5) for each sample were inserted into an *ArcGIS* Kriging model (Oliver and Webster, 1990). The Kriging model was selected as it is an inverse distance weighted and spline interpolation tool which accounts for the uncertainty in data and allows for the overall trend within the data to be easily visualised (Fig. 2.7). The model is constrained by the locations of the samples in addition to data from samples collected south of the study region by Mitchell et al. (1998). The resulting map highlights the lateral extent of the heterogeneous thermal gradient within the Olympic Domain. Clearly, the thermal environment is complex and further thermochronological work is needed to better constrain the model.

The map shows a clear trend of younger AFT ages within a central NW-SE corridor through the Olympic Domain study area, while the periphery records older (>250 Ma) AFT ages. The oldest mapped age regions are only constrained by the two old AFT samples (2131363/2131364 from RED 2, and 2131355 from SAE 11). The age gradients show a weak correlation with the location of major faults in the region (Fig. 2.7), and no correlation with the east – west trending Andamooka Fault Zone (Direen and Lyons, 2002). We therefore suggest that the anomalies on the map are primary thermal anomalies and interpret the central `young` corridor is a primary feature, and may be a region of weaker crust where thermal events occurred in more recent times (~200 Ma) compared to the periphery. Magneto-telluric data collected within the Olympic Domain reveals a similar trend of more conductive crust that trends NW-SE, while the periphery of the study region is dominated by more resistive rocks (Thiel et al., 2016). Previous studies have attributed more conductive zones to weaker zones in which fluids more readily flow through (e.g. Wei et al., 2001). Interestingly, the IOCG deposits lie on the edge of the youngest modelled zones in the 'corridor' (Fig. 2.7). The relationship between the location of the IOCG deposits and the zones of young AFT ages is unclear, but may indicate that these zones record more favourable thermal conditions and/or exposure levels for IOCG discoveries. More work is needed, particularly in the north, to investigate the extent of the young thermal anomalies with respect to the occurrence of IOCG

deposits, but these preliminary results indicate that low-temperature thermochronology could aid mineral exploration in the Olympic Domain study area.

2.5.5 Comparisons with neighbouring regions

AFT studies from the Peake and Denison Inliers to the north (Hall et al., 2016), central Gawler Craton, to the west (Reddy et al., 2015; Boone et al., 2016), and in the Mt. Painter Region to the east (McLaren et al., 2002; Mitchell et al., 2002; Weisheit et al., 2014) all record thermal events relating to deformation from the Delamerian Orogeny (Foden et al., 2006) and the final pulses of the Alice Springs Orogeny (Haines et al., 2001). Delamerian Orogeny related thermal activity is not preserved within the northern Olympic Domain, instead, the AFT ages within the Olympic Domain dominantly relate to various pulses of the Alice Springs Orogeny potentially coupled with the Benrambran and Kanimblan Orogenies of the Lachlan Orogen. The peripheries of the Olympic Domain record the oldest AFT age populations currently known for South Australia. These age populations are ~100 Ma older than the oldest ages recorded in the central Gawler Craton (Reddy et al., 2015), ~500 Ma older than the northern or southern Gawler Craton (Gleadow et al., 2002; Boone et al., 2016; Hall et al., 2016), and pre-date the deposition of the Adelaide Rift Complex. Early Jurassic thermal activity is not only preserved in the Olympic Domain, but also in the central Gawler Craton (Reddy et al., 2015) and recorded by hydrothermal activity in the Mt. Painter Region (Weisheit et al., 2014) indicating that this thermal event was not restricted to the Olympic Domain. Finally, other study regions within the Gawler Craton preserve localised Cretaceous cooling or hydrothermal activity (Boone et al., 2016; Hall et al., 2016) which is thus far has only been recognised in close vicinity to the Olympic Dam deposit where localised Cretaceous AFT ages are preserved.

2.6 Conclusions

Multi-method thermochronology within the Olympic Domain records a complex thermal history. Apatite U-Pb and muscovite $^{40}Ar/^{39}Ar$ ages date the timing of post-magmatic cooling of the Donington Suite, the Hiltaba Suite and Gawler Range Volcanics. Potassium feldspar $^{40}Ar/^{39}Ar$ and apatite fission track analysis record hydrothermal alteration through the Neoproterozic within the Adelaide Rift Complex. The sedimentary record of the Adelaide Rift Complex preserves unconformities, indicating the region was at near surface temperatures during the late Neoproterozoic. The 515 – 490 Ma Delamerian Orogeny terminated sedimentation but is not preserved within the Olympic Domain data. Thermal activity is recorded by AFT data at ~430 – 400 Ma and ~350 – 330 Ma, interpreted to be caused by the Alice Springs Orogeny. Regional Early Jurassic cooling reinstated the region to near surface temperatures. Evidence of a Cretaceous thermal event is preserved within one sample proximal to the Olympic Dam deposit, and is likely related to localised hydrothermal activity in the vicinity of mineralisation.

At a regional scale, a central `young` thermal corridor where thermal events occurred in more recent times (~200 Ma) can be seen in AFT data. Furthermore, the abundant IOCG deposits within the Olympic Domain are located on the edge of the youngest thermal anomalies in the 'corridor'. The relationship between the location of IOCG deposits and the zones of young AFT ages is unclear, but may indicate that these zones record more favourable thermal conditions and/or exposure levels for IOCG discoveries.

2.7 Acknowledgements

This paper was made possible thanks to the financial support of the Geological Survey of South Australia and an Australian Research Council grant (ARC LE150100145). ASC is funded by an Australian Research Council Future Fellowship (FT120100340). Christopher Trenouth is thanked for his assistance in apatite fission track data collection. Bradley McDonald (John De Laeter Center at Curtin University) and Ben Wade (Adelaide Microscopy) are thanked for their assistance with the U–Th–Sm/He methods and the use of the LA-ICP-MS respectively. U and Th determinations for AHe and ZHe were made at TSW Analytical in Perth and Chris May is gratefully acknowledged for his assistance. István Dunkl is acknowledged for sharing PepiFlex software for solution ICP-MS data reduction. Vadim Kamenetsky and Caroline Tiddy are thanked for their insightful reviews. MD was funded by Curtin Research Fellowship. AR publishes with permission of the director of the Geological Survey of South Australia. This paper forms TRaX# 396.

2.8 References

Arne, D.C., Green, P.F., Duddy, I.R., Gleadow, A.J.W., Lambert, I.B., Lovering, J.F., 1989. Regional thermal history of the Lennard shelf, Canning Basin, from apatite fission track analysis: Implications for the formation of Pb-Zn ore deposits. Australian Journal of Earth Sciences 36, 495-513.

Ballèvre, M., Möller, A., Hensen, B.J., 2000. Exhumation of the lower crust during crustal shortening: an Alice Springs (380 Ma) age for a prograde amphibolite facies shear zone in the Strangways Metamorphic Complex (central Australia). Journal of Metamorphic Geology 18, 737-747.

Belperio, A., Flint, R., Freeman, H., 2007. Prominent Hill: A Hematite-Dominated, Iron Oxide Copper-Gold System. Economic Geology 102, 1499-1510.

Boone, S.C., Seiler, C., Reid, A.J., Kohn, B., Gleadow, A., 2016. An Upper Cretaceous paleo-aquifer system in the Eromanga Basin of the central Gawler Craton, South Australia: evidence from apatite fission track thermochronology. Australian Journal of Earth Sciences 63, 315-331.

Budd, A.R., Wyborn, L.A., Bastrakova, I.V., 2001. The metallogenic potential of Australian Proterozoic granites. Geoscience Australia, Record 2001/12.

Burtner, R.L., Nigrini, A., Donelick, R.A., 1994. Thermochronology of Lower Cretaceous Source Rocks in the Idaho-Wyoming Thrust Belt. American Association of Petroleum Geologists Bulletin 78, 1613-1636.

Carpena, J., Kienast, J.-R., Ouzegane, K., Jehanno, C., 1988. Evidence of the contrasted fission-track clock behavior of the apatites from In Ouzzal carbonatites (northwest Hoggar): The low-temperature thermal history of an Archean basement. Geological Society of America Bulletin 100, 1237-1243.

Cherry, A.R., McPhie, J., Kamenetsky, V.S., Ehrig, K., Keeling, J.L., Kamenetsky, M.B., Meffre, S., Apukhtina, O.B., 2017. Linking Olympic Dam and the Cariewerloo Basin: Was a sedimentary basin involved in formation of the world's largest uranium deposit? Precambrian Research 300, 168-180.

Chew, D.M., Petrus, J.A., Kamber, B.S., 2014. U–Pb LA–ICPMS dating using accessory mineral standards with variable common Pb. Chemical Geology 363, 185-199.

Chew, D.M., Spikings, R.A., 2015. Geochronology and Thermochronology Using Apatite: Time and Temperature, Lower Crust to Surface. Elements 11, 189-194.

Clarke, J., Poznik, N., Ehrig, K., 2016. Unravelling the Giant: Evidence for post-mineralisation modification of the Olympic Dam Cu-Au-U-Ag deposit, Gawler Craton, South Australia, Australian Earth Sciences Convention. Geological Society of Australia, Adelaide, p. 81.

Cowley, W.M., 1993. Cariewerloo Basin, In: Drexel, J.F., Preiss, W.V., Parker, A.J. (Eds.), The geology of South Australia. Vol.1 , The Precambrian, South Australia Geological Survey, Bulletin 54.

Cowley, W.M., Conor, C.H.H., Zang, W., 2003. New and revised Proterozoic stratigraphic units on northern Yorke Peninsula. Minerals and Energy South Australia Journal 29, 46-58.

Creaser, R.A., 1996. Petrogenesis of a Mesoproterozoic quartz latite-granitoid suite from the Roxby Downs area, South Australia. Precambrian Research 79, 371-394.

Creaser, R.A., White, A.J.R., 1991. Yardea Dacite; large-volume, high temperature felsic volcanism from the middle Proterozoic of South Australia. Geology 19, 48-51.

Daly, S.J., Fanning, C.M., Fairclough, M.C., 1998. Tectonic evolution and exploration potential for the Gawler Craton, South Australia. AGSO Journal of Australian Geology and Geophysics 17, 145-168.

Danišík, M., Štěpančíková, P., Evans, N.J., 2012. Constraining long-term denudation and faulting history in intraplate regions by multisystem thermochronology: An example of the Sudetic Marginal Fault (Bohemian Massif, central Europe). Tectonics 31, TC2003.

Davidson, G.J., Paterson, H., Meffre, S., Berry, R.F., 2007. Characteristics and Origin of the Oak Dam East Breccia-Hosted, Iron Oxide Cu-U-(Au) Deposit: Olympic Dam Region, Gawler Craton, South Australia. Economic Geology 102, 1471-1498.

Direen, N.G., Lyons, P., 2002. Geophysical interpretation of the Olympic Cu-Au province map. Geoscience Australia, Canberra.

Direen, N.G., Lyons, P., 2007. Regional Crustal Setting of Iron Oxide Cu-Au Mineral Systems of the Olympic Dam Region, South Australia: Insights from Potential-Field Modeling. Economic Geology 102, 1397-1414.

Donelick, R.A., Ketcham, R.A., Carlson, W.D., 1999. Variability of apatite fission-track annealing kinetics; II, Crystallographic orientation effects. American Mineralogist 84, 1224-1234.

Donelick, R.A., O'Sullivan, P.B., Ketcham, R.A., 2005. Apatite Fission-Track Analysis. Reviews in Mineralogy and Geochemistry 58, 49-94.

Ehlers, T.A., Farley, K.A., 2003. Apatite (U–Th)/He thermochronometry: methods and applications to problems in tectonic and surface processes. Earth and Planetary Science Letters 206, 1-14.

Elburg, M.A., Andersen, T., Bons, P.D., Simonsen, S.L., Weisheit, A., 2013. New constraints on Phanerozoic magmatic and hydrothermal events in the Mt Painter Province, South Australia. Gondwana Research 24, 700-712.

Fanning, C.M., Flint, R.B., Preiss, W.V., 1983. Geochronology of the Pandurra Formation. . Geological Survey of South Australia Quarterly Geological Notes 88, 11-16.

Fanning, C.M., Reid, A.J., Teale, G., 2007. A geochronological framework for the Gawler Craton, South Australia. . South Australia. Geological Survey. Bulletin 55.

Flint, R.B., Rankin, L.R., Fanning, C.M., 1990. Definition; the Palaeoproterozoic St. Peter Suite of the western Gawler craton. Geological Survey of South Australia, Quarterly Geological Notes 114, 2-8.

Foden, J., Elburg, M.A., Dougherty-Page, J., Burtt, A., 2006. The Timing and Duration of the Delamerian Orogeny: Correlation with the Ross Orogen and Implications for Gondwana Assembly. The Journal of Geology 114, 189-210.

Foster, D.A., Murphy, J.M., Gleadow, A.J.W., 1994. Middle tertiary hydrothermal activity and uplift of the northern flinders ranges, South Australia: Insights from apatite fission-track thermochronology. Australian Journal of Earth Sciences 41, 11-17.

Fraser, G., McAvaney, S., Neumann, N., Szpunar, M., Reid, A., 2010. Discovery of early Mesoarchean crust in the eastern Gawler Craton, South Australia. Precambrian Research 179, 1-21.

Galbraith, R.F., 1981. On statistical models of fission track count. Journal of the International Association for Mathematical Geology 13, 471-478.

Galbraith, R.F., Laslett, G.M., 1993. Statistical models for mixed fission track ages. Nuclear Tracks and Radiation Measurements 21, 459-470.

Galbraith, R.F., Roberts, R.G., Laslett, G.M., Yoshida, H., Olley, J.M., 1999. Optical dating of single and multiple grains of quartz from jinmium rock shelter, northern australia: Part i, experimental design and statistical models*. Archaeometry 41, 339-364.

Gallagher, K., 2012. Transdimensional inverse thermal history modeling for quantitative thermochronology. Journal of Geophysical Research: Solid Earth 117, n/a-n/a.

Giles, C.W., 1988. Petrogenesis of the Proterozoic Gawler Range Volcanics, South Australia. Precambrian Research 40–41, 407-427.

Gillespie, J., Glorie, S., Xiao, W., Zhang, Z., Collins, A.S., Evans, N., McInnes, B., De Grave, J., 2017. Mesozoic reactivation of the Beishan, southern Central Asian Orogenic Belt: Insights from low-temperature thermochronology. Gondwana Research 43, 107–122.

Gleadow, A.J.W., Duddy, I.R., Green, P.F., Hegarty, K.A., 1986. Fission track lengths in the apatite annealing zone and the interpretation of mixed ages. Earth and Planetary Science Letters 78, 245-254.

Gleadow, A.J.W., Gleadow, S.J., Belton, D.X., Kohn, B.P., Krochmal, M.S., Brown, R.W., 2009. Coincidence mapping - a key strategy for the automatic counting of fission tracks in natural minerals. Geological Society, London, Special Publications 324, 25-36.

Gleadow, A.J.W., Kohn, B.P., Brown, R.W., O'Sullivan, P.B., Raza, A., 2002. Fission track thermotectonic imaging of the Australian continent. Tectonophysics 349, 5-21.

Glen, R.A., 2005. The Tasmanides of eastern Australia. Geological Society, London, Special Publications 246, 23-96.

Glorie, S., Agostino, K., Dutch, R., Pawley, M., Hall, J., Danišík, M., Evans, N.J., Collins, A.S., 2017a. Thermal history and differential exhumation across the Eastern Musgrave Province, South Australia: Insights from low-temperature thermochronology. Tectonophysics 703–704, 23-41.

Glorie, S., Alexandrov, I., Nixon, A., Jepson, G., Gillespie, J., Jahn, B.-M., 2017b. Thermal and exhumation history of Sakhalin Island (Russia) constrained by apatite U-Pb and fission track thermochronology. Journal of Asian Earth Sciences 143, 326-342.

Gow, P.A., Wall, V.J., Valenta, R.K., 1993. The regional geophysical response of the Stuart Shelf, South Australia. Exploration Geophysics 24, 513-520.

Guenthner, W.R., Reiners, P.W., Ketcham, R.A., Nasdala, L., Giester, G., 2013. Helium diffusion in natural zircon: Radiation damage, anisotropy, and the interpretation of zircon (U-Th)/He thermochronology. American Journal of Science 313, 145-198.

Haines, P.W., Hand, M., Sandiford, M., 2001. Palaeozoic synorogenic sedimentation in central and northern Australia: a review of distribution and timing with implications for the evolution of intracontinental orogens. Australian Journal of Earth Sciences 48, 911-928.

Hall, J.W., Glorie, S., Collins, A.S., Reid, A., Evans, N., McInnes, B., Foden, J., 2016. Exhumation history of the Peake and Denison Inliers: insights from low-temperature thermochronology. Australian Journal of Earth Sciences 63, 805-820.

Hand, M., Mawby, J.O., Kinny, P., Foden, J., 1999. U–Pb ages from the Harts Range, central Australia: evidence for early Ordovician extension and constraints on Carboniferous metamorphism. Journal of the Geological Society 156, 715-730.

Hand, M., Reid, A., Jagodzinski, L., 2007. Tectonic Framework and Evolution of the Gawler Craton, Southern Australia. Economic Geology 102, 1377-1395.

Hayward, N., Skirrow, R.G., 2010. Geodynamic setting and controls on iron oxide Cu-Au (±U) ore in the Gawler Craton, South Australia, In: Porter, T.M. (Ed.), Hydrothermal Iron Oxide Copper-Gold & Related Deposits: A Global Perspective, v. 3 - Advances in the Understanding of IOCG Deposits;. PGC Publishing, Adelaide.

Hendriks, B.W.H., Redfield, T.F., 2005. Apatite fission track and (U-Th)/He data from Fennoscandia: An example of underestimation of fission track annealing in apatite. Earth and Planetary Science Letters 236, 443-458.

Hoek, J.D., Schaefer, B.F., 1998. Palaeoproterozoic Kimban mobile belt, Eyre Peninsula: Timing and significance of felsic and mafic magmatism and deformation. Australian Journal of Earth Sciences 45, 305-313.

Houseman, G.A., Cull, J.P., Muir, P.M., Paterson, H.L., 1989. Geothermal signatures and uranium ore deposits on the Stuart Shelf of South Australia. Geophysics 54, 158-170.

Ismail, R., Lin, Y., Ciobanu, C.L., Cook, N.J., 2014. The Hillside Cu-Au Deposit, South Australia: A Preliminary Fluid Inclusion Study. Acta Geologica Sinica - English Edition 88, 1454-1456.

Jagodzinski, E., 2005. Compilation of SHRIMP U-Pb geochronological data, Olympic Domain, Gawler Craton, South Australia, 2001-2003. Geoscience Australia Record 20, 197.

Jagodzinski, E., 2014. The age of magmatic and hydrothermal zircon at Olympic Dam, Australian Earth Sciences Convention (AESC), Sustainable Australia. Geological Society of Australia, Newcastle, New South Wales.

Jourdan, F., Sharp, W.D., Renne, P.R., 2012. 40Ar/39Ar ages for deep (~3.3 km) samples from the Hawaii Scientific Drilling Project, Mauna Kea volcano, Hawaii. Geochemistry, Geophysics, Geosystems 13, n/a-n/a.

Kamenetsky, V.S., Ehrig, K., Maas, R., Apukhtina, O., Kamenetsky, M., Meffre, S., McPhie, J., Huang, Q., Thompson, J., Ciobanu, C.L., Cook, N.J., 2016. The Olympic Dam Cu-U-Au-Ag ore deposit: towards a new genetic model, Australian Earth Sciences Convention. Geological Society of Australia, Adelaide.

Keeling, J., Wilson, T., Zwingmann, H., van der wielen, S., Mauger, A., 2016. Mesoproterozoic Cariewerloo Basin, South Australia: spectral approach to mapping mineral diagenesis as a guide to fluid flow and unconformity uranium potential, Australian Earth Sciences Convention. Geological Society of Australia Adelaide.

Ketcham, R., A., Carter, A., Donelick, R., A., Barbarand, J., Hurford, A., J., 2007. Improved modeling of fission-track annealing in apatite, American Mineralogist, p. 799.

Kirchenbaur, M., Maas, R., Ehrig, K., Kamenetsky, V.S., Strub, E., Ballhaus, C., Münker, C., 2016. Uranium and Sm isotope studies of the supergiant Olympic Dam Cu–Au–U–Ag deposit, South Australia. Geochimica et Cosmochimica Acta 180, 15-32.

Koppers, A.A.P., 2002. ArArCALC—software for 40Ar/39Ar age calculations. Computers & Geosciences 28, 605-619.

Le Heron, D.P., 2012. The Cryogenian record of glaciation and deglaciation in South Australia. Sedimentary Geology 243, 57-69.

Le Heron, D.P., Cox, G., Trundley, A., Collins, A., 2011. Sea ice−free conditions during the Sturtian glaciation (early Cryogenian), South Australia. Geology 39, 31-34.

Ludwig, K.R., 2012. User's manual for Isoplot 3.75, A Geochronological Toolkit for Microsoft Excel. Berkeley Geochronology Center Special Publication No. 5

Maas, R., Kamenetsky, V., Ehrig, K., Meffre, S., McPhie, J., Diemar, G., 2011. Olympic Dam U-Cu–Au deposit, Australia: new age constraints. Mineral Magazine 75, 1375.

Macmillan, E., Cook, N.J., Ehrig, K., Ciobanu, C.L., Pring, A., 2016. Uraninite from the Olympic Dam IOCG-U-Ag deposit: Linking textural and compositional variation to temporal evolution. American Mineralogist 101, 1295-1320.

Mahan, K.H., Wernicke, B.P., Jercinovic, M.J., 2010. Th–U–total Pb geochronology of authigenic monazite in the Adelaide rift complex, South Australia, and implications for the age of the type Sturtian and Marinoan glacial deposits. Earth and Planetary Science Letters 289, 76-86.

Matthews, C., 2009. Geothermal energy prospectivity of the Torrens Hinge Zone: evidence from new heat flow data. Exploration Geophysics 40, 288-300.

Mawby, J., Hand, M., Foden, J., 1999. Sm–Nd evidence for high-grade Ordovician metamorphism in the Arunta Block, central Australia. Journal of Metamorphic Geology 17, 653-668.

McDougall, I., Harrison, M., 1999. Geochronology and Thermochronology by the 40Ar/39Ar Method. Oxford University Press, New York.

McDowell, F.W., McIntosh, W.C., Farley, K.A., 2005. A precise 40Ar–39Ar reference age for the Durango apatite (U–Th)/He and fission-track dating standard. Chemical Geology 214, 249-263.

McLaren, S., Dunlap, W.J., Sandiford, M., McDougall, I., 2002. Thermochronology of high heat-producing crust at Mount Painter, South Australia: Implications for tectonic reactivation of continental interiors. Tectonics 21, 2-1-2-18.

Mclaren, S., Sandiford, M., Hand, M., Neumann, N., Wyborn, L., Bastrakova, I., 2003. The hot southern continent: heat flow and heat production in Australian Proterozoic terranes. Geological Society of America Special Papers 372, 157-167.

McPhie, J., Kamenetsky, V.S., Chambefort, I., Ehrig, K., Green, N., 2011. Origin of the supergiant Olympic Dam Cu-U-Au-Ag deposit, South Australia: Was a sedimentary basin involved? Geology 39, 795-798.

Mitchell, M.M., Kohn, B.P., Foster, D.A., 1998. Post-Orogenic Cooling History of Eastern South Australia from Apatite FT Thermochronology, In: van den Haute, P., de Corte, F. (Eds.), Advances in Fission-Track Geochronology: A selection of papers presented at the International Workshop on Fission-Track Dating, Ghent, Belgium, 1996. Springer Netherlands, Dordrecht, pp. 207-224.

Mitchell, M.M., Kohn, B.P., O'Sullivan, P.B., Hartley, M.J., Foster, D.A., 2002. Low-temperature thermochronology of the Mt Painter Province, South Australia. Australian Journal of Earth Sciences 49, 551-563.

Murray, K.E., Orme, D.A., Reiners, P.W., 2014. Effects of U–Th-rich grain boundary phases on apatite helium ages. Chemical Geology 390, 135-151.

Neumann, N., Sandiford, M., Foden, J., 2000. Regional geochemistry and continental heat flow: implications for the origin of the South Australian heat flow anomaly. Earth and Planetary Science Letters 183, 107-120.

O'Sullivan, P.B., Parrish, R.R., 1995. The importance of apatite composition and single-grain ages when interpreting fission track data from plutonic rocks: a case study from the Coast Ranges, British Columbia. Earth and Planetary Science Letters 132, 213-224.

Oliver, M.A., Webster, R., 1990. Kriging: a method of interpolation for geographical information systems. International Journal of Geographical Information Systems 4, 313-332.

Osadetz, K.G., Kohn, B.P., Feinstein, S., O'Sullivan, P.B., 2002. Thermal history of Canadian Williston basin from apatite fission-track thermochronology—implications for petroleum systems and geodynamic history. Tectonophysics 349, 221-249.

Parker, A.J., Lemon, N.M., 1982. Reconstruction of the early Proterozoic stratigraphy of the Gawler craton, South Australia. Journal of the Geological Society of Australia 29, 221-238.

Paton, C., Hellstrom, J., Paul, B., Woodhead, J., Hergt, J., 2011. Iolite: Freeware for the visualisation and processing of mass spectrometric data. Journal of Analytical Atomic Spectrometry 26, 2508-2518.

Payne, J.L., Ferris, G., Barovich, K.M., Hand, M., 2010. Pitfalls of classifying ancient magmatic suites with tectonic discrimination diagrams: An example from the Paleoproterozoic Tunkillia Suite, southern Australia. Precambrian Research 177, 227-240.

Polak, E.J., Horsfall, C.L., 1979. Geothermal gradients in the Great Artesian Basin, Australia. Exploration Geophysics 10, 144-148.

Preiss, W.V., 1993. Neoproterozoic, In: Drexel, J.F., Preiss, W.V., Parker, A.J. (Eds.), The geology of South Australia. Vol.1 , The Precambrian, South Australia Geological Survey, Bulletin 54.

Preiss, W.V., 1995. Early and middle Palaeozoic orogenesis, In: Drexel, J.F., Preiss, W.V. (Eds.), The Geology of South Australia. Vol. 2, The Phanerozoic, South Australia Geological Survey. Bulletin 54.

Preiss, W.V., 2000. The Adelaide Geosyncline of South Australia and its significance in Neoproterozoic continental reconstruction. Precambrian Research 100, 21-63.

Preiss, W.V., Dyson, I.A., Reid, P.W., Cowley, W.M., 1998. Revision of lithostratigraphic classification of the Umberatana Group. Mesa Journal 9, 36-42.

Rankin, L.R., Flint, R.B., Fanning, C.M., 1990. Palaeoproterozoic Nuyts Volcanics of the western Gawler craton, South Australia. Department of Primary Industries and Resources, Report Book 90/60, 17.

Reddy, M., Glorie, S., Reid, A.J., Collins, A.S., 2015. Phanerozoic cooling history of the central Gawler Craton: implications of new low-temperature thermochronological data. MESA Journal 75, 56-60.

Reid, A., Hand, M., Jagodzinski, E., Kelsey, D., Pearson, N., 2008. Paleoproterozoic orogenesis in the southeastern Gawler Craton, South Australia. Australian Journal of Earth Sciences 55, 449-471.

Reid, A.J., Fabris, A., 2015. Influence of Preexisting Low Metamorphic Grade Sedimentary Successions on the Distribution of Iron Oxide Copper-Gold Mineralization in the Olympic Cu-Au Province, Gawler Craton. Economic Geology 110, 2147-2157.

Reid, A.J., Jagodzinski, E.A., Fraser, G.L., Pawley, M.J., 2014. SHRIMP U–Pb zircon age constraints on the tectonics of the Neoarchean to early Paleoproterozoic transition within the Mulgathing Complex, Gawler Craton, South Australia. Precambrian Research 250, 27-49.

Reid, A.J., Jourdan, F., Jagodzinski, E.A., 2017. Mesoproterozoic fluid events affecting Archean crust in the northern Olympic Cu–Au Province, Gawler Craton: insights from 40Ar/39Ar thermochronology. Australian Journal of Earth Sciences 64, 103-119.

Reiners, P.W., Spell, T.L., Nicolescu, S., Zanetti, K.A., 2004. Zircon (U-Th)/He thermochronometry: He diffusion and comparisons with 40Ar/39Ar dating. Geochimica et Cosmochimica Acta 68, 1857-1887.

Renne, P.R., Balco, G., Ludwig, K.R., Mundil, R., Min, K., 2011. Response to the comment by W.H. Schwarz et al. on "Joint determination of 40K decay constants and 40Ar∗/40K for the Fish Canyon sanidine standard, and improved accuracy for 40Ar/39Ar geochronology" by P.R. Renne et al. (2010). Geochimica et Cosmochimica Acta 75, 5097-5100.

Rollison, L., 2016. Stratigraphy, Sedimentology, and Geochemistry of the Pandurra Formation, Geology and Geophysics. The University of Adelaide, p. 145.

Sahu, H.S., Raab, M.J., Kohn, B.P., Gleadow, A.J.W., Bal, K.D., 2013. Thermal history of the Krishna–Godavari basin, India: Constraints from apatite fission track thermochronology and organic maturity data. Journal of Asian Earth Sciences 73, 1-20.

Schmidt, P.W., Williams, G.E., 2011. Paleomagnetism of the Pandurra Formation and Blue Range Beds, Gawler Craton, South Australia, and the Australian Mesoproterozoic apparent polar wander path. Australian Journal of Earth Sciences 58, 347-360.

Schoene, B., Bowring, S.A., 2007. Determining accurate temperature–time paths from U–Pb thermochronology: An example from the Kaapvaal craton, southern Africa. Geochimica et Cosmochimica Acta 71, 165-185.

Skirrow, R.G., Bastrakov, E.N., Barovich, K., Fraser, G.L., Creaser, R.A., Fanning, C.M., Raymond, O.L., Davidson, G.J., 2007. Timing of Iron Oxide Cu-Au-(U) Hydrothermal Activity and Nd Isotope

Constraints on Metal Sources in the Gawler Craton, South Australia. Economic Geology 102, 1441-1470.

Skirrow, R.G., Bastrakov, E.N., Davidson, G.J., Raymond, O.L., Heithersay, P., 2002. The geological framework, distribution and controls of Fe-oxide and related alteration, and Cu-Au mineralisation in the Gawler craton, South Australia. Part II: Alteration and mineralisation, In: Porter, T.M. (Ed.), Hydrothermal iron oxide copper-gold and related deposits: A global perspective, 2. Porter GeoConsultancy Publishing, Adelaide, pp. 33-47.

Szpunar, M., Hand, M., Barovich, K., Jagodzinski, E., Belousova, E., 2011. Isotopic and geochemical constraints on the Paleoproterozoic Hutchison Group, southern Australia: Implications for Paleoproterozoic continental reconstructions. Precambrian Research 187, 99-126.

Thiel, S., Heinson, G., Reid, A.J., Robertson, K., 2016. Insights into Lithospheric Architecture, Fertilisation and Fluid Pathways from AusLAMP MT, ASEG Extended Abstracts, pp. 1-6.

Thomson, S.N., Gehrels, G.E., Ruiz, J., Buchwaldt, R., 2012. Routine low-damage apatite U-Pb dating using laser ablation–multicollector–ICPMS. Geochemistry, Geophysics, Geosystems 13.

Tingate, P.R., Duddy, I.R., 2002. The thermal history of the eastern Officer Basin (South Australia): evidence from apatite fission track analysis and organic maturity data. Tectonophysics 349, 251-275.

Veevers, J.J., 2012. Reconstructions before rifting and drifting reveal the geological connections between Antarctica and its conjugates in Gondwanaland. Earth-Science Reviews 111, 249-318.

Verati, C., Jourdan, F., 2014. Modelling effect of sericitization of plagioclase on the 40K/40Ar and 40K/39Ar chronometers: implication for dating basaltic rocks and mineral deposits. Geological Society Special Publication 378, 155-174.

Vermeesch, P., 2009. RadialPlotter: a Java application for fission track, luminescence and other radial plots. Radiation Measurements 44, 409-410.

Vermeesch, P., 2017. Statistics for LA-ICP-MS based fission track dating. Chemical Geology 456, 19-27.

Wagner, G.A., van den Haute, P., 1992. Fission track dating. Kluwer.

Wei, W., Unsworth, M., Jones, A., Booker, J., Tan, H., Nelson, D., Chen, L., Li, S., Solon, K., Bedrosian, P., Jin, S., Deng, M., Ledo, J., Kay, D., Roberts, B., 2001. Detection of Widespread Fluids in the Tibetan Crust by Magnetotelluric Studies. Science 292, 716-719.

Weisheit, A., Bons, P.D., Danisík, M., Elburg, M.A., 2014. Crustal-scale folding: Palaeozoic deformation of the Mt Painter Inlier, South Australia. Geological Society, London, Special Publications 394, 53-77.

Williams, G.E., 1998. Late Neoproterozoic periglacial aeolian sand sheet, Stuart Shelf, South Australia. Australian Journal of Earth Sciences 45, 733-741.

Wise, T.W., Cowley, W.M., Fabris, A.J., 2015. Eastern Gawler Archaean - Middle Mesoproterozoic Solid Geology map. Geological Survey of South Australia, Adelaide.

Wyborn, L.A.I., Wyborn, D., Warren, R.G., Drummond, B.J., 1992. Proterozoic granite types in Australia: implications for lower crust composition, structure and evolution. Earth and Environmental Science Transactions of the Royal Society of Edinburgh 83, 201-209.

Chapter 3

Fault reactivation at the northern margin of the Gawler Craton

(Prepared for publication)

Statement of Authorship

Title of Paper	Carboniferous fault reactivation at the Palaeoproterozoic northern margin of the Gawler Craton, South Australia; insights from apatite fission track thermochronology
Publication Status	☐ Published ☐ Accepted for Publication ☐ Submitted for Publication ☑ Unpublished and Unsubmitted work written in manuscript style
Publication Details	Hall, J.W., Glorie, S., Reid, A.J., and Collins, A.S., prepared for publication. Carboniferous fault reactivation at the Palaeoproterozoic northern margin of the Gawler Craton, South Australia; insights from apatite fission track thermochronology.

Principal Author

Name of Principal Author (Candidate)	James Hall		
Contribution to the Paper	Sample collection, data collection, data interpretation, manuscript and figure composition.		
Overall percentage (%)	80 %		
Certification:	This paper reports on original research I conducted during the period of my Higher Degree by Research candidature and is not subject to any obligations or contractual agreements with a third party that would constrain its inclusion in this thesis. I am the primary author of this paper.		
Signature		Date	1/05/18

Co-Author Contributions

By signing the Statement of Authorship, each author certifies that:

i. the candidate's stated contribution to the publication is accurate (as detailed above);

ii. permission is granted for the candidate in include the publication in the thesis; and

iii. the sum of all co-author contributions is equal to 100% less the candidate's stated contribution.

Name of Co-Author	Stijn Glorie		
Contribution to the Paper	Assistance in data collection, assistance in data interpretation, manuscript review. 10% contribution.		
Signature		Date	1/05/18

Name of Co-Author	Anthony Reid		
Contribution to the Paper	Sample collection, assistance in data interpretation, manuscript review . 5% contribution.		
Signature		Date	11/05/18

Name of Co-Author	Alan Collins		
Contribution to the Paper	Assistance in data interpretation, manuscript review . 5% contribution.		
Signature		Date	27/06/18

Abstract

Low-temperature thermochronology applied to basement rocks across the Karari Shear Zone in the northern Gawler Craton of South Australia revealed two regional cooling events. Regional cooling during the Neoproterozoic to Cambrian and regional Carboniferous cooling were revealed using apatite fission track thermochronology. An additional, localised Triassic thermal event was identified when combined with previous regional studies of the central Gawler Craton. We interpret the Neoproterozoic to Cambrian cooling as the beginning of low temperature monotonic cooling and the earliest recorded time the basement rocks reached shallow crustal temperatures in the last 1000 Ma. The Carboniferous cooling is interpreted to be a result of southward thrusting of the Karari Shear Zone resulting from compression caused by the Alice Springs Orogeny, centred to the north. This event induced regional cooling and exhumation throughout South Australia by reactivating older fault zones. This time period is marked by the unconformity between the Neoproterozoic – Devonian Officer Basin and the late Carboniferous to Early Permian Arckaringa Basin. Therefore, this compression event ceased deposition within the Officer Basin. After the end of the Alice Springs Orogeny, deposition recommenced to form the Arckaringa Basin at ~300 Ma. Following Carboniferous compression, a localised Triassic thermal pulse was preserved, to the south of the Karari Shear Zone. This thermal pulse correlates with apatite fission track data from a previous study at the Challenger Au deposit, and forms an E-W 'corridor'. This younger thermal event represents the final thermal activity recorded in the region and may be related to a localised increase in the geothermal gradient.

3.1 Introduction

Large scale structures such as crustal scale shear zones are widely documented to act as fluid pathways in mineral systems (e.g. Heinson et al., 2006), and can create accommodation space for sedimentary basins and petroleum systems (e.g. Speksnijder, 1985; Yugui, 1993). Therefore, constraining movement along these structures is paramount to understanding the mineral and petroleum systems that result from structural movement (e.g. Sutriyono, 1998; Maksaev and Zentilli, 1999; Osadetz et al., 2002; McInnes et al., 2005). In older regions, such as the Gawler Craton of South Australia, mid - high temperature thermochronometers often do not record the shallow crustal thermal activity (Foster and Ehlers, 1998; Gleadow et al., 2002). Here, we present new apatite fission track (AFT) data, which records cooling through 120 – 60 °C (Wagner and van den Haute, 1992), to assess Phanerozoic cooling related to movement along the Karari Shear Zone.

The Karari Shear Zone is a crustal scale shear zone located in the northern Gawler Craton of South Australia (Fig. 3.1; Rankin et al., 1989; Fraser et al., 2012). The history of movement along the Karari Shear Zone is long lived with multiple periods of movement since its formation as a bounding extensional fault in the Palaeoproterozoic (Stewart and Betts, 2010; Fraser et al., 2012). Rankin et al. (1989) suggested that the Karari Shear Zone was active during the Phanerozoic, however, this

activity was only constrained through differences in sedimentary packages across the Karari Shear Zone. Therefore, the activity across the Karari Shear Zone is relatively unconstrained since ~1450 Ma. Previous low-temperature thermochronological studies from Tingate and Duddy (2002) and Reddy et al. (2015), at a distance of over 80kms from both sides of the Karari Shear Zone, suggest a dominant cooling phase during the Carboniferous. We sampled in more close vicinity to the main structure and present a comprehensive low temperature thermal history for the Karari Shear Zone and northern Gawler Craton using AFT dating.

3.2 Geological setting

3.2.1 Gawler Craton

The geology of South Australia is dominated by the Archaean – Mesoproterozoic Gawler Craton (Daly et al., 1998; Hand et al., 2007; Kositcin, 2010). The craton is separated into different tectonic domains based on their total magnetic intensity (TMI) and gravity models (Ferris et al., 2002; Fairclough et al., 2003). The north-western Gawler Craton is dominated by the Palaeoproterozoic Nawa and Christie Domains, which are separated from each other by the Karari Shear Zone (Rankin et al., 1989; Fraser et al., 2012). To the east, the Gawler Craton is made up of the Coober Pedy Ridge, the Mt. Woods Inlier, the Peake and Denison Inliers, and the Olympic Domain (Fig. 3.1).

The oldest basement rocks within the northern Gawler Craton comprise the Mugathing Complex, which is a series of ~2.5 Ga, mostly high grade, metamorphic rocks (Reid et al., 2009; Reid et al., 2014) that span approximately 55,000 km^2 across the subsurface of the central to northern Gawler Craton (Fig. 3.1) within the Christie Domain. Following a period of quiescence from ~ 2500 – 1850 Ma, rift basin formation along the eastern and northern margin of the Gawler Craton resulted in the deposition of undifferentiated metasedimentary rocks of the Nawa Domain (Hand et al., 2007; Korsch and Kositcin, 2010; Howard et al., 2011b). Within the Fowler Domain, metasedimentary rocks preserve Palaeoproterozoic deposition ages (Teasdale, 1997; Fanning et al., 2007; Howard et al., 2011a), indicating basin formation in the west, in addition to the northern and eastern Gawler Craton. Termination of these metasedimentary sequences occurred as a result of the onset of the 1730 – 1690 Kimban Orogeny (Hand et al., 2007; Payne et al., 2008; Dutch et al., 2010; Howard et al., 2011a; Howard et al., 2011b).

The late Palaeoproterozoic – early Mesoprotrozoic history of the Gawler Craton was dominated by igneous activity in the central and eastern Gawler Craton. Formation of the 1690 – 1670 Ma I-type Tunkillia Suite at the end of the Kimban Orogeny (Fanning et al., 2007; Payne et al., 2010) initiated a period of intense igneous activity. This period was followed by the formation of the ca. 1630 Ma Nuyts Volcanics and the ca. 1620 – 1610 Ma St. Peter Suite (Flint et al., 1990; Rankin et al., 1990) in the southern Gawler Craton. However, this period is most notable for the ~1590 – 1570 Ma co-magmatic Hiltaba Event (Giles, 1988; Creaser and White, 1991; Creaser, 1996; Hand et al., 2007) that erupted the Gawler Range Volcanics while synchronously forming the A-type

granites of the Hiltaba Suite. This event occurred throughout the Gawler Craton and is associated with the formation of Iron-Oxide-Copper-Gold (IOCG) ore deposits at Olympic Dam, Prominent Hill, and Carrapateena (Skirrow et al., 2002; Skirrow et al., 2007).

3.2.2 Karari Shear Zone

The Karari Shear Zone is a ~400 km north-east orientated shear zone in the northern Gawler Craton (Figs. 1 & 2) that is sub-vertical in the western Gawler Craton (Rankin et al., 1989). Based on deep crustal reflection seismic data, Korsch et al. (2010) concluded that the Karari Shear Zone dips to the north along the southern margin of the Coober Pedy Ridge (CPR), with the northern margin of the CPR being defined by a splay from the Karari Shear Zone, called the Horse Camp Fault (Fig. 3.2b). The exact location of the Karari Shear Zone to the east of the CPR is largely undefined (Rankin et al., 1989; Fraser et al., 2012). Formation of the Karari Shear Zone has been linked to the 1570 – 1540 Ma Kararan Orogeny (Daly et al., 1998). However, Swain et al. (2005) and Fraser et al. (2012) suggested that the Karari Shear Zone was active during orogenic events prior to the Kararan Orogeny. Furthermore, differing depositional ages across the Karari Shear Zone may indicate that the shear zone was an extensional basin bounding structure prior to the 1730 – 1690 Ma Kimban Orogeny (Stewart and Betts, 2010; Fraser et al., 2012). In addition to movement during ca. 1750 – 1720 Ma extension, three other periods of movement are recorded in the Palaeo-Mesoproterozoic. These are reactivation during the Kimban Orogeny, thrusting during the Hiltaba event (at ~1580 – 1560 Ma,) and strike-slip movement at ~1450 Ma (Fraser et al., 2012). Phanerozoic movement has been poorly constrained by sedimentary packages across the Karari Shear Zone, namely in the Tertiary (Rankin et al., 1989). However, the shear zone is interpreted to have been active during the Palaeozoic, where it is marked in the subsurface by deeply incised Carboniferous glacial canyons along the southern margin of the Arckaringa Basin (Menpes, 2013).

3.2.3 Phanerozoic tectonics

The periphery of the Gawler Craton underwent deformation as a result of the Cambro-Ordovician Delamerian Orogeny (Foden et al., 2006). Exhumation associated with this event is evident in the Peake and Denison Inliers (Hall et al., 2016), the Officer Basin (Tingate and Duddy, 2002) and the northern central Gawler Craton (Reddy et al., 2015). The southern central Gawler Craton, by contrast, has been reset by later events (Boone et al., 2016). Since the Silurian, cooling and exhumation relating to the long lived Alice Springs Orogeny (450 - 300 Ma; Bradshaw and Evans, 1988; Mawby et al., 1999; Ballèvre et al., 2000; Haines et al., 2001; Buick et al., 2008) affected the majority of South Australia, peaking during the Carboniferous (Gibson and Stüwe, 2000; Tingate and Duddy, 2002; Weisheit et al., 2014; Reddy et al., 2015; Boone et al., 2016; Hall et al., 2016).

3.2.4 Officer and Arckaringa Basins

North of the Karari Shear Zone, sedimentary rocks of the Officer and Arckaringa basins bury the crystalline basement (Wopfner, 1970; Hibburt, 1984, 1995; Morton and Drexel, 1997; Tingate and Duddy, 2002; Debenham, 2015). The successions of the Neoproterozoic to Frasnian Officer Basin (Womer et al., 1987; Long et al., 1988; Gravestock, 1997) include aeolian, shallow marine, lacustrine, fluvial, and glacial deposits (Fig. 3.3; Gravestock, 1997) within multiple episodes of deposition, separated by at least three unconformities, most notably during the early Cryogenian, Ediacaran, and Cambrian (Gravestock, 1997; Tingate and Duddy, 2002). These packages exceed 450 m across the sampled region, north of the Karari Shear Zone (measured in drill hole OBD 12). Unconformably overlying the Officer Basin is the late Carboniferous – Early Permian, restricted marine, Arckaringa Basin (Fig. 3.3; Wopfner, 1970; Hibburt, 1984; Hibburt, 1995). The main depocentre is located to the north east of the Karari Shear Zone, however the basin reaches up to ~750 m depth west of the Mount Woods Inlier (Hibburt, 1995) where the basal unconformity traces out a series of fjord-like glacial valleys (Menpes, 2013; Debenham, 2015). Holocene aolian sands uncomformably overlie the region (Benbow, 1986).

3.3 Methodology

Granitoid samples were collected from drill core and outcrop across the Nawa and Christie Domains, Coober Pedy Ridge and Mt. Woods Inlier to target the low-temperature thermal history across the Karari Shear Zone. These samples were subsequently crushed and separated via conventional methods.

3.3.1 Apatite fission track dating

Apatite fission track (AFT) dating constrains the age and estimates the rate of cooling through the apatite partial annealing zone (APAZ) 60 – 120 °C (e.g. Wagner and van den Haute, 1992). In order to expose the fission tracks, the apatites were mounted in epoxy resin, ground, polished and etched in 20 ± 0.5 °C 5 M HNO^3 for 20 ± 0.5 seconds. The etched samples were imaged and counted using *an Autoscan system* on a Zeiss AX10 microscope (Gleadow et al., 2009). A *New Wave* UP 213 Laser-Ablation Inductively-Coupled-Plasma *Agilent* 7500 quadrupole Mass-Spectrometer (LA-ICP-MS) was used to collect the uranium, lead, thorium, and chlorine concentrations for the counted regions within the apatite samples. The data were reduced using *Iolite* (Paton et al., 2011) following Hasebe et al. (2004), Glorie et al. (2017a), and Glorie et al. (2017b). NIST 610 (Pearce et al., 1997), and Madagascar apatite (Thomson et al., 2012) were primary standards during analysis. Durango apatite was used as a secondary standard (McDowell et al., 2005).

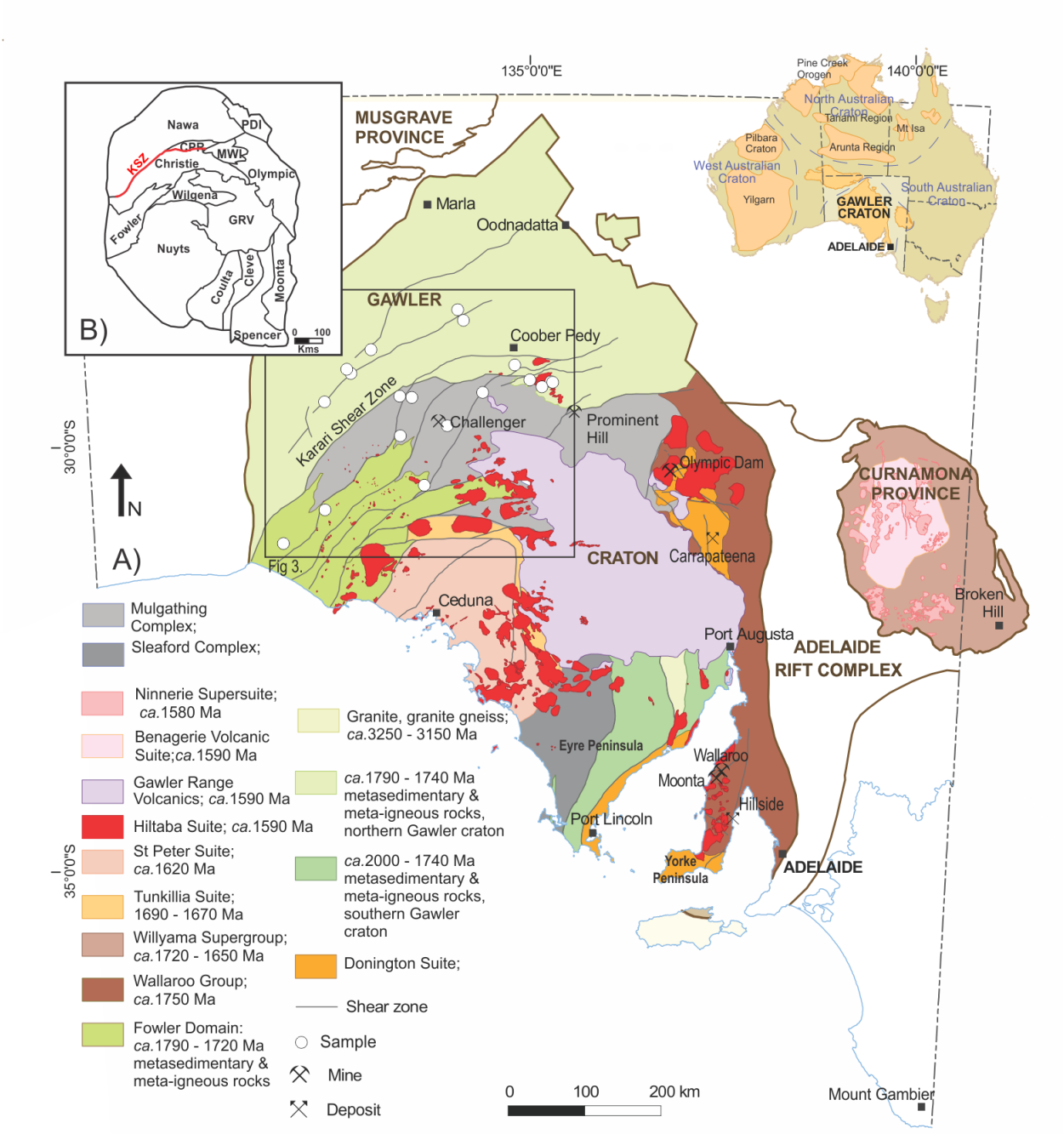

Figure 3.1: (A) Simplified geological map of the Gawler Craton, indicating the locations of all apatite fission track samples. Inset (B) illustrating the boundaries of of all the domains within the Gawler Craton. Abbreviations are: PDI-Peake and Denison Inliers; CPR-Coober Pedy Ridge; MWI-Mt. Woods Inliers; KSZ-Karari Shear Zone; GRV-Gawler Range Volcanics. Modified from Reid et al. (2014).

Sample	Drill hole name	Latitude	Longitude	Depth (m)	Rock type	Formation age	AFT age population 1:	AFT age population 2:
Mt Woods Inlier								
1039419	*-*	*-29.396233*	*135.313564*	*-*	*granite*	1590 Ma	331 ± 18	-
1039420	*-*	*-29.389993*	*135.295242*	*-*	*granite*	1590 Ma	331 ± 17	-
2131371	*KDD 005*	*-29.3758388*	134.9082905	*333-336*	*orthogneiss*	1740 Ma	352 ± 13	-
1039423	*-*	-29.4616	*135.145611*	*-*	*granite*	1590 Ma	270 ± 36	-
Nawa Domain								
2131373	*AM/PB 2*	*-28.8199561*	*133.8273135*	*344-345*	*paragneiss*	1740 Ma	335 ± 10	-
2131376	*Karkaro 1*	*-28.5980026*	*133.7754952*	*476-477*	*adamellite*	2500 Ma	245 ± 12	-
2131380	*OBD 8*	*-29.017528*	*132.8058533*	*183-184*	*granite*	1750 Ma	229 ± 19	-
2131386	*OBD 01*	*-29.310519*	*132.568165*	*139-140*	*paragneiss*	1750 Ma	360 ± 14	-
2131379	*OBD 7*	*-29.2831073*	*132.5062594*	*261-262*	*granite*	1750 Ma	329 ± 12	-
2131385	*OBD 12*	*-29.6008065*	*132.2554548*	*470-471*	*paragneiss*	1750 Ma	592 ± 42	-
Coober Pedy Ridge +	*Christie Domain*							
2131367	*DD87LR3*	*-29.2146561*	*134.619117*	*93-95*	*gabbro*	1740 Ma	375 ± 20	673 ± 38
650666	*Wallira 1*	*-29.4493925*	*134.0766141*	*217-218*	*Paragneiss*	2500 Ma	643 ± 49	-
0501	*-*	*-29.63513888*	*133.3580277*	*-*	*tonalite*	2500 Ma	509 ± 75	-
2131395	*CH 1*	*-29.9253457*	*133.7903421*	*68-80*	*granite*	2500 Ma	229 ± 29	471 ± 45
0307	*-*	*-30.15667473*	*133.08812111*	*-*	*granite*	1695 Ma	201 ± 14	569 ± 47
2131381	*NNL IL2 DDH 1*	*-29.6372204*	*133.0799559*	*48-49*	*granulite*	2500 Ma	531 ± 57	-
Fowler Domain								
1472758	*Tal 9*	*-30.9871284*	*132.2473098*	*21.8-22.5*	*paragneiss*	1760–1700 Ma	260 ± 23	524 ± 29
1472763	*Tal 65*	*-30.6371679*	*133.0589695*	*56-59.5*	*gabbronorite*	1760–1700 Ma	564 ± 27	-
1472783	*BAC 28*	*-30.945723*	*132.402688*	*54-57*	*paragneiss*	1760–1700 Ma	492 ± 74	-

Table 3.1: Sample details. Formation ages from Finlay (1993), Daly et al. (1998), Cowley (2005), Payne et al. (2006), Hand et al. (2007), Jagodzinski et al. (2009), Jagodzinski and Reid (2010), Howard et al. (2011a), Howard et al. (2011b), Reid et al. (2014), Reid and Fabris (2015), and Dawson (2016).

3.3.2 Radial plots and thermal history modelling

All AFT central ages (Galbraith and Laslett, 1993; Galbraith et al., 1999) were produced using *Radial Plotter* (Vermeesch, 2009). Samples that contain a large dispersion (>25%) and fail the $P(X^2)$ test (<0.05) were statistically separated into multiple age populations using *Radial Plotter's* automatic mixing model. Dispersion of Cl % and ^{238}U within the apatite grains were used as a visual aid in identifying age populations in the radial plots (Stormer et al., 1993; Stock et al., 2015; Glorie et al., 2017a).

AFT ages and confined track lengths from applicable samples were compiled into *QTqt* (Gallagher, 2012) to produce time-temperature models for the various regions across the Karari Shear Zone.

3.4 Results

3.4.1 Mt. Woods Inlier

Sample 1039419 and 1039420 were taken from Hiltaba granites that crop out within 2km from each other. Both samples produced consistent Carboniferous AFT central ages of 331 ± 18 Ma (based on 28 apatite grains) and 331 ± 17 Ma (based on 12 apatite grains), respectively. Dispersion values were moderate to low (19% and 9%, respectively), suggesting a simple thermal history (Fig. 4). An insufficient number of AFT lengths were recorded to produce reliable fission track length histograms.

Sample 2131371 was collected from an orthogneiss from drill hole KDD 005 at a depth of 333 m and preserves a central age of 352 ± 13 Ma with a low dispersion of 9%, based on 20 grains. This age is within error to the central age obtained for previous samples. A total of 68 confined tracks were measured, yielding an average confined track length of 13.38 µm with a standard deviation of 1.32 µm, suggesting rather fast cooling through the APAZ at that time.

Sample 1039423, is an outcropping Hiltaba Granite. A central age of 270 ± 36 Ma with a dispersion of 46% and a P(X2) value of 0.00 was recorded from 14 grains for sample 1039423. This sample records an average confined track length of 12.52 µm with a standard deviation of 1.23 µm from 78 confined tracks.

Overall, the Mt. Woods Inlier samples preserve single, Carboniferous-age populations, with the exception of sample 1039423, which records a mixed Permian central age.

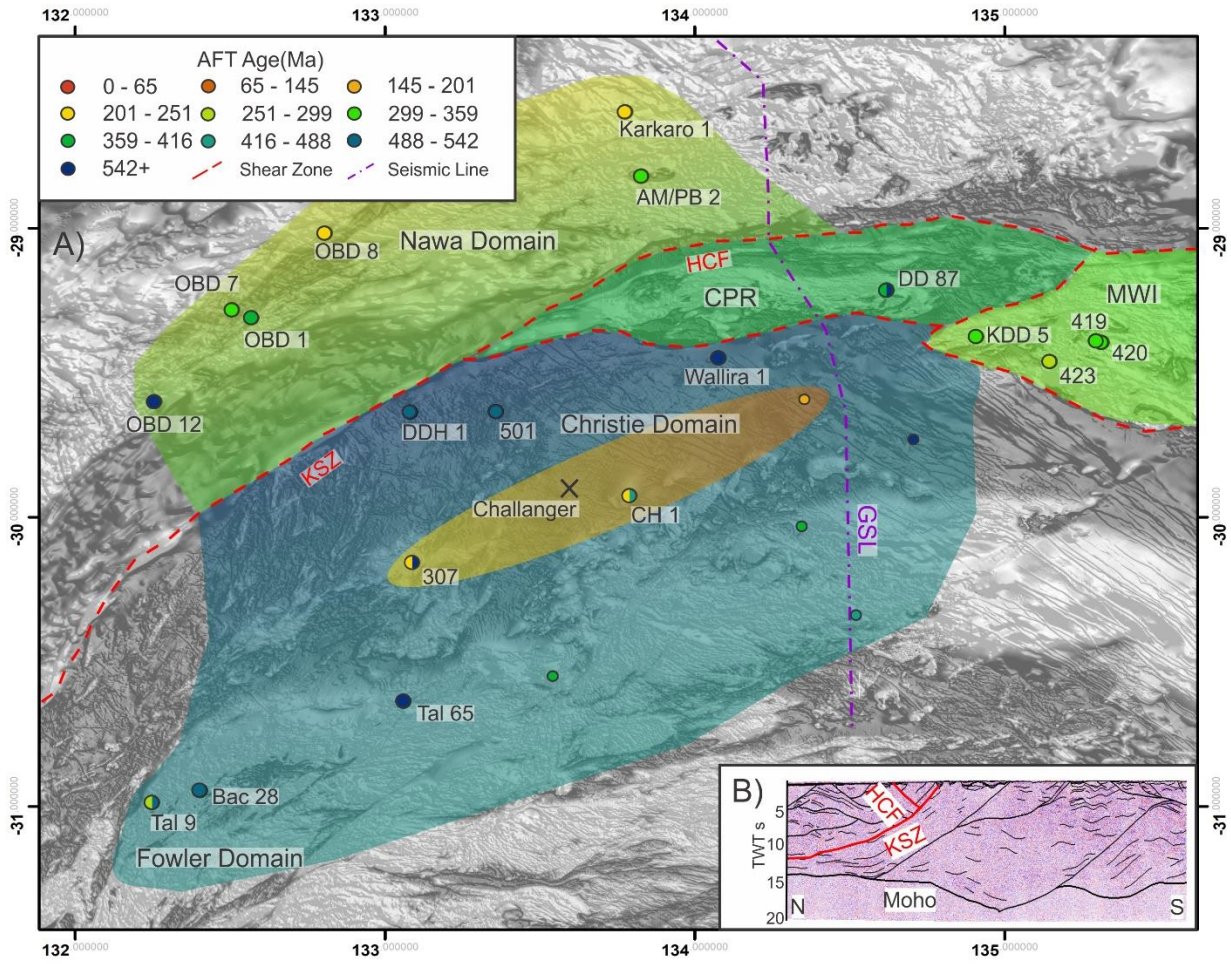

Figure 3.2: A) A total magnetic intensity map of the northern Gawler Craton indicating the location, apatite fission track (AFT) central age (or age populations), and (abbreviated) drill hole names of samples. The locations of the Karari Shear Zone (KSZ), Horse Camp Fault (HCF), GOMA seismic line (GSL), Challenger mine, and studied geological domains (CPR; Coober Pedy Ridge, MWI; Mt. Woods Inlier) are indicated by their respective names and dashed lines. The unlabelled dots are AFT central ages from Reddy et al. (2015). The coloured shading indicates the preserved AFT age for that region. Abbreviations are: DD 87; DD87LR 3, KDD 5; KDD 005, DDH 1; NNL IL2 DDH 1, 419; 1039419, 420; 1039420, and 423; 1039423. B) The GOMA seismic line with interpreted shear zones. Adapted from Korsch et al. (2010).

3.4.2 Nawa Domain

Sample 2131373 was collected from a paragneiss in drill hole AM/PB 2 at a depth of 334 m (Table 3.1). This sample records an AFT central age of 335 ± 10 Ma with a modest dispersion value of 15 % (based on analysed 42 grains). The AFT central age is within error to the samples obtained for the Mt. Woods Inlier. An average confined track length of 12.66 µm with a standard deviation of 1.36 µm from 90 grains was measured for this sample.

Sample 2131376, which was collected from an adamellite within drill hole Karkaro 1 at a depth of 476m, records an AFT central age of 245 ± 12 Ma, based on eight analysed grains. This is the youngest obtained AFT central age in this study, at the northern margin of the study area. The analysed grains show only little single-grain age dispersion (4.3 %). An insufficient number of AFT lengths were recorded to yield a length histogram.

Sample 2131380 was collected from a granite within drill hole OBD 8 at a depth of 183 m. A central age of 285 ± 35 Ma, with a large single-grain age dispersion of 46 %, was produced for this sample, from 15 grains. The oldest grains in this sample correlate with the Carboniferous AFT age obtained for most samples discussed above (Fig. 3.4). The lower central AFT age is governed by the presence of some younger (Mesozoic) apatites, which may be indicative of prolonged residence in the APAZ or a subsequent (Meso-Cenozoic) thermal event, similar as for sample 1039423 from the Mt Woods Inlier. There were insufficient AFT confined track lengths to produce a reliable length histogram for this sample.

Sample 2131386, which was sampled from a paragneiss at 139 m depth in drill hole OBD 01, records an AFT central age of 360 ± 14 Ma (from 26 grains). The single-grain age dispersion is moderate to low (12 %). AFT confined length measurements for this sample yielded an average length of 12.20 µm with a standard deviation of 1.18 µm from 67 confined tracks.

Sample 2131379 was collected from a granite from drill hole OBD 7 at a depth of 261 m. This sample preserves a central age of 329 ± 12 Ma with a modest single-grain age dispersion of 21 %. The average AFT confined track length recorded for this sample is 11.35 µm with a standard deviation of 1.82 µm from 100 confined tracks. This broad length distribution and the significant single-grain age dispersion suggest a prolonged residence within the APAZ.

Sample 2131385, collected from a paragneiss at 470 m down drill hole OBD 12, records a central age of 592 ± 42 Ma, with a moderate dispersion of 21 %. This is the oldest sample of the study, at the western margin of the study area. There were not enough AFT confined track lengths preserved in this sample to produce a reliable length frequency histogram.

Similar to the Mt. Woods Inlier, the Nawa Domain samples preserves dominant Carboniferous age populations. Samples 2131376 and 2131380 both preserve Triassic age populations. Sample 2131385 forms an outlier in the Nawa Domain and records a Neoproterozoic AFT central age.

Sample	Drill hole Name	ρ_s	Ns	N	^{238}U	AFT age population 1:	AFT age population 2:	l_m	n	σc	D_{par} (µm)
Mt Woods Inlier											
1039419	-	1.17 (0.64)	967	28	7.14 (0.48)	331 ± 18	-	-	-	-	-
1039420	-	1.76 (0.54)	534	12	10.52 (0.37)	331 ± 17	-	-	-	-	-
2131371	*KDD 005*	2.26 (0.77)	1508	20	12.76 (0.87)	352 ± 13	-	13.38	68	1.32	2 .1 ()
1039423	-	2.46 (1)	704	14	22.76 (1.38)	270 ± 36	-	12.52	78	1.23	3 ()
Nawa Domain											
2131373	*AM/PB 2*	2.5 (1.19)	3176	42	14.99 (0.6)	335 ± 10	-	12.66	90	1.36	1.69 ()
2131376	*Karkaro 1*	3.52 (1.92)	731	8	28.6 (2)	245 ± 12	-	-	-	-	
2131380	*OBD 8*	3.25 (1.33)	796	16	15.12 (1.53)	285 ± 35	-	-	-	-	
2131386	*OBD 01*	3.16 (0.88)	1510	26	16.9 (1)	360 ± 14	-	12.20	67	1.18	1.8 ()
2131379	*OBD 7*	4.44 (1.66)	7551	40	27.1 (1.44)	329 ± 12	-	11.35	100	1.82	1.8 ()
2131385	*OBD 12*	4.47 (1.37)	893	13	14.2 (0.88)	592 ± 42	-	-	-	-	
Coober Pedy Ridge + Christie Domain											
2131367	*DD87LR 3*	1.71 (0.72)	1094	37	6.81 (0.33)	375 ± 20	673 ± 38	-	-	-	-
650666	*Wallira 1*	1.45 (0.63)	334	14	5.3 (0.33)	643 ± 49	-	-	-	-	-
0501	-	1.13 (0.84)	56	6	3.95 (0.42)	509 ± 75	-	-	-	-	
2131395	*CH 1*	3.6 (1.35)	1095	16	16.8 (1.41)	229 ± 29	471 ± 45	12.16	57	1.63	1.9 ()
0307	-	1.23 (0.87)	487	22	8.18 (0.84)	201 ± 14	569 ± 47	-	-	-	
2131381	*NNL IL2 DDH 1*	2.17 (1.01)	227	4	9.62 (1.51)	531 ± 57	-	-	-	-	
Fowler Domain											
1472758	*Tal 9*	1.18 (0.71)	1017	35	5.98 (0.54)	260 ± 23	524 ± 29	-	-	-	
1472763	*Tal 65*	6.76 (1.94)	1305	26	19.87 (1.84)	564 ± 27	-	11.63	74	2.30	1.66 ()
1472783	*BAC 28*	1.6 (0.76)	49	4	5.65 (0.46)	492 ± 74	-	-	-	-	

Table 3.2: Apatite fission track (AFT) age and length details. ρ_s is AFT density in 10^5 tracks/cm^2, Ns is number of fission tracks counted, N is number of counted grains, ^{238}U is concentration of ^{238}U, AFT age population 1 is the apatite fission track central age in Ma (or the lower age population when there is more than one age population present), l_m is average confined AFT length, n is number of confined tracks counted, σc is standard deviation of the confined tracks, D_{par} is the average D_{par} for each sample with the standard deviation in brackets. All brackets contain their respective standard deviations.

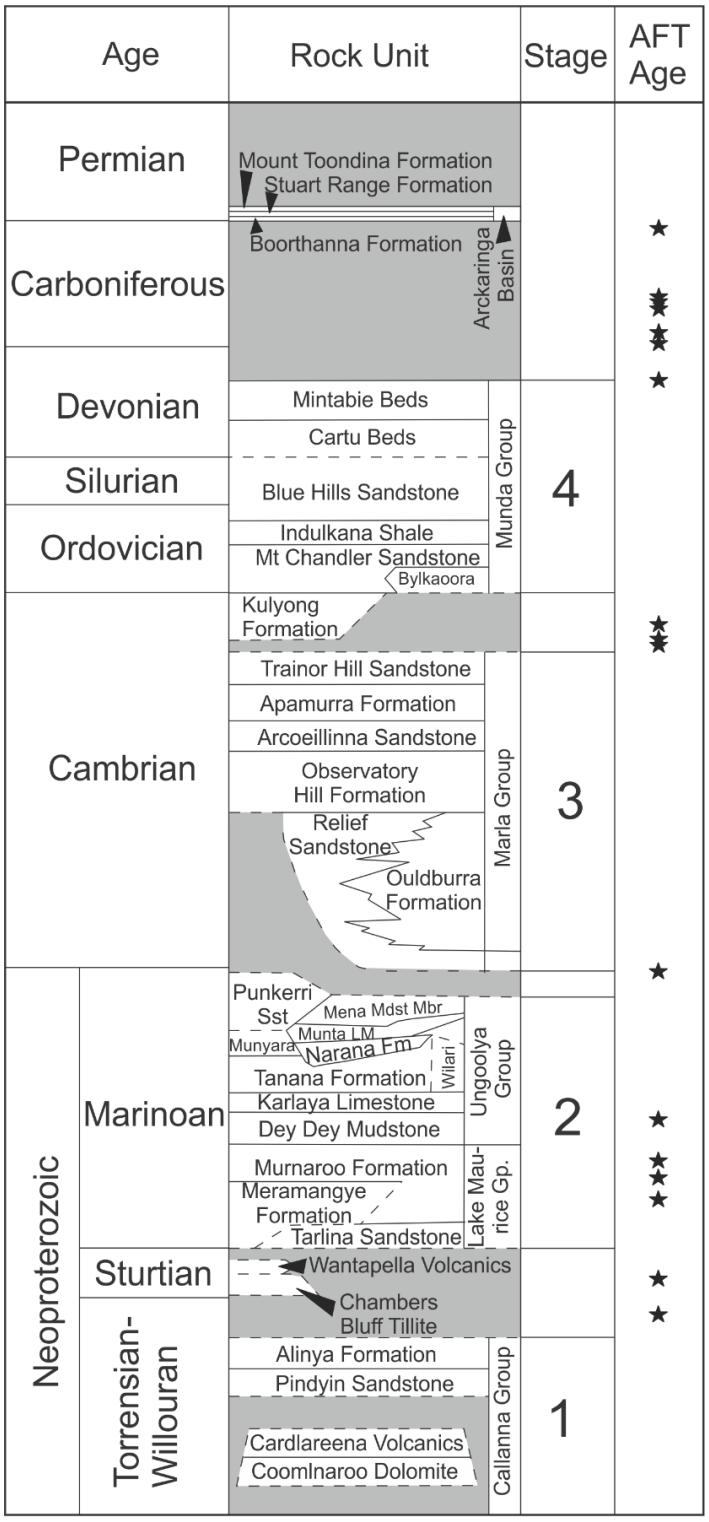

Figure 3.3: Simplified stratigraphic column of the Officer and Arckaringa basins indicating the ages of the stratigraphic successions, four stages of Officer Basin deposition, and apatite fission track (AFT) populations from this study. Adapted from Wade et al. (2005).

3.4.3 Coober Pedy Ridge and Christie Domain

Sample 2131367 was collected from a gabbro from drill hole DD87LR 3 at a depth of 93 m and yielded a central age of 491 ± 29 Ma (37 measured grains) with a large dispersion of 30% ($P(X^2)$ value = 0.00). Given the significant dispersion and typical open-jaw display of the data on a radial plot (e.g. O'Sullivan and Parrish, 1995; Glorie et al., 2017a; Glorie et al., 2017b), the AFT ages for this sample were subdivided into two age populations. The youngest population of 375 ± 20 Ma is only slightly older than the abundant Carboniferous AFT ages in this study. The oldest population was calculated at 673 ± 38 Ma, which is similar to the Neoproterozoic AFT central age obtained in sample 2131385. There were insufficient confined track lengths preserved in this sample to produce a length histogram.

Sample 650666 was collected from a paragneiss from drill hole Wallira 1 at a depth of 217 m. This sample produced a central age of 541 ± 74 Ma from 14 grains, with a large single-grain

dispersion of 45 %. A well-defined population of 643 ± 49 Ma (which is within error to the old population of the Cooper Pedy Ridge sample) was identified with four grains that preserved younger ages. An insufficient number of confined track lengths were recorded to produce a reliable length histogram.

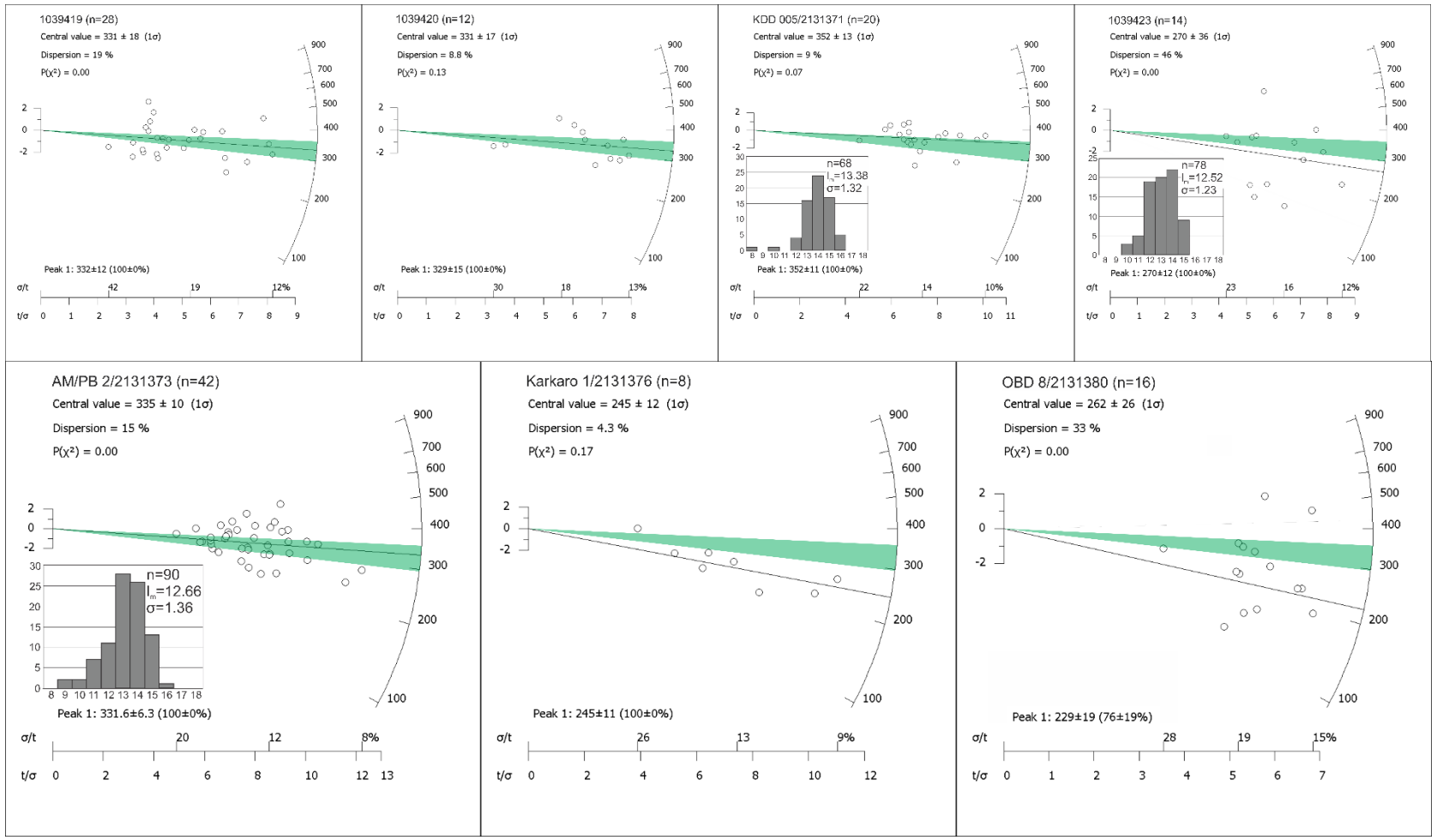

Figure 3.4: Apatite fission track (AFT) radial plots for samples 1039419, 1039420, 1039423, 650666, 2131367, 2131371, 2131373, 2131376, 2131379, 2131380, 2131381, 2131385, 2131386, 2131395, 0501, 0307, 1472758, 1472763, and 1472783. 'n' indicates the number of grains measured, the central value indicates the calculated central age, 'dispersion' indicates the percentage of age dispersion within the sample, and '$P(X^2)$' indicates the calculated $P(X^2)$ value. When multiple populations of ages are present, as calculated by less than 0.05 on the $P(X^2)$ value, the Automatic Mixture model of Radial Plotter (Vermeesch, 2009) splits the central age into age populations. The blue (Neoproterozoic) and green (Carboniferous) shaded regions are the two interpreted phases of cooling within the sampled region. Where applicable, radial plots are accompanied by AFT length frequency histogram. On each histogram, the x-axis is AFT length in µm while the y-axis is frequency, n is the number of tracks measured, l_m indicates average track length, while σ is the standard deviation of the sample. All radial plots were constructed using Radial Plotter (Vermeesch, 2009).

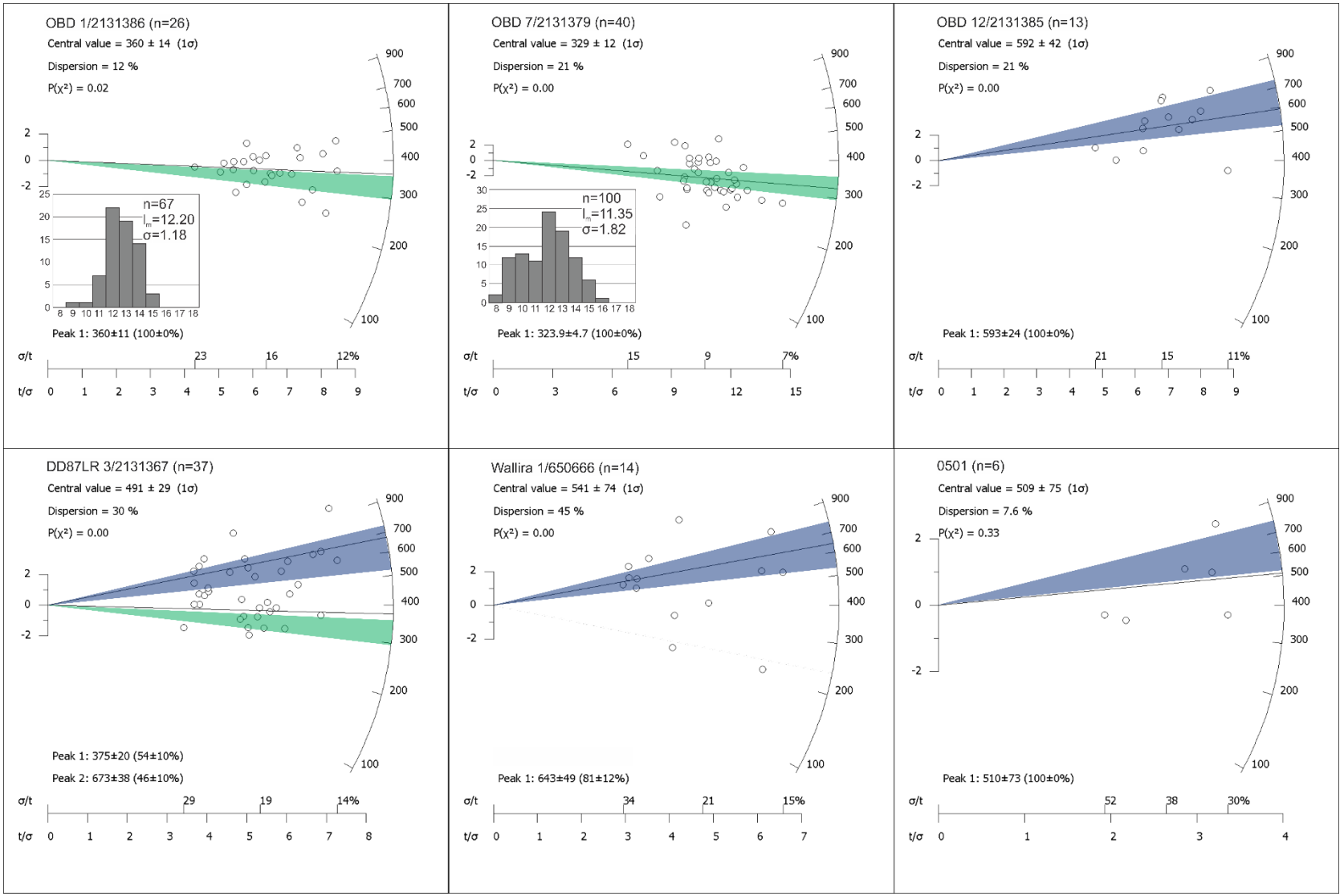

Figure 4: Continued.

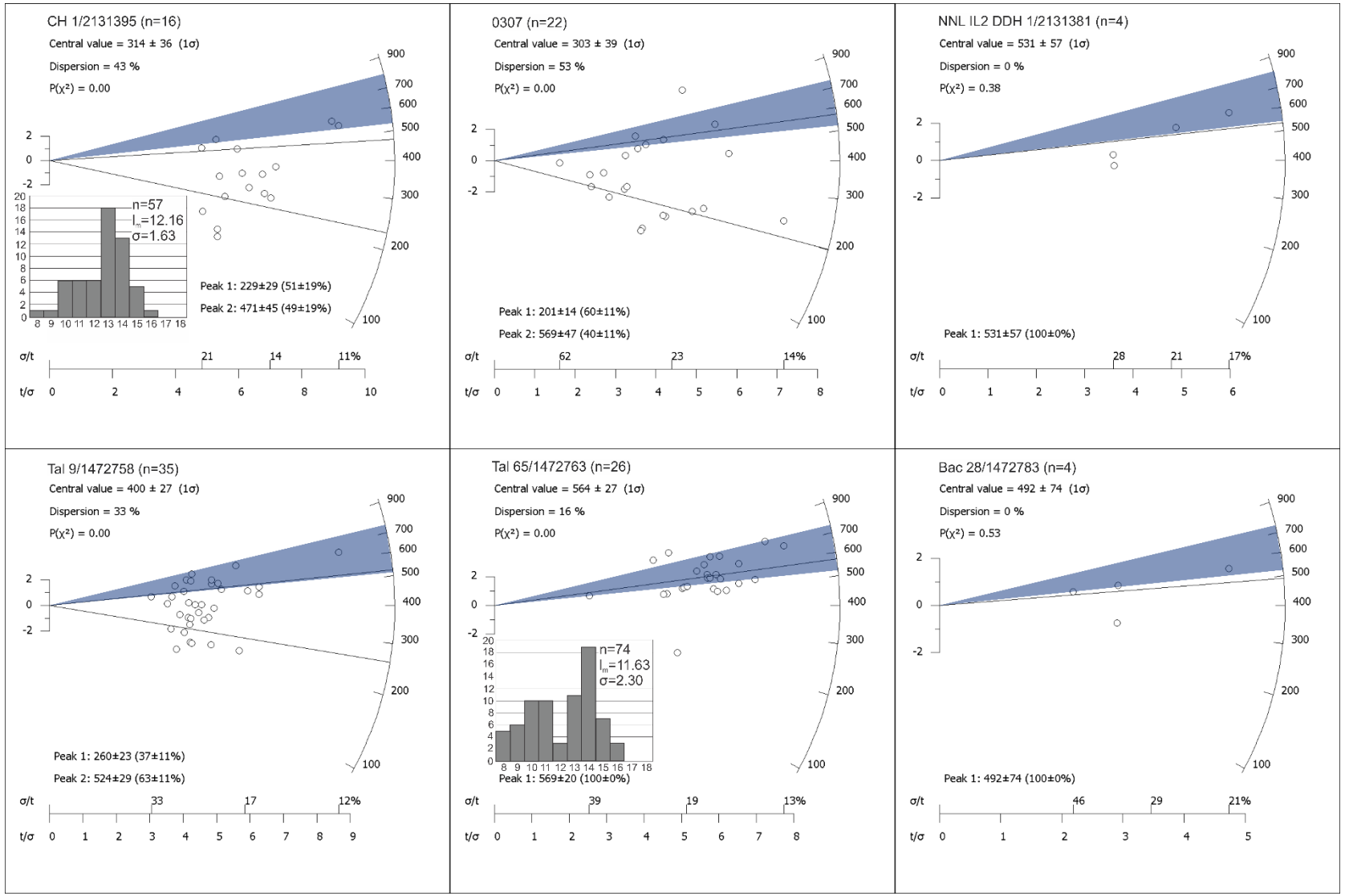

Figure 4: Continued.

Sample 501 is an outcropping tonalite with a central age recorded at 509 ± 75 Ma from six grains with a little dispersion (7.6 %). There were not enough confined tracks in this sample to produce a length histogram.

Sample 2131395 was collected from a granite within drill hole CH 1, which is located ~20 km south east of Challenger gold mine (Bonwick, 1997; Tomkins and Mavrogenes, 2002; Tomkins et al., 2004; McFarlane et al., 2007; McGee et al., 2010), yielding a central age of 314 ± 36 Ma. The sample shows rather large single-grain age dispersion (recorded as 43 %) without an open-jaw display in the radial plot. Two age populations of 229 ± 29 Ma and 471 ± 45 Ma were recorded, representing the minimum and maximum AFT age for the sample. The sample yielded 57 confined tracks for an average of 12.16 µm with a standard deviation of 1.63 µm.

Sample 0307, an outcropping granite, yielded a central age of 303 ± 39 Ma from 22 grains with a large dispersion of 53 % and a characteristic open-jaw radial plot display (e.g. O'Sullivan and Parrish, 1995). Two age populations were calculated at 201 ± 14 Ma and 569 ± 47 Ma. The younger age is within error the same as in sample 2131395. The older age matches well with the abundant Neoproterozoic AFT ages obtained in the study area. Insufficient confined track lengths were preserved to produce a reliable length histogram.

Sample 2131381, located ~25 km west of sample 0501, was collected from a granulite within drill hole NNL IL2 DDH 1 at a depth of 48 m. This sample produced a central age of 531 ± 57 Ma from four grains, with a dispersion of 0 %. There was not enough data to produce a reliable length histogram.

When compared to the samples in the Mt. Woods Inlier and Nawa Domain, the samples of the Coober Pedy Ridge and Christie Domain record more diffuse age populations, often recording an older (Neoproterozoic – early Cambrian; ~680 – 530 Ma) AFT central age or age populations. In clear contrast to the Mt. Woods Inlier and the Nawa Domain, only one sample (2131367) records a Carboniferous age population. The samples from the south of the Christie Domain, near the Challenger deposit, also record a Mesozoic age population that is not recorded anywhere else in the study area (Fig. 3.2).

3.4.4 Fowler Domain

Sample 1472758 was collected from a paragneiss within drill hole Tal 9 at a depth of 22 m and records a central age 400 ± 27 Ma from 36 grains, with a rather large single-grain age dispersion of 39 %. This central age was separated into two age populations, a well-defined older age of 524 ± 29 Ma and a poorly defined younger age of 260 ± 23 Ma. There were not enough measured confined track lengths to create a reliable length histogram.

Sample 1472763 preserved a central age of 564 ± 27 Ma, which was collected from a gabbronorite within drill hole Tal 65 at a depth of 56 m. The dispersion of this sample was recorded as moderate

(16 %). A total of 74 confined tracks were measured in this sample with an average of 11.63 µm and a standard deviation of 2.30 µm. The length frequency histogram has a bimodal characteristic.

Sample 1472783 was collected from a paragneiss, 54 m down drill hole BAC 28. Only 4 grains could be analysed, producing a central age 492 ± 74 Ma with a dispersion of 0 %. Due to the lack of grains, there were not enough confined track lengths to produce a length histogram.

Similar to the Christie Domain, the samples of the Fowler Domain record Neoproterozoic age populations, with sample 1472758 also preserving a Permian age population.

3.4.5 Thermal history modelling

Samples with sufficient confined track lengths were used further to model their time-temperature history (Fig. 3.5) using QT-qt (Gallagher, 2012).

There are two general thermal histories recorded in the thermal history models (Fig. 3.5), shaded based on the timing of the main cooling period. For those samples where Neoproterozoic – early Cambrian AFT ages were dominant, both radial plots and thermal history models were shaded in blue. Samples with mostly Carboniferous AFT ages were shaded green (Figs. 3.4 & 3.5).

Samples 2131395 and 1472763 were the only two samples south of the Karari Shear Zone to be modelled. These two samples both reveal protracted cooling through the APAZ since ~650 Ma while samples 1039423, 2131371, 2131373, 2131386, and 2131379, to the north of the Karari Shear Zone preserve a rapid phase of cooling through the APAZ at ~ 400 – 300 Ma. All models preserve thermal quiescence following the Carboniferous.

3.5 Discussion

The oldest AFT ages within the region span the Neoproterozoic to early Cambrian from ~680 – 530 Ma (Fig. 4). These ages are almost entirely restricted to the south of the Karari Shear Zone (with one exception: sample 2131385 at the north-western margin of the study area). Associated thermal history models show protracted slow cooling or thermal quiescence since ~650 Ma, indicating that the Christie and Fowler domains were exhumed to temperatures less than the APAZ during the Neoproterozoic – Cambrian and didn`t experience younger regional thermal events. The samples of the Nawa Domain are interpreted to be at temperatures greater than 120 °C, likely due to the continued deposition of the Officer Basin throughout this time period (Gravestock, 1997; Morton and Drexel, 1997).

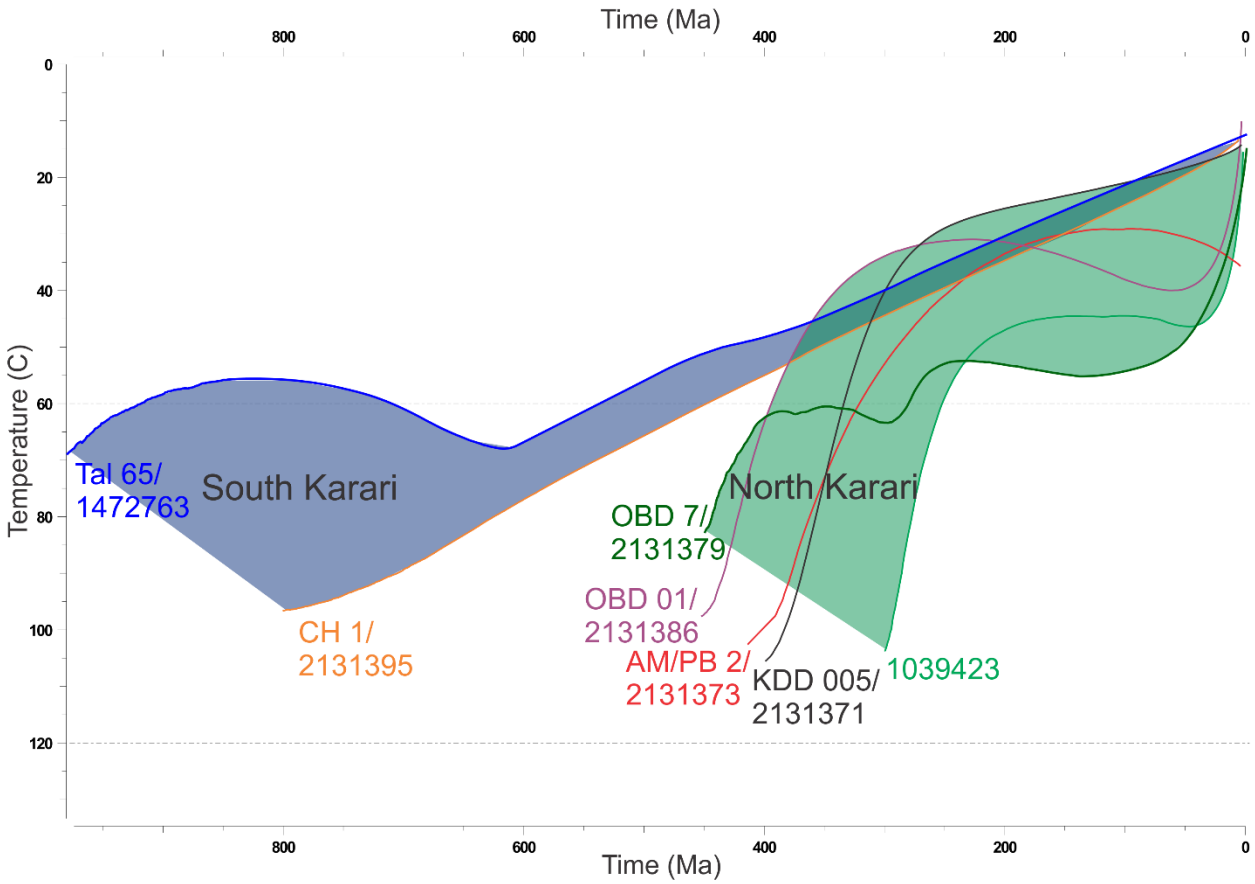

Figure 3.5: Time-temperature plot containing modelled average thermal histories for samples 1472763 (Tal 65; blue), 2131395 (CH 1; orange), 2131373 (AM/PB 2; red), 2131386 (OBD 1; purple), 2131379 (OBD 7; dark green), 2131371 (KDD 005; black), and 1039423 (light green). All models were produced in QT-qt (Gallagher, 2012) by using the apatite fission track ages and length measurements. The blue and green shading correlates to the shading within figure 4, where the purple indicates cooling during the Neoproterozoic while the green indicates cooling during the Carboniferous.

In contrast to the Christie Domain, the samples from the Nawa Domain, Coober Pedy Ridge, and Mt. Woods Inlier, to the north of the Karari shear zone, record a major phase of fast cooling at ~350 – 300 Ma (Fig. 3.4; green shading in Fig. 3.5). This cooling period coincides with a break in sedimentation above the Nawa Domain between the top of the Officer Basin during the Eifelian – Frasnian (Womer et al., 1987; Long et al., 1988) and the bottom of the Arckaringa Basin at ~300 Ma (Hibburt, 1995). Our data show that this compressional event induced cooling in the Nawa Domain, Coober Pedy Ridge and Mt. Woods Inlier. Given the clear difference in thermal history on either side of the Karari Shear Zone, we interpret the Carboniferous cooling to be related to fault reactivation of the Karari Shear Zone, in a compressional regime, related to the southward vergent Alice Springs Orogeny (Ballèvre et al., 2000; Haines et al., 2001), which resulted in the cessation of sedimentation and minor folding within the Officer Basin during this time (Gravestock et al., 1997). The presence of one older AFT age in the far western Nawa Domain may indicate that

this compressional event was not uniform and was focused in the central Nawa Domain and Mt. Woods Inlier. Movement along smaller, separating faults could have accommodated some of the compression stresses, thus, decreasing the amount of thrusting within the western Nawa Domain. The southward dipping Horse Camp Fault, which bounds the northern margin of the Coober Pedy Ridge (Fig. 3.2), would have minimised thrusting of the Coober Pedy Ridge over the Christie Domain, as seen by the more modest Devonian – Carboniferous AFT signal and preserved older signal in sample 2131367. To the east, compressional structures from the base of the Arckaringa Basin have been reported to be Devonian (Wopfner, 1970; Jensen-Schmidt et al., 2006; Debenham, 2015), similar to our interpreted timing of reactivation of the Karari Shear Zone. Carboniferous AFT ages are widespread in the northern Gawler Craton, suggesting that the Alice Springs Orogeny induced phanerozoic cooling and fault reactivation on a regional scale (e.g. in the Officer Basin, Mt. Painter Inlier, Peake and Denison Inliers, and Musgrave Province; Tingate and Duddy, 2002; Weisheit et al., 2014; Hall et al., 2016; Glorie et al., 2017a). The Christie and northern Fowler Domains are anomalously lacking AFT evidence for the Carboniferous Alice Springs Orogeny deformation as these domains were at surface temperatures prior to the Devonian - Carboniferous (Fig. 3.5).

Immediately following the Alice Springs Orogeny and its far-field exhumation and cooling, widespread sedimentation returned to South Australia with deposition of the Boorthanna, Stuart Range, and Mount Toondina formations of the Arckaringa Basin (Hibburt, 1995). In addition to extensive deposition within the Pedirka, Cooper, Denman, Polda, Troubridge, Padthaway, Nadda and Blinman Basins throughout South Australia (Youngs, 1976; Moore, 1986; Alley, 1995; Alley and Bourman, 1995).

Besides the regional differential exhumation with respect to the Karari fault zone, discussed above, an additional young thermal corridor is apparent around the Challenger deposit (Bonwick, 1997), south of the Karari Shear Zone, consisting of samples 307, 2131395, and 111 from Reddy et al. (2015). These samples contain a ~240 – 200 Ma thermal event that is not seen elsewhere (Fig. 3.2). Reddy et al. (2015) attributed this age to uplift associated with rifting of Antarctica from Australia, however, this thermal event is not seen unanimously throughout the northern and central Gawler Craton (Gleadow et al., 2002; Reddy et al., 2015; Boone et al., 2016) and only becomes prominent in the southern Gawler Craton (Gleadow et al., 2002). The Mesozoic ages could be caused by compression along faults to the south of the Karari Shear Zone. However, there is no continuous fault zone that lines up with these ages (Stewart and Betts, 2010). We, therefore, suggest that the thermal anomaly is more likely related with a localised increase in the geothermal gradient, potentially related with hot hydrothermal fluid flow and/or the concentration of heat-producing elements. The relation of this Triassic thermal anomaly with the location of the Challenger deposit is curious and may suggest that the Triassic anomaly provided preferable conditions for ore

exhumation and preservation at minable depths. More data would be required to test any correlations with the thermal anomaly and deposit preservation.

3.6 Conclusions

Apatite fission track dating revealed two main periods of basement cooling on either side of the Karari fault zone. The oldest AFT age population, to the south of the Karari fault, records Neoproterozoic – early Cambrian regional monotonic cooling. To the north of the Karari fault zone, late Devonian – Carboniferous cooling was recorded, suggesting that the Karari fault zone was reactivated at that time. In further detail, our data corresponds with previous models, indicating that southward directed deformation from the Alice Springs Orogeny during the Carboniferous resulted in southward thrusting of the Karari Shear Zone, which in turn terminated deposition in the Officer Basin. In addition, a Triassic thermal event is recorded south of the Karari Shear Zone, in the vicinity of the Challenger deposit, which may be related with a localised geothermal gradient at that time.

3.7 Acknowledgements

This paper was made possible thanks to the financial support of the Geological Survey of South Australia and an Australian Research Council grant (ARC LE150100145). ASC is funded by an Australian Research Council Future Fellowship (FT120100340). Bradley McDonald (John De Laeter Center at Curtin University) is thanked for assistance with the U-Th-Sm/He methods and Ben Wade (Adelaide Microscopy) for assistance with the use of the LA-ICP-MS. Jack Dawson and Katie Howard are thanked for supplying sample separates. This paper forms TRaX# XXX.

3.8 References

Alley, N.F., 1995. Late Palaeozoic, in: Drexel, J.F., Preiss, W.V. (Eds.), The Geology of South Australia. Vol. 2, The Phanerozoic. South Australia Geological Survey, South Australia.

Alley, N.F., Bourman, R.P., 1995. Troubridge Basin, in: Drexel, J.F., Preiss, W.V., Parker, A.J. (Eds.), The geology of South Australia, Volume 2, The Phanerozoic, Bulletin 54. Geological Survey of South Australia, Adelaide, pp. 65-70.

Ballèvre, M., Möller, A., Hensen, B.J., 2000. Exhumation of the lower crust during crustal shortening: an Alice Springs (380 Ma) age for a prograde amphibolite facies shear zone in the Strangways Metamorphic Complex (central Australia). Journal of Metamorphic Geology 18, 737-747.

Benbow, M.C., 1986. Tallaringa 1:250,000 SA Geological Map SH5305, in: Australia, G.S.o.S. (Ed.). Geological Survey of South Australia Adelaide.

Bonwick, C.M., 1997. Discovery of the Challenger gold deposit: Implications for future exploration on the Gawler craton: Case Histories of Discovery, New Generation Gold Mines ,97. Case Histories of Discovery., Glenside, Australia, pp. 7.1-7.15.

Boone, S.C., Seiler, C., Reid, A.J., Kohn, B., Gleadow, A., 2016. An Upper Cretaceous paleo-aquifer system in the Eromanga Basin of the central Gawler Craton, South Australia: evidence from apatite fission track thermochronology. Australian Journal of Earth Sciences 63, 315-331.

Bradshaw, J.D., Evans, P.R., 1988. Palaeozoic tectonics, Amadeus Basin, central Australia. APEA Journal 28, 267-282.

Buick, I.S., Storkey, A., Williams, I.S., 2008. Timing relationships between pegmatite emplacement, metamorphism and deformation during the intra-plate Alice Springs Orogeny, central Australia. Journal of Metamorphic Geology 26, 915-936.

Cowley, W.M., 2005, Solid Geology South Australia 1:2 000 000. map produced for St Barbara's Day Explorers Conference Primary Industries and Resources.

Creaser, R.A., 1996. Petrogenesis of a Mesoproterozoic quartz latite-granitoid suite from the Roxby Downs area, South Australia. Precambrian Research 79, 371-394.

Creaser, R.A., White, A.J.R., 1991. Yardea Dacite; large-volume, high temperature felsic volcanism from the middle Proterozoic of South Australia. Geology 19, 48-51.

Daly, S.J., Fanning, C.M., Fairclough, M.C., 1998. Tectonic evolution and exploration potential for the Gawler Craton, South Australia. AGSO Journal of Australian Geology and Geophysics 17, 145-168.

Dawson, J., 2016, Characterising Magmatic Suites in the Western Gawler Craton: Geochemical and Geochronological Constraints. University of Adelaide.

Debenham, N., 2015. Controls on organic carbon enrichment in a Permian periglacial setting (Arckaringa Basin). Sydney, Australia : Macquarie University.

Dutch, R.A., Hand, M., Kelsey, D.E., 2010. Unravelling the tectonothermal evolution of reworked Archean granulite facies metapelites using in situ geochronology: an example from the Gawler Craton, Australia. Journal of Metamorphic Geology 28, 293-316.

Fairclough, M.C., Schwarz, M.P., Ferris, G.M., 2003. Interpreted crystalline basement geology of the Gawler Craton. South Australia, Geological Survey, Special Map, 1:1,000,000.

Fanning, C.M., Reid, A.J., Teale, G., 2007. A geochronological framework for the Gawler Craton, South Australia. . South Australia. Geological Survey. Bulletin 55.

Ferris, G., Schwarz, M.P., Heithersay, P., 2002. The geological frame-work, distribution and controls of Fe-oxide and related alteration, and Cu- Au mineralisation in the Gawler craton, South Australia. Part I: geological and tectonic framework, in: Porter, T.M. (Ed.), Hydrothermal iron oxide cop- per-gold and related deposits: A global perspective, 2. Porter GeoConsultancy Publishing, Adelaide, pp. 9-31.

Finlay, J., 1993, Structural Interpretation of the Mount Woods Inlier. Honours Thesis, Monash University

Flint, R.B., Rankin, L.R., Fanning, C.M., 1990. Definition; the Palaeoproterozoic St. Peter Suite of the western Gawler craton. Geological Survey of South Australia, Quarterly Geological Notes 114, 2-8.

Foden, J., Elburg, M.A., Dougherty-Page, J., Burtt, A., 2006. The Timing and Duration of the Delamerian Orogeny: Correlation with the Ross Orogen and Implications for Gondwana Assembly. The Journal of Geology 114, 189-210.

Foster, D.A., Ehlers, K., 1998. 40Ar-39Ar thermochronology of the southern Gawler Craton, Australia: Implications for Mesoproterozoic and Neoproterozoic tectonics of East Gondwana and Rodinia. Journal of Geophysical Research 103, 10,177-110,193.

Fraser, G., Reid, A., Stern, R., 2012. Timing of deformation and exhumation across the Karari Shear Zone, north-western Gawler Craton, South Australia. Australian Journal of Earth Sciences 59, 547-570.

Galbraith, R.F., Laslett, G.M., 1993. Statistical models for mixed fission track ages. Nuclear Tracks and Radiation Measurements 21, 459-470.

Galbraith, R.F., Roberts, R.G., Laslett, G.M., Yoshida, H., Olley, J.M., 1999. Optical dating of single and multiple grains of quartz from jinmium rock shelter, northern australia: Part i, experimental design and statistical models*. Archaeometry 41, 339-364.

Gallagher, K., 2012. Transdimensional inverse thermal history modeling for quantitative thermochronology. Journal of Geophysical Research: Solid Earth 117, n/a-n/a.

Gibson, H.J., Stüwe, K., 2000. Multiphase cooling and exhumation of the southern Adelaide Fold Belt: constraints from apatite fission track data. Basin Research 12, 31-45.

Giles, C.W., 1988. Petrogenesis of the Proterozoic Gawler Range Volcanics, South Australia. Precambrian Research 40–41, 407-427.

Gleadow, A.J.W., Gleadow, S.J., Belton, D.X., Kohn, B.P., Krochmal, M.S., Brown, R.W., 2009. Coincidence mapping - a key strategy for the automatic counting of fission tracks in natural minerals. Geological Society, London, Special Publications 324, 25-36.

Gleadow, A.J.W., Kohn, B.P., Brown, R.W., O'Sullivan, P.B., Raza, A., 2002. Fission track thermotectonic imaging of the Australian continent. Tectonophysics 349, 5-21.

Glorie, S., Agostino, K., Dutch, R., Pawley, M., Hall, J., Danišík, M., Evans, N.J., Collins, A.S., 2017a. Thermal history and differential exhumation across the Eastern Musgrave Province, South Australia: Insights from low-temperature thermochronology. Tectonophysics 703–704, 23-41.

Glorie, S., Alexandrov, I., Nixon, A., Jepson, G., Gillespie, J., Jahn, B.-M., 2017b. Thermal and exhumation history of Sakhalin Island (Russia) constrained by apatite U-Pb and fission track thermochronology. Journal of Asian Earth Sciences 143, 326-342.

Gravestock, D.I., 1997. Geological setting and structural history., in: Morton, J., Drexel, J.F. (Eds.), Petroleum Geology of South Australia, vol. 3. Officer Basin. South Australian Department of Mines and Energy Resources (SADME) Report Book 97/19., pp. 5-44.

Haines, P.W., Hand, M., Sandiford, M., 2001. Palaeozoic synorogenic sedimentation in central and northern Australia: a review of distribution and timing with implications for the evolution of intracontinental orogens. Australian Journal of Earth Sciences 48, 911-928.

Hall, J.W., Glorie, S., Collins, A.S., Reid, A., Evans, N., McInnes, B., Foden, J., 2016. Exhumation history of the Peake and Denison Inliers: insights from low-temperature thermochronology. Australian Journal of Earth Sciences 63, 805-820.

Hand, M., Reid, A., Jagodzinski, L., 2007. Tectonic Framework and Evolution of the Gawler Craton, Southern Australia. Economic Geology 102, 1377-1395.

Hasebe, N., Barbarand, J., Jarvis, K., Carter, A., Hurford, A.J., 2004. Apatite fission-track chronometry using laser ablation ICP-MS. Chemical Geology 207, 135-145.

Heinson, G.S., Direen, N.G., Gill, R.M., 2006. Magnetotelluric evidence for a deep-crustal mineralizing system beneath the Olympic Dam iron oxide copper-gold deposit, southern Australia. Geology 34, 573-576.

Hibburt, J.E., 1984. Review of exploration activity in the Arckaringa Basin region 1858 to 1983. Report Book 84/1. Department of Mines and Energy. South Australia.

Hibburt, J.E., 1995. Arckaringa Basin, in: Drexel, J.F., Preiss, W.V. (Eds.), The geology of South Australia. Vol. 2, The Phanerozoic. South Australia. Geological Survey. Bulletin, pp. 73 - 76.

Howard, K.E., Hand, M., Barovich, K.M., Payne, J.L., Belousova, E.A., 2011a. U–Pb, Lu–Hf and Sm–Nd isotopic constraints on provenance and depositional timing of metasedimentary rocks in the western Gawler Craton: Implications for Proterozoic reconstruction models. Precambrian Research 184, 43-62.

Howard, K.E., Hand, M., Barovich, K.M., Payne, J.L., Cutts, K.A., Belousova, E.A., 2011b. U–Pb zircon, zircon Hf and whole-rock Sm–Nd isotopic constraints on the evolution of Paleoproterozoic rocks in the northern Gawler Craton. Australian Journal of Earth Sciences 58, 615-638.

Jagodzinski, E.A., Reid, A.J., and Fraser, G., 2009, Compilation of Shrimp U-Pb Geochronological Data for the Mulgathing Complex, Gawler Craton, South Australia, 2007-09. South Australia. Department of Primary Industries and Resources. Report Book 2009/00016.

Jagodzinski, E. and Reid, A.J., 2010, New Zircon and Monazite Geochronology Using Shrimp and La-Icpms, from Recent Goma Drilling, on Samples from the Northern Gawler Craton. in R. J. Korsch and N.

Kositcin (eds.) Goma (Gawler Craton–Officer Basin–Musgrave Province–Amadeus Basin) Seismic and Mt Workshop 2010. , Geoscience Australia, 108-17.

Jensen-Schmidt, B., Alexander, E.M., Cotton, T.B., 2006. Structural and tectonic setting, in: Cotton, T.B., F., S.M., Hibburt, J.E. (Eds.), The petroleum geology of South Australia, Volume 2: Eromanga Basin., 2 ed. Department of Primary Industries and Resources, South Australia, pp. 1-27.

Korsch, R.J., Blewett, R.S., Giles, D., Reid, A.J., Neumann, N.L., Fraser, G.L., Holzschuh, J., Costelloe, R.D., Roy, I.G., Kennett, B.L.N., Cowley, W.M., Baines, G., Carr, L.K., Duan, J., Milligan, P.R., Armit, R.J., Betts, P.G., Preiss, W.V., Bendall, B.R., 2010. Geological interpretation of the deep seismic reflection and magnetotelluric line 08GA-OM1: Gawler Craton–Officer Basin–Musgrave Province–Amadeus Basin (GOMA), South Australia and Northern Territory., in: Korsch, R.J., Kositcin, N. (Eds.), GOMA (Gawler Craton–Officer Basin–Musgrave Province–Amadeus Basin) Seismic and MT Workshop 2010. Geoscience Australia, pp. 63-86.

Korsch, R.J., Kositcin, N., 2010. GOMA (Gawler Craton–Officer Basin–Musgrave Province–Amadeus Basin) Seismic and MT Workshop 2010. Record 2010/39. Geoscience Australia.

Kositcin, N., 2010. Geodynamic synthesis of the Gawler Craton and Curnamona Province. Record 2010/27. Geoscience Australia. Canberra.

Long, J.A., Turner, S., Young, G.C., 1988. A Devonian fish fauna from subsurface sediments in the eastern Officer Basin, South Australia. Alcheringa: An Australasian Journal of Palaeontology 12, 61-78.

Maksaev, V., Zentilli, M., 1999. Fission track thermochronology of the Domeyko Cordillera, Northern Chile: implications for Andean tectonics and porphyry copper metallogenesis. . Exploration Mining Geology 8, 65-89.

Mawby, J., Hand, M., Foden, J., 1999. Sm–Nd evidence for high-grade Ordovician metamorphism in the Arunta Block, central Australia. Journal of Metamorphic Geology 17, 653-668.

McDowell, F.W., McIntosh, W.C., Farley, K.A., 2005. A precise 40Ar–39Ar reference age for the Durango apatite (U–Th)/He and fission-track dating standard. Chemical Geology 214, 249-263.

McFarlane, C.R.M., Mavrogenes, J.A., Tomkins, A.G., 2007. Recognizing hydrothermal alteration through a granulite facies metamorphic overprint at the challenger Au deposit, South Australia. Chemical Geology 243, 64-89.

McGee, B., Giles, D., Kelsey, D.E., Collins, A.S., 2010. Protolith heterogeneity as a factor controlling the feedback between deformation, metamorphism and melting in a granulite-facies gold deposit. Journal of the Geological Society, London 167, 1089-1104.

McInnes, B.I.A., Evans, N.J., Fu, F.Q., Garwin, S., 2005. Application of Thermochronology to Hydrothermal Ore Deposits. Reviews in Mineralogy and Geochemistry 58, 467-498.

Menpes, S.A., 2013. Organic Rich Shale in Permian Fjords – A Potential Resource Play in the Arckaringa Basin, South Australia. . Search and Discovery Article #10538

Moore, P.S., 1986. An exploration overview of the Eromanga Basin. In: Contributions to the Geology and Hydrocarbon Potential of the Eromanga Basin, in: Gravestock, D.I., Moore, P.S., Pitt, G.M. (Eds.). Geological Society of Australia, Special Publication, pp. 1-8.

Morton, J.G.G., Drexel, J.F., 1997. Petroleum Geology of South Australia, vol. 3. Officer Basin., South Australian Department of Mines and Energy Resources (SADME). Report Book 97/19.

O'Sullivan, P.B., Parrish, R.R., 1995. The importance of apatite composition and single-grain ages when interpreting fission track data from plutonic rocks: a case study from the Coast Ranges, British Columbia. Earth and Planetary Science Letters 132, 213-224.

Osadetz, K.G., Kohn, B.P., Feinstein, S., O'Sullivan, P.B., 2002. Thermal history of Canadian Williston basin from apatite fission-track thermochronology—implications for petroleum systems and geodynamic history. Tectonophysics 349, 221-249.

Paton, C., Hellstrom, J., Paul, B., Woodhead, J., Hergt, J., 2011. Iolite: Freeware for the visualisation and processing of mass spectrometric data. Journal of Analytical Atomic Spectrometry 26, 2508-2518.

Payne, J.L., Barovich, K.M., and Hand, M., 2006, Provenance of Metasedimentary Rocks in the Northern Gawler Craton, Australia: Implications for Palaeoproterozoic Reconstructions. Precambrian Research 148, 275-91.

Payne, J.L., Ferris, G., Barovich, K.M., Hand, M., 2010. Pitfalls of classifying ancient magmatic suites with tectonic discrimination diagrams: An example from the Paleoproterozoic Tunkillia Suite, southern Australia. Precambrian Research 177, 227-240.

Payne, J.L., Hand, M., Barovich, K.M., Wade, B.P., 2008. Temporal constraints on the timing of high-grade metamorphism in the northern Gawler Craton: implications for assembly of the Australian Proterozoic. Australian Journal of Earth Sciences 55, 623-640.

Pearce, N.J.G., Perkins, W.T., Westgate, J.A., Gorton, M.P., Jackson, S.E., Neal, C.R., Chenery, S.P., 1997. A Compilation of New and Published Major and Trace Element Data for NIST SRM 610 and NIST SRM 612 Glass Reference Materials. Geostandards Newsletter 21, 115-144.

Rankin, L.R., Flint, R.B., Fanning, C.M., 1990. Palaeoproterozoic Nuyts Volcanics of the western Gawler craton, South Australia. Department of Primary Industries and Resources, Report Book 90/60, 17.

Rankin, L.R., Martin, A.R., Parker, A.J., 1989. Early Proterozoic history of the Karari Fault Zone, northwest Gawler Craton, South Australia. Australian Journal of Earth Sciences 36, 123-133.

Reddy, M., Glorie, S., Reid, A.J., Collins, A.S., 2015. Phanerozoic cooling history of the central Gawler Craton: implications of new low-temperature thermochronological data. MESA Journal 75, 56-60.

Reid, A.J., Fricke, C.E., Cowley, W.M., 2009. Extent of low-grade Archaean metavolcanics in the northeastern Gawler Craton: new evidence and definition of the Devils Playground Volcanics. MESA Journal 054, 009-019.

Reid, A.J., Jagodzinski, E.A., Fraser, G.L., Pawley, M.J., 2014. SHRIMP U–Pb zircon age constraints on the tectonics of the Neoarchean to early Paleoproterozoic transition within the Mulgathing Complex, Gawler Craton, South Australia. Precambrian Research 250, 27-49.

Reid, A.J. and Fabris, A., 2015, Influence of Preexisting Low Metamorphic Grade Sedimentary Successions on the Distribution of Iron Oxide Copper-Gold Mineralization in the Olympic Cu-Au Province, Gawler Craton. Economic Geology 110, 2147-57.

Skirrow, R.G., Bastrakov, E.N., Barovich, K., Fraser, G.L., Creaser, R.A., Fanning, C.M., Raymond, O.L., Davidson, G.J., 2007. Timing of Iron Oxide Cu-Au-(U) Hydrothermal Activity and Nd Isotope Constraints on Metal Sources in the Gawler Craton, South Australia. Economic Geology 102, 1441-1470.

Skirrow, R.G., Bastrakov, E.N., Davidson, G.J., Raymond, O.L., Heithersay, P., 2002. The geological framework, distribution and controls of Fe-oxide and related alteration, and Cu-Au mineralisation in the Gawler craton, South Australia. Part II: Alteration and mineralisation, in: Porter, T.M. (Ed.), Hydrothermal iron oxide copper-gold and related deposits: A global perspective, 2. Porter GeoConsultancy Publishing, Adelaide, pp. 33-47.

Speksnijder, A., 1985. Anatomy of a strike-slip fault controlled sedimentary basin, Permian of the Southern Pyrenees, Spain. Sedimentary Geology 44, 179-223.

Stewart, J.R., Betts, P.G., 2010. Implications for Proterozoic plate margin evolution from geophysical analysis and crustal-scale modeling within the western Gawler Craton, Australia. Tectonophysics 483, 151-177.

Stock, M.J., Humphreys, M.C.S., Smith, V.C., Johnson, R.D., Pyle, D.M., 2015. New constraints on electron-beam induced halogen migration in apatite. American Mineralogist 100, 281-293.

Stormer, J., Pierson, M.L., Tacker, R.C., 1993. Variation of F and Cl X-ray intensity due to anisotropic diffusion in apatite during electron microprobe analysis. American Mineralogist 78, 641-648.

Sutriyono, E., 1998. Cenozoic thermotectonic history of the Sunda–Asri basin, southeast Sumatra: new insights from apatite fission track thermochronology. Journal of Asian Earth Sciences 16, 485-500.

Swain, G.M., Hand, M., Teasdale, J., Rutherford, L., Clark, C., 2005. Age constraints on terrane-scale shear zones in the Gawler Craton, southern Australia. Precambrian Research 139, 164-180.

Teasdale, J., 1997. The interpretive geology and tectonothermal evolution of the western Gawler Craton, Ph.D. thesis, University of Adelaide. (Unpublished). 1–142.

Thomson, S.N., Gehrels, G.E., Ruiz, J., Buchwaldt, R., 2012. Routine low-damage apatite U-Pb dating using laser ablation–multicollector–ICPMS. Geochemistry, Geophysics, Geosystems 13.

Tingate, P.R., Duddy, I.R., 2002. The thermal history of the eastern Officer Basin (South Australia): evidence from apatite fission track analysis and organic maturity data. Tectonophysics 349, 251-275.

Tomkins, A.G., Dunlap, W.J., Mavrogenes, J.A., 2004. Geochronological constraints on the polymetamorphic evolution of the granulite-hosted Challenger gold deposit: implications for assembly of the northwest Gawler Craton*. Australian Journal of Earth Sciences 51, 1-14.

Tomkins, A.G., Mavrogenes, J.A., 2002. Mobilization of Gold as a Polymetallic Melt during Pelite Anatexis at the Challenger Deposit, South Australia: A Metamorphosed Archean Gold Deposit. Economic Geology 97, 1249-1271.

Vermeesch, P., 2009. RadialPlotter: a Java application for fission track, luminescence and other radial plots. Radiation Measurements 44, 409-410.

Wagner, G.A., van den Haute, P., 1992. Fission track dating. Kluwer.

Weisheit, A., Bons, P.D., Danisík, M., Elburg, M.A., 2014. Crustal-scale folding: Palaeozoic deformation of the Mt Painter Inlier, South Australia. Geological Society, London, Special Publications 394, 53-77.

Womer, M.B., Baker, R.N., J., N.E., van Nieuwenhuise, R., 1987. Technical evaluation of PEL 29, east Officer Basin, South Australia, for Amoco Australia Petroleum Co. South Australia. Department of Mines and Energy. Open File Envelope.

Wopfner, H., 1970. Permian paleogeography and depositional environment of the Arckaringa Basin, South Australia. , Second Gondwana symposium, Council for Scientific and Industrial Research, Scientia, South Africa, pp. 273-291.

Youngs, B.C., 1976. The geology and hydrocarbon potential of the Pedirka Basin. Govt. Pr., Adelaide.

Yugui, Y., 1993. Fault-controlled hydrocarbon distribution in the junggar basin, nw china. Journal of Petroleum Geology 16, 109-114.

Chapter 4

Constraining (hydro)thermal activity within the Willouran Ranges

(Prepared for publication)

Statement of Authorship

Title of Paper	Constraining (hydro)thermal activity within the Willouran Ranges, South Australia, through apatite double dating
Publication Status	☐ Published ☐ Accepted for Publication ☐ Submitted for Publication ☑ Unpublished and Unsubmitted work written in manuscript style
Publication Details	Hall, J.W., Glorie, S., Collins, A.S., and Reid, A.J., prepared for publication. Constraining (hydro)thermal activity within the Willouran Ranges, South Australia, through apatite double dating

Principal Author

Name of Principal Author (Candidate)	James Hall		
Contribution to the Paper	Sample collection, data collection, data interpretation, manuscript and figure composition.		
Overall percentage (%)	80 %		
Certification:	This paper reports on original research I conducted during the period of my Higher Degree by Research candidature and is not subject to any obligations or contractual agreements with a third party that would constrain its inclusion in this thesis. I am the primary author of this paper.		
Signature		Date	1/05/18

Co-Author Contributions

By signing the Statement of Authorship, each author certifies that:

i. the candidate's stated contribution to the publication is accurate (as detailed above);

ii. permission is granted for the candidate in include the publication in the thesis; and

iii. the sum of all co-author contributions is equal to 100% less the candidate's stated contribution.

Name of Co-Author	Stijn Glorie		
Contribution to the Paper	Assistance in data collection, assistance in data interpretation, manuscript review. 10% contribution.		
Signature		Date	1/05/18

Name of Co-Author	Alan Collins		
Contribution to the Paper	Assistance in data interpretation, manuscript review . 5% contribution.		
Signature		Date	27/06/18
Name of Co-Author	Anthony Reid		
Contribution to the Paper	Assistance in data interpretation, manuscript review . 5% contribution.		
Signature		Date	11/05/18

Abstract

Apatite thermochronology was applied to Neoproterozoic sedimentary samples from the Willouran Ranges to unravel their post-depositional thermal history. Apatite U-Pb (~550 – 350 °C) analysis reveals Proterozoic (~1100 Ma) detrital ages throughout the study area, with the exception of samples taken in close proximity to major fault zones, where consistent late Permian - early Triassic (~250 Ma) ages were obtained. Apatite fission track (~120 – 60 °C) data regionally reveals a mix between ~550 Ma and ~200 Ma age populations. Samples located closer to major fault zones record a single age population of ~100 Ma. The 550 Ma apatite fission track ages are interpreted to be mixing ages between a pre-depositional thermal event and a thermal response to the Cambrian Delamerian Orogeny. The presence of pre-Delamarian AFT ages suggests the region did not reach temperatures above the apatite partial annealing zone (>120 °C) during the ~500 Ma Delamerian Orogeny. The ~250 Ma apatite U-Pb ages and the ~200 Ma apatite fission track ages are interpreted to be caused by hydrothermal activity along the major fault zones. The ~100 Ma apatite fission track ages are interpreted to be caused by slow cooling following the ~250 Ma hydrothermal activity along the major fault zones. Evidence for hydrothermal alteration is present and witnessed in thin section analysis, with the presence of quartz veins, rutile veins, and sericite alteration and infill located in samples within close proximity to fault zones. It is suggested that this hydrothermal activity is correlated with the hydrothermal activity within the Mount Painter Inlier and forms part of a larger hydrothermal system.

4.1 Introduction

The timing and characteristics of hydrothermal activity has been well documented and has previously been linked to the formation and enrichment of mineral deposits (e.g. Clarke and Govett, 1990; Márton et al., 2010; Zhu et al., 2011). Within South Australia, Neoproterozoic - Phanerozoic hydrothermal activity has been documented in numerous locations, including the Mount Painter Inlier region (Fig. 4.1; Coats and Blissett, 1971; Foster et al., 1994; Brugger et al., 2011), Adelaide Rift Complex (Fig. 4.1; Preiss, 1993; Groves et al., 2003; Pollock et al., 2018), Peake and Denison Inliers (Fig. 4.1; Ambrose et al., 1981), and within the Olympic Dam deposit (Kamenetsky et al., 2016). Hydrothermal activity within the Mount Painter Inlier, Olympic Domain, and Adelaide Rift Complex have been associated with mineral deposits or enrichment (Preiss, 1993; Groves et al., 2003; Brugger et al., 2011; Hall et al., 2018b; Pollock et al., 2018). The Willouran Ranges (Fig. 4.1) are located at the intersection between these regions and represents a rather understudied region of the Adelaide Rift Complex that hosts poorly constrained hydrothermal Cu deposits (Benade et al., 1983). To date, the only post-depositional geochronological data collected in the region are metamorphic Monazite U-Pb ages collected by Mackay (2011), which predominately preserve ~500 Ma Delamerian Orogeny related ages. A single ~430 Ma Monazite U-Pb age is reported and interpreted to be related to hydrothermal activity recorded ~ 50 km to the southeast (Groves et al., 2003). Yet no correlation is made between this hydrothermal age and

the Cu deposits in the Willouran Ranges. As a result, the hydrothermal activity within the Willouran Ranges is poorly constrained. Moreover, this hydrothermal activity's correlation with other documented hydrothermal activity in the Adelaide Rift Complex, namely within the Mount Painter Inlier (Foster et al., 1994; Brugger et al., 2011; Elburg et al., 2013; Weisheit et al., 2014) is poorly understood.

This study applies apatite thermochronology, apatite U-Pb (Chew and Spikings, 2015) and apatite fission track dating (Wagner and van den Haute, 1992) to reveal the post-depositional thermal history and timing of hydrothermal activity within the Willouran Ranges. By combining the ~550 – 350 °C apatite U-Pb with the comparatively low temperature but complimentary ~120 – 60 °C apatite fission track dating, the entire thermal history can be constrained. The resulting thermochronometric data was subsequently modelled to reveal the thermal events that affected the study area.

4.2 Geological setting

4.2.1 Stratigraphy of the Adelaide Rift Complex

The Adelaide Rift Complex (ARC) is a Neoproterozoic – Cambrian rift complex located on the eastern margin of the Gawler Craton of South Australia (Fig. 4.1). Deposition of the Adelaide Rift Complex began on the Gawler Craton Margin at ~840 Ma as a result of an intra-cratonic rift during the break-up of Rodinia (Powell et al., 1994). The ARC is comprised of three supergroups; ~840 – 710 Ma Warrina, ~700 – 530 Ma Heysen, and ~530 – 515 Ma Moralana (Fig. 4.2; Preiss, 2000; Mahan et al., 2010). Deposition of the ARC began with the Warrina Supergroup which is divided into the older Callanna (7000m) and younger Burra (10400m) Groups (Preiss, 1993, 2000). The ~700 – 500 Ma Heysen Supergroup unconformably overlies the Burra Group and is divided into the Umberatana (9000m) and Wilpena groups (6000m) (Preiss, 1982, 1993, 2000). Finally, the uppermost sediments of the Moralana Supergroup unconformably overlie the region (Preiss, 1982).

4.1.1 Phanerozoic tectonics and hydrothermal activity

The deposition of the ARC was ceased by the onset of the subduction related Cambro-Ordovician Delamerian Orogeny (515 - 490 Ma; Foden et al., 2006). This orogenic event uplifted and deformed the sedimentary packages of the ARC and formed the major structures within the Willouran Ranges (Fig. 4.3). The Delamerian Orogeny not only affected the ARC, but also the central Gawler Craton, Olympic Domain (Reddy et al., 2015; Hall et al., 2016) and Officer Basin (Tingate and Duddy, 2002). As the subduction zone along the proto-eastern margin of Australia moved east, the deformation continued to the east with the 490 – 440 Ma Benambran Orogeny, 430 – 380 Ma Tabberabberan Orogeny, and the 380 – 320 Ma Kanimblan Orogeny of the Lachlan Orogen and the 265 – 230 Ma Hunter-Bowen of the New England Orogen (Glen, 2005).

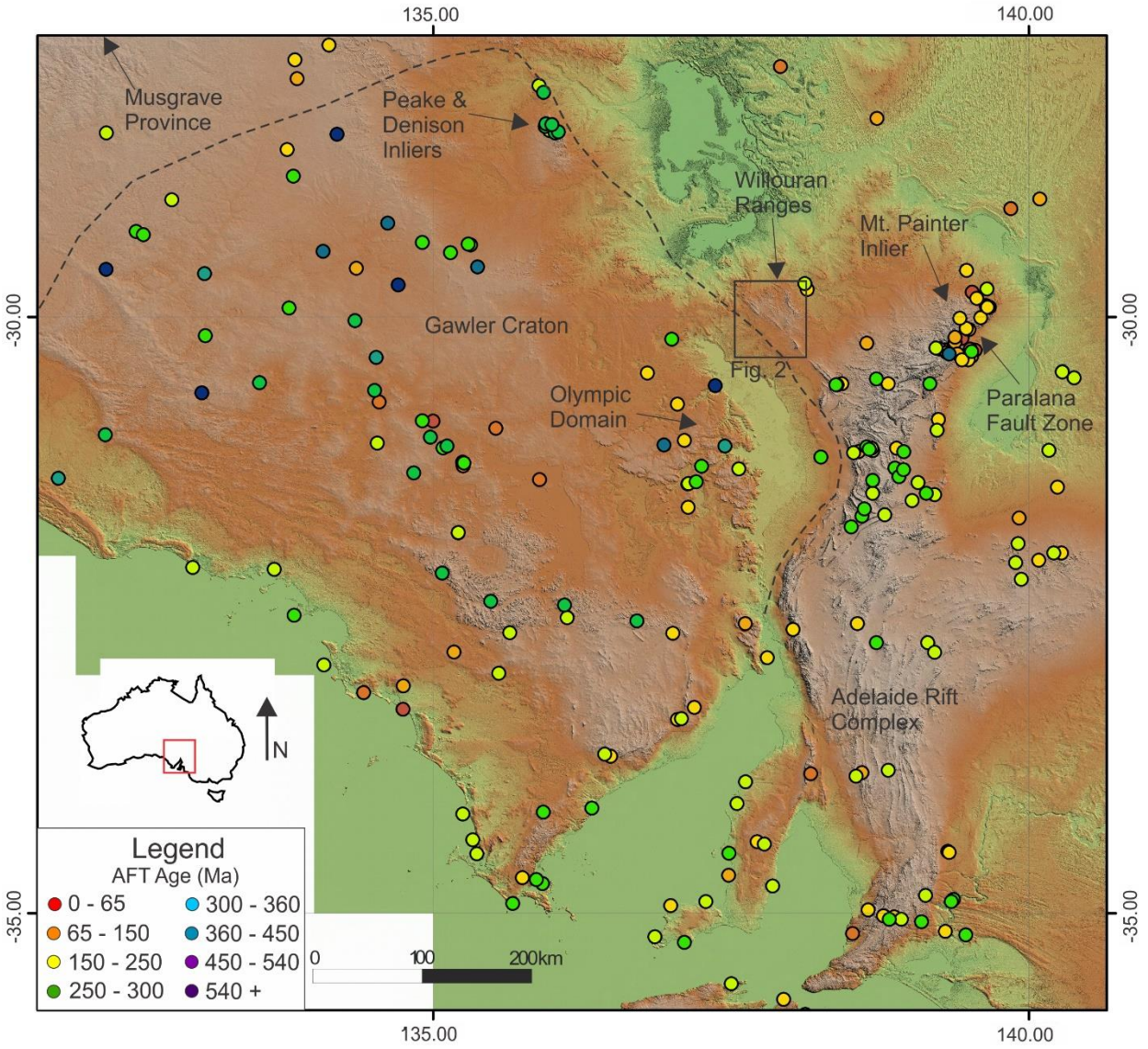

Figure 4.1: Digital elevation model of South Australia, indicating the locations of major geological domains and apatite fission track data for South Australia (Foster et al., 1994; Gibson and Stüwe, 2000; Gleadow et al., 2002; Mitchell et al., 2002; Tingate and Duddy, 2002; Weisheit et al., 2014; Reddy et al., 2015; Boone et al., 2016; Hall et al., 2016; Glorie et al., 2017a; Hall et al., 2018b).

To the north, the 450 – 300 Ma Alice Springs Orogeny deformed much of central and south Australia (Fig. 4.1; Bradshaw and Evans, 1988; Mawby et al., 1999; Ballèvre et al., 2000; Haines et al., 2001; Buick et al., 2008). Deformation relating to this orogenic event is recorded within the ARC in the Mt. Painter Inlier (McLaren et al., 2002; Weisheit et al., 2014), and the Mt. Lofty Ranges (Gibson and Stüwe, 2000). Further afield, it is also recorded within the northern Gawler Craton (Reddy et al., 2015; Boone et al., 2016; Hall et al., 2016; Hall et al., 2018b).

From ~320 Ma to present, there has been prevalent hydrothermal activity within the Mount Painter Inlier and Paralana Fault Zone (Foster et al., 1994; Weisheit et al., 2014). This began with the Mount Gee sinter formation by near-surface boiling of 140 – 100 °C fluids (Bakker and Elburg, 2006). It was originally suggested that all the hydrothermal activity from ~290 Ma to present was part of the same long-lived hydrothermal system (Bakker and Elburg, 2006; Brugger et al., 2011). However, more recent work suggests that the pre and post-Permian hydrothermal activity are two separate events (Elburg et al., 2013; Weisheit et al., 2013).

Sample	Latitude	Longitude	Formation	Rock type	Formation age	Apatite U/Pb age	AFT age population 1:	AFT age population 2:
WR 16	-29.9610833°	137.69925°	Tapley Hill Formation	Fine sandstone	~680 Ma	-	533±114 Ma	201±35 Ma
WR 17	-29.9868888°	137.6913056°	Amberoona Formation	Fine sandstone	~680 Ma	-	568±121 Ma	215±25 Ma
WR 24	-29.9290555°	137.74075°	Coorana Formation	sandstone	~800 Ma	250.9±7.4 Ma	106±11 Ma	-
WR 25	-29.9204444°	137.7496944°	Skillogalee Dolomite	sandstone	~800 Ma	-	328±26 Ma	102±15 Ma
WR 26	-29.9123611°	137.7545°	Skillogalee Dolomite	Interbedded sandstone	~800 Ma	1115±15 Ma	280±23 Ma	-
WR 29	-29.8580833°	137.8113611°	Skillogalee Dolomite	Immature sandstone	~800 Ma	-	333±19 Ma	134±14 Ma
WR 34	-29.8595°	137.9033889°	Myrtle Springs Formation	sandstone	~800 Ma	279.3±4.5 Ma	137±12 Ma	-
WR 37	-29.8533055°	137.9506111°	Top Mount Sandstone	sandstone	~800 Ma	-	-	-
WR 38	-29.9693055°	137.9548333°	Myrtle Springs Formation	Dirty sandstone	~800 Ma	238.1±5.5 Ma	101.1±8.1 Ma	-

Table 4.1: Sample details. Formation ages are from Mahan et al. (2010), and Drexel (2009).

4.1.1 Domain sub-division

The Willouran Ranges is sub-divided into ten domains and two sub-domains that are separated by major fault zones (Fig. 4.3; Mackay, 2011). The western-most domain is the West Mount Domain which is separated from the Berlina Domain by the Norwest Fault. The Norwest Fault encompasses the Rocky Point, and Track Sub-Domains, in addition to the Stony Range Domain. The eastern margin of the Berlina Domain is truncated by the Bungarider Fault, a fault that encompasses the Rischbeith Domain. To the east of the Bungarider Fault is the Kingston Domain, the largest domain in the Willouran Ranges. The eastern-most fault zone in the Willouran Ranges is the West Willouran Fault which separates the Kingston Domain from the Trial Hole Domain. There are numerous mineral deposits located along the West Willouran Fault, including the West Willouran Mine (Fig. 4.3). The northest of the Willouran Ranges is comprised of the Euraminna and Euchre Pack Domains while the south is comprised of the South Hill, Witchelina and Delusion Hill Domains.

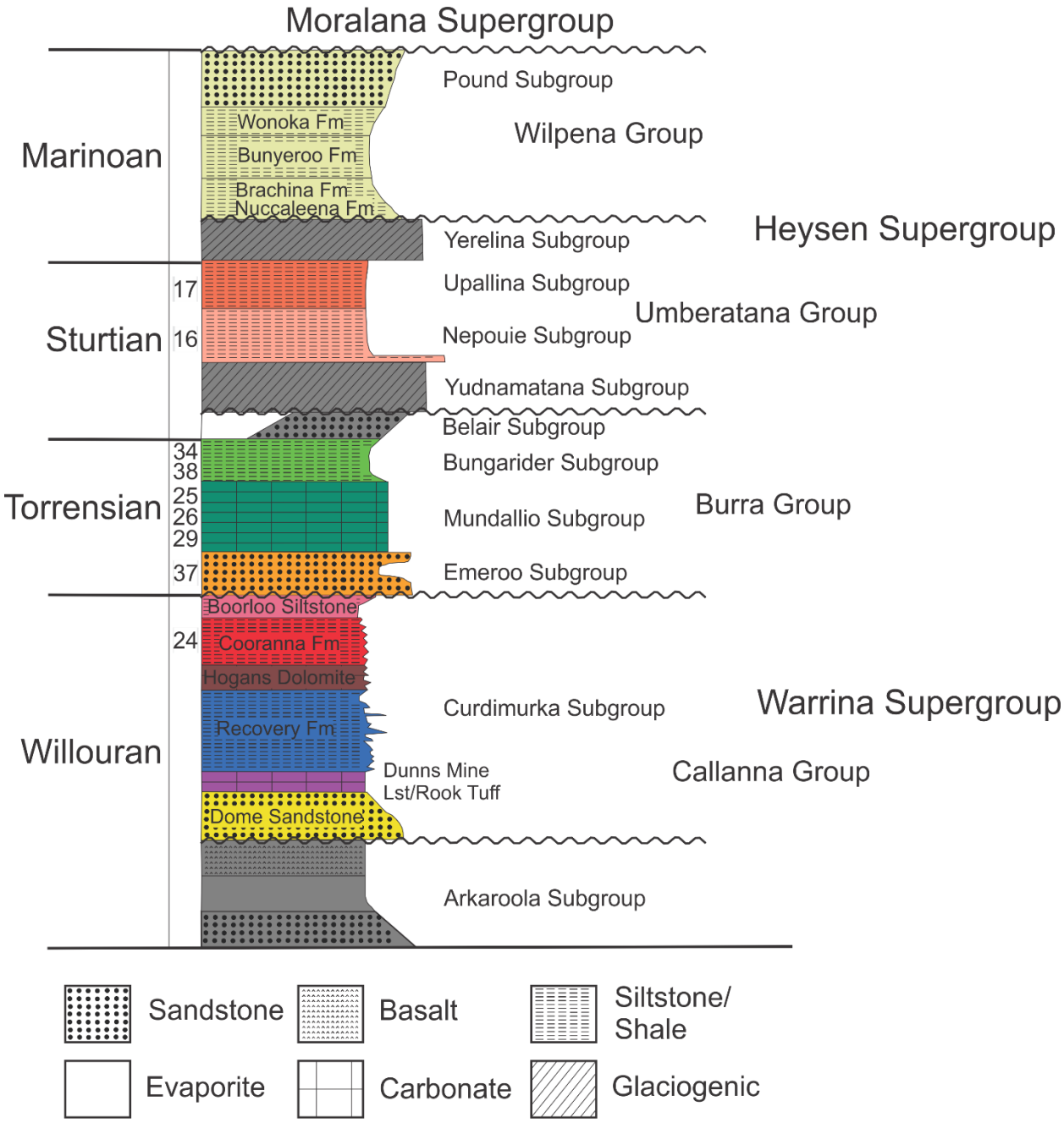

Figure 4.2: Simplified stratigraphic log for the Willouran Ranges indicating the lithologies that samples were taken from, as indicated by the numbers, adapted from Mackay (2011).

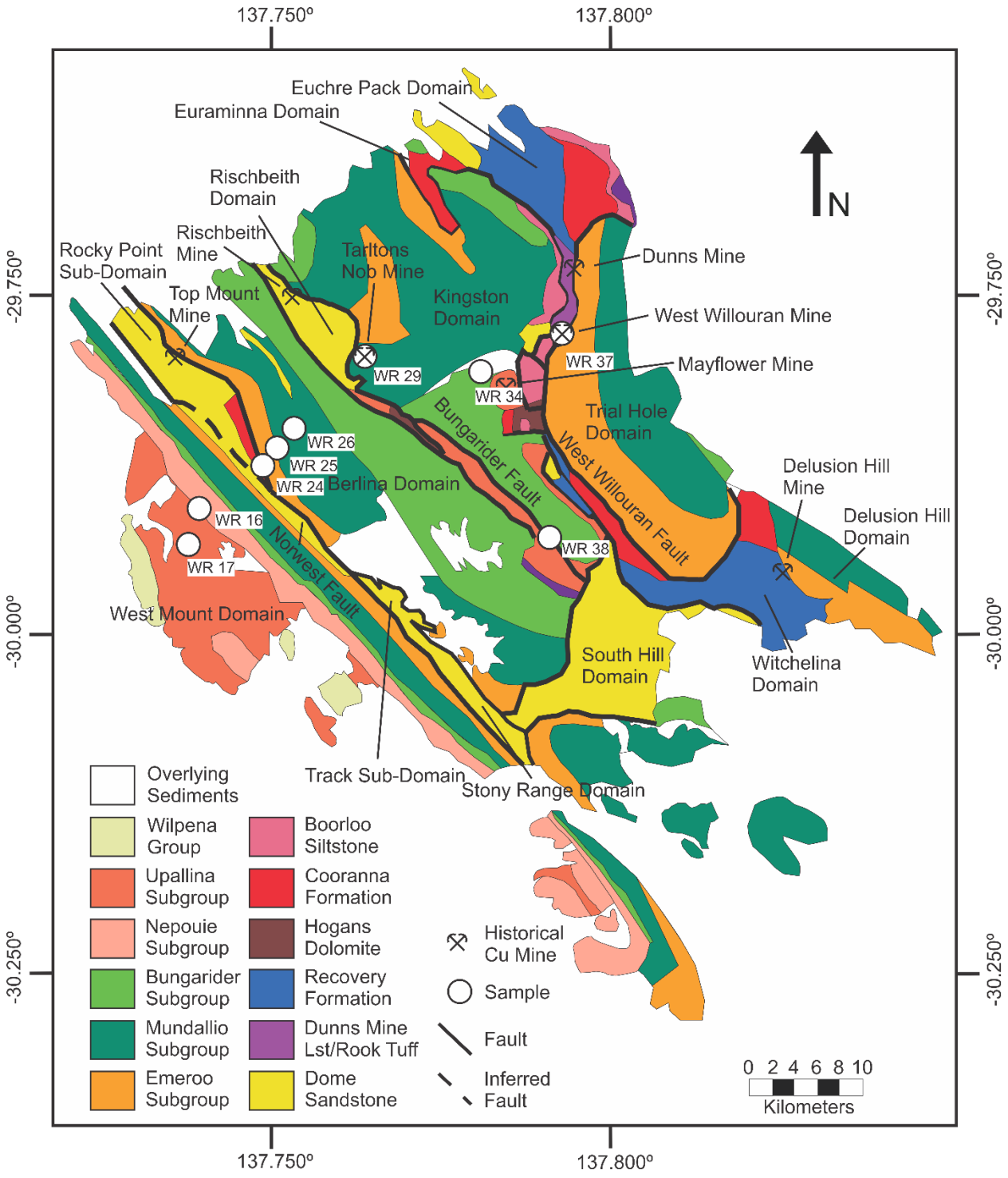

Figure 4.3: Simplified geological map of the Willouran Ranges showing all sample locations, domains, and major fault zones. Adapted from Mackay (2011).

4.2 Methodology

4.2.1 Apatite fission track analysis

The samples were collected along east-west transects with the intention of analysing the differential cooling across the major fault zones in the region. In addition, samples were preferentially collected near the ore deposits in the region.

Samples were crushed and separated using conventional techniques. Apatite separates were collected, mounted in Epoxy resin before being ground and polished to reveal internal surfaces. The apatites were subsequently etched in 5 M HNO3 at 20 °C for 20 seconds to reveal the fission tracks. Imaging and counting was conducted using an Autoscan system on a Zeiss AX10 microscope (Gleadow et al., 2009). Uranium, lead, thorium, and chlorine concentrations were collected on a New Wave UP 213 Laser-Ablation Inductively-Coupled-Plasma Agilent 7900 quadrupole Mass-Spectrometer (LA-ICP-MS). Madagascar apatite was used as a primary standard (Thomson et al., 2012) with Durango used as a secondary standard, which produced an age of 31.5 ± 1.1 Ma from 37 grains. This correlates well with the published age of 31.44 ± 0.18 Ma (McDowell et al., 2005). Data reduction was completed offline in Iolite (Paton et al., 2011). The AFT central ages (Galbraith and Laslett, 1993; Galbraith et al., 1999) were produced using Radial Plotter (Vermeesch, 2009). Samples which fail the P(X2) test (<0.005) and contain large internal dispersions (>25%) were separated into multiple age populations with the use of Radial Plotter's automatic mixing model. Samples which contained sufficient confined track lengths and AFT ages were modelled in QT-qt (Gallagher, 2012) to produce time-temperature models. More details on the procedures can be found in Glorie et al. (2017b) and Gillespie et al. (2017).

4.2.2 Apatite U-Pb analysis

Apatite U-Pb analysis was conducted synchronously on the same samples along with apatite fission track analysis. Uranium and lead concentrations were collected on a LA-ICP-MS with data reduction completed in iolite (Paton et al., 2011). Madagascar apatite was used as a primary standard (Thomson et al., 2012) with Mount McClure (Thomson et al., 2012) and Durango (McDowell et al., 2005) used as secondary standards. Mount McClure apatite was measured at 515 ± 10 Ma which is within error of the published age of 523.51 ± 2.07 Ma (Thomson et al., 2012). Durango is measured at 33.0 ± 1.6 Ma which is also within error of the published age of 31.44 ± 0.18 Ma (McDowell et al., 2005). Weighted mean and concordia plots were created using Isoplot (Ludwig, 2012). Details on the procedure can be found in Glorie et al. (2017b) and Hall et al. (2018a).

4.2.3 Time-temperature models

Applicable samples with sufficient AFT ages, D_{par} kinematics (Donelick et al., 1999), and length data were compiled into *QTqt* (Gallagher, 2012) to produce time-temperature models. All samples were constrained at near surface temperatures during the Neoproterozoic and samples with apatite U-Pb ages were added as box constraints.

4.3 Results

4.3.1 West Mount Domain

Sample WR 17 is a fine grained sandstone from the Amberoona Formation of the Upallina Subgroup (Table 4.1). This sample is dominated by laminations with no fractures or alteration present (Fig. 4.4b). An AFT central age of 319 ± 26 Ma with a dispersion of 55 % and a P(X2) of 0.00 was obtained for WR 17 from 56 grains (Fig. 4.5). This sample preserves mixed AFT ages centred around two end-member age populations of 215 ± 25 Ma and 568 ± 121 Ma. A total of 52 confined tracks were measured with an average length of 10.80 µm and a standard deviation of 1.69 µm (Fig. 4.5). This indicates this sample underwent prolonged residence within the APAZ. The associated length histogram revealed slight bi-modality. Proterozoic detrital apatite U-Pb ages ranging from ~2000 – 1000 Ma are preserved within this sample (Fig. 4.6). The late Mesoproterozoic apatite U-Pb ages correlate well with the detrital zircon U-Pb ages reported by Lloyd et al., (in prep.) for the same sample.

Similarly to WR 17, Sample WR 16 is a fine grained sandstone from the ~680 Ma Tapley Hill Formation from the Nepouie Subgroup. Thin section petrographic analysis reveals the sample is well laminated with minor unfilled fractures and contains no evidence of alteration (Fig 4a). A total of five grains were measured with an AFT central age of 306 ± 72 Ma (43 % dispersion, P(X2) = 0.01; Fig. 4.5; Table 4.2). Two age populations are noted within this sample, three grains in a line at 201 ± 35 Ma and two grains centred around 533 ± 114 Ma. These ages correlate well with the ages from WR 17. There were insufficient confined track lengths to produce a reliable length distribution model. Apatite U-Pb analysis indicates this sample preserved Proterozoic detrital ages at ~2000 Ma and ~1100 Ma (Fig. 4.6).

4.3.2 Rocky Point Sub-Domain and Berlina Domain

A quartz dominated medium sandstone sample collected from the ~800 Ma Skillogalee Dolomite, sample WR 25, preserved fractures with sericite infill (Fig. 4.4e). An AFT central age of 249 ± 56 Ma from 11 grains (dispersions = 69%, P(X2) = 0.00) was recorded in this sample. Due to high dispersion, this sample has been separated into two age populations of 102 ± 15 Ma and 328 ± 26 Ma (Fig. 4.5). There were insufficient confined track lengths preserved in the sample to produce a reliable length distribution model. The apatite U-Pb data preserve two age populations, with an older age of 1059 ± 110 Ma (MSWD = 3.5, n = 4) and a younger age of 209 ± 30 Ma (MSWD =

3.8, n = 7; Fig. 4.6). The older apatite U-Pb age population correlates well with the youngest detrital zircon U-Pb age population reported by Lloyd et al., (in prep.) for this sample.

An interbedded shale and sandstone, Sample WR 26, was collected from the Skillogalee Dolomite. A prominent quartz vein is present within the analysed thin section (Fig. 4.4g). The 21 apatite grains that were analysed recorded a central age of 280 ± 23 Ma (dispersion of 32 % and a P(X2) of 0.00; Fig. 4.5). A total of 55 confined tracks were measured, at an average length of 11.5 µm, and a standard deviation of 2.01 µm. The associated length histogram reveals a unimodal curve (Fig. 4.5). The apatite U-Pb data preserve Proterozoic detrital ages with a clear isochron lower intercept of 1097 ± 23 Ma (MSWD = 2.3; Fig. 4.6). This lower intercept produced a ^{207}Pb corrected weighted mean ^{206}Pb-^{238}U age of 1115 ± 15 Ma with a MSWD of 1.6. This age is not well preserved in the detrital zircon U-Pb for this sample (Lloyd et al., in prep.). However, this age is preserved between two major zircon populations at ~1000 Ma and ~1200 Ma.

Sample WR 24 is a quartz dominated medium sandstone that was collected from the ~800 Ma Coorana Formation. This sample preserves evidence for hydrothermal activity with the presence of sericite infilling a fractured quartz (Fig. 4.4c). Sample WR 24 produced an AFT central age of 106 ± 11 Ma with a dispersion of 0 % and a P(X2) of 0.85 from 4 grains (Fig. 4.5). This age correlates well with the younger AFT age from WR 25. There were insufficient confined tracks lengths to produce a length histogram. Apatite U-Pb analysis preserves a lower intercept age of 255 ± 33 Ma (MSWD = 1.4) from 4 grains (Fig. 4.6; Table 4.3). The associated ^{207}Pb corrected weighted mean ^{206}Pb-^{238}U age is preserved at 250.9 ± 7.4 Ma with a MSWD of 1.01.

4.4.3 Kingston and Trial Hole domains

Sample WR 29 was collected from an immature, sandstone from the Skillogalee Dolomite located near Tarltons Nob Cu mine. Fracturing is present within the thin section (Fig. 4.4i). An AFT central age of 268 ± 30 Ma with a dispersion of 46 % and a P(X2) of 0.00 (from 22 grains) was produced from WR 29. Two age populations were calculated at 134 ± 14 Ma and 333 ± 19 Ma (Fig. 4.5). A reliable length distribution model was unable to be produced. There is partial preservation of a younger apatite U-Pb population of 280 ± 21 Ma with an MSWD of 1.1. All other apatite U-Pb ages preserve Proterozoic detrital ages (Fig. 4.6) that correlate well with the detrital zircon U-Pb ages reported by Lloyd et al., (in prep.) for this sample. The ~280 Ma apatite U-Pb age is absent within the zircon U-Pb data.

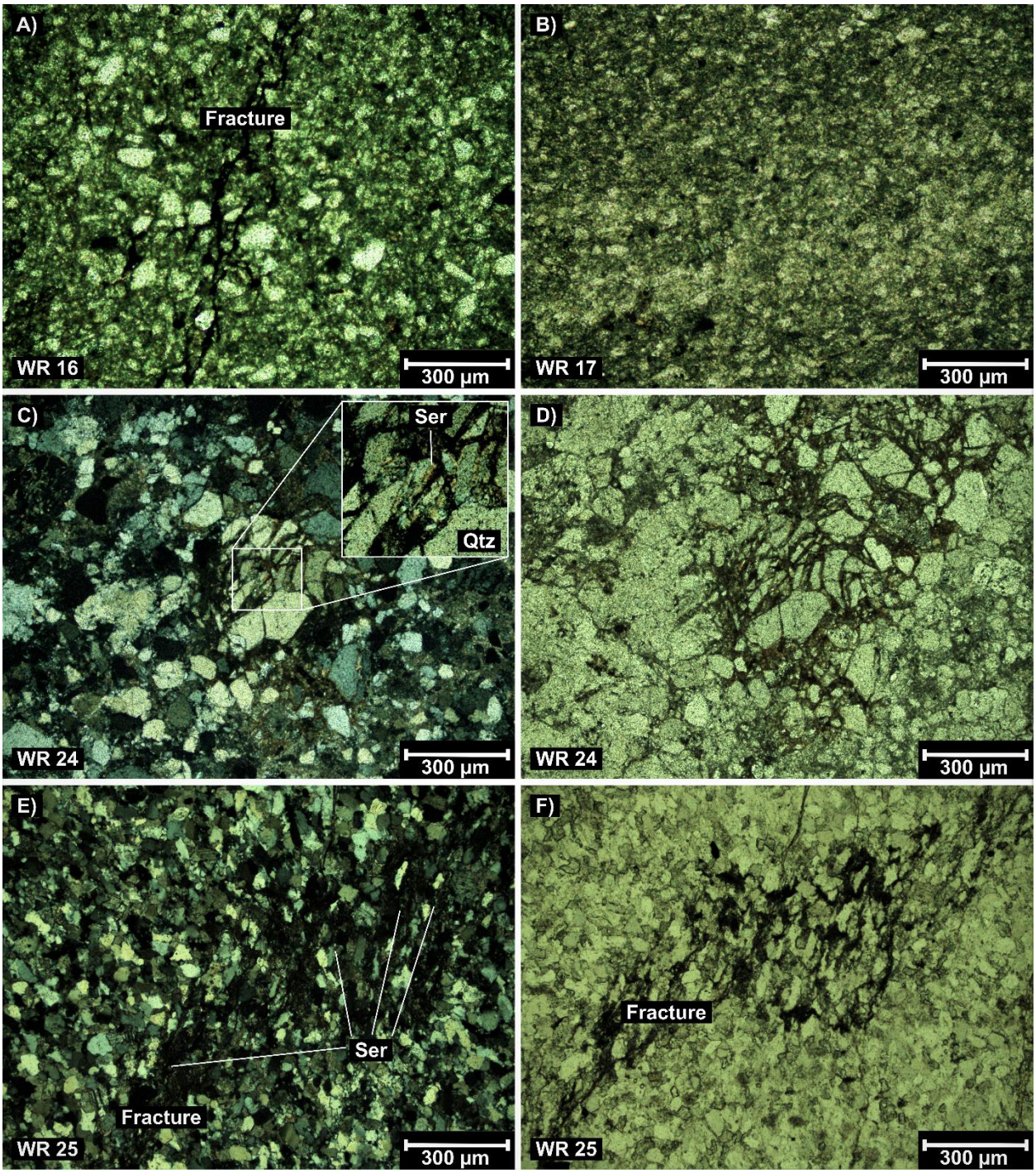

Figure 4.4: Cross-polarised (a, b, c, e, g, i, k, m, o, q) and plane-polarised (d, f, h, j, l, n, p, r) light images for all thin section samples. Abbreviations: Ser; sericite, Qtz; quartz, Rut; rutile.

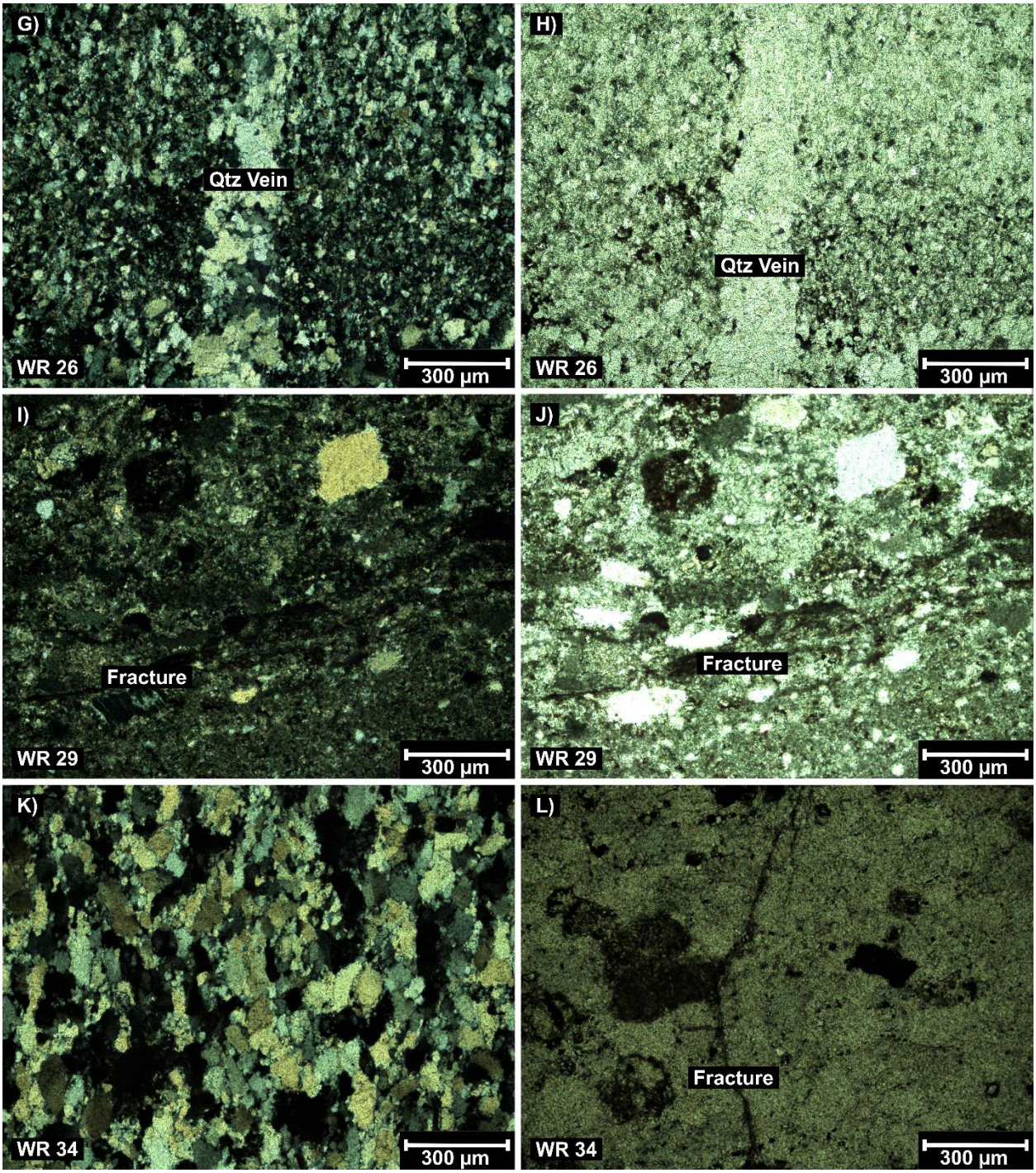

Figure 4.4: Continued.

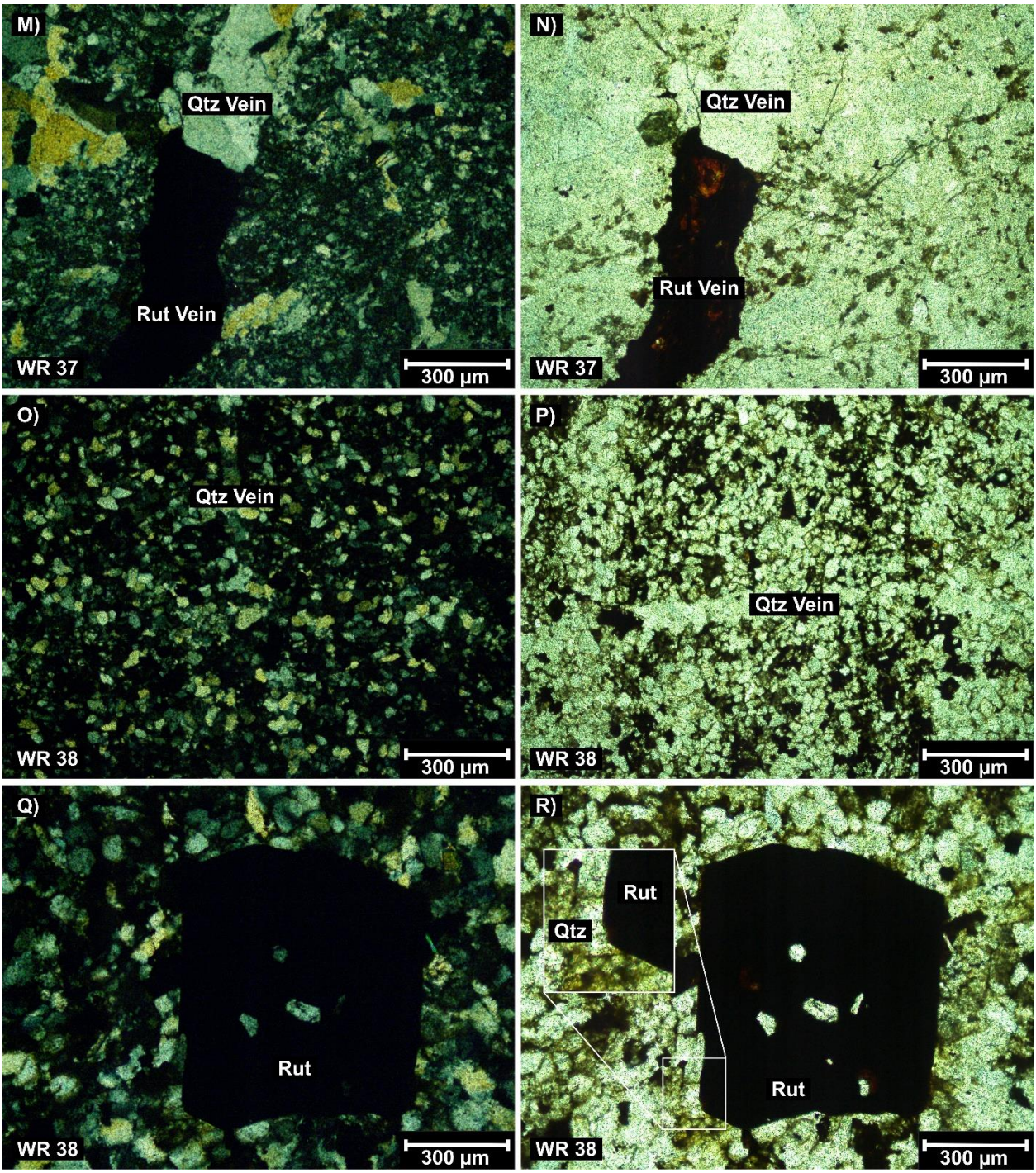

Figure 4.4: Continued.

Sample	ρ_s	Ns	N	^{238}U	Central age	Lower age	Upper Age	l_m	n	σc	D_{par} (µm)
WR 16	1.6 (0.5)	60	5	10.9 (0.66)	306±72 Ma	201±35 Ma	533±114 Ma	-	-	-	-
WR 17	3.29 (2.7)	1407	56	25.3 (1.8)	319±26 Ma	215±25 Ma	568±121 Ma	10.8	52	1.69	1.37 (0.35)
WR 24	1.62 (0.26)	96	4	30.9 (1.6)	106±11 Ma	-	-	-	-	-	-
WR 25	1.92 (1.41)	220	11	18.75 (0.83)	249±56 Ma	102±15 Ma	328±26 Ma	-	-	-	-
WR 26	3.36 (3)	823	21	28.5 (1.43)	280±23 Ma	-	-	11.5	55	2.01	1.4 (0.52)
WR 29	2.64 (2.7)	438	22	20.41 (0.9)	268±30 Ma	134±14 Ma	333±19 Ma	-	-	-	-
WR 34	4.03 (1.45)	369	12	57.77 (6.05)	137±12 Ma	-	-	-	-	-	-
WR 38	1.58 (1.36)	562	24	33.3 (2.21)	101.1±8.1 Ma	-	-	-	-	-	-

Table 4.2: Apatite fission track (AFT) details for all samples. ρ_s is counted AFT density in 10^5 tracks/cm^2 (standard deviation in brackets), Ns is number of fission tracks counted, N is number of counted grains, ^{238}U is concentration of ^{238}U (standard deviation in brackets), Central age is the apatite fission track central age in Ma, lower and upper age are all AFT age populations of their respected samples, l_m is average confined AFT length, n is number of confined tracks counted, σc is standard deviation of the confined tracks, D_{par} is the average D_{par} for each sample (standard deviation in brackets).

Sample	n	Concordia Intercept	MSWD	$^{207}Pb/^{206}Pb$ intercept	^{207}Pb corrected ^{206}Pb-^{238}U age	MSWD	Probability
WR 16	*5*	-	-	-	-	-	-
WR 17	*51*	-	-	-	-	-	-
WR 24	*4*	*255±30 Ma*	1.3	*0.837*	*250.9±7.4 Ma*	*1.01*	0.4
WR 25	*11*	*1059±110 Ma* *209±30 Ma*	3.5 *3.8*	-	-	-	-
WR 26	21	1097*±23 Ma*	*2.4*	*0.821*	*1115±15 Ma*	*1.6*	0.054
WR 29	22	280*±21 Ma*	*1.1*	-	-	-	-
WR 34	*14*	*275±12 Ma*	*2*	*0.793*	*279.3±4.5 Ma*	*1.5*	0.1
WR 38	*22*	*257±12 Ma*	*2.9*	*0.856*	*238.1±5.5 Ma*	*1.9*	0.014

Table 4.3: Apatite U/Pb data.

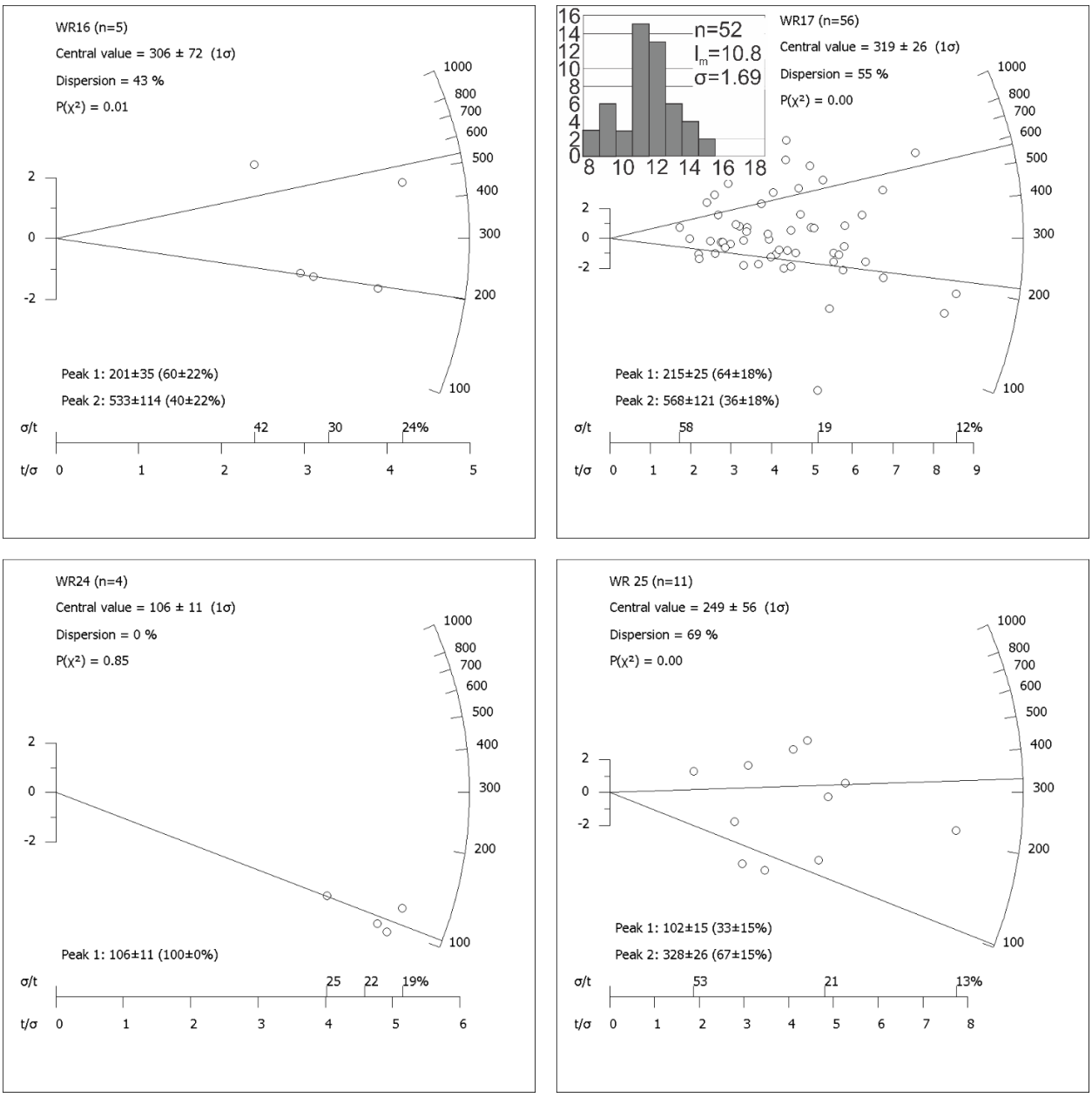

Figure 4.5: Radial plots of apatite fission track (AFT) data from samples WR 16, WR 17, WR 24, WR 25, WR 26, WR 29, WR 34, and WR38. 'n' indicates the number of grains measured, the central age indicates the calculated central age, 'dispersion' indicates the percentage of age dispersion within the sample, when multiple populations of ages are present, the Automatic Mixture model of *Radial Plotter* splits the central age into age populations. All ages acquired from radial plots are presented in Table 4.2. All radial plots were constructed using *Radial Plotter* (Vermeesch, 2009). Confined track length histogram are inset into applicable radial plots. Where, AFT length is in µm, n indicates the number of tracks measured, l_m is average track length, and σ is the standard deviation of the sample.

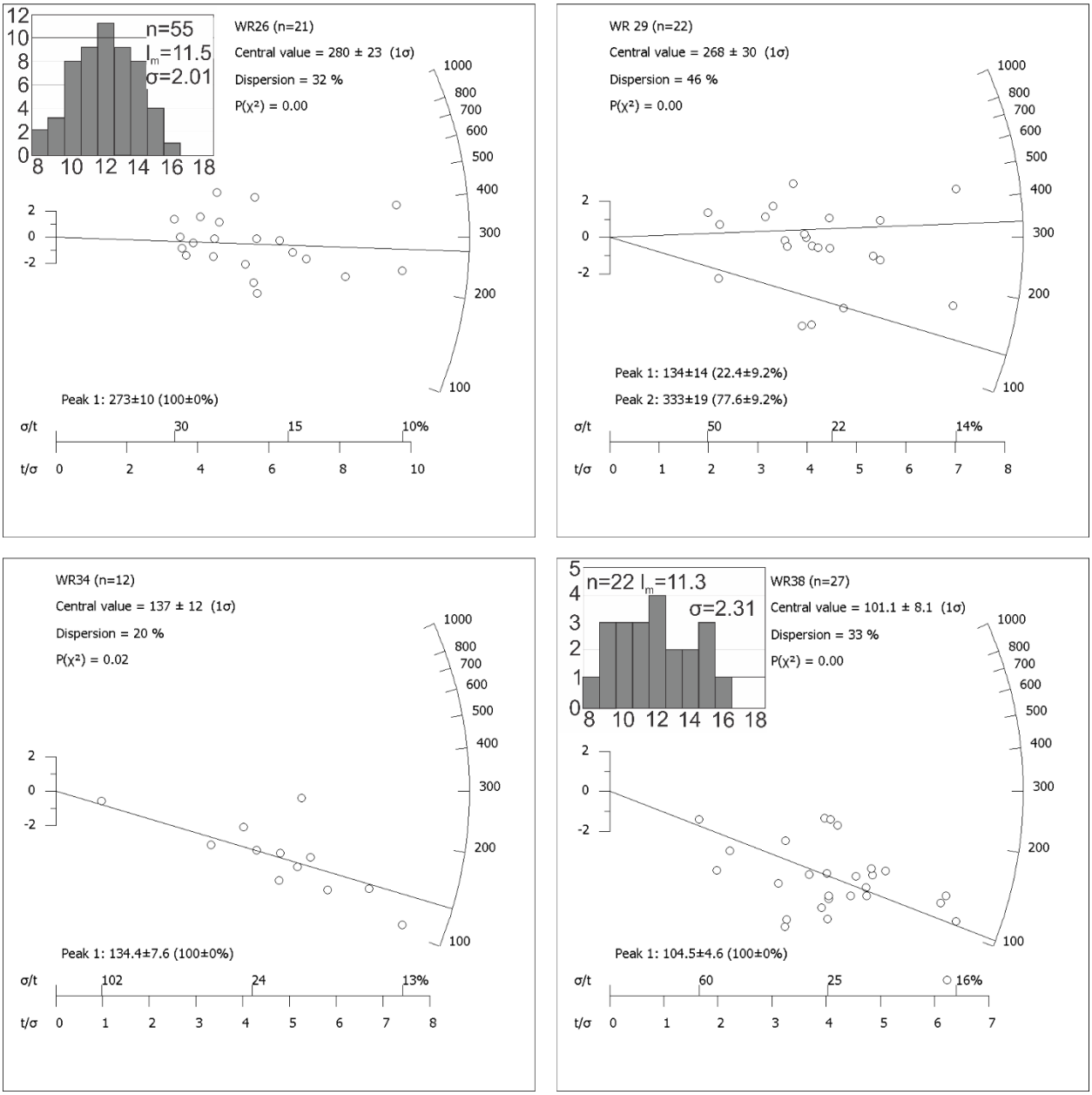

Figure 4.5: Continued.

A clean medium sandstone, sample WR 34, was collected from the ~800 Ma Myrtle Springs Formation (Table 4.1). The thin sections preserve minor fractures without infill (Fig. 4.4l). A total of 12 grains were measured for sample WR 34. From that, a central AFT age of 137 ± 12 Ma (dispersion = 20 %, P(X2) = 0.02) was calculated (Fig. 4.5). A length histogram was unable to be produced for this sample. This sample preserved a ^{207}Pb corrected weighted mean ^{206}Pb-^{238}U age 279.3 ± 4.5 Ma with a MSWD of 1.5. The accompanying Tera-Wasserburg plot revealed an isochron with lower intercept of 275 ± 12 Ma with an MSWD of 2 (Fig 4.6).

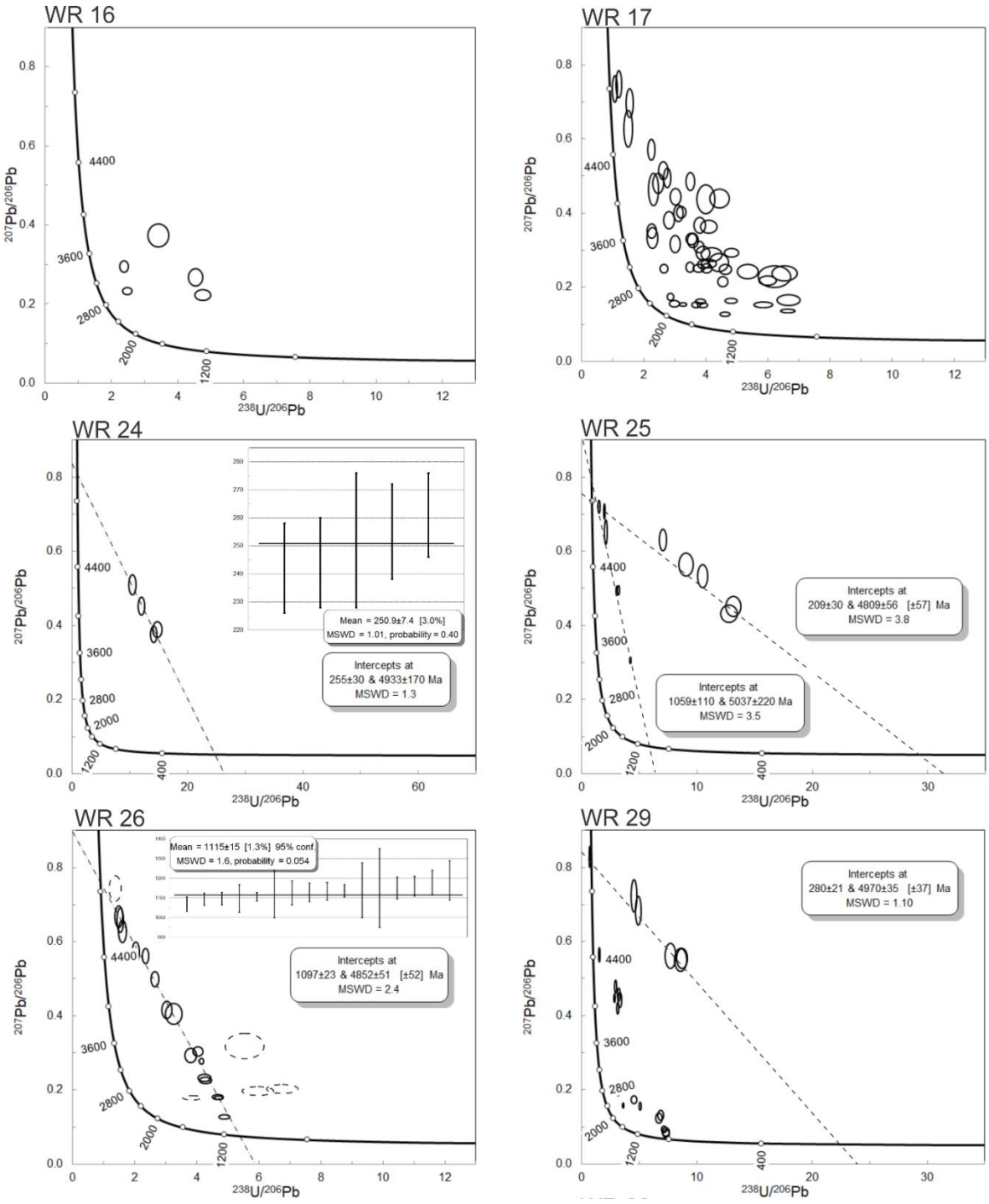

Figure 4.6: Tera-Wasserburg concordia plots and associated ^{207}Pb corrected weighted mean ^{206}Pb-^{238}U age plots for samples WR 16, WR 17, WR 24, WR 25, WR 26, WR 29, WR 34, and WR38. Tera-Wasserburg plots that contain dashed data-symbols indicate these analyses were not included the ^{207}Pb corrected ^{206}Pb-^{238}U weighted mean plot as they were detrital outliers, in the case of WR 26, or found to only hold information on the common Pb line but little accurate information in the weighted mean plots, in the case of WR 38.

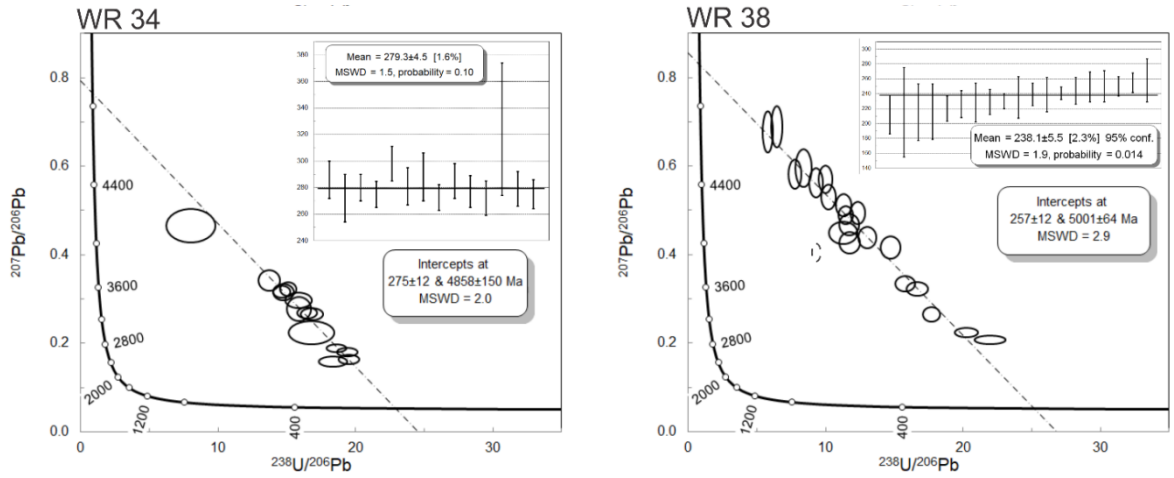

Figure 4.6: Continued.

Sample WR 37 was collected from the ~800 Ma Top Mount Sandstone within the Emeroo Subgroup of the Burra group. This sample was located at the West Willouran Cu Mine (Fig 4.3) and preserves quartz and rutile veins, hydrothermally disseminated quartz, and fractures (Fig. 4.4m; Fig. 4.4n). No apatite was present in this sample.

A lithic sandstone collected from the Myrtle Springs Formation, WR 38, revealed quartz veins (Fig. 4.4o; Fig. 4.4p), and rutile overprinting and truncating detrital quartz (Fig 4r). This sample produced a central age of 101.1 ± 8.1 Ma with a dispersion of 33 % and a P(X2) of 0.00 (from 27 grains; Fig. 4.5). This sample preserved 22 measurable confined tracks, with an average of 11.3 µm and a standard deviation of 2.31 µm. In addition, this sample recorded a common Pb line lower intercept of 257 ± 12 Ma with a MSWD of 2.9. The associated ^{207}Pb corrected ^{206}Pb-^{238}U weighted mean produced an age of 238.1 ± 5.5 Ma with an MSWD of 1.9 from 18 grains (Fig. 4.6).

Overall, samples from the West Mount Domain (samples WR 16 and WR 17) preserve AFT ages during the Ediacaran, and Triassic. Across the Norwest Fault, samples from the Rocky Point Sub-Domain and Berlina Domain preserve Carboniferous – Permian and Cretaceous AFT age populations. Sample WR 25 preserves both Carboniferous and Cretaceous AFT age populations, Sample WR 26 only preserves a Permian AFT age while WR 24 only preserves a Cretaceous AFT age. These Carboniferous and Cretaceous AFT age populations are also preserved in samples from the Kingston and Trial Hole domains. Sample WR 29 mimics WR 25 with Carboniferous and Cretaceous AFT age populations while WR 34 and WR 38 only preserve Cretaceous AFT ages. These age trends are also preserved in apatite U-Pb data where samples from the West Mount Domain preserve detrital Proterozoic ages while samples WR 24 (Rocky Point Sub-Domain), WR 34 and WR 38 (Kingston Domain) preserve Permo-Triassic ^{207}Pb corrected weighted mean ^{206}Pb-

^{238}U ages. Samples WR 25 (Berlina Domain) and WR 29 (Kingston Domain) preserve mixed apatite U-Pb ages, with a Permo-Triassic lower intercept age and a Proterozoic detrital component. WR 26 is the only sample east of the Norwest Fault to solely preserve a detrital Proterozoic apatite U-Pb age, with a ^{207}Pb corrected weighted mean ^{206}Pb-^{238}U age of 1115 ± 15 Ma.

4.4.4 Time-temperature models

Three samples, WR 17, WR 26, and WR 38, were modelled using *QTqt* (Fig. 4.7; Gallagher, 2012). Sample WR 17 preserves slow cooling from ~750 Ma to ~100 Ma, at which point the model cools out of the APAZ (~60 °C). Samples WR 26 and WR 38 preserve heating during the Neoproterozoic following deposition. The main period of cooling for WR 26 is recorded during the Carboniferous where the model cools to the upper APAZ (~70 °C) before cooling out of the APAZ at ~100 Ma. The model for WR 38 continues heating to ~150 °C at ~250 Ma due to the presence of apatite U-Pb data for this sample. At ~250 Ma, the sample cools back through the APAZ and cools out of the APAZ at ~ 70 Ma.

4.5 Discussion

4.5.1 Regional cooling

Samples from the West Mount Domain preserve Neoproterozoic detrital apatite U-Pb spectra (Fig. 4.6) which indicates this region doesn`t record significant heating to reset the apatite U-Pb ages (Fig. 4.7). Similarly, WR 26 within the Berlina Domain also preserves Neoproterozoic spectra with an apatite U-Pb age of 1091 ± 45 Ma.

Apatite fission track data from the West Mount Domain record a mixing of thermal ages between ~ 550 Ma and ~200 Ma. The poorly constrained ~550 Ma ages indicate that the West Mount Domain partially preserves Delamerian Orogeny. The time-temperature model for sample WR 17 suggests the West Mount Domain didn't reach temperatures hotter than 120 °C (Fig. 4.7). However, the slight bimodal length frequency histogram for this sample suggests there may have been two cooling periods. WR 26 also preserves a mixed age between 500 Ma and 200 Ma. The region remained within the APAZ until at least ~200 Ma, with the model for WR 26 suggesting that the period of greatest cooling occurred during the Carboniferous, likely caused by deformation relating to the Alice Springs Orogeny. The ~200 Ma AFT ages correlate with the ~250 Ma apatite U-Pb ages located in close proximity to the fault zones and are interpreted to be related to distal cooling of the hydrothermal activity that caused these ages, as discussed below. However, these ~200 Ma ages are not preserved in the time-temperature models which could indicate they are reflecting slow regional cooling.

4.5.2 Hydrothermally reset data

Unlike the West Mount Domain, the Berlina Domain does not ubiquitously preserve detrital spectra as samples WR 24 and WR 25 either partially preserve, in the case of WR 25, or completely preserve, for WR 24, a ~250 Ma apatite U-Pb age. It is important to recognise that there is only minimal data within these samples and, as a result, have been cautiously interpreted to indicate a reheating pulse located proximal to the Norwest Fault at ~250 Ma. This is reflected in the AFT ages with WR 24 preserving a single ~100 Ma age and WR 25 recording two ages at; ~330 Ma and ~100 Ma with a central age of ~250 Ma. Secondary minerals are also preserved within these samples with sericite infill present within fractures (Fig. 4.4c; Fig. 4.4e). These minerals are indicative of potassium-rich hydrothermal alteration (Lanson et al., 2002; Ruiz Cruz et al., 2009) of temperatures in excess of 240 °C (Cloutier et al., 2010). These alteration minerals are absent within the samples of the West Mount Domain and sample WR 26 (Fig. 4.4). Therefore, it is probable that the alteration minerals formed simultaneously with apatite U-Pb (partial) reset or new growth as a result of hydrothermal fluids travelling through fault zones at elevated temperatures.

Within the Kingston Domain, sample WR 29 mimics sample WR 25's partial preservation of a younger ~250 Ma apatite U-Pb age in addition to Neoproterozoic detrital ages and AFT age populations of ~330 Ma and ~130 Ma with a central age of ~250 Ma. Sample 29 is located within close proximity to Tarltons Nob mine, a hydrothermal Cu deposit, and is interpreted to have influenced the younger ages preserved in this sample. Samples WR 34 and WR 38 do not record any detrital apatite U-Pb ages as all ages fall on a single common Pb line with a ^{207}Pb corrected weighted mean ^{206}Pb-^{238}U age of ~280 Ma (275 ± 12 Ma lower intercept age) and ~240 Ma (257 ± 12 Ma lower intercept age) respectively. These ages are interpreted to be caused by hydrothermal fluids hotter than 350 °C travelling through the major fault zones in the region ~ 280 – 240 Ma. AFT ages for both WR 34 and WR 38 match the youngest ages recorded by WR 24, WR 25, and WR 26 (~130 – 100 Ma). The pervasiveness of the 130 – 100 Ma ages throughout the hydrothermally altered samples indicates the presence of a second, younger (but colder, <300°C) hydrothermal pulse within the Willouran Ranges or the timing when these samples cooled above the APAZ after the ~250 Ma hydrothermal activity. Given the presence of short confined track lengths within sample WR 38, it is unlikely to be caused by hydrothermal activity alone and is more likely related to cooling following the ~250 Ma hydrothermal activity potentially couple with uppermost crustal exhumation as suggested by the thermal model for this sample. Veining is preserved in samples WR 26, WR 37 and WR 38. These veins are predominantly quartz, however, rutile is also present in veins in samples WR 37 and WR 38. In WR 38 the rutile is truncating primary quartz (Fig. 4.4r) that indicates the rutile is a secondary mineral. A quartz and rutile vein is present in WR 37 (Fig 4m), a sample that is located at the West Willouran mine, a hydrothermal copper mine that contains no apatite. Given the presence of rutile in both samples, it is interpreted that both are formed through hydrothermal fluids at ~250 Ma.

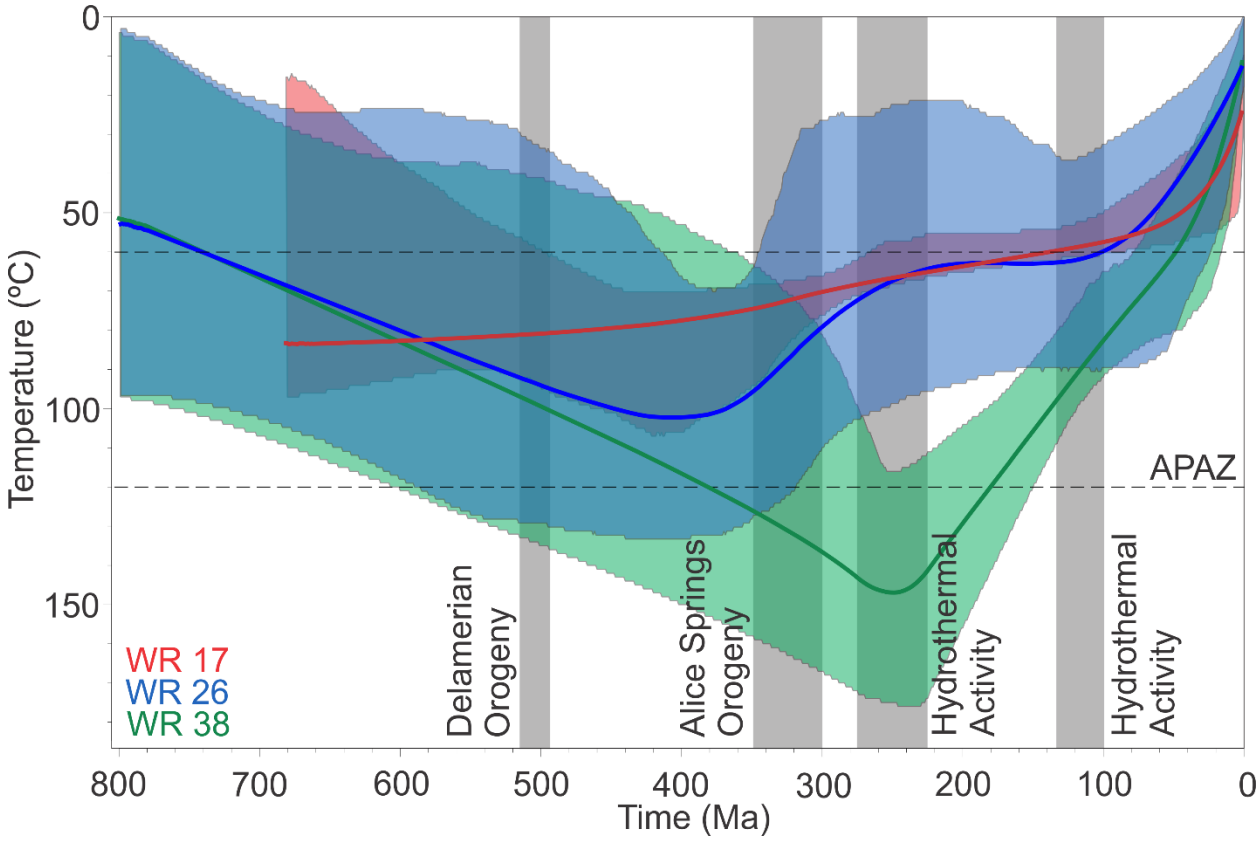

Figure 4.7: Time-temperature models for samples WR 17 (red), WR 26 (blue), and WR 38 (green). Samples were modelled using their apatite fission track ages and confined track lengths in QT-qt (Gallagher, 2012). The shaded columns indicate the Delamerian Orogeny, the last pulse of the Alice Springs Orogeny or interpreted hydrothermal activity.

4.5.3 Comparisons with surrounding regions

A potential source for the sediment input of the ARC is hinted at by the single defined Neoproterozoic apatite U-Pb age in the region. This ~1100 Ma age and the youngest grain ages within the West Mount Domain correlate well with apatite U-Pb from the eastern Musgrave province, and in particular, the Giles Event (Glorie et al., 2017a). Other sources are hinted at by the detrital apatite U-Pb spectra but it is difficult to deconvolute these ages. Therefore, no interpretation is made on these data.

The preserved Delamerian AFT ages within the Willouran Ranges are not pervasive throughout the ARC. To the east, the Mount Painter Inlier was at hotter temperatures during the Delamerian Orogeny (Elburg et al., 2003; McLaren et al., 2006; Wülser, 2009; Brugger et al., 2011; Elburg et al., 2013; Weisheit et al., 2014) and is interpreted to only play a minor role in Delamerian Orogeny deformation (Weisheit et al., 2014). Similarly, to the south, the Delamerian Orogeny is not

preserved in the AFT data and is likely overprinted by the Alice Springs Orogeny (Gibson and Stüwe, 2000; Gleadow et al., 2002). The Alice Springs Orogeny overprinting the Delamerian signal is also preserved in the basement below the Stuart Shelf, to the west (Hall et al., 2018b). However, the overlying Stuart Shelf preserves Delamerian Orogeny ages (Mitchell et al., 1998). The Peake and Denison Inliers, to the north, also partially preserve Delamerian Orogeny AFT ages (Hall et al., 2016), which indicates that the Delamerian Orogeny is only preserved in samples to the north west (i.e. Willouran Ranges, Stuart Shelf, and Peake and Denison Inliers). Therefore, these regions underwent less exhumation during and following the Delamerian Orogeny when compared to the Mount Painter Inlier and ARC.

As mentioned above, the Alice Springs Orogeny is preserved in the ARC, and Olympic Domain. It is also preserved within the Mount Painter Inlier (McLaren et al., 2002), and Peake and Denison Inliers (Hall et al., 2016). However, it is not preserved within the Willouran Ranges with the exception of the time-temperature model of WR 26 (Fig. 4.7). It has potentially been overprinted by later hydrothermal activity.

The ~250 Ma hydrothermal activity is not restricted to the Willouran Ranges, as it is widely preserved within the Mount Gee sinter of the Mount Painter Inlier (Weisheit et al., 2014). Given the close proximity and timing between the two hydrothermal events, we suggest these hydrothermal systems are linked and hint towards a more widespread hydrothermal system in the ARC.

There are equivalent ages to youngest ~100 Ma AFT ages preserved within the Willouran Ranges present as apatite (U-Th-Sm)/He ages in the Mount Painter Inlier. Weisheit et al. (2014) suggested these ages within the Mount Painter Inlier were caused by burial and subsequent exhumation relating to the Eromanga Basin. The ~100 Ma ages within the Willouran Ranges are restricted to faults zones with only minimal Phanerozoic cover in the Ranges (Fig. 4.5). Therefore, it is possible these ages are related. Similarly, in the Peake and Denison Inliers, apatite (U-Th-Sm)/He ages are preserved at ~100 Ma and are attributed to be caused by exhumation from shallow burial of Phanerozoic sediments (Hall et al., 2016). This indicates there was potential widespread shallow crustal fault related exhumation along the eastern margin of the Gawler Craton and northern Flinders Ranges during this time.

4.6 Conclusions

Apatite doubling dating and thin section analysis was used to reveal the timing and extent of Phanerozoic hydrothermal activity within the Willouran Ranges. Apatite U-Pb data is differentiated by proximity to major fault zones, where samples in the West Mount Domain and samples located distally to fault zones preserve Proterozoic detrital ages. Conversely, samples located proximally to fault zones either partially or completely preserve ~250 Ma apatite U-Pb ages, interpreted to be caused by hydrothermal alteration. Apatite fission track analysis is consistent with the apatite

U-Pb analysis as samples in the West Mount Domain preserve the oldest age populations within the region at ~550 Ma in addition to a younger ~ 200 Ma age population. Samples that preserve mixed or Proterozoic apatite U-Pb ages within the Berlina and Kingston Domains preserve mixed AFT ages of between ~500 Ma and ~100 Ma. Samples that preserve ~250 Ma apatite U-Pb ages preserve the youngest AFT ages within the region at ~100 Ma. The ~250 Ma ages are caused by hydrothermal activity located proximally to fault zones and are supported by the presence of hydrothermal rutile, quartz and sericite. These ages suggest the hydrothermal system that is widely documented in the Mount Painter Inlier is more widespread throughout the ARC than previously thought. The ~100 Ma ages are interpreted to be the upmost cooling of the region.

4.7 Acknowledgements

This study is funded by the Geological Survey of South Australia and was made possible through an Australian Research Council grant (ARC LE150100145). Sarah Gilbert (Adelaide Microscopy) is thanked for her assistance with the use of the LA-ICP-MS. Natalie Debenham is thanked for her assistance with field work. AR publishes with permission of the director of the Geological Survey of South Australia. This paper forms TRaX#**** and is a contribution to IGCP projects 628 (Gondwana Map) and 648 (Supercontinents).

4.8 References

Ambrose, G.J., Flint, R.B., Webb, A.W., 1981. Precambrian and Palaeozoic Geology of the Peake and Denison Ranges. Geological Survey of South Australia Bullitin 50.

Bakker, R., J., Elburg, M., 2006. A magmatic- hydrothermal transition in Arkaroola (Northern Flinders Ranges, South Australia): from diopside-titanite pegmatites to hematite-quartz growth. Contributions to Mineralogy and Petrology 152, 541-569.

Ballèvre, M., Möller, A., Hensen, B.J., 2000. Exhumation of the lower crust during crustal shortening: an Alice Springs (380 Ma) age for a prograde amphibolite facies shear zone in the Strangways Metamorphic Complex (central Australia). Journal of Metamorphic Geology 18, 737-747.

Benade, D.R., Rowlands, N.J., Jarvis, D.M., Rayner, R.A., Blight, P.G., Circosta, G., 1983. Willouran Ranges Stratiform Copper Project. Quarterly, annual and surrender reports for the period 4/4/79 to 19/7/83. Utah Development Co.

Boone, S.C., Seiler, C., Reid, A.J., Kohn, B., Gleadow, A., 2016. An Upper Cretaceous paleo-aquifer system in the Eromanga Basin of the central Gawler Craton, South Australia: evidence from apatite fission track thermochronology. Australian Journal of Earth Sciences 63, 315-331.

Bradshaw, J.D., Evans, P.R., 1988. Palaeozoic tectonics, Amadeus Basin, central Australia. APEA Journal 28, 267-282.

Brugger, J., Foden, J., Wulser, P.-A., 2011. Genesis and preservation of a uranium-rich paleozoic epithermal system with a surface expression (Northern Flinders Ranges, South Australia): radiogenic heat driving regional hydrothermal circulation over geological timescales. Astrobiology 11, 499+.

Buick, I.S., Storkey, A., Williams, I.S., 2008. Timing relationships between pegmatite emplacement, metamorphism and deformation during the intra-plate Alice Springs Orogeny, central Australia. Journal of Metamorphic Geology 26, 915-936.

Chew, D.M., Spikings, R.A., 2015. Geochronology and Thermochronology Using Apatite: Time and Temperature, Lower Crust to Surface. Elements 11, 189-194.

Clarke, D.S., Govett, G.J.S., 1990. Southwest Pacific epithermal gold: a rock-geochemistry perspective. Journal of Geochemical Exploration 35, 225-240.

Cloutier, J., Kyser, K., Olivo, G.R., Alexandre, P., 2010. Contrasting Patterns of Alteration at the Wheeler River Area, Athabasca Basin, Saskatchewan, Canada: Insights into the Apparently Uranium-Barren Zone K Alteration System. Economic Geology 105, 303-324.

Coats, R.P., Blissett, A.H., 1971. Regional and economic geology of the Mount Painter Province. Bulletin - Geological Survey of South Australia 43, 426.

Donelick, R.A., Ketcham, R.A., Carlson, W.D., 1999. Variability of apatite fission-track annealing kinetics; II, Crystallographic orientation effects. American Mineralogist 84, 1224-1234.

Drexel, J.F., 2009. Review of the Burra Mine project, 1980 – 2008 – a progress report, South

Australia. Department of Primary Industries and Resources, Report Book 2008/16, 40.

Elburg, M.A., Andersen, T., Bons, P.D., Simonsen, S.L., Weisheit, A., 2013. New constraints on Phanerozoic magmatic and hydrothermal events in the Mt Painter Province, South Australia. Gondwana Research 24, 700-712.

Elburg, M.A., Bons, P.D., Foden, J., Brugger, J., 2003. A newly defined Late Ordovician magmatic–thermal event in the Mt Painter Province, northern Flinders Ranges, South Australia. Australian Journal of Earth Sciences 50, 611-631.

Foden, J., Elburg, M.A., Dougherty-Page, J., Burtt, A., 2006. The Timing and Duration of the Delamerian Orogeny: Correlation with the Ross Orogen and Implications for Gondwana Assembly. The Journal of Geology 114, 189-210.

Foster, D.A., Murphy, J.M., Gleadow, A.J.W., 1994. Middle tertiary hydrothermal activity and uplift of the northern flinders ranges, South Australia: Insights from apatite fission-track thermochronology. Australian Journal of Earth Sciences 41, 11-17.

Galbraith, R.F., Laslett, G.M., 1993. Statistical models for mixed fission track ages. Nuclear Tracks and Radiation Measurements 21, 459-470.

Galbraith, R.F., Roberts, R.G., Laslett, G.M., Yoshida, H., Olley, J.M., 1999. Optical dating of single and multiple grains of quartz from jinmium rock shelter, northern australia: Part i, experimental design and statistical models*. Archaeometry 41, 339-364.

Gallagher, K., 2012. Transdimensional inverse thermal history modeling for quantitative thermochronology. Journal of Geophysical Research: Solid Earth 117, n/a-n/a.

Gibson, H.J., Stüwe, K., 2000. Multiphase cooling and exhumation of the southern Adelaide Fold Belt: constraints from apatite fission track data. Basin Research 12, 31-45.

Gillespie, J., Glorie, S., Xiao, W., Zhang, Z., Collins, A.S., Evans, N., McInnes, B., De Grave, J., 2017. Mesozoic reactivation of the Beishan, southern Central Asian Orogenic Belt: Insights from low-temperature thermochronology. Gondwana Research 43, 107–122.

Gleadow, A.J.W., Gleadow, S.J., Belton, D.X., Kohn, B.P., Krochmal, M.S., Brown, R.W., 2009. Coincidence mapping - a key strategy for the automatic counting of fission tracks in natural minerals. Geological Society, London, Special Publications 324, 25-36.

Gleadow, A.J.W., Kohn, B.P., Brown, R.W., O'Sullivan, P.B., Raza, A., 2002. Fission track thermotectonic imaging of the Australian continent. Tectonophysics 349, 5-21.

Glen, R.A., 2005. The Tasmanides of eastern Australia. Geological Society, London, Special Publications 246, 23-96.

Glorie, S., Agostino, K., Dutch, R., Pawley, M., Hall, J., Danišík, M., Evans, N.J., Collins, A.S., 2017. Thermal history and differential exhumation across the Eastern Musgrave Province, South Australia: Insights from low-temperature thermochronology. Tectonophysics 703–704, 23-41.

Glorie, S., Alexandrov, I., Nixon, A., Jepson, G., Gillespie, J., Jahn, B.-M., 2017. Thermal and exhumation history of Sakhalin Island (Russia) constrained by apatite U-Pb and fission track thermochronology. Journal of Asian Earth Sciences 143, 326-342.

Haines, P.W., Hand, M., Sandiford, M., 2001. Palaeozoic synorogenic sedimentation in central and northern Australia: a review of distribution and timing with implications for the evolution of intracontinental orogens. Australian Journal of Earth Sciences 48, 911-928.

Hall, J.W., Glorie, S., Collins, A.S., Reid, A., Evans, N., McInnes, B., Foden, J., 2016. Exhumation history of the Peake and Denison Inliers: insights from low-temperature thermochronology. Australian Journal of Earth Sciences 63, 805-820.

Hall, J.W., Glorie, S., Reid, A.J., Boone, S.C., Collins, A.S., Gleadow, A., 2018. An apatite U–Pb thermal history map for the northern Gawler Craton, South Australia. Geoscience Frontiers.

Hall, J.W., Glorie, S., Reid, A.J., Collins, A.S., Jourdan, F., Danišík, M., Evans, N., 2018. Thermal history of the northern Olympic Domain, Gawler Craton; correlations between thermochronometric data and mineralising systems. Gondwana Research 56, 90-104.

Kamenetsky, V.S., Ehrig, K., Maas, R., Apukhtina, O., Kamenetsky, M., Meffre, S., McPhie, J., Huang, Q., Thompson, J., Ciobanu, C.L., Cook, N.J., 2016. The Olympic Dam Cu-U-Au-Ag ore deposit: towards a new genetic model, Australian Earth Sciences Convention. Geological Society of Australia, Adelaide.

Lanson, B., Beaufort, D., Berger, G., Bauer, A., Cassagnabere, A., Meunier, A., 2002. Authigenic kaolin and illitic minerals during burial diagenesis of sandstones: a review. Clay Minerals 37, 1-22.

Lloyd, J., Blades, M., Collins, A. S., Hore, S., Wade, B., Hall, J. W., Job, A., Prohoroff, A., Drabsch, M., Shahin, S., In Prep. An investigation into the chronological and provenance framework of the Flinders Ranges. Australian Journal of Earth Sciences special addition.

Ludwig, K.R., 2012. User's manual for Isoplot 3.75, A Geochronological Toolkit for Microsoft Excel. Berkeley Geochronology Center Special Publication No. 5

Mackay, W., 2011. Structure and sedimentology of the Curdimurka Subgroup, northern Adelaide Fold Belt, South Australia. University of Tasmania.

Mahan, K.H., Wernicke, B.P., Jercinovic, M.J., 2010. Th–U–total Pb geochronology of authigenic monazite in the Adelaide rift complex, South Australia, and implications for the age of the type Sturtian and Marinoan glacial deposits. Earth and Planetary Science Letters 289, 76-86.

Márton, I., Moritz, R., Spikings, R., 2010. Application of low-temperature thermochronology to hydrothermal ore deposits: Formation, preservation and exhumation of epithermal gold systems from the Eastern Rhodopes, Bulgaria. Tectonophysics 483, 240-254.

Mawby, J., Hand, M., Foden, J., 1999. Sm–Nd evidence for high-grade Ordovician metamorphism in the Arunta Block, central Australia. Journal of Metamorphic Geology 17, 653-668.

McDowell, F.W., McIntosh, W.C., Farley, K.A., 2005. A precise 40Ar–39Ar reference age for the Durango apatite (U–Th)/He and fission-track dating standard. Chemical Geology 214, 249-263.

McLaren, S., Dunlap, W.J., Sandiford, M., McDougall, I., 2002. Thermochronology of high heat-producing crust at Mount Painter, South Australia: Implications for tectonic reactivation of continental interiors. Tectonics 21, 2-1-2-18.

McLaren, S., Sandiford, M., Powell, R., Neumann, N., Woodhead, J., 2006. Palaeozoic Intraplate Crustal Anatexis in the Mount Painter Province, South Australia: Timing, Thermal Budgets and the Role of Crustal Heat Production. Journal of Petrology 47, 2281-2302.

Mitchell, M.M., Kohn, B.P., Foster, D.A., 1998. Post-orogenic cooling history of eastern South Australia from apatite FT thermochronology., In: Van den haute, P., De Corte, F. (Eds.), Advances in FissionTrack Geochronology. Kluwer Academic Publishers, Dordrecht, pp. 207-224.

Mitchell, M.M., Kohn, B.P., O'Sullivan, P.B., Hartley, M.J., Foster, D.A., 2002. Low-temperature thermochronology of the Mt Painter Province, South Australia. Australian Journal of Earth Sciences 49, 551-563.

Paton, C., Hellstrom, J., Paul, B., Woodhead, J., Hergt, J., 2011. Iolite: Freeware for the visualisation and processing of mass spectrometric data. Journal of Analytical Atomic Spectrometry 26, 2508-2518.

Pollock, M.V., Spry, P.G., Tott, K.A., Koenig, A., Both, R.A., Ogierman, J., 2018. The origin of the sediment-hosted Kanmantoo Cu-Au deposit, South Australia: Mineralogical considerations. Ore Geology Reviews 95, 94-117.

Powell, C.M., Preiss, W.V., Gatehouse, C.G., Krapez, B., Li, Z.X., 1994. South Australian record of a Rodinian epicontinental basin and its mid-neoproterozoic breakup (~700 Ma) to form the Palaeo-Pacific Ocean. Tectonophysics 237, 113-140.

Preiss, W.V., 1982. Supergroup classification in the Adelaide Geosyncline. (Brief communication.). Royal Society of South Australia. Transactions 106 (2), 81-83.

Preiss, W.V., 1987. The Adelaide Geosyncline: Late Proterozoic stratigraphy, sedimentation, palaentology and tectonics. The Geological Survey of South Australia, Bulletin 53, 438.

Preiss, W.V., 1993. Neoproterozoic, In: Drexel, J.F., Preiss, W.V., Parker, A.J. (Eds.), The geology of South Australia. Vol.1 , The Precambrian, South Australia Geological Survey, Bulletin 54.

Preiss, W.V., 2000. The Adelaide Geosyncline of South Australia and its significance in Neoproterozoic continental reconstruction. Precambrian Research 100, 21-63.

Reddy, M., Glorie, S., Reid, A.J., Collins, A.S., 2015. Phanerozoic cooling history of the central Gawler Craton: implications of new low-temperature thermochronological data. MESA Journal 75, 56-60.

Ruiz Cruz, M.D., Rodriguez-Ruiz, M., Novak, J.K., 2009. The illitization of dickite: Chemical and structural evolution of illite from diagenetic to metamorphic conditions.

Thomson, S.N., Gehrels, G.E., Ruiz, J., Buchwaldt, R., 2012. Routine low-damage apatite U-Pb dating using laser ablation–multicollector–ICPMS. Geochemistry, Geophysics, Geosystems 13.

Tingate, P.R., Duddy, I.R., 2002. The thermal history of the eastern Officer Basin (South Australia): evidence from apatite fission track analysis and organic maturity data. Tectonophysics 349, 251-275.

Vermeesch, P., 2009. RadialPlotter: a Java application for fission track, luminescence and other radial plots. Radiation Measurements 44, 409-410.

Weisheit, A., Bons, P.D., Danisík, M., Elburg, M.A., 2014. Crustal-scale folding: Palaeozoic deformation of the Mt Painter Inlier, South Australia. Geological Society, London, Special Publications 394, 53-77.

Weisheit, A., Bons, P.D., Elburg, M.A., 2013. Long-lived crustal-scale fluid flow: the hydrothermal mega-breccia of Hidden Valley, Mt. Painter Inlier, South Australia. International Journal of Earth Sciences 102, 1219-1236.

Wülser, P.A., 2009. Uranium metallogeny in North Flinders Ranges region of South Australia, Environmental and Earth Sciences. Adelaide University, Adelaide.

Zhu, Y., An, F., Tan, J., 2011. Geochemistry of hydrothermal gold deposits: A review. Geoscience Frontiers 2, 367-374.

Chapter 5

Exhumation of the Peake and Denison Inliers

Published as:

Hall, J.W., Glorie, S., Collins, A.S., Reid, A., Evans, N., McInnes, B., and Foden, J., 2016, Exhumation History of the Peake and Denison Inliers: Insights from Low-Temperature Thermochronology. Australian Journal of Earth Sciences 63, 805-20.

Title of Paper	Exhumation history of the Peake and Denison Inliers: insights from low-temperature thermochronology
Publication Status	☑ Published ☐ Accepted for Publication ☐ Submitted for Publication ☐ Unpublished and Unsubmitted work written in manuscript style
Publication Details	Hall, J.W., Glorie, S., Collins, A.S., Reid, A., Evans, N., McInnes, B., and Foden, J., 2016, Exhumation History of the Peake and Denison Inliers: Insights from Low-Temperature Thermochronology. Australian Journal of Earth Sciences 63, 805-20.

Principal Author

Name of Principal Author (Candidate)	James Hall		
Contribution to the Paper	Data collection, data interpretation, manuscript and figure composition.		
Overall percentage (%)	70 %		
Certification:	This paper reports on original research I conducted during the period of my Higher Degree by Research candidature and is not subject to any obligations or contractual agreements with a third party that would constrain its inclusion in this thesis. I am the primary author of this paper.		
Signature		Date	1/05/18

Co-Author Contributions

By signing the Statement of Authorship, each author certifies that:

i. the candidate's stated contribution to the publication is accurate (as detailed above);

ii. permission is granted for the candidate in include the publication in the thesis; and

iii. the sum of all co-author contributions is equal to 100% less the candidate's stated contribution.

Name of Co-Author	Stijn Glorie		
Contribution to the Paper	Assistance in data collection, assistance in data interpretation, manuscript review. 10% contribution.		
Signature		Date	1/05/18

Statement of Authorship

Name of Co-Author	Alan Collins		
Contribution to the Paper	Assistance in data interpretation, manuscript review . 4% contribution.		
Signature		Date	27/06/18
Name of Co-Author	Anthony Reid		
Contribution to the Paper	Assistance in data interpretation, manuscript review . 4% contribution.		
Signature		Date	11/05/18
Name of Co-Author	Noreen Evans		
Contribution to the Paper	Data collection, manuscript review . 4% contribution.		
Signature		Date	10/04/18
Name of Co-Author	Brent McInnes		
Contribution to the Paper	Data collection, manuscript review . 4% contribution.		
Signature		Date	10/04/18
Name of Co-Author	John Foden		
Contribution to the Paper	Sample collection, manuscript review . 4% contribution.		
Signature		Date	10/04/18

Abstract

Multi-method thermochronology applied to the Peake and Denison Inliers (northern South Australia) reveals multiple low-temperature thermal events. Apatite fission track (AFT) data suggest two main time periods of basement cooling and/or reheating into AFT closure temperatures (~60–120°C); at ca 470–440 Ma, and ca 340–300 Ma. We interpret the Ordovician pulse of rapid basement cooling as a result of post-orogenic cooling after the Delamerian Orogeny, followed by deformation related with the start of the Alice Springs Orogeny and orocline formation relating to the Benambran Orogeny. This is supported by a titanite U-Pb age of 479 ± 7 Ma. Our thermal history models indicate that subsequent denudation and sedimentary burial during the Devonian brought the basement rocks back to zircon U–Th–Sm/He (ZHe) closure temperatures (~200–150°C). This period was followed by a renewal of rapid cooling during the Carboniferous, likely as the result of the final pulses of the Alice Springs Orogeny, which exhumed the inlier to ambient surface temperatures. This thermal event is supported by the presence of the Mount Margaret erosion surface, which indicates that the inlier was exposed at the surface during the early Permian. During the Late Triassic–Early Jurassic, the inlier was subjected to minor reheating to AFT closure temperatures; however, the exact timing cannot be deduced from our dataset. Cretaceous apatite U–Th–Sm/He (AHe) ages coupled with the presence of contemporaneous coarse-grained terrigenous rocks suggest a temporally thermal perturbation related with shallow burial during this time before late Cretaceous exhumation cooled the inliers back to ambient surface temperatures.

5.1 Introduction

Although Australia is widely perceived to be a relatively stable continent, especially during the Mesozoic–Cenozoic, there is growing awareness that the subdued Australian landscape belies a dynamic history (e.g. Czarnota, Hoggard, White, & Winterbourne, 2013; Czarnota, Roberts, White, & Fishwick, 2014; Müller, Flament, Matthews, Williams, & Gurnis, 2016; Russell & Gurnis, 1994; Sandiford, 2003, 2007). Previous studies on the Phanerozoic landscape evolution of Australia are mainly focused on the Australian coastline (especially in the eastern States), and therefore, only sparse data exist from within inland Australia. Czarnota et al. (2014) started to address this issue by including low-temperature thermochronologic data such as the apatite fission track (AFT) data from A. J. W. Gleadow, Kohn, Brown, O'Sullivan, and Raza (2002) into dynamic topography models. However, large gaps remain due to lack of data from inland Australia, especially South Australia. The vast majority of the low temperature thermochronological work completed in South Australia has been mainly focused on the Adelaide Fold Belt (Gibson & Stüwe, 2000) and the Flinders Ranges (northern Adelaide Fold Belt; Marlina A. Elburg, Andersen, Bons, Simonsen, & Weisheit, 2013; Foster, Murphy, & Gleadow, 1994; McLaren, Dunlap, Sandiford, & McDougall, 2002; Mitchell, Kohn, O'Sullivan, Hartley, & Foster, 2002; Weisheit, Bons, Danisík, & Elburg, 2014). Only a few studies have inquired into the thermal history of inland South Australia, such as the Gawler Craton (Boone,

Seiler, Reid, Kohn, & Gleadow, 2016; A. J. W. Gleadow et al., 2002; Reddy, Glorie, Reid, & Collins, 2015; Tingate & Duddy, 2002).

The Peake and Denison Inliers are located at the northeastern margin of the Gawler Craton (Figure 5.1) and its current topography forms a north–south trending line of hills that expose Paleoproterozoic–Ordovician basement. While the age and composition of the rocks within the Peake and Denison Inliers have been studied (Ambrose, Flint, & Webb, 1981; Hopper, 2001; Morrison, 1989), to date, no low-temperature thermochronological study has been conducted on the inliers to determine the timing of basement cooling and exhumation to shallow crustal levels. Two early low-temperature thermochronological and structural studies on the exhumation history of the Peake and Denison Inliers determined vastly different time-scales of basement cooling during the Permian (~266 ± 23 Ma; Radke, 1973) and Miocene to Pleistocene (Wopfner, 1968); however, they are inconclusive and seem to largely disagree with more recent data sets from elsewhere within Australia. In this study, we provide a multi-method thermochronological dataset for the Peake and Denison Inliers using complementary apatite fission track (AFT), and apatite (AHe) and zircon (ZHe) (U–Th–Sm)/He analyses. This combined dataset is then used to model the low-T thermal history of the inliers between ~200–50°C (Kenneth A. Farley, 2002; Reiners, Spell, Nicolescu, & Zanetti, 2004; Wagner & van den Haute, 1992). Within this model, time periods of basement cooling or reheating are identified and are linked with the sedimentary record of adjacent basins (Figure 5.1) to provide a detailed reconstruction of the exhumation history of the region. This model is further linked with the regional tectonic history of South Australia, aiming to increase our understanding of the dynamic response of intracontinental Australia to plate-margin processes.

The exhumation of the region encompassing the Peake and Denison Inliers, in northern South Australia is particularly topical as it lies in the broad path of a proposed Cretaceous transcontinental Ceduna River (Bryan et al., 1997; Lloyd et al., 2015; J. MacDonald, D. et al., 2013; Tucker, Roberts, Hu, Kemp, & Salisbury, 2013; Veevers, 2000). J. MacDonald, D. et al. (2013), deviated from previous intepretations of a long-lived northeast Queensland-originating river system, suggesting that an original Cenomanian transcontinental river was terminated in the late Cretaceous by uplift along a broad arc stretching from the Flinders Ranges, through the Peake and Denison Inlier regions, through to the Musgrave Ranges in the north. This uplift was interpreted to have rejuvenated deposition in the Bight Basin, depositing the upper lobe of the Ceduna Delta (J. Macdonald, Backé, King, Holford, & Hillis, 2012), which was sourced from a more restricted upper Cretaceous basin, enclosed within the modern borders of South Australia. The Peake and Denison Inliers occupy a key location within the pathway of this suggested river system and, therefore, its thermal history can provide important constraints on the evolution of Mesozoic inland Australia and potential source regions for the Cretaceous Bight Basin.

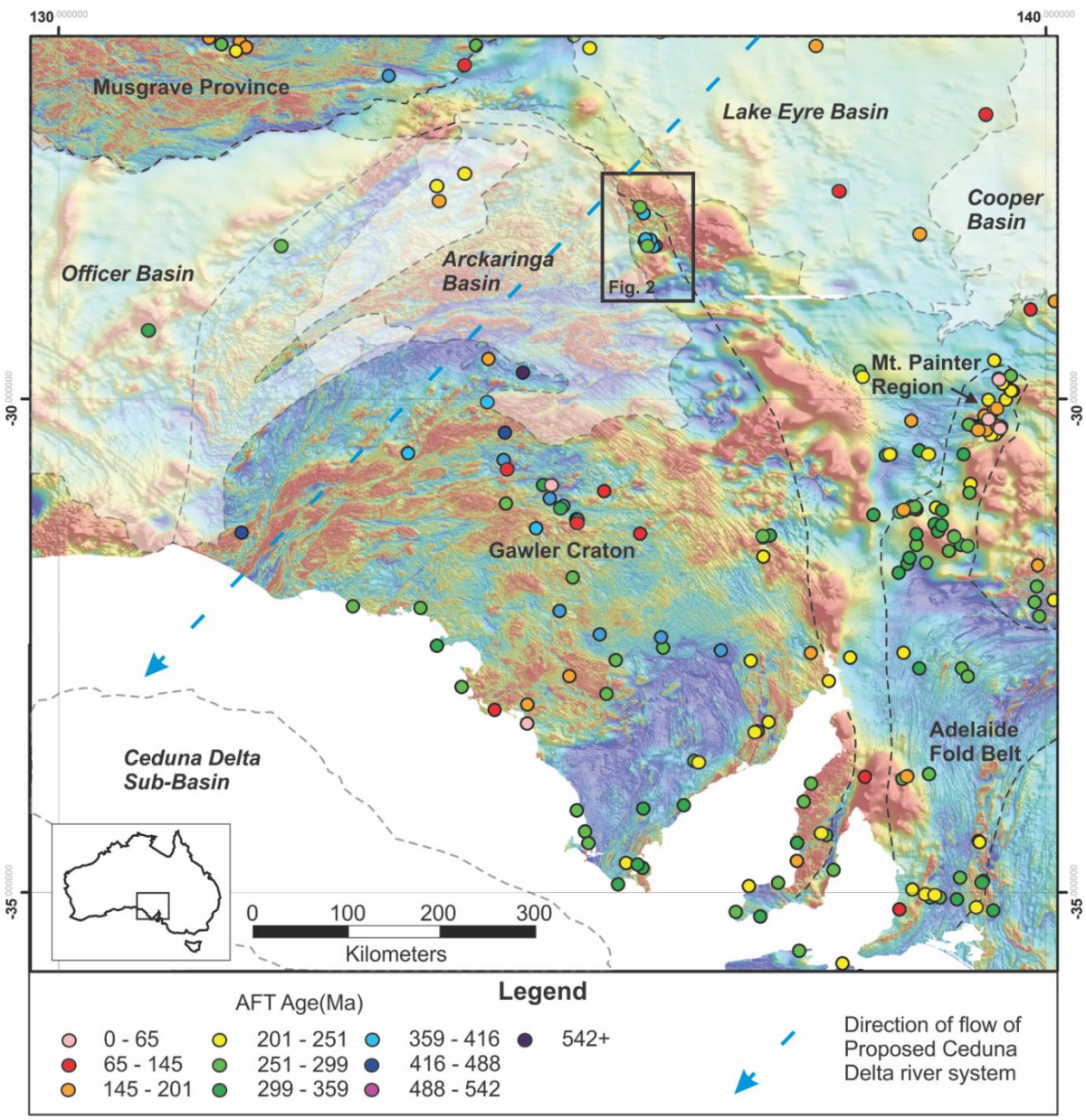

Figure 5.1: A total magnetic intensity (TMI) map of South Australia illustrating the outlines of the main geological units, the main sedimentary basins, the Peake and Denison Inliers, which are located within the black box, and the locations of the Ceduna Basin and the proposed paleo-river (after; MacDonald et al., 2013). The ages of all previously obtained AFT data are indicated by the coloured circles (e.g. Boone et al., 2016; Gleadow et al., 2002; McLaren et al., 2002; Mitchell et al., 2002; Reddy et al., 2015; Tingate & Duddy, 2002; Weisheit et al., 2014).

5.2 Geological setting

The Peake and Denison Inliers, also referred to as the Peake and Davenport Inliers, are named after the Denison Range (Figure 5.2) and the Peake Ruins, which are located between the Denison and Davenport ranges. They contain Mesoproterozoic metamorphic rocks, Neoproterozoic sedimentary rocks and Paleoproterozoic to Ordovician igneous intrusive and extrusive rocks (Ambrose et al., 1981). The surrounding landscape is covered by Cretaceous

sedimentary rocks and Miocene to Pleistocene sediments of the Lake Eyre Basin (Figure 5.2). The main igneous units in the study area are the Wirriecurrie Granite, the Tidnamurkuna Volcanics and the Bungadillina Monzonite. The Wirriecurrie Granite is dated to the Paleoproterozoic (1793 ± 8 Ma; Rogers & Freeman, 1994) and is deformed towards its margins. This deformation is interpreted to be related to both the Stenian Musgravian and 515–490 Ma Delamerian orogenies (J. Foden, Elburg, Dougherty-Page, & Burtt, 2006; Smithies et al., 2011), due to the retrieval of K–Ar ages attributed to both events (ca. 1080 and 519 Ma; Ambrose et al., 1981). However, more recent mapping suggests that the deformation is much older (Hopper, 2001). The Tidnamurkuna Volcanics are Paleoproterozoic (1806 ± 27 Ma; Fanning, Flint, Parker, Ludwig, & Blissett, 1988) basalt-dominated flows interrupted by rhyolitic volcanism. The Bungadillina Monzonite is the name given to a series of monzonites, syenites, gabbros, and dykes that have been interpreted to be a result of the Delamerian Orogeny based on their Ordovician age (497.5 ± 10 Ma; Rogers & Freeman, 1994).

A series of sedimentary rocks post-date the Bungadillina Monzonite. These begin with the informally named Nultaddy Seismic Unit, a poorly studied shale unit of Devonian age that is located in seismic sections within the Boorthanna Trough (Allender, Taylor, & Gilby, 1987; Alley & Gravestock, 1995). This unit is unconformably overlain by the upper Carboniferous to lower Permian sedimentary rocks of the Arckaringa Basin, which include the Boorthanna, Stuart Range, and Mount Toondina formations. These sediments were deposited as alternating shales and sandstone layers with extensive coal deposits preserved towards the top (Figure 5.2). The presence of coal indicates that some of the basin formed in a terrestrial environment.

An erosional peneplain, known as the Mount Margaret Surface (MMS), is located on the Davenport Range (Figure 5.2) and has been dated to be late Permian in age (Rogers & Freeman, 1994), demonstrating that the ranges were at the surface during this time. There are no recorded sedimentary rocks from the lower Permian until the Upper Jurassic, when the medium to coarse grained Algebuckina Sandstone was deposited. The top of this sandstone unit is silicified and contains plant fossils (Alexander & Krieg, 1995), which is indicative of a terrestrial origin. Renewed sedimentation during the Lower Cretaceous resulted with the deposition of the Neales River Group; consisting of sandstones and shales of the Mt Anna Sandstone Member, Cadna-Owie Formation, the Bulldog Shale, the Coorikiana Sandstone, and the Oodnadatta Formation (Rogers & Freeman, 1994). Cenozoic deposition consists of mostly coarse terrestrial units including the Mirackina Conglomerate, which is a paleochannel deposit (Callen, Alley, & Greenwood, 1995), as well as unnamed conglomerates, gravels, alluvial deposits, clay deposits, and eolian sands (Figure 5.2).

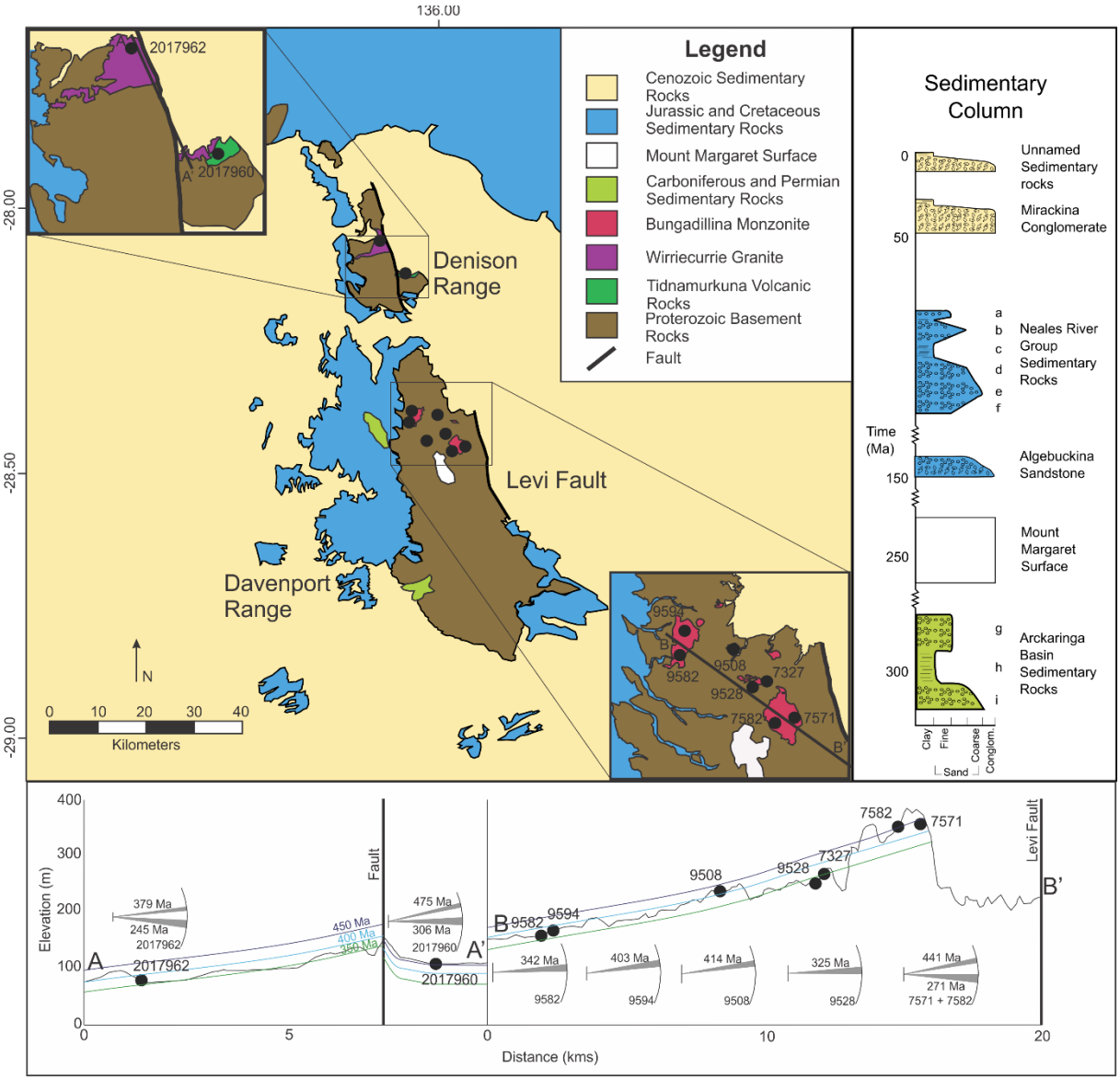

Figure 5.2: Simplified geological map, stratigraphic column, and elevation cross section of the Peake and Denison Inliers, indicating the ages and relationships of different geological units, the location of major faults, and sample localities. (a) Oodnadatta Formation, (b) Coorikiana Sandstone, (c) Bulldog Shale, (d) Cadna-Owie Formation, (e) Mt Anna Sandstone, (f) Mount Toondina Formation, (g) Stuart Range Formation, and (h) Boorthanna Formation. Elevation cross section illustrates the apatite fission track age isochrons in Ma. Map modified after Hopper (2001).

In addition to the older Musgravian Orogeny, several younger exhumation and/or deformation events, which may have induced exhumation of the region, are documented in the vicinity of the study area. The Ordovician Bungadillina Monzonite is thought to relate to the Cambrian–Ordovician Delamerian Orogeny (J. Foden et al., 2006). Metamorphism and deformation associated with this orogeny has been demonstrated from the Mount Lofty Ranges, Kangaroo Island and Curnamona Province (J. Foden et al., 2006; J. D. Foden et al., 2002; Rutherford, Hand, & Mawby, 2006). In the northern Flinders Ranges, both thin and thick-skinned thrusting with associated folds have been inferred to have occurred during the Delamerian orogeny (Armit,

Betts, Schaefer, & Ailleres, 2012). However, evidence for extensive Cambrian–Ordovician mountain building north of the central Flinders Ranges is less convincing. In the northeast Flinders Ranges (the Mount Painter Inlier), high temperature themochronometers yield ages that are ca 60 million years younger than those from the Adelaide region (ca. 450 – 430 Ma; Marlina A. Elburg et al., 2013; M. A. Elburg, Bons, Foden, & Brugger, 2003; McLaren et al., 2002), suggesting that the recorded deformation and cooling, were reset in this region during the Silurian as a result of the Benambran Orogeny (Cayley, 2011; Moresi, Betts, Miller, & Cayley, 2014). A subsequent period of enigmatic exhumation occurred at ca 400 Ma (McLaren et al., 2002; Weisheit et al., 2014), but it appears that the orogen was largely inactive for the next 70 Ma. At this point, a period of elevated cooling and exhumation was recorded that has been linked with extensive deformation in the Alice Springs orogeny of central Australia (McLaren et al., 2002; Weisheit et al., 2014).

Radke (1973) obtained AFT data for the Peake and Denison Inliers and proposed an exhumation event during the Permian (266 ± 23 Ma), thus suggesting an exhumation link with Mt Painter (McLaren et al., 2002; Mitchell et al., 2002). In addition, several studies (Boone et al., 2016; B. P. Kohn et al., 2002; J. MacDonald, D. et al., 2013; Reddy et al., 2015; Twidale, 1994) have reported phases of widespread Mesozoic exhumation in the Gawler Craton to the southwest of the study area. More recent, Miocene–Pleistocene, deformation-related exhumation is suggested by the displacement of morphological features such as gypsite surfaces (Wopfner, 1968) across the Levi Fault (Figure 5.2). This was supported by Foster et al. (1994) who concluded that there was exhumation during the Miocene in the northern Flinders Ranges. Further geological evidence for neo-tectonic activity exists in the presence of widespread pre-Pliocene fault-related deformation throughout Australia's interior (Raiber & Webb, 2008; Reynolds, Mildren, Hillis, & Meyer, 2006; Waclawik, Lang, & Krapf, 2008), including in the Arckaringa and Lake Eyre basins (Wopfner, 1964).

Sample	Latitude	Longitude	Altitude (m)	Lithology	Formation age (Ma)
7327	-28.432353°	135.997402°	250	Lamprophyre	497 ± 10
7571	-28.447945°	136.050133°	400	Syenite	497 ± 10
7582	-28.456493°	136.024390°	400	Syenite	497 ± 10
9508	-28.388469°	135.996963°	200	Syenite	497 ± 10
9528	-28.437468°	135.976050°	300	Monzonite	497 ± 10
9582	-28.402859°	135.940473°	200	Monzonite	497 ± 10
9583	-28.402047°	135.940482°	200	Monzonite	497 ± 10
9594	-28.381071°	135.947927°	150	Monzonite	497 ± 10
2017960	-28.118600°	135.927900°	150	Rhyolite	1806 ± 27
2017962	-28.060300°	135.887500°	100	Granite	1793 ± 8

Table 5.1: Sample details. Formation ages were collected by Fanning et al. (1988) and Rogers and Freeman (1994).

5.3 Methodology

Granitoid outcrops were sampled in both the Denison and Davenport ranges within the Peake and Denison Inliers. Sample 2017962 was taken from the Paleoproterozoic Wirriecurrie granite, 2017960 was collected from the Tidnamurkuna Volcanics, both within the Denison Range, while samples 9594, 9582, 9528, 9508, 7582, 7571, and 7327 were taken from the Ordovician Bungadillina Monzonite within the Davenport Range (Figure 5.2; Table 5.1).

5.3.1 Apatite fission track dating

The apatite fission track (AFT) method is used to determine the thermal history of rock samples between the so-called AFT partial annealing zone at temperatures of ~60–120°C (Andrew J.W. Gleadow, Belton, Kohn, & Brown, 2002; Wagner & van den Haute, 1992). Following rock crushing and conventional density and magnetic mineral separation techniques, apatite grains were hand-picked, mounted in epoxy resin and ground and polished to expose internal sections. Subsequent fission track revelation was performed using chemical etching in a 5M HNO_3 solution for 20 seconds at 20°C. The fission track density within individual apatite grains was determined by counting the number of tracks in a reference grid using an *Olympus BX-51* microscope at 1000x total magnification. Uranium concentrations for each grain were determined using a *Resonetics* Laser-Ablation Inductively-Coupled-Plasma *Argilent 7700s* quadrupole Mass-Spectrometer (LA-ICP-MS) at Adelaide Microscopy, following analytical details based on Hasebe, Barbarand, Jarvis, Carter, and Hurford (2004), De Grave et al. (2012) and outlined in Gillespie *et al.* (2015). NIST 610, 612 and 614 glass standards (Pearce et al., 1997) were repeatedly measured and used as primary standards for calibration purposes. All samples were ablated once to an average depth of 9.15 µm. Data accuracy was monitored using Durango apatite (30.4 ± 1.2 Ma for Durango samples collected in this study, compared to 31.44 ± 0.18 Ma; McDowell, McIntosh, & Farley, 2005) and an in-house standard as secondary standards; ^{44}Ca was used as an internal standard. Data reduction was carried out using in-house *Excel* spreadsheets. A minimal amount of unreliable U-concentrations, mainly due to heavily zoned U-concentrations through apatite grains, were not used further in the AFT age calculations. Additional D_{par} measurements were collected (Table 5.2), which are a measure of the apatite chemistry and annealing kinetics (Burtner, Nigrini, & Donelick, 1994; Raymond A. Donelick, Ketcham, & Carlson, 1999; R.A. Donelick, O'Sullivan, & Ketcham, 2005) to be used in subsequent thermal history modelling. Apatite electron microprobe analysis was conducted to complement the AFT data with an independent chemical control by measuring and calculating the Cl % of individual grains (Carlson, Donelick, & Ketcham, 1999; Green, Duddy, Gleadow, Tingate, & Laslett, 1986; Stock, Humphreys, Smith, Johnson, & Pyle, 2015). Samples 2017962, 2017960, 9594, and 7571 + 7582 were analysed for their Cl % on the *CAMECA SXFive* electron microprobe. Data reduction was conducted on probe for *EPMA* software and the electron microprobe was calibrated against an Astimex Apatite, and a Tugtupite standard.

5.3.2 Apatite (U–Th–Sm)/He (AHe) and zircon (U–Th–Sm)/He (ZHe) dating

AHe and ZHe analyses were conducted to complement the AFT data and to refine subsequent thermal history modelling between ~75–45°C and ~200–170°C, respectively (Kenneth A. Farley, 2002; Reiners et al., 2004). Two apatite and one zircon separates were chosen based on grain quality and analysed at the John De Laeter Centre at Curtin University. The method for both apatite and zircon (U–Th–Sm)/He analysis is detailed in full in Danišík, Štěpančíková, and Evans (2012). Each grain was loaded into Pt (for apatite) and Nb (for zircon) tubes, degassed at about 960°C (apatite) and about 1250°C (zircon), after which, the concentration of ^{4}He was measured using a *Pfeiffer Prisma QMS-200* mass spectrometer. The samples were digested in acid and the concentrations of U, Th, and Sm were recorded using an *Agilent 7500CS* mass spectrometer.

5.3.3 Titanite U-Pb dating

One additional sample, 9583, located 100 m north of sample 9582, was analysed for titanite U-Pb dating. This method records cooling through a temperature range of ~700–650°C (Frost, Chamberlain, & Schumacher, 2001). GJ zircon was used as primary standards and Mount Dromedary titanate was used for accuracy check. Data-reduction was done off-line using *Iolite* software (Paton, Hellstrom, Paul, Woodhead, & Hergt, 2011) with ^{207}Pb corrected ages calculated following Chew, Petrus, and Kamber (2014). Figures were then produced in *Isoplot* (Ludwig, 1999).

5.3.4 Radial plots and thermal history modelling

AFT central ages (Galbraith & Laslett, 1993; Galbraith, Roberts, Laslett, Yoshida, & Olley, 1999) were calculated using *Radial Plotter* (Vermeesch, 2009). Samples that yielded large age-dispersions were decomposed into multiple age-components, which were identified using the automatic mixture model in the *Radial Plotter* software and, where possible, by using the dispersion in D_{par}, ^{238}U and Cl % measurements (Burtner et al., 1994; Donelick et al., 1999, 2005; Stock et al., 2015; Stormer, Pierson, & Tacker, 1993) as a visual aid to validate the modelled age-components. AFT age results, horizontal confined track length distributions and (U–Th–Sm)/He age results were subsequently used to model the cooling history using the *HeFTy* software (Ketcham, 2005), which simulate the thermal history evolution of the study region between ~200°C and surface outcrop temperatures.

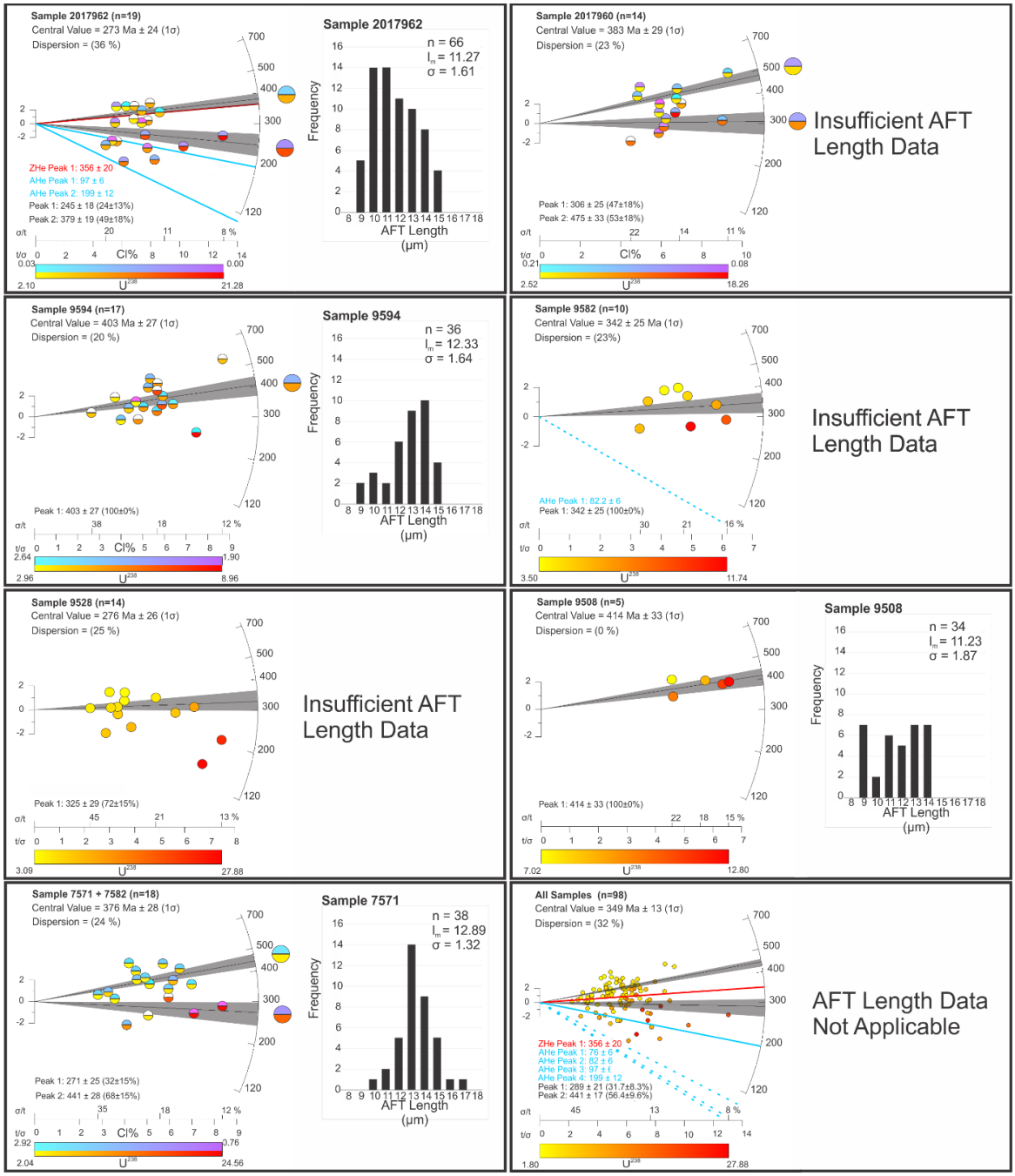

Figure 5.3: Radial plots of apatite fission track (AFT) ages from samples 2017962, 2017960, 9594, 9582, 9528, 9508, and 7571 + 7582, as well as a radial plot containing all samples. 'n' indicates the number of grains measured, the 'central value' indicates the central age of the sample, 'dispersion' indicates the percentage of age dispersion within the sample, the yellow to red colour difference indicates the different ^{238}U concentrations for each measured grain. ^{238}U is measured in ppm. Samples which were analysed for Cl % ratio are also displayed with the blue to pink colour scale on the upper half of the grains. Where more than one population of ages is present, the central age is split into age peaks using the Automatic Mixture model of *Radial Plotter*. The average ^{238}U and Cl % values for each age peak are plotted as larger circles to the right of their respective peak. All ages acquired from radial plots are presented in Table 5.2. To the right of each applicable radial plot is the accompanying AFT length frequency histogram (samples with not enough data are excluded). On each histogram, AFT length is in µm, n indicates the number of tracks measured, l_m is average track length, and σ is the standard deviation of the sample. Radial plots were constructed using *Radial Plotter* (Vermeesch, 2009).

Sample	ρ_s	Ns	N	^{238}U	Central age	Lower age (Cl%)	Upper Age (Cl%)	l_m	n	σc	Cl %	F%	D_{par} (μm)
7571 + 7582	1.298 (0.09)	549	18	7.491 (0.15)	376 ± 28	271 ± 25 (1.63)	441 ± 28 (2.37)	12.89	38	1.32	1.88 (0.58)	0.63 (0.56)	1.59
9508	2.14 (0.17)	170	5	6.286 (0.157)	414 ± 33	-	-	11.23	34	1.87	-		1.3
9528	1.236 (0.16)	293	14	9.590 (0.128)	276 ± 26	-	325 ± 29	-	-	-	4.69 (0.34)	0.48 (0.18)	1.51
9582	1.063 (0.1)	186	8	6.286 (0.157)	342 ± 25	-	-	-	-	-	-		1.13
9594	1.088 (0.08)	538	17	5.086 (0.055)	403 ± 27	-	-	12.33	36	1.64	2.31 (0.26)	0.38 (0.25)	1.14
2017960	1.33 (0.18)	611	14	7.321 (0.221)	383 ± 29	306 ± 25 (0.111)	475 ± 33 (0.145)	-	-	-	0.144 (0.04)	2.64 (0.15)	1.3
2017962	1.178 (0.15)	1115	19	8.786 (0.128)	273 ± 24	245 ± 18 (0.012)	379 ± 19 (0.024)	11.27	66	1.61	0.0171 (0.01)	3.28 (0.34)	1.27

Table 5.2: Apatite fission track (AFT) results for each sample. Measured data is also shown, where ρs = counted AFT density (in 10^5 tracks/ cm^2) with the standard deviation in brackets, Ns = number of fission tracks counted, N = number of grains counted, ^{238}U = concentration of ^{238}U with the standard deviation of the ^{238}U indicated by the brackets, Central age = apatite fission track central age in Ma (lower and upper age are all AFT age populations of their respected samples (Cl % is the chlorine percentage for their respected age peak)), l_m = average confined AFT length, n = number of confined tracks counted, σc = standard deviation of the confined tracks, Cl % = the average chlorine percentage) with the standard deviation in brackets, F % = the average fluorine percentage) with the standard deviation in brackets, and D_{par} = the average etch pit length in μm.

5.4 Results

5.4.1 Apatite fission track data

All AFT data are displayed in Table 5.2 and radial plots for all samples are shown in Figure 5.3.

Sample 2017962 yields a central age of 273 ± 24 Ma with significant age dispersion (36%). Using the automatic mixture model in *Radial Plotter* (Vermeesch, 2009), two age-components were differentiated of 379 ± 19 Ma (49% of data) and 245 ± 18 Ma (24% of data) with minor younger resetting occurring on select grains. This open jaw feature (Figure 5.3) has been identified in previous work on plutonic rocks, such as O'Sullivan and Parrish (1995), who suggest the two populations are differentiated by Cl percentage, as varying Cl concentrations are known to influence the annealing rate for each grain (Green et al., 1986). There is evidence for further separation indicated by the differing ^{238}U ppm (Figure 5.3). The effects of U ppm on AFT annealing has been debated by the community (e.g. Green & Duddy, 2006; Hendriks & Redfield, 2005; Kohn et al., 2009), however, the variation in ^{238}U concentration across age populations from this study indicate it may have some effect on annealing and there seems to be an apparent trend of higher uranium concentrations for the younger age-group and vice versa. Overall, more data is required to understand the meaning of this relationship as uranium concentrations are currently not used as a kinetic parameter for fission track annealing.

The older age peak consists of apatites with a higher average Cl % of 0.0239 wt% and lower U contents (mean 5.8 ppm). The younger age peak consists of grains with a lower average Cl %

of 0.0123 grains and higher U contents (mean 14.5 ppm). The AFT length distribution yields a mean length of ~11.3 µm with a standard deviation of 1.61 µm.

The central age for sample 2017960 is 383 ± 29 Ma with a dispersion of 23%, which was decomposed into two age populations of 475 ± 33 Ma (53% of data) and 306 ± 25 Ma (47% of data). The individual AFT ages show minor scatter between these two age populations. Similar to sample 2017962, the older age population contains the higher Cl % (average of 0.151 wt%) with lower U contents (average of 4.37 ppm), while the lower Cl % (average of 0.134 wt%) with higher U (average of 11.3 ppm) grains make up the younger age population. For this sample, insufficient AFT length data were obtained for a reliable length-frequency distribution.

Sample 9594 yields a central age of 403 ± 27 Ma (20% dispersion) with only one age population present in the sample (average U of 5.2 ppm, average Cl % of 2.4 wt%). However, the presence of younger grains indicates there has been some reheating post ca 400 Ma. The AFT length distribution is slightly bi-modal (mean length of ~12.3 µm) with a relatively large standard deviation of 1.64 µm, which further supports the minor reheating after ca 400 Ma.

Excluding two outliers in sample 9582, a central age of 343 ± 26 Ma was obtained with only 4.6% dispersion (average U of 5.6 ppm). No reliable length-frequency distribution could be obtained due to insufficient AFT length data.

Sample 9528 yields a central age of 276 ± 26 Ma with a dispersion of ~25%. One age population can be defined at 325 ± 29 Ma (72% of data) with minor resetting of younger, high U (average U of 17.8 ppm) grains. This Carboniferous AFT age peak correlates well with the populations defined in the previously discussed samples and consists of the lower U (average U of 6.3 ppm) grains. No reliable length-frequency distribution could be obtained due to insufficient AFT length data.

Most apatite grains from sample 9508 suffered from having extensive U zonation and large inclusions. Therefore, only five reliable age determinations could be used, which returned a central age of 414 ± 33 Ma (average U of 17.8 ppm). The AFT length-distribution is relatively broad with a mean length of 11.2 µm and 1.9 µm standard deviation.

Samples 7582 and 7571 are from the same monzonite body (sampled very close to each other), and since sample 7582 returned few reliable age determinations, both samples were pooled in the same radial plot. Their pooled central age was calculated as 376 ± 28 Ma. Given the large age dispersion (24%), they were separated into two populations with ages of 441 ± 28 Ma (68% of data) and 271 ± 25 Ma (32% of data). The age-discrimination is supported by relatively large Cl% variations, with high Cl % (average of 2.37 wt%) and low U (average of 4.2 ppm) grains forming the older age population and the low Cl% (average 1.55 wt%) with high U (average of 14.1 ppm) grains constraining the younger age population. The AFT length-distribution (mean length of 12.9 µm, 1.3 µm standard deviation) suggests moderately fast cooling through the AFT partial annealing zone (e.g. Wagner & van den Haute, 1992).

For one additional sample (7327), no reliable AFT age determination could be obtained due to anomalously low ^{238}U concentrations in the apatite grains (Table 5.3) and, therefore, no results are displayed in Figure 5.3 for this sample. However, this sample was still analysed for (U–Th–Sm)/He dating, since the minimum uranium concentration required for (U–Th–Sm)/He dating is considerably lower (~1 ppm; Lippolt, Leitz, Wernicke, & Hagedorn, 1994) than the uranium concentration requirements for AFT dating.

When all the samples are pooled on the same radial plot, two main AFT age-populations are distinguished: 446 ± 18 Ma (56.4% of data, average U of 5.3 ppm), and 296 ± 17 Ma (31.7% of data, average U of 9.5 ppm), suggesting thermal events during the Late Ordovician, and early Permian. In addition, some grains with higher U concentrations seem to be partially reset by a younger event (Figure 5.3).

5.4.2 (U–Th–Sm)/He thermochronology

Apatite grains from samples 2017962, 9582 and 7327 and zircons from 2017962 (Table 5.3) were chosen for (U–Th–Sm)/He thermochronology, based on grain quality. The zircon (U–Th–Sm)/He (ZHe) results obtained for sample 2017962 show little dispersion with an average ZHe age of 356.4 ± 20.4 Ma, which is in good agreement with the oldest AFT population obtained for this sample (379 ± 19 Ma). However, it is worth noting that the zircon crystals yield relatively high concentrations of U and Th (Table 5.3) and therefore, these grains have likely undergone a degree of He diffusion due to alpha-radiation damage (Guenthner, Reiners, Ketcham, Nasdala, & Giester, 2013). The reported ZHe age for this sample should, therefore, be regarded as the minimum age at which this sample cooled through the ZHe closure temperature (Reiners et al., 2004). The apatite grains from 2017962, in comparison, produced highly dispersed (U–Th–Sm)/He (AHe) age data that can be clustered into two components of 199.6 ± 12.8 Ma based on two grains and 97.2 ± 6.6 Ma based on two grains (Table 5.3). The older of these two AHe clusters slightly post-dates the youngest obtained AFT population for this sample (245 ± 18 Ma). However, this age does not correlate well with the AHe ages collected from samples 9582 and 7327. It is possible this age is "too old" (Belton, Brown, Kohn, Fink, & Farley, 2004; Farley, 2002) and could be affected by He zonations, micro-inclusions, zoned grain-boundary phases, He implantations, grain size or grain-fragment length (Belton et al., 2004; Farley, 2002; Murray, Orme, & Reiners, 2014; Wildman et al., 2016). Thus, only minimal interpretation has been made on this age. The youngest AHe data (ca 97 Ma), however, match with the youngest single-grain AFT age obtained for this sample. These results confirm that the study area was affected by a thermal event post-Permian event that has partially reset the high uranium apatite grains.

The analyses from sample 9582 produced an average AHe age of 82.2 ± 6.1 Ma from four grains, which is significantly younger than the corresponding AFT age (342 ± 25 Ma) and therefore represents a separate thermal event or prolonged residence at upper AFT partial annealing zone temperatures. Sample 7327 records an average AHe age of 76.1 ± 6 Ma based

on five grains. As demonstrated, most AHe results for the study area are in good agreement with each other.

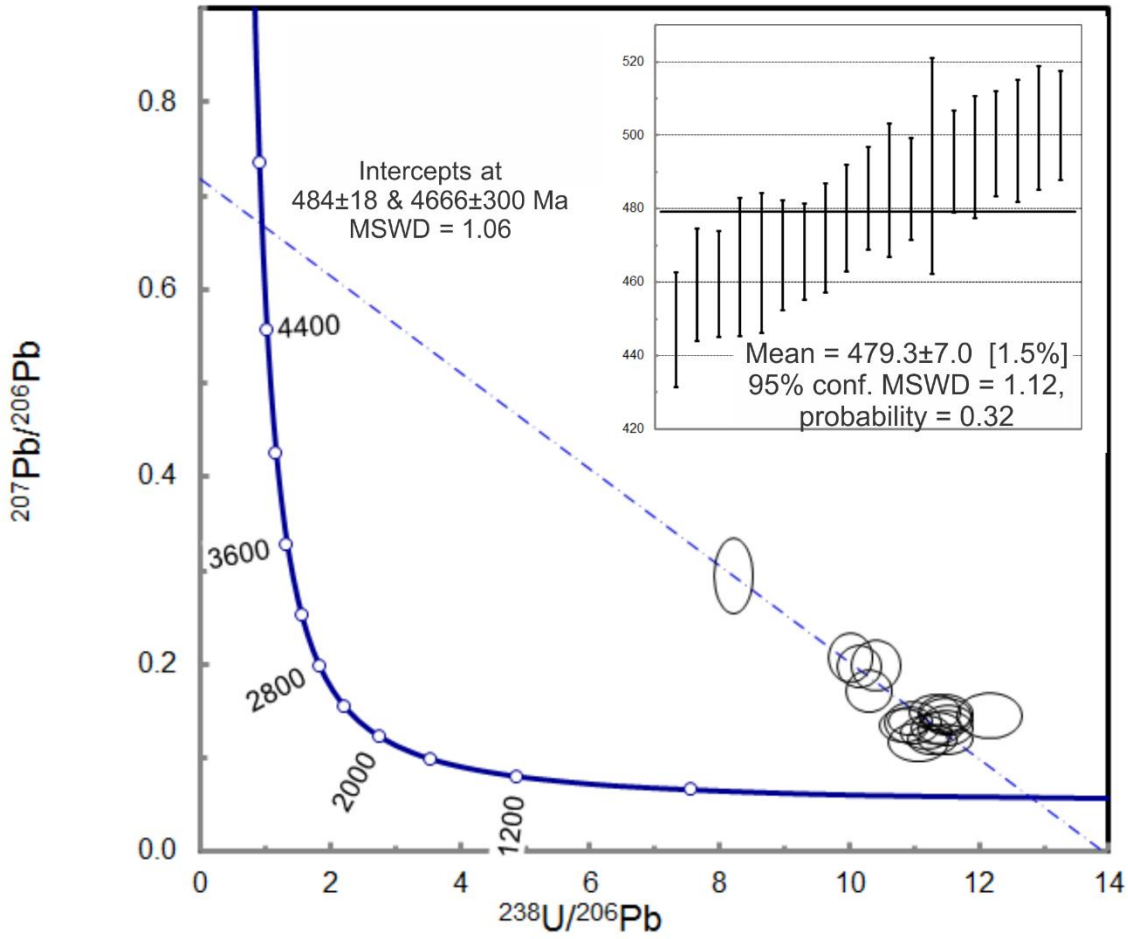

Figure 5.4: Terra-Wasserburg U-Pb plot of sample 9583 with a weighted mean plot for sample 9583 inset. All ages are given in Ma.

5.4.3 Titanite U-Pb dating

For sample 9583, an U-Pb intercept age was obtained of 484 ± 18 Ma. This is within error of the zircon U-Pb age of 497.5 ± 10 Ma for the Bundgadillina Monzonite (Rogers & Freeman, 1994). A ^{207}Pb corrected weighted mean age of 479 ± 7 Ma was also obtained (Figure 5.4). This was calibrated against the Mount Dromedary standard (measured lower intercept age of 94.5 ± 6 Ma compared to the accepted age of 98 ± 1 Ma; Smith, White, Chappell, & Eggleton, 1988). The age is interpreted as dating the cooling of the intrusion during crystallisation.

Sample	n	^{238}U	^{232}Th	^{147}Sm	$^{232}Th/^{238}U$	^{4}He	Ft	He Age	Avg He Age	AFT age
2017962 (ZHe)	3	882.7	172.1	-	0.19	28.56	0.63	352.2 ± 17.2	356.4 ± 20.4	245 ± 19 379 ± 19
		784.9	421.4	-	0.54	28.05	0.63	367.5 ± 24.6	356.4 ± 20.4	
		1013.7	318.9	-	0.31	59.53	0.70	349.4 ± 19.2	356.4 ± 20.4	
2017962 (AHe)	4	14.55	27.25	34.22	1.86	0.12	0.62	91.8 ± 6.7	97.2 ± 6.6	245 ± 19 379 ± 19
		37.76	97.61	93.81	2.57	0.18	0.53	102.6 ± 6.5	97.2 ± 6.6	
		40.77	132.29	104.36	3.22	1.09	0.64	190.2 ± 11.7	199.6 ± 12.8	
		29.32	51.88	56.87	1.76	0.31	0.56	209.0 ± 13.9	199.6 ± 12.8	
9582 (AHe)	4	15.45	63.47	11.08	4.08	0.07	0.56	61.1 ± 5.1	82.2 ± 6.1	342 ± 25
		12.93	60.12	15.99	4.62	0.10	0.61	65.7 ± 4.3	82.2 ± 6.1	
		13.77	63.86	20.03	4.60	0.11	0.56	99.2 ± 7	82.2 ± 6.1	
		17.68	63.89	20.47	3.59	0.08	0.50	102.9 ± 8.1	82.2 ± 6.1	
7327 (AHe)	5	16.70	51.99	26.61	3.09	0.03	0.48	62.6 ± 8.4	76.1 ± 6	-
		4.73	24.69	15.98	5.18	0.20	0.74	81.9 ± 5.4	76.1 ± 6	
		6.69	36.04	23.90	5.35	0.14	0.69	71.2 ± 4.6	76.1 ± 6	
		6.34	35.26	19.39	5.52	0.14	0.69	76.6 ± 4.9	76.1 ± 6	
		15.67	64.64	45.18	4.10	0.08	0.53	88.1 ± 6.8	76.1 ± 6	

Table 5.3: (U–Th–Sm)/He results indicating the helium (He) age, apatite fission track (AFT) age, number of grains within each age population (n), ^{238}U concentration (ppm), ^{232}Th concentration (ppm), ^{147}Sm concentration (ppm), $^{232}Th/^{238}U$, concentration of ^{4}He (ncc per µg), and Ft (Farley, Wolf, & Silver, 1996).

5.4.4 Thermal history modelling

The low temperature thermal history of the region was modelled using the computer software *HeFTy* (Ketcham, 2005), which models the path the rocks travelled in time–temperature space from a set time to the present using a combination of AFT age and length data, and other geological or thermochronometric constraints. In order to create a statistically acceptable model, fission tracks age and length data are the minimum input requirement. Length data were collected for samples 2017962, 9594, 9508 and 7571, all of which contained at least 34 confined track measurements. These were modelled using their thermochronometric constraints, a high temperature endpoint at 600 Ma and a low temperature constraint at present-day outcrop temperatures. All samples were assumed to be at, or near, the surface during the late Permian due to the presence of the Mount Margaret Surface (MMS; Figure 5.2).

For the Davenport Range, three samples were modelled based on AFT data only (samples 9594, 9508 and 7571; Figure 5.5a). The models for samples 9508 and 9594 show a broadly consistent thermal history of rapid cooling to subsurface temperatures from Delamerian times (ca 510–470 Ma) to ca 450 Ma, followed by a second, subtler cooling step at ca 350–300 Ma and minor reheating and cooling during the Cretaceous. The model for sample 7571 lacks a clear thermal event at ca 350–300 Ma and instead shows a slight thermal disturbance during the Jurassic (reheating to max. ~90°C), followed by slow cooling to the surface during the Cretaceous (Figure 5.5a).

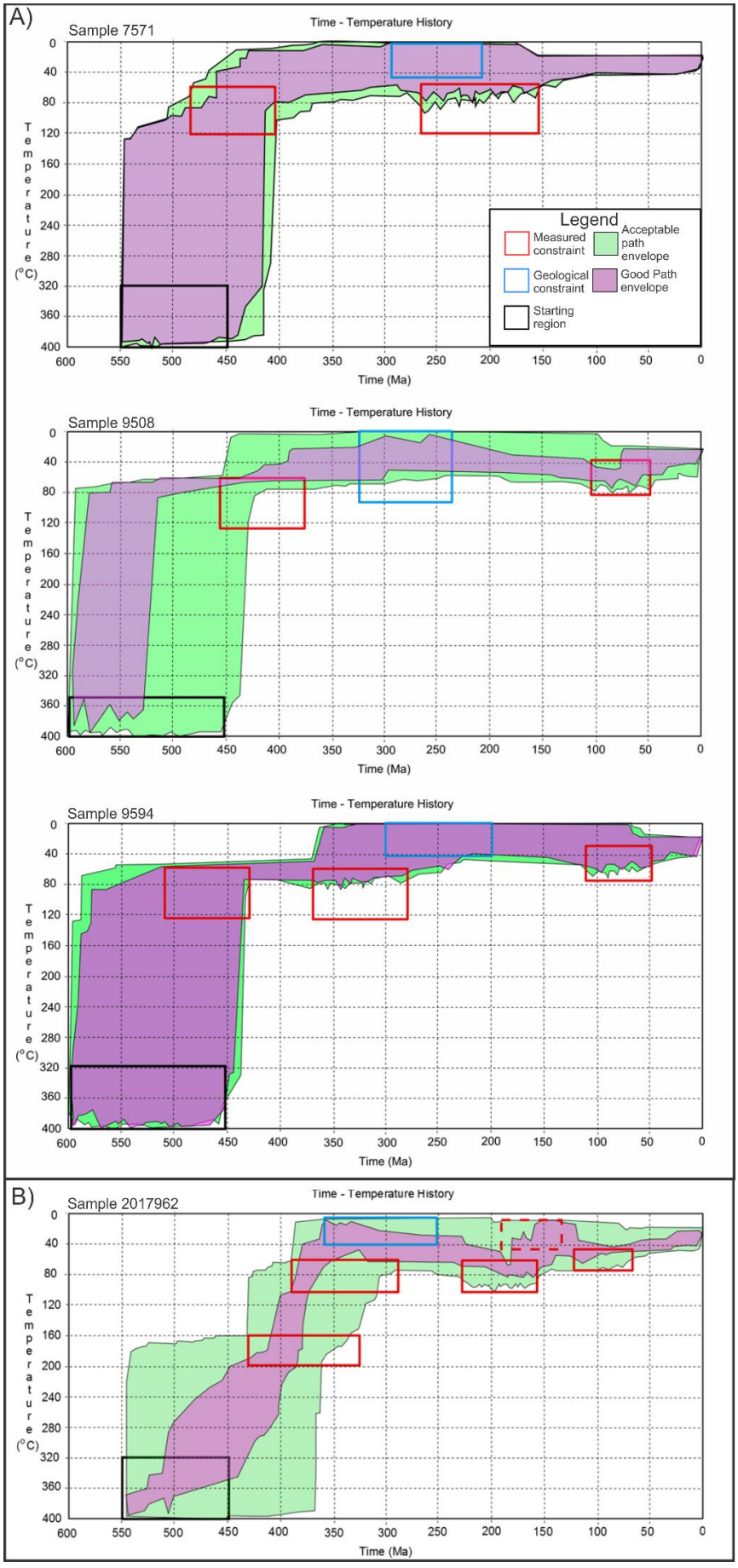
A)
Sample 7571
Time - Temperature History
Temperature (°C)
Time (Ma)
Legend
Measured constraint
Acceptable path envelope
Geological constraint
Good Path envelope
Starting region
Sample 9508
Time - Temperature History
Temperature (°C)
Time (Ma)
Sample 9594
Time - Temperature History
Temperature (°C)
Time (Ma)
B)
Sample 2017962
Time - Temperature History
Temperature (°C)
Time (Ma)

Figure 5.5 (previous page): The exhumation histories of samples 2017962, 7571, 9508 and 9594, modelled with the *HeFTy* software (Ketcham, 2005). Temperature plot illustrates the modelled pathway for each sample (A indicates samples from the Denison range while B indicates samples from the Davenport Range) from 400°C at 600–500 Ma to surface temperatures at the present. Each sample is constrained by measured constraints (apatite fission track ages, apatite helium ages, or zircon helium ages; indicated by red boxes on each plot) from this paper, geological constraints (indicated by blue boxes on each plot) such as the Mount Margaret Surface, and a high temperature starting constraint (indicated by a black box on each plot), where the rocks are assumed to be from 600–450 Ma. The dashed red box on sample 2017962 indicates a constraint based on AHe data, which needed a slight shift towards lower temperatures to find a sufficient number of statistically good model paths. The green region on each plot is the acceptable path envelope, while the pink region is the good path envelope. The goodness of fit merits for these paths are stated in Table 5.4.

The low temperature thermal history of sample 2017962, from the Denison Range, was modelled based on a combination of ZHe, AHe, AFT and geological data and therefore gives the most reliable model (Figure 5.5b). The model shows two-phases of cooling during the early Paleozoic. Initially, post-Delamerian cooling brought the samples to temperatures of ~200°C at ca 400 Ma, before increased cooling during the Devonian–Carboniferous bought the basement to surface temperatures. Geological evidence for early Permian exposure comes from the occurrence of the MMS, which was inserted as a modelling constraint. Subsequently, the model for the Denison Ranges shows two additional thermal perturbations at ca 220–180 Ma and ca 120–100 Ma. After the mid-Cretaceous event, cooling rates were modelled to be rather slow until surface exposure in the Neogene (Figure 5.6).

Sample	Paths tried	Acceptable paths	Good paths	Acceptable merit	Good merit
2017962	278491	2848	10	0.05	0.2
9594	10000	637	271	0.05	0.5
9508	35498	808	19	0.05	0.5
7571	10000	440	133	0.05	0.5

Table 5.4: *HeFTy* parameters including number of paths tried, number of acceptable paths, number of good paths, goodness of fit for acceptable paths merit, and goodness of fit for good paths merit for the four samples (2017962, 9594, 9508, and 7571).

5.5 Discussion

All the *HeFTy* models produced in this study are indicative of fast cooling from Delamerian times (ca 510–470 Ma) to near-surface temperatures at ca 450–300 Ma, depending on sample location. The main difference observed in the models for both ranges is the timing of cooling to shallow levels. For the Davenport Ranges models, near-surface temperatures were reached at ca 450 Ma shortly after the crystallisation age of the Bungadillina Monzonite. In contrast, the Denison Ranges model indicates that exposure was delayed until ca 380 Ma. Taking in account the ZHe age of ca 356 Ma, this requires rapid cooling during the early Carboniferous and little preservation of a pre-existing Delamerian signal (discussed further below).

During the Mesozoic, the thermal history models either indicate that (1) the rocks stayed at or near surface temperatures, or (2) minor thermal disturbances occurred during the Late Triassic–Early Jurassic and/or middle–late Cretaceous, followed by rapid shallow cooling to the surface. As discussed, none of the *HeFTy* models are unambiguous and fully encompass the full exhumation history of the ranges as no model takes all obtained thermochronological data into account. For this reason, a model that fits the multitude of thermochronological and geological data was created in Figure 5.6. Aside from the thermochonometric constraints, this model also takes into account the sedimentary history of the adjacent sedimentary basins to derive whether the cooling and reheating pulses can be linked to exhumation and sedimentary burial, respectively. This model is discussed further below.

5.5.1 Late Cambrian–Early Carboniferous

The first significant period of cooling within the ranges occurred from ca 470–440 Ma (Figure 5.3). These ages are interpreted as a result of the shallow intrusion and post-magmatic cooling of the Bungadillina Monzonite (titanite U-Pb from this study; Ambrose et al., 1981; Morrison, 1989; Rogers & Freeman, 1994), which post-dates the main Delamerian Orogeny in the Adelaide region (514–490 Ma; Foden et al., 2006), but overlaps with the first pulse of the Alice Springs Orogeny (ca 475 Ma; Haines, Hand, & Sandiford, 2001; Hand, Mawby, Kinny, & Foden, 1999; Mawby, Hand, & Foden, 1999) and the beginning of oroclinal bending during the Benambran Orogeny (Glen, 2005; Moresi et al., 2014).

The Denison and Davenport ranges show a somewhat different thermal history through the Paleozoic, where the Denison samples reveal differential cooling across the Denison Range, while the Davenport Range reveals cooling over a 200 m change in elevation (Figure 5.2; transects A–A′ and B–B′). The two samples from the Denison Range are separated by a large fault and exhibit different cooling histories (Figure 5.3). The eastern sample (2017960) preserves the oldest cooling event in the region and is ca 100 Ma older than the oldest preserved age of the western sample (2017962). This is caused by movement along the dividing fault, cooling and exhuming the western side from deeper crustal level compared to the eastern side. This is witnessed in the thermal history model (Figure 5.6) as the proposed path indicates the path the eastern sample cooled through time–temperature space during this time while the alternative path indicates the path the western sample cooled through.

In comparison, the samples on the Davenport Range preserve similar cooling histories. Samples 7571 and 7582 are located at the highest point in the region and preserve the oldest ages in the Davenport Range while the rest of the samples either preserve a younger Early Devonian or Carboniferous age. As all of the Davenport samples are located west of the Levi Fault, the difference in AFT ages are caused by the differing elevation of the samples (Figure 5.2; isochrons along transect B–B′) coupled with differing chemistry (Figure 5.3). The Devonian period of cooling is interpreted to be fuelled by south-directed deformation from the Alice Springs Orogeny (Haines et al., 2001) coupled with deformation from the Tabberabberan Orogeny (Glen, 2005).

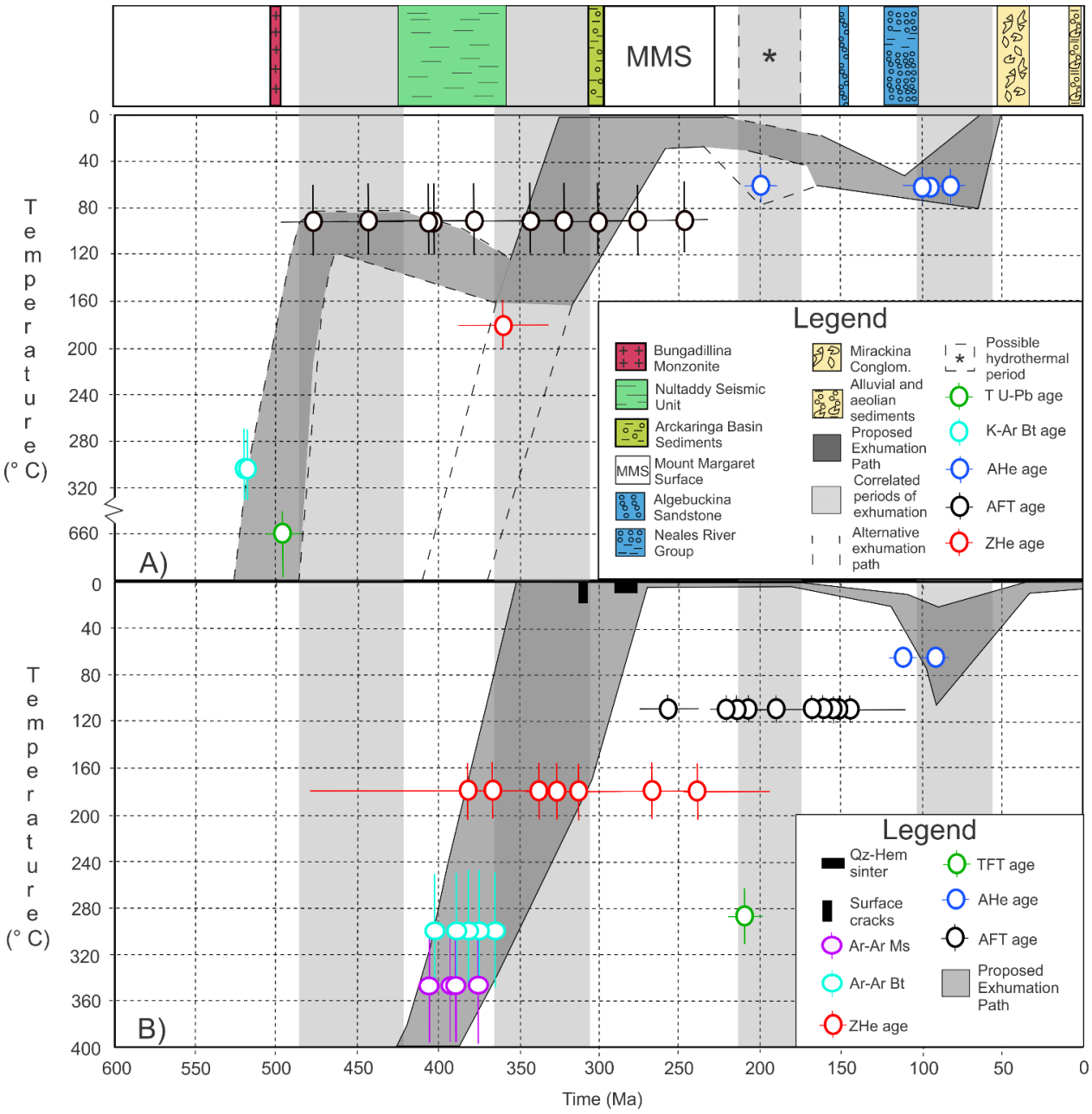

Figure 5.6: Proposed thermal history of the Peake and Denison Inliers through time–temperature space (Panel a) with inclusion of sedimentary constraints and compared to the exhumation history model of the Mt Painter region (Panel b; Weisheit et al., 2014). Apatite helium ages are indicated by blue dots, zircon helium ages by red dots, titanite uranium–lead ages by the green dot, Biotite Potassium–Argon ages by the light blue dots, and apatite fission track age populations by black dots. Through these ages, a best-fit exhumation model was constructed that matches all data, the sedimentological record of the adjacent basins and the estimated cooling rates from the *HeFTy* models. Alternative exhumation paths are indicated by dashed lines. The Mount Margaret Surface is also plotted, since this is a period of time where the rocks are known to be at the surface. The box containing the asterisk is a period of known hydrothermal activity in the Mt Painter region and possible hydrothermal activity in the Peake and Denison Inliers. The Mt Painter region time–temperature graph was adapted from Weisheit et al. (2014) and contains compiled data from Brugger, Foden, and Wulser (2011); Krieg, Alexander, and Rogers (1995); McLaren et al. (2002); Mitchell et al. (2002).

5.5.2 Middle Carboniferous–Middle Triassic

The next period of rapid cooling (samples 2017960, 9582, and 9528) was induced during the Carboniferous–early Permian, which placed the ranges at near surface temperatures at ca 320–280 Ma. This cooling period was quickly followed by the deposition of coarse clastic detritus of the Boorthanna Formation, and fine to medium clastic detritus of the Stuart Range and Mount Toondina Formations in the adjacent Arckaringa Basin at ca 300 Ma, providing independent sedimentological evidence for sediment-producing relief in the Peake and Denison study area (Figure 5.2). The lowest of those formations was deposited on a glacially incised surface (Crowell & Frakes, 1971; Wopfner, 1970). The lower Arckaringa Basin formed a restricted marine basin at that time (Hibburt, 1984, 1995; Wopfner, 1970) indicating that the ranges were near sea level during the early Permian. The presence of the upper Permian MMS, coupled with the presence of the Arckaringa Basin sediments, points towards the ranges undergoing exhumation from ca 340–250 Ma.

We interpret the Carboniferous exhumation as a response to the final phases of the southward directed deformation from the Alice Springs Orogeny. Several studies have shown that the Alice Springs Orogeny caused substantial crustal thickening throughout South Australia (Ballèvre, Möller, & Hensen, 2000), and locally shear-zone movement in the north Flinders Ranges (Pointon, 2010). It is also widely documented to have caused exhumation in South Australia within regions such as the Adelaide Fold Belt (Gibson & Stüwe, 2000) and the Flinders Ranges (Weisheit et al., 2014). More regional studies within South Australia have demonstrated the regional extent of this exhumation event (Boone et al., 2016; Gleadow et al., 2002; Kohn et al., 2002; Reddy et al., 2015).

5.5.3 Mesozoic–Cenozoic

There is evidence for shallow thermal perturbations during this time as indicated by AFT data (Figure 5.3) and AHe data (Table 5.3). As mentioned above, and illustrated in the radial plots, several high-U apatites yield AFT ages of ca 250–120 Ma, suggesting that a Cretaceous event may have partially reset older thermal events in the deeper exhumed samples of the study area. Given that the data are rather poorly constrained, the exact timing of this thermal perturbation cannot be clearly concluded from our AFT data-set. However, our abundant ca 100–75 Ma AHe data throughout the study area suggests a Late Cretaceous timing for a shallow cooling event.

Most of southern Australia was inundated by shallow marine conditions from ca 150 Ma to 100 Ma, as reflected in the deposition of the Algebuckina Sandstone and the Neales River Group sedimentary rocks (Rogers & Freeman, 1994). The Upper Cretaceous–lower Paleogene is characterised by a hiatus in the sedimentary record, which correlates well with the abundant ca 100–75 Ma AHe ages reported. It is therefore suggested that the ranges experienced renewed exhumation during the Late Cretaceous after sedimentary burial brought the basement rocks to ~80°C. There is evidence for thermal activity during this time both proximal and distal to the Peake and Denison Inliers (Gleadow et al., 2002; Kohn et al., 2002;

Mavromatidis, 2007; Mitchell et al., 2002; O'Sullivan, Kohn, Foster, & Gleadow, 1995; Tingate & Duddy, 2002), which supports the interpreted exhumation.

MacDonald et al. (2013), suggested that the Bight Basin (Figure 5.1) was sourced in a two stage process, firstly by a Cenomanian transcontinental river system (Lloyd et al., 2015; MacDonald et al., 2013; Veevers, 2000) before a younger evolution of this river system was rejuvenated in the Turonian–Maastrichtian by a phase of uplift along a broad arc stretching from the northern Flinders Ranges, through the Peake and Denison Inliers, to the eastern Musgraves (Tingate & Duddy, 2002) (Figure 5.1). The Late Cretaceous–early Paleogene AHe ages reported here could be used to support this rejuvenation model as it indicates cooling during this time. However, the Late Cretaceous is also the timing of deposition of the extensive fluvial Winton Formation, with paleocurrents and detrital zircons indicating a source from northeast Queensland and containing extensive labile volcanic detritus (Bryan et al., 1997; Tucker et al., 2013), similar to that seen in the upper delta lobe in the Bight Basin (J. Macdonald et al., 2012). It is also the time of continental rupture in Queensland (Bryan et al., 1997), and uplift (Zhang, Min, & Bryan, 2014), with northern Zealandia rifting from Australia.

Cretaceous exhumation has been widely observed throughout coastal South Australia (Gibson & Stüwe, 2000; Kohn et al., 2002; Mavromatidis, 2007). Stump and Fitzgerald (1992), and B. P. Kohn et al. (2002) previously linked exhumation in both Australia and Antarctica during this time period to the rifting and opening of the Southern Ocean. However, the apparent absence of similar age exhumation from the extensive Gawler Craton that makes up much of inland South Australia (Reddy et al., 2015) suggests that this northern extension may have a different origin. Heine, Müller, Steinberger, and DiCaprio (2010) modelled the dynamic topographic consequences of Australia moving over mantle gravity anomalies through the Cenozoic. Their model predicted that during the early Paleogene, southeast Australia moved off a dynamically supported high towards a low that advanced across the country from northwest to southeast. The model does not stretch back to the Late Cretaceous, but perhaps dynamic topography had a role in this phase of uplift witnessed in the AHe ages.

5.5.4 Comparison with exhumation studies within the Flinders Ranges

The Peake and Denison Inliers reveal several notable similarities with many other exhumation models. As seen in Figure 5.6b, Mt Painter is one region that has a comparable exhumation history, including AFT age peaks at 200–180 Ma, and a phase of burial before Late Cretaceous exhumation (Mitchell et al., 2002; Weisheit et al., 2014). Two out of the four periods of exhumation highlighted in the Peake and Denison Inliers are present in the Mt Painter Region as well. The only main difference between both models is the lack of evidence for pre-Devonian upper crustal exhumation in the Mt Painter region, indicating deeper exhumation levels. In this respect, a greater amount of overburden would have been erased by subsequent events as the total amount of exhumation in the Mt Painter region during the Devonian–Carboniferous is estimated to be over 10 km (Weisheit et al., 2014). The models also slightly differ around ca 200 Ma, where the Peake and Denison model suggests a poorly constrained, minor heating

event while the Mt Painter model puts forward a hydrothermal event during that time. This 200 Ma thermal period has also been noted with the Officer Basin, Cooper Basin, Gawler Craton, and in parts of the Adelaide Fold Belt (Boone et al., 2016; Gibson & Stüwe, 2000; Gleadow et al., 2002; Mavromatidis, 2007; Reddy et al., 2015; Tingate & Duddy, 2002).

5.6 Conclusions

Low-temperature thermochronology of the Peake and Denison Inliers revealed the following conclusions:

1. Apatite fission track data suggest that initially post-orogenic cooling from the Delamerian Orogeny, followed by initiation of the Alice Springs Orogeny, and orocline formation during the Benambran Orogeny cooled the basement to shallow crustal temperatures from temperatures in excess of 400°C during the Ordovician. The Tabberabberan Orogeny and the southward directed deformation from the Alice Springs Orogeny induced exhumation of the Peake and Denison Inliers to surface temperatures during the Devonian to Carboniferous, which is recorded by the presence of the upper Permian Mount Margaret erosion surface.
2. Final exhumation occurred during the Late Cretaceous–early Paleogene as recorded by apatite U–Th–Sm/He ages of 100–60 Ma. This exhumation pulse is thought to be related with the break-up of Australia from Zealandia in the east or Antarctica to the south. Dynamic topographic support may also have played a role.

5.7 Acknowledgements

This paper was made possible thanks to the financial support of the Geological Survey of South Australia and an Australian Research Council grant (ARC LE150100145). ASC is funded by an Australian Research Council Future Fellowship (FT120100340). Bradley McDonald (John De Laeter Center at Curtin University) is thanked for assistance with the U–Th–Sm/He methods and Ben Wade (Adelaide Microscopy) for assistance with the use of the LA-ICP-MS. AR publishes with permission of the director of the Geological Survey of South Australia. Barry Kohn, Peter Betts and an anonymous reviewer are thanked for their constructive reviews. This paper forms TRaX# 357.

5.8 References

Alexander, E. M., & Krieg, G. W. (1995). Stratigraphy – lower non-marine succession. In J. F. Drexel & W. V. Preiss (Eds.), *The Geology of South Australia. Vol. 2, The Phanerozoic* (Vol. Bulletin 54). Adelaide: South Australian Geological Survey.

Allender, J. F., Taylor, B. W., & Gilby, A. R. (1987). *Geophysical interpretations report. 1984 Hogarth-ARC. PELs 5 and 6 Arckaringa Block*. Open File Envelope South Australia Department of Mines and Energy.

Alley, N. F., & Gravestock, D. I. (1995). Middle Palaeozoic (Devonian). In J. F. Drexel & W. V. Preiss (Eds.), *The Geology of South Australia* (Vol. 54, pp. 43–45): South Australia Geological Survey. Bulletin.

Ambrose, G. J., Flint, R. B., & Webb, A. W. (1981). Precambrian and Palaeozoic geology of the Peake and Denison Ranges. *Geological Survey of South Australia Bullitin, 50*.

Armit, R. J., Betts, P. G., Schaefer, B. F., & Ailleres, L. (2012). Constraints on long-lived Mesoproterozoic and Palaeozoic deformational events and crustal architecture in the northern Mount Painter Province, Australia. *Gondwana Research, 22*(1), 207–226. doi:http://dx.doi.org/10.1016/j.gr.2011.11.003

Ballèvre, M., Möller, A., & Hensen, B. J. (2000). Exhumation of the lower crust during crustal shortening: an Alice Springs (380 Ma) age for a prograde amphibolite facies shear zone in the Strangways Metamorphic Complex (central Australia). *Journal of Metamorphic Geology, 18*(6), 737–747. doi:10.1046/j.1525-1314.2000.00289.x

Belton, D. X., Brown, R. W., Kohn, B. P., Fink, D., & Farley, K. A. (2004). Quantitative resolution of the debate over antiquity of the central Australian landscape: implications for the tectonic and geomorphic stability of cratonic interiors. *Earth and Planetary Science Letters, 219*(1–2), 21–34. doi:http://dx.doi.org/10.1016/S0012-821X(03)00705-2

Boone, S. C., Seiler, C., Reid, A. J., Kohn, B., & Gleadow, A. (2016). An Upper Cretaceous paleo-aquifer system in the Eromanga Basin of the central Gawler Craton, South Australia: evidence from apatite fission track thermochronology. *Australian Journal of Earth Sciences, 63*(3), 315–331. doi:10.1080/08120099.2016.1199050

Brugger, J., Foden, J., & Wulser, P.-A. (2011). Genesis and preservation of a uranium-rich paleozoic epithermal system with a surface expression (Northern Flinders Ranges, South Australia): radiogenic heat driving regional hydrothermal circulation over geological timescales. *Astrobiology, 11*, 499+.

Bryan, S. E., Constantine, A. E., Stephens, C. J., Ewart, A., Schön, R. W., & Parianos, J. (1997). Early Cretaceous volcano-sedimentary successions along the eastern Australian continental margin: Implications for the break-up of eastern Gondwana. *Earth and Planetary Science Letters, 153*(1–2), 85–102. doi:http://dx.doi.org/10.1016/S0012-821X(97)00124-6

Burtner, R. L., Nigrini, A., & Donelick, R. A. (1994). Thermochronology of Lower Cretaceous source rocks in the Idaho–Wyoming Thrust Belt. *American Association of Petroleum Geologists Bulletin, 78*(10), 1613–1636.

Callen, R. A., Alley, N. F., & Greenwood, D. R. (1995). Lake Eyre Basin. In J. F. Drexel & W. V. Preiss (Eds.), *The Geology of South Australia. Vol. 2, The Phanerozoic* (Vol. Bulletin 54). Adelaide: South Australia Geological Survey.

Carlson, W. D., Donelick, R. A., & Ketcham, R. A. (1999). Variability of apatite fission-track annealing kinetics; I, Experimental results. *American Mineralogist, 84*(9), 1213–1223. doi:10.2138/am-1999-0901

Cayley, R. A. (2011). Exotic crustal block accretion to the eastern Gondwanaland margin in the Late Cambrian–Tasmania, the Selwyn Block, and implications for the Cambrian–Silurian evolution of the Ross, Delamerian, and Lachlan orogens. *Gondwana Research, 19*(3), 628–649. doi:http://dx.doi.org/10.1016/j.gr.2010.11.013

Chew, D. M., Petrus, J. A., & Kamber, B. S. (2014). U–Pb LA–ICPMS dating using accessory mineral standards with variable common Pb. *Chemical Geology, 363*, 185–199. doi:http://dx.doi.org/10.1016/j.chemgeo.2013.11.006

Crowell, J. C., & Frakes, L. A. (1971). Late Paleozoic glaciation: Part IV, Australia. *Geological Society of America Bulletin, 82*, 2515–2540.

Czarnota, K., Hoggard, M. J., White, N., & Winterbourne, J. (2013). Spatial and temporal patterns of Cenozoic dynamic topography around Australia. *Geochemistry, Geophysics, Geosystems, 14*(3), 634–658. doi:10.1029/2012GC004392

Czarnota, K., Roberts, G. G., White, N. J., & Fishwick, S. (2014). Spatial and temporal patterns of Australian dynamic topography from River Profile Modeling. *Journal of Geophysical Research: Solid Earth, 119*(2), 1384–1424. doi:10.1002/2013JB010436

Danišík, M., Štěpančíková, P., & Evans, N. J. (2012). Constraining long-term denudation and faulting history in intraplate regions by multisystem thermochronology: An example of the Sudetic

Marginal Fault (Bohemian Massif, central Europe). *Tectonics, 31*(2), TC2003. doi:10.1029/2011TC003012

De Grave, J., Glorie, S., Ryabinin, A., Zhimulev, F., Buslov, M. M., Izmer, A., . . . Van den haute, P. (2012). Late Palaeozoic and Meso-Cenozoic tectonic evolution of the southern Kyrgyz Tien Shan: Constraints from multi-method thermochronology in the Trans-Alai, Turkestan-Alai segment and the southeastern Ferghana Basin. *Journal of Asian Earth Sciences, 44*(0), 149–168. doi:http://dx.doi.org/10.1016/j.jseaes.2011.04.019

Donelick, R. A., Ketcham, R. A., & Carlson, W. D. (1999). Variability of apatite fission-track annealing kinetics; II, Crystallographic orientation effects. *American Mineralogist, 84*(9), 1224–1234.

Donelick, R. A., O'Sullivan, P. B., & Ketcham, R. A. (2005). Apatite Fission-Track Analysis. *Reviews in Mineralogy and Geochemistry, 58*, 49–94.

Elburg, M. A., Andersen, T., Bons, P. D., Simonsen, S. L., & Weisheit, A. (2013). New constraints on Phanerozoic magmatic and hydrothermal events in the Mt Painter Province, South Australia. *Gondwana Research, 24*(2), 700–712. doi:http://dx.doi.org/10.1016/j.gr.2012.12.017

Elburg, M. A., Bons, P. D., Foden, J., & Brugger, J. (2003). A newly defined Late Ordovician magmatic–thermal event in the Mt Painter Province, northern Flinders Ranges, South Australia. *Australian Journal of Earth Sciences, 50*(4), 611–631. doi:10.1046/j.1440-0952.2003.01016.x

Fanning, C. M., Flint, R. B., Parker, A. J., Ludwig, K. R., & Blissett, A. H. (1988). Refined Proterozoic evolution of the Gawler Craton, South Australia, through U–Pb zircon geochronology. *Precambrian Research, 40–41*, 363–386. doi:10.1016/0301-9268(88)90076-9

Farley, K. A. (2002). (U–Th)/He dating: techniques, calibrations, and applications. *Reviews in Mineralogy and Geochemistry, 47*(1), 819–844. doi:10.2138/rmg.2002.47.18

Farley, K. A., Wolf, R. A., & Silver, L. T. (1996). The effects of long alpha-stopping distances on (U–Th)/He ages. *Geochimica et Cosmochimica Acta, 60* (21), 4223–4229. doi:http://dx.doi.org/10.1016/S0016-7037(96)00193-7

Foden, J., Elburg, M. A., Dougherty-Page, J., & Burtt, A. (2006). The timing and duration of the Delamerian Orogeny: correlation with the Ross Orogen and implications for Gondwana assembly. *The Journal of Geology, 114* (2), 189–210. doi:10.1086/499570

Foden, J. D., Elburg, M. A., Turner, S. P., Sandiford, M., O'Callaghan, J., & Mitchell, S. (2002). Granite production in the Delamerian Orogen, South Australia. *Journal of the Geological Society, 159* (5), 557–575. doi:10.1144/0016-764901-099

Foster, D. A., Murphy, J. M., & Gleadow, A. J. W. (1994). Middle Tertiary hydrothermal activity and uplift of the northern Flinders Ranges, South Australia: Insights from apatite fission-track thermochronology. *Australian Journal of Earth Sciences, 41* (1), 11–17. doi:10.1080/08120099408728108

Frost, B. R., Chamberlain, K. R., & Schumacher, J. C. (2001). Sphene (titanite): phase relations and role as a geochronometer. *Chemical Geology, 172* (1–2), 131–148. doi:http://dx.doi.org/10.1016/S0009-2541(00)00240-0

Galbraith, R. F., & Laslett, G. M. (1993). Statistical models for mixed fission track ages. *Nuclear Tracks and Radiation Measurements, 21* (4), 459–470. doi:http://dx.doi.org/10.1016/1359-0189(93)90185-C

Galbraith, R. F., Roberts, R. G., Laslett, G. M., Yoshida, H., & Olley, J. M. (1999). Optical dating of single and multiple grains of quartz from Jinmium Rock Shelter, northern Australia: Part i, experimental design and statistical models. *Archaeometry, 41* (2), 339–364. doi:10.1111/j.1475-4754.1999.tb00987.x

Gibson, H. J., & Stüwe, K. (2000). Multiphase cooling and exhumation of the southern Adelaide Fold Belt: constraints from apatite fission track data. *Basin Research, 12* (1), 31–45. doi:10.1046/j.1365-2117.2000.00110.x

Gillespie, J., Glorie, S., Zhang, Z., Xiao, W., Collins, A. S., Evans, N., . . . De Grave, J. (2015). Mesozoic reactivation of the Beishan, southern Central Asian Orogenic Belt: Insights from low-temperature

thermochronology. *Gondwana Research, in press. DOI: 10.1016/j.gr.2015.10.004*. doi:10.1016/j.gr.2015.10.004

Gleadow, A. J. W., Belton, D. X., Kohn, B. P., & Brown, R. W. (2002). Fission track dating of phosphate minerals and the thermochronology of apatite. *Reviews in Mineralogy and Geochemistry, 48* (1), 579–630. doi:10.2138/rmg.2002.48.16

Gleadow, A. J. W., Kohn, B. P., Brown, R. W., O'Sullivan, P. B., & Raza, A. (2002). Fission track thermotectonic imaging of the Australian continent. *Tectonophysics, 349* (1–4), 5–21. doi:http://dx.doi.org/10.1016/S0040-1951(02)00043-4

Glen, R. A. (2005). The Tasmanides of eastern Australia. *Geological Society, London, Special Publications, 246* (1), 23–96. doi:10.1144/gsl.sp.2005.246.01.02

Green, P. F., & Duddy, I. R. (2006). Interpretation of apatite (U–Th)/He ages and fission track ages from cratons. *Earth and Planetary Science Letters, 244* (3–4), 541–547. doi:http://dx.doi.org/10.1016/j.epsl.2006.02.024

Green, P. F., Duddy, I. R., Gleadow, A. J. W., Tingate, P. R., & Laslett, G. M. (1986). Calibration of the Phanerozoic Time Scale: thermal annealing of fission tracks in apatite. *Chemical Geology: Isotope Geoscience section, 59*, 237–253. doi:http://dx.doi.org/10.1016/0168-9622(86)90074-6

Guenthner, W. R., Reiners, P. W., Ketcham, R. A., Nasdala, L., & Giester, G. (2013). Helium diffusion in natural zircon: Radiation damage, anisotropy, and the interpretation of zircon (U–Th)/He thermochronology. *American Journal of Science, 313* (3), 145–198. doi:10.2475/03.2013.01

Haines, P. W., Hand, M., & Sandiford, M. (2001). Palaeozoic synorogenic sedimentation in central and northern Australia: a review of distribution and timing with implications for the evolution of intracontinental orogens. *Australian Journal of Earth Sciences, 48* (6), 911–928. doi:10.1046/j.1440-0952.2001.00909.x

Hand, M., Mawby, J. O., Kinny, P., & Foden, J. (1999). U–Pb ages from the Harts Range, central Australia: evidence for early Ordovician extension and constraints on Carboniferous metamorphism. *Journal of the Geological Society, 156* (4), 715–730. doi:10.1144/gsjgs.156.4.0715

Hasebe, N., Barbarand, J., Jarvis, K., Carter, A., & Hurford, A. J. (2004). Apatite fission-track chronometry using laser ablation ICP-MS. *Chemical Geology, 207*, 135–145.

Heine, C., Müller, R. D., Steinberger, B., & DiCaprio, L. (2010). Integrating deep Earth dynamics in paleogeographic reconstructions of Australia. *Tectonophysics, 483* (1–2), 135–150. doi:http://dx.doi.org/10.1016/j.tecto.2009.08.028

Hendriks, B. W. H., & Redfield, T. F. (2005). Apatite fission track and (U–Th)/He data from Fennoscandia: An example of underestimation of fission track annealing in apatite. *Earth and Planetary Science Letters, 236* (1–2), 443–458. doi:http://dx.doi.org/10.1016/j.epsl.2005.05.027

Hibburt, J. E. (1984). Review of exploration activity in the Arckaringa Basin region 1858 to 1983. *Report Book 84/1. Department of Mines and Energy. South Australia*.

Hibburt, J. E. (1995). Arckaringa Basin. In J. F. Drexel & W. V. Preiss (Eds.), *The geology of South Australia. Vol. 2, The Phanerozoic. South Australia.* (Vol. 54, pp. 73–76): Geological Survey. Bulletin.

Hopper, D. J. (2001). *Crustal evolution of paleo- to mesoproterozoic rocks in the Peake and Denison Ranges, South Australia.* (PhD Thesis), The University of Queensland, Brisbane (unpubl.). Retrieved from http://espace.library.uq.edu.au/view/UQ:273259

Ketcham, R. A. (2005). Forward and inverse modeling of low-temperature thermochronometry data. *Reviews in Mineralogy and Geochemistry, 58* (1), 275–314. doi:10.2138/rmg.2005.58.11

Kohn, B. P., Gleadow, A. J. W., Brown, R. W., Gallagher, K., O'Sullivan, P. B., & Foster, D. A. (2002). Shaping the Australian crust over the last 300 million years: insights from fission track thermotectonic imaging and denudation studies of key terranes. *Australian Journal of Earth Sciences, 49* (4), 697–717. doi:10.1046/j.1440-0952.2002.00942.x

Kohn, B. P., Lorencak, M., Gleadow, A. J. W., Kohlmann, F., Raza, A., Osadetz, K. G., & Sorjonen-Ward, P. (2009). A reappraisal of low-temperature thermochronology of the eastern Fennoscandia Shield

and radiation-enhanced apatite fission-track annealing. *Geological Society, London, Special Publications, 324* (1), 193–216. doi:10.1144/sp324.15

Krieg, G. W., Alexander, E. M., & Rogers, P. (1995). Eromanga Basin. In J. F. Drexel & W. V. Preiss (Eds.), *The Geology of South Australia, vol. 2, The Phanerozoic. South Australia Geological Survey, Bulletin* (Vol. 54, pp. 101–105).

Lippolt, H. J., Leitz, M., Wernicke, R. S., & Hagedorn, B. (1994). (Uranium + thorium)/helium dating of apatite: experience with samples from different geochemical environments. *Chemical Geology, 112* (1–2), 179–191. doi:http://dx.doi.org/10.1016/0009-2541(94)90113-9

Lloyd, J., Collins, A. S., Payne, J. L., Glorie, S., Holford, S., & Reid, A. J. (2015). Tracking the Cretaceous transcontinental Ceduna River through Australia: The hafnium isotope record of detrital zircons from offshore southern Australia. *Geoscience Frontiers*(0). doi:http://dx.doi.org/10.1016/j.gsf.2015.06.001

Ludwig, K. R. (1999). Using Isoplot/Ex, Version 2.01: a geochronological toolkit for Microsoft Excel. *Berkeley Geochronology Center Special Publication, No. 1a: 47*.

Macdonald, J., Backé, G., King, R., Holford, S., & Hillis, R. (2012). Geomechanical modelling of fault reactivation in the Ceduna Sub-basin, Bight Basin, Australia. *Geological Society, London, Special Publications, 367*(1), 71–89. doi:10.1144/sp367.6

MacDonald, J., D., Holford, S. P., Green, P. F., Duddy, I. R., King, R. C., & Backé, G. (2013). Detrital zircon data reveal the origin of Australia's largest delta system. *Journal of the Geological Society, London, 170*, 3–6.

Mavromatidis, A. (2007). Exhumation Study in the Cooper-Eromanga Basins, Australia and the Implications for Hydrocarbon Exploration. *Energy Sources, Part A: Recovery, Utilization, and Environmental Effects, 29*(7), 631–648. doi:10.1080/009083190957775

Mawby, J., Hand, M., & Foden, J. (1999). Sm–Nd evidence for high-grade Ordovician metamorphism in the Arunta Block, central Australia. *Journal of Metamorphic Geology, 17* (6), 653–668. doi:10.1046/j.1525-1314.1999.00224.x

McDowell, F. W., McIntosh, W. C., & Farley, K. A. (2005). A precise ^{40}Ar–^{39}Ar reference age for the Durango apatite (U–Th)/He and fission-track dating standard. *Chemical Geology, 214* (3–4), 249–263. doi:http://dx.doi.org/10.1016/j.chemgeo.2004.10.002

McLaren, S., Dunlap, W. J., Sandiford, M., & McDougall, I. (2002). Thermochronology of high heat-producing crust at Mount Painter, South Australia: Implications for tectonic reactivation of continental interiors. *Tectonics, 21* (4), 2-1-2-18. doi:10.1029/2000TC001275

Mitchell, M. M., Kohn, B. P., O'Sullivan, P. B., Hartley, M. J., & Foster, D. A. (2002). Low-temperature thermochronology of the Mt Painter Province, South Australia. *Australian Journal of Earth Sciences, 49* (3), 551–563. doi:10.1046/j.1440-0952.2002.00937.x

Moresi, L., Betts, P. G., Miller, M. S., & Cayley, R. A. (2014). Dynamics of continental accretion. *Nature, 508* (7495), 245–248. doi:10.1038/nature13033 http://www.nature.com/nature/journal/v508/n7495/abs/nature13033.html - supplementary-information

Morrison, R. S. (1989). *The Igneous Intrusive Rocks of the Peake and Denison Ranges within the Adelaide Geosyncline Volume II: Figures, Plates, Captions, Maps, Tables and Appendicies.* (Bachelor of Science PhD Thesis), University of Adelaide, Adelaide (unpubl.).

Müller, R. D., Flament, N., Matthews, K. J., Williams, S. E., & Gurnis, M. (2016). Formation of Australian continental margin highlands driven by plate–mantle interaction. *Earth and Planetary Science Letters, 441*, 60–70. doi:http://dx.doi.org/10.1016/j.epsl.2016.02.025

Murray, K. E., Orme, D. A., & Reiners, P. W. (2014). Effects of U–Th-rich grain boundary phases on apatite helium ages. *Chemical Geology, 390*, 135–151. doi:http://dx.doi.org/10.1016/j.chemgeo.2014.09.023

O'Sullivan, P. B., Kohn, B. P., Foster, D. A., & Gleadow, A. J. W. (1995). Fission track data from the Bathurst Batholith: Evidence for rapid mid-Cretaceous uplift and erosion within the eastern

highlands of Australia. *Australian Journal of Earth Sciences, 42* (6), 597–607. doi:10.1080/08120099508728228

O'Sullivan, P. B., & Parrish, R. R. (1995). The importance of apatite composition and single-grain ages when interpreting fission track data from plutonic rocks: a case study from the Coast Ranges, British Columbia. *Earth and Planetary Science Letters, 132* (1–4), 213–224. doi:http://dx.doi.org/10.1016/0012-821X(95)00058-K

Paton, C., Hellstrom, J., Paul, B., Woodhead, J., & Hergt, J. (2011). Iolite: Freeware for the visualisation and processing of mass spectrometric data. *Journal of Analytical Atomic Spectrometry, 26* (12), 2508–2518. doi:10.1039/C1JA10172B

Pearce, N. J. G., Perkins, W. T., Westgate, J. A., Gorton, M. P., Jackson, S. E., Neal, C. R., & Chenery, S. P. (1997). A Compilation of New and Published Major and Trace Element Data for NIST SRM 610 and NIST SRM 612 Glass Reference Materials. *Geostandards Newsletter, 21* (1), 115–144. doi:10.1111/j.1751-908X.1997.tb00538.x

Pointon, V. (2010). *Structure and Thermochronology of an E–W profile through the Mount Painter Province, Northern Flinders Ranges, South Australia: is this a southern example of deformation and exhumation driven by the Alice Springs Orogeny?* Thesis. Geology and Geophysics. The University of Adelaide, School of Earth and Environmental Sciences. Unpublished.

Radke, F. (1973). *Fission-Track dating*. Retrieved from (unpubl.):

Raiber, M., & Webb, J. A. (2008). Tectonic control of Tertiary deposition in the Streatham Deep-Lead System in western Victoria. *Australian Journal of Earth Sciences, 55* (4), 493–508. doi:10.1080/08120090801888610

Reddy, M., Glorie, S., Reid, A. J., & Collins, A. S. (2015). Phanerozoic cooling history of the central Gawler Craton: implications of new low-temperature thermochronological data. *Mesa Journal, 75*, 56–60.

Reiners, P. W., Spell, T. L., Nicolescu, S., & Zanetti, K. A. (2004). Zircon (U–Th)/He thermochronometry: He diffusion and comparisons with $^{40}Ar/^{39}Ar$ dating. *Geochimica et Cosmochimica Acta, 68* (8), 1857–1887. doi:http://dx.doi.org/10.1016/j.gca.2003.10.021

Reynolds, S. D., Mildren, S. D., Hillis, R. R., & Meyer, J. J. (2006). Constraining stress magnitudes using petroleum exploration data in the Cooper–Eromanga Basins, Australia. *Tectonophysics, 415*, 123–140.

Rogers, P., & Freeman, P. (1994). *Explanatory Notes for the Warrina 1 : 250 000 Geological Map*. Retrieved from

Russell, M., & Gurnis, M. (1994). The planform of epeirogeny: vertical motions of Australia during the Cretaceous. *Basin Research, 6* (2–3), 63–76. doi:10.1111/j.1365-2117.1994.tb00076.x

Rutherford, L., Hand, M., & Mawby, J. (2006). Delamerian-aged metamorphism in the southern Curnamona Province, Australia: implications for the evolution of the Mesoproterozoic Olarian Orogeny. *Terra Nova, 18* (2), 138–146. doi:10.1111/j.1365-3121.2006.00673.x

Sandiford, M. (2003). Neotectonics of southeastern Australia: linking the Quaternary faulting record with seismicity and in situ stress. *Geological Society of America Special Papers, 372*, 107–119. doi:10.1130/0-8137-2372-8.107

Sandiford, M. (2007). The tilting continent: A new constraint on the dynamic topographic field from Australia. *Earth and Planetary Science Letters, 261* (1–2), 152–163. doi:http://dx.doi.org/10.1016/j.epsl.2007.06.023

Smith, I. E. M., White, A. J. R., Chappell, B. W., & Eggleton, R. A. (1988). Fractionation in a zoned monzonite pluton: Mount Dromedary, southeastern Australia. *Geological Magazine, 125* (03), 273–284. doi:doi:10.1017/S0016756800010219

Smithies, R. H., Howard, H. M., Evins, P. M., Kirkland, C. L., Kelsey, D. E., Hand, M., . . . Belousova, E. (2011). High-temperature granite magmatism, crust–mantle interaction and the Mesoproterozoic intracontinental evolution of the Musgrave Province, Central Australia. *Journal of Petrology, 52* (5), 931–958.

Stock, M. J., Humphreys, M. C. S., Smith, V. C., Johnson, R. D., & Pyle, D. M. (2015). New constraints on electron-beam induced halogen migration in apatite. *American Mineralogist, 100* (1), 281–293. doi:10.2138/am-2015-4949

Stormer, J., Pierson, M. L., & Tacker, R. C. (1993). Variation of F and Cl X-ray intensity due to anisotropic diffusion in apatite during electron microprobe analysis. *American Mineralogist, 78*, 641–648.

Stump, E., & Fitzgerald, P. G. (1992). Episodic uplift of the Transantarctic Mountains. *Geology, 20* (2), 161–164. doi:10.1130/0091-7613(1992)020<0161:euottm>2.3.co;2

Tingate, P. R., & Duddy, I. R. (2002). The thermal history of the eastern Officer Basin (South Australia): evidence from apatite fission track analysis and organic maturity data. *Tectonophysics, 349* (1–4), 251–275.

Tucker, R. T., Roberts, E. M., Hu, Y., Kemp, A. I. S., & Salisbury, S. W. (2013). Detrital zircon age constraints for the Winton Formation, Queensland: Contextualizing Australia's Late Cretaceous dinosaur faunas. *Gondwana Research, 24* (2), 767–779. doi:http://dx.doi.org/10.1016/j.gr.2012.12.009

Twidale, C. R. (1994). Gondwanan (Late Jurassic and Cretaceous) palaeosurfaces of the Australian Craton. *Palaeogeography, Palaeoclimatology, Palaeoecology, 112* (1–2), 157–186.

Veevers, J. J. (2000). *Billion-year earth history of Australia and neighbours in Gondwanaland* (J. J. Veevers Ed.). Sydney: GEMOC Press.

Vermeesch, P. (2009). RadialPlotter: a Java application for fission track, luminescence and other radial plots. *Radiation Measurements, 44*, 409–410.

Waclawik, V. G., Lang, S. C., & Krapf, C. B. E. (2008). Fluvial response to tectonic activity in an intra-continental dryland setting: The Neales River, Lake Eyre, Central Australia. *Geomorphology, 102* (1), 179–188. doi:http://dx.doi.org/10.1016/j.geomorph.2007.06.021

Wagner, G. A., & van den Haute, P. (1992). *Fission track dating*: Kluwer.

Weisheit, A., Bons, P. D., Danisík, M., & Elburg, M. A. (2014). Crustal-scale folding: Palaeozoic deformation of the Mt Painter Inlier, South Australia. *Geological Society, London, Special Publications, 394*, 53–77. doi:10.1144/SP394.9

Wildman, M., Brown, R., Beucher, R., Persano, C., Stuart, F., Gallagher, K., . . . Carter, A. (2016). The chronology and tectonic style of landscape evolution along the elevated Atlantic continental margin of South Africa resolved by joint apatite fission track and (U–Th–Sm)/He thermochronology. *Tectonics, 35* (3), 511–545. doi:10.1002/2015TC004042

Wopfner, H. (1964). Permain–Jurassic history of the western Great Artesian Basin. *Transactions of the Royal Society of South Australia, 88*, 117–128.

Wopfner, H. (1968). Cretaceous sediments on the Mount Margaret Plateau and evidence for Neo-tectonism. *Quarterly Geological Notes, Geological Survey of South Australia, 28*, 7–11.

Wopfner, H. (1970). *Permian paleogeography and depositional environment of the Arckaringa Basin, South Australia.* Paper presented at the Second Gondwana symposium, Council for Scientific and Industrial Research, Scientia, South Africa.

Zhang, W., Min, K. K., & Bryan, S. E. (2014). *Thermal History of Drummond Basin, Queensland (Australia) from Apatite and Zircon (U–Th)/He Thermochronology.* Paper presented at the Abstract V43D-4923 presented at 2014 Fall Meeting, AGU, San Francisco, Calif., 15–19 Dec.

Summary and conclusions

The aim of this thesis was to constrain the thermal evolution of an intracontinental region over the last two billion years and explore the causes behind the differing thermal histories within different regions. This section summarizes the entire thermal history for the Gawler Craton and northern Adelaide Rift Complex.

Craton formation began at ~2550 Ma with basement development and coeval magmatism of the Sleaford and Mulgathing Complexes (Daly et al., 1998; Hand et al., 2007). These complexes were deformed and metamorphosed during the collisional ~2450 Ma Sleafordian Orogeny and reached temperatures of ~850 °C (Daly et al., 1998; Fanning et al., 2007; Reid et al., 2014; Halpin and Reid, 2016). **Chapter 1** revealed the rocks of the Sleaford and Mulgathing Complexes remained at high temperatures before cooling below ~550 – 350 °C at ~2300 Ma. Between ~2300 Ma and ~1850 Ma the study area likely experienced slow cooling and/or thermal quiescence, or the thermal record has been overprinted by later events.

In the eastern Gawler Craton, the emplacement of the Donington Suite and coeval Cornian Orogeny at ~1850 Ma initiated the second phase of craton formation (Jagodzinski, 2005; Hand et al., 2007). This orogeny reached temperatures of ~750 °C (Reid et al., 2008) with rocks from the Donington Suite cooling below >350 °C from high temperatures in the succeeding 150 Ma, as recorded in **Chapter 1**. This cooling was facilitated by rifting along the eastern margin of the Gawler Craton, which also resulted in the deposition of the Wallaroo Group sediments at ~1770 – 1740 Ma (Cowley et al., 2003). Moreover, a number of other volcano-sedimentary cover sequences were deposited onto the Archean basement around this time including the Price Metasediments, Moonabie Formation, Mount Woods Inlier Sediments, Peake Metamorphics, and metasediments within the Fowler and Nawa domains (Fanning et al., 1988; Parker et al., 1993; Oliver and Fanning, 1997; Daly et al., 1998; Jagodzinski, 2005; Hand et al., 2007; Lane et al., 2015). The widespread 1730 – 1690 Ma Kimban Orogeny ceased deposition of the Wallaroo Group while deforming and metamorphosing the central, western, and southern Gawler Craton (Hand et al., 2007; Reid and Fabris, 2015). The Kimban Orogeny heated the central Gawler Craton to temperatures of over 800 °C (Parker et al., 1993; Payne et al., 2008). The lack of preservation of this event in the apatite U-Pb dataset within **Chapter 1** suggests cooling relating to the Kimban Orogeny is poorly preserved and largely overprinted by later events.

Emplacement of the Hiltaba Suite and comagmatic Gawler Range Volcanics at shallow crustal levels began at ~1590 Ma (Giles, 1988; Creaser and White, 1991; Creaser, 1996; Daly et al., 1998; Budd et al., 2001; Skirrow et al., 2002; Allen et al., 2003; Allen et al., 2008). The Iron-Oxide-Copper-Gold deposits of the Olympic Domain also formed at this time, in association with emplacement of these igneous rocks and the associated hydrothermal fluid movement (McPhie et al., 2011; Ehrig et al., 2012). Moreover, the Hiltaba Event was associated with deformation within the Mt. Woods Inlier, which reached peak metamorphic temperatures of 750 °C during this time (Forbes et al., 2011). Due to the shallow emplacement, the Hiltaba Suite and Gawler Range Volcanics rocks

within the eastern Gawler Craton rapidly cooled from high temperatures and **Chapter 1** suggests that this happened within the 100 Ma following their emplacement at ~1590 Ma.

The youngest Proterozoic orogenic event recorded within the Gawler Craton is the ~1590 – 1560 Ma Kararan Orogeny, which deformed and metamorphosed the northeast and centre of the craton, including the Karari Shear Zone (Rankin et al., 1989; Fraser et al., 2012). **Chapter 1** suggests the rocks of the northwestern Nawa Domain cooled to mid-crustal levels at ~1400 – 1300 Ma after either remaining at high temperatures following the Kimban Orogeny or cooling after the Kimban and Kararan Orogenies before being reheated to high temperatures (> 350 °C) at ~1400 Ma. Throughout the Coompana, Musgrave and Madura provinces, there is evidence for juvenile magmatism and orogenesis at ~1500 – 1300 Ma which has been linked to a destructive plate margin and eventual amalgamation between cratonic Western Australia and the combined cratonic south and north Australia (Howard et al., 2015; Kirkland et al., 2017). This amalgamation caused cooling within the far northwestern Nawa Domain and also would have provided a source for reheating if the region had previously cooled below 350 °C following the Kararan Orogeny. This hypothesis is backed by the presence of Kararan aged Ar-Ar data closer to the Karari Shear Zone, indicating that the Karari region cooled below deep-crustal temperatures (>500 °C) following the Kararan Orogeny.

Following the cooling in the northwestern Nawa Domain, the northern Gawler Craton remained at temperatures below ~350 °C. **Chapter 2** reveals the oldest recorded time that the Gawler Craton cooled to shallow crustal temperatures (~120 – 60 °C), was in the Olympic Domain at ~1000 Ma. It is possible that other regions reached shallow crustal levels around this time but were later reheated above ~120 °C. In the northern Gawler Craton, deposition of the Officer Basin was occurring concurrently with the deposition of the Stuart Shelf (Gravestock, 1997). To the south of the Karari Shear Zone, the Mulgathing Complex reached surface temperatures during the Neoproterozoic, as revealed by **Chapter 3**. This region slowly cooled through the ~120 – 60 °C apatite partial annealing zone in the following ~300 Ma.

Neoproterozoic Rifting along the eastern margin of the Gawler Craton resulted in the deposition of the Adelaide Rift Complex and the Stuart Shelf, which overlies the Olympic Domain (Preiss, 1993). Alteration (likely of hydrothermal nature) is recorded in the basement rocks of the Olympic Domain (**Chapter 2**) and is associated with the deposition of the Adelaide Rift Complex.

The deposition of the Adelaide Rift Complex was terminated by the 515 – 490 Ma Delamerian Orogeny which deformed and metamorphosed the Adelaide Rift Complex (Foden et al., 2006). This event is recorded as regional cooling in the thermal history of the adjacent Gawler Craton, and Peake and Denison Inliers, as indicated by Reddy et al. (2015) and **Chapter 5**. The Delamerian Orogeny is not pervasively recorded throughout the Gawler Craton, likely due to reheating during subsequent events.

Chapters 2, 3, & 5 reveal that from 450 to 300 Ma multiple pulses of the Alice Springs Orogeny (Bradshaw and Evans, 1988; Mawby et al., 1999; Ballèvre et al., 2000; Haines et al., 2001; Buick et

al., 2008) affected a majority of the Gawler Craton. These orogenic pulses were southward directed from the orogenic centre in central Australia (Ballèvre et al., 2000). The first pulse, from ~450 – 400 Ma caused cooling through ~120 – 60 °C in the Olympic Domain, Peake and Denison Inliers, and central Gawler Craton. This is considered to be regional cooling in the central Gawler Craton and Olympic Domain but is interpreted to be fault-driven cooling within the Peake and Denison Inliers.

The Carboniferous pulse of the Alice Springs Orogeny is preserved consistently throughout the Gawler Craton. The southward directed deformation resulted in uplift of the Nawa Domain of the northern Gawler Craton causing reactivation along the Karari Shear Zone (**Chapter 3**). This uplift resulted in the cessation of deposition in the Neoproterozoic to late Devonian Officer Basin that overlies the Nawa Domain. The Christie Domain, to the South of the Karari Shear Zone, does not preserve any evidence of cooling at this time, suggesting that most of the deformation in this region was accommodated by the fault reactivation along the Karari Shear Zone or any uplift was not preserved due to the region being cooler than 60 ° C during the Phanerozoic. To the east, the Peake and Denison Inliers were exhumed to surface temperatures at this time (**Chapter 5**), while the Olympic Domain experienced regional cooling to average temperatures below 60 ° C (**Chapter 2**). The Adelaide Rift Complex underwent a majority of its shallow crustal cooling during the Carboniferous Pulse of the Alice Springs Orogeny (Weisheit et al., 2014) with the notable exception of the Willouran Ranges. **Chapter 4** suggests the Willouran Ranges were either at surface temperatures by this time or were later reheated by hydrothermal activity that reset the thermochronological data. By the end of this orogeny, a majority of the northern Gawler Craton and Adelaide Rift Complex are considered to be at surface temperatures.

The orogenic events of the Tasmanides assisted cooling within the Gawler Craton during the Alice Springs Orogeny. In particular, deformation relating to orocline development during the Late Ordovician to Early Silurian Benambran Orogeny (Moresi et al., 2014; Rosenbaum, 2018) coalesced with deformation from the early Alice Springs Orogeny to cool the Olympic Domain, Peake and Denison Inliers and the Mt. Painter Inlier (**Chapters 1 & 5**; Weisheit et al., 2014). While the Carboniferous Kanimblan Orogeny (Glen, 2005) is suggested to have facilitated deformation from the late Alice Springs Orogeny throughout the eastern Gawler Craton and Adelaide Rift Complex (**Chapters 1 & 5**; Weisheit et al., 2014).

Throughout the Gawler Craton and Adelaide Rift Complex, localised regions were reheated and cooled through later events. Hydrothermal activity within the Willouran Ranges and Mount Painter Inlier of the Adelaide Rift Complex reheated these regions at ~250 Ma and lasted for ~ 100 Ma within the Mount Painter Inlier, as reported in **Chapter 5** and by Weisheit et al. (2014). Within the Willouran Ranges, this hydrothermal activity was only short-lived, largely restricted to a narrow band along the major faults in the region and is suggested to have caused the Cu mineralisation throughout the region.

Chapter 5 reveals the Peake and Denison Ranges underwent minor burial during the Triassic – Jurassic before cooling to surface temperatures during the late Cretaceous, likely facilitated by the

rifting of Australia and Antarctica. A contemporaneous yet unrelated thermal age population is preserved within the Christie Domain, to the south of the Karari Shear Zone, during the Triassic (Chapter 3). However, more data are required to properly understand the cause of it. The youngest regional event within the Olympic Domain of Chapter 2 is recorded at ~200 Ma and is the result of the geothermal gradient within the Olympic Domain relaxing to temperatures cooler than ~ 60 °C at that time. However, the local area around the Olympic Dam deposit remained at higher temperatures until ~140 Ma, likely due to the enrichment of high-heat producing elements within the Olympic Dam deposit.

Although the presence of deformation events that effected the northern Gawler Craton are relatively consistent across the craton, the magnitude of the deformation varies greatly and how they are preserved in the thermal history. Furthermore, the northern Flinders Ranges differs again from the Gawler Craton despite being affected by the same Phanerozoic deformation events. The differences between the regions can be accounted for by key factors in each region. Crustal scale shear zones, such as the Karari Shear Zone, are the greatest factor in the differing apatite U-Pb ages within the Gawler Craton as they localise deformation by accommodating the stresses. However, the orientation is important as not all shear zones were reactivated within Apatite U-Pb temperatures. These major structures remain important avenues for stresses to be released at colder temperatures but deformation along them is often restricted to the margin of the craton.

Another important thermal history factor is the thickness of the overlying sedimentary packages. These can cover a region and act as a thermal blanket, particularly in regions with elevated geothermal gradients, such as the Olympic Domain. Moreover, the geothermal gradient itself plays an important role in the thermal architecture, especially at cooler temperatures where the sensitivity of a particular thermochronometer is high.

This can all be of little consequence if the region was reheated through hydrothermal activity. As is the case in the northern Adelaide Rift Complex, where hydrothermal activity has reset various thermochronometers and is even suggested to have caused the growth of new apatite grains. As a result, the region preserves little of its pre-hydrothermal thermal history.

References

Allen, S.R., McPhie, J., Ferris, G., Simpson, C., 2008. Evolution and architecture of a large felsic Igneous Province in western Laurentia: The 1.6 Ga Gawler Range Volcanics, South Australia. Journal of Volcanology and Geothermal Research 172, 132-147.

Allen, S.R., Simpson, C.J., McPhie, J., Daly, S.J., 2003. Stratigraphy, distribution and geochemistry of widespread felsic volcanic units in the Mesoproterozoic Gawler Range Volcanics, South Australia. Australian Journal of Earth Sciences 50, 97-112.

Ballèvre, M., Möller, A., Hensen, B.J., 2000. Exhumation of the lower crust during crustal shortening: an Alice Springs (380 Ma) age for a prograde amphibolite facies shear zone in the Strangways Metamorphic Complex (central Australia). Journal of Metamorphic Geology 18, 737-747.

Bradshaw, J.D., Evans, P.R., 1988. Palaeozoic tectonics, Amadeus Basin, central Australia. APEA Journal 28, 267-282.

Budd, A.R., Wyborn, L.A., Bastrakova, I.V., 2001. The metallogenic potential of Australian Proterozoic granites. Geoscience Australia, Record 2001/12.

Buick, I.S., Storkey, A., Williams, I.S., 2008. Timing relationships between pegmatite emplacement, metamorphism and deformation during the intra-plate Alice Springs Orogeny, central Australia. Journal of Metamorphic Geology 26, 915-936.

Cowley, W.M., Conor, C.H.H., Zang, W., 2003. New and revised Proterozoic stratigraphic units on northern Yorke Peninsula. Minerals and Energy South Australia Journal 29, 46-58.

Creaser, R.A., 1996. Petrogenesis of a Mesoproterozoic quartz latite-granitoid suite from the Roxby Downs area, South Australia. Precambrian Research 79, 371-394.

Creaser, R.A., White, A.J.R., 1991. Yardea Dacite; large-volume, high temperature felsic volcanism from the middle Proterozoic of South Australia. Geology 19, 48-51.

Daly, S.J., Fanning, C.M., Fairclough, M.C., 1998. Tectonic evolution and exploration potential for the Gawler Craton, South Australia. AGSO Journal of Australian Geology and Geophysics 17, 145-168.

Ehrig, K., McPhie, J., Kamenetsky, V.S., 2012. Geology and mineralogical zonation of the Olympic Dam iron oxide Cu-U-Au-Ag deposit, South Australia. Society of Economic Geologists Special Publication.

Fanning, C.M., Flint, R.B., Parker, A.J., Ludwig, K.R., Blissett, A.H., 1988. Refined Proterozoic evolution of the Gawler Craton, South Australia, through U-Pb zircon geochronology. Precambrian Research 40–41, 363-386.

Fanning, C.M., Reid, A.J., Teale, G., 2007. A geochronological framework for the Gawler Craton, South Australia. . South Australia. Geological Survey. Bulletin 55.

Foden, J., Elburg, M.A., Dougherty-Page, J., Burtt, A., 2006. The Timing and Duration of the Delamerian Orogeny: Correlation with the Ross Orogen and Implications for Gondwana Assembly. The Journal of Geology 114, 189-210.

Forbes, C.J., Giles, D., Hand, M., Betts, P.G., Suzuki, K., Chalmers, N., Dutch, R., 2011. Using P–T paths to interpret the tectonothermal setting of prograde metamorphism: An example from the northeastern Gawler Craton, South Australia. Precambrian Research 185, 65-85.

Fraser, G., Reid, A., Stern, R., 2012. Timing of deformation and exhumation across the Karari Shear Zone, north-western Gawler Craton, South Australia. Australian Journal of Earth Sciences 59, 547-570.

Giles, C.W., 1988. Petrogenesis of the Proterozoic Gawler Range Volcanics, South Australia. Precambrian Research 40–41, 407-427.

Glen, R.A., 2005. The Tasmanides of eastern Australia. Geological Society, London, Special Publications 246, 23-96.

Gravestock, D.I., 1997. Geological setting and structural history., In: Morton, J., Drexel, J.F. (Eds.), Petroleum Geology of South Australia, vol. 3. Officer Basin. South Australian Department of Mines and Energy Resources (SADME) Report Book 97/19., pp. 5-44.

Haines, P.W., Hand, M., Sandiford, M., 2001. Palaeozoic synorogenic sedimentation in central and northern Australia: a review of distribution and timing with implications for the evolution of intracontinental orogens. Australian Journal of Earth Sciences 48, 911-928.

Halpin, J.A., Reid, A.J., 2016. Earliest Paleoproterozoic high-grade metamorphism and orogenesis in the Gawler Craton, South Australia: The southern cousin in the Rae family? Precambrian Research 276, 123-144.

Hand, M., Reid, A., Jagodzinski, L., 2007. Tectonic Framework and Evolution of the Gawler Craton, Southern Australia. Economic Geology 102, 1377-1395.

Howard, H.M., Smithies, R.H., Kirkland, C.L., Kelsey, D.E., Aitken, A., Wingate, M.T.D., Quentin de Gromard, R., Spaggiari, C.V., Maier, W.D., 2015. The burning heart — The Proterozoic geology and geological evolution of the west Musgrave Region, central Australia. Gondwana Research 27, 64-94.

Jagodzinski, E., 2005. Compilation of SHRIMP U-Pb geochronological data, Olympic Domain, Gawler Craton, South Australia, 2001-2003. Geoscience Australia Record 20, 197.

Kirkland, C.L., Smithies, R.H., Spaggiari, C.V., Wingate, M.T.D., Quentin de Gromard, R., Clark, C., Gardiner, N.J., Belousova, E.A., 2017. Proterozoic crustal evolution of the Eucla basement, Australia: Implications for destruction of oceanic crust during emergence of Nuna. Lithos 278–281, 427-444.

Lane, K., Jagodzinski, E.A., Dutch, R., Reid, A.J., Hand, M., 2015. Age constraints on the timing of iron ore mineralisation in the southeastern Gawler Craton. Australian Journal of Earth Sciences 62, 55-75.

Mawby, J., Hand, M., Foden, J., 1999. Sm–Nd evidence for high-grade Ordovician metamorphism in the Arunta Block, central Australia. Journal of Metamorphic Geology 17, 653-668.

McPhie, J., Kamenetsky, V.S., Chambefort, I., Ehrig, K., Green, N., 2011. Origin of the supergiant Olympic Dam Cu-U-Au-Ag deposit, South Australia: Was a sedimentary basin involved? Geology 39, 795-798.

Moresi, L., Betts, P.G., Miller, M.S., Cayley, R.A., 2014. Dynamics of continental accretion. Nature 508, 245-248.

Oliver, R.L., Fanning, C.M., 1997. Australia and Antarctica; precise correlation of Palaeoproterozoic terrains, In: Ricci Carlo, A. (Ed.), The Antarctic region; Geological evolution and processes: Proceedings of the VII International Symposium on Antarctic Earth Sciences. Terra Antarctica Publication, Siena, Italy, pp. 163-172.

Parker, A.J., Daly, S.J., Flint, D.J., Flint, R.B., Preiss, W.V., Teale, G., 1993. Palaeoproterozoic, In: Drexel, J.F., Preiss, W.V., Parker, A.J. (Eds.), The geology of South Australia; Volume 1, The Precambrian: South Australia Geological Survey, Bulletin 54.

Payne, J.L., Hand, M., Barovich, K.M., Wade, B.P., 2008. Temporal constraints on the timing of high-grade metamorphism in the northern Gawler Craton: implications for assembly of the Australian Proterozoic. Australian Journal of Earth Sciences 55, 623-640.

Preiss, W.V., 1993. Neoproterozoic, In: Drexel, J.F., Preiss, W.V., Parker, A.J. (Eds.), The geology of South Australia. Vol.1, The Precambrian, South Australia Geological Survey, Bulletin 54.

Rankin, L.R., Martin, A.R., Parker, A.J., 1989. Early Proterozoic history of the Karari Fault Zone, northwest Gawler Craton, South Australia. Australian Journal of Earth Sciences 36, 123-133.

Reddy, M., Glorie, S., Reid, A.J., Collins, A.S., 2015. Phanerozoic cooling history of the central Gawler Craton: implications of new low-temperature thermochronological data. MESA Journal 75, 56-60.

Reid, A., Hand, M., Jagodzinski, E., Kelsey, D., Pearson, N., 2008. Paleoproterozoic orogenesis in the southeastern Gawler Craton, South Australia. Australian Journal of Earth Sciences 55, 449-471.

Reid, A.J., Fabris, A., 2015. Influence of Preexisting Low Metamorphic Grade Sedimentary Successions on the Distribution of Iron Oxide Copper-Gold Mineralization in the Olympic Cu-Au Province, Gawler Craton. Economic Geology 110, 2147-2157.

Reid, A.J., Jagodzinski, E.A., Fraser, G.L., Pawley, M.J., 2014. SHRIMP U–Pb zircon age constraints on the tectonics of the Neoarchean to early Paleoproterozoic transition within the Mulgathing Complex, Gawler Craton, South Australia. Precambrian Research 250, 27-49.

Rosenbaum, G., 2018. The Tasmanides: Phanerozoic Tectonic Evolution of Eastern Australia. Annual Review of Earth and Planetary Sciences 46, 291-325.

Skirrow, R.G., Bastrakov, E.N., Davidson, G.J., Raymond, O.L., Heithersay, P., 2002. The geological framework, distribution and controls of Fe-oxide and related alteration, and Cu-Au mineralisation in the Gawler craton, South Australia. Part II: Alteration and mineralisation, In: Porter, T.M. (Ed.), Hydrothermal iron oxide copper-gold and related deposits: A global perspective, 2. Porter GeoConsultancy Publishing, Adelaide, pp. 33-47.

Weisheit, A., Bons, P.D., Danisík, M., Elburg, M.A., 2014. Crustal-scale folding: Palaeozoic deformation of the Mt Painter Inlier, South Australia. Geological Society, London, Special Publications 394, 53-77.

Appendix 1

Chapter 1; Apatite U-Pb data.

2131385

Sample	U ppm	±	Th ppm	±	^{207}Pb-^{206}Pb	±	^{238}U-^{206}Pb	±	Error Correlation	^{206}Pb-^{238}U age	±	^{207}Pb corrected ^{206}Pb-^{238}U age	±	Discordance %	±
1	14.75	0.9	0.68	0.13	0.336	0.041	2.659574	0.3183	0.52822	2040	200	1340	220	78	14
2	16.8	1.2	0.202	0.061	0.274	0.018	3.484321	0.1942	0.51179	1624	81	1221	93	92	14
4	26.9	1.5	0.97	0.14	0.223	0.016	3.745318	0.2385	0.46794	1523	87	1250	100	64	14
5	53.7	4.2	0.46	0.085	0.1875	0.0087	4.166667	0.2951	0.655	1381	89	1192	95	56	12
6	23.4	1.6	0.134	0.057	0.237	0.019	3.690037	0.2451	0.33285	1544	92	1240	110	62	15
8	14.93	0.91	0.244	0.075	0.302	0.031	3.30033	0.2941	0.38114	1700	140	1230	150	72	17
9	28.6	1.9	0.39	0.072	0.223	0.018	3.745318	0.2244	0.21292	1523	80	1249	95	57	12
10	16.48	0.99	0.277	0.073	0.306	0.022	3.095975	0.2013	0.38418	1800	100	1290	110	71	16
11	10.4	0.52	0.287	0.053	0.287	0.02	3.058104	0.2525	0.30525	1820	130	1360	150	60	14
13	28.4	2.7	1.82	0.2	0.216	0.015	3.322259	0.309	0.10649	1690	130	1370	110	51	12
14	23.9	2.5	1.61	0.17	0.243	0.014	3.472222	0.1808	0.19574	1630	74	1289	82	54	12
16	15.37	0.72	0.117	0.031	0.289	0.017	3.215434	0.1758	0.35574	1741	81	1360	92	45	18
17	31.7	1.8	0.249	0.052	0.198	0.012	3.802281	0.1735	0.26887	1504	60	1319	66	40	17
18	7.16	0.3	0.15	0.038	0.425	0.039	2.631579	0.1385	0.60495	2073	91	1310	150	71	27
19	23.7	1.6	0.062	0.025	0.233	0.016	3.496503	0.2323	0.69003	1618	95	1370	110	64	29

2131379

Sample	U ppm	±	Th ppm	±	^{207}Pb-^{206}Pb	±	^{238}U-^{206}Pb	±	Error Correlation	^{206}Pb-^{238}U age	±	^{207}Pb corrected ^{206}Pb-^{238}U age	±	Discordance %	±
1	47.8	2.5	29	1.4	0.1671	0.0096	3.831418	0.1615	0.50633	1495	54	1365	65	32.3	7.5
2	38.6	1.7	29	1.3	0.1647	0.007	3.921569	0.1692	0.37368	1465	55	1339	61	33.2	7.2
3	14.7	0.81	1.4	0.12	0.299	0.017	3.058104	0.1403	0.063796	1822	72	1399	81	63.2	9.6
4	17.76	0.81	4.01	0.29	0.273	0.022	3.389831	0.1609	0.33507	1667	68	1323	86	61.3	6.4
5	32.7	1.7	6.9	0.37	0.1653	0.0079	3.745318	0.1543	0.28832	1524	59	1397	65	31.3	6.9
6	14.41	0.69	4.16	0.31	0.258	0.016	3.508772	0.1724	0.51439	1616	70	1310	80	59.2	9.2
7	13.27	0.5	3.95	0.24	0.231	0.016	3.472222	0.1326	0.24291	1630	55	1351	57	51	8.3
8	22.1	1.3	5.86	0.34	0.187	0.0096	3.597122	0.1294	-0.032892	1579	52	1409	58	38.9	7.1
9	45.5	2.8	24.2	1.6	0.1418	0.0075	4.175365	0.1709	0.2866	1383	51	1293	55	31.2	7
10	37.9	2.1	15.38	0.88	0.1522	0.0069	3.891051	0.212	0.27323	1472	70	1369	76	32.5	7
11	25.9	1.2	17.12	0.87	0.174	0.01	3.703704	0.1509	0.13492	1539	55	1395	61	37.4	7.1
12	11.98	0.61	1.72	0.16	0.305	0.019	2.949853	0.1392	0.23138	1879	78	1437	92	67.7	9.7
14	12.6	1	1.67	0.2	0.32	0.019	2.994012	0.1882	0.52323	1852	99	1380	110	70	12
15	16.58	0.98	4.53	0.3	0.237	0.015	3.378378	0.1826	0.25727	1668	79	1397	87	56.2	9.8
16	29.4	2.1	12.7	1.4	0.1666	0.008	3.787879	0.1722	0.18834	1510	62	1375	72	34.4	6.3
17	37.7	2.2	19.1	1	0.1578	0.0079	3.773585	0.1851	0.33349	1514	67	1402	75	33.1	7.3
18	37.6	2	17.17	0.68	0.1725	0.0083	3.773585	0.1709	0.42411	1515	63	1375	69	43.1	8.9
19	21.11	0.98	2.87	0.16	0.214	0.014	3.623188	0.1575	0.13088	1567	60	1346	66	55.9	9.3
20	22.7	1.4	7.05	0.45	0.224	0.011	3.424658	0.129	0.05326	1649	55	1404	62	53.4	7.1
21	27.5	2.3	9.07	0.87	0.212	0.013	3.344482	0.1902	0.36915	1681	85	1463	97	44	9.3
22	27.2	1.4	13.69	0.74	0.1833	0.0082	3.684598	0.091	-0.38252	1547	34	1383	32	36.5	6.8
23	32.3	2	25.1	1.5	0.1639	0.0076	3.846154	0.1479	-0.14659	1488	51	1359	56	32.2	6.3
24	50.7	3.2	20.7	1.4	0.1633	0.0075	3.918495	0.152	0.17573	1464	51	1340	55	37.4	6.5
25	24.3	1.2	5.38	0.31	0.196	0.013	3.597122	0.1294	0.001256	1581	51	1394	59	45.3	7.9
26	36.8	1.9	18	1	0.168	0.014	3.802281	0.2313	0.44428	1503	81	1375	97	31.5	7
27	28.1	1.8	17.2	1.2	0.186	0.01	3.546099	0.1509	0.25826	1598	63	1429	71	38	6.6
28	36.5	1.8	18.25	0.79	0.1668	0.0081	3.759398	0.212	0.22225	1520	76	1391	81	34.6	7.8
29	32.1	1.4	9.83	0.48	0.187	0.01	3.636364	0.1983	0.14529	1563	73	1397	81	35.6	5.4
30	57.8	3.5	30.6	1.9	0.1659	0.0089	3.636364	0.1455	0.60456	1565	57	1438	68	28.9	6.6
31	45.8	2.5	25.6	1.2	0.1534	0.0069	3.558719	0.1773	0.50587	1593	68	1490	79	28.2	7.5
32	40.5	2.3	11.34	0.62	0.177	0.011	3.745318	0.1824	0.48152	1522	66	1375	75	33.5	6.8
33	45.6	3.3	36.6	2.7	0.1598	0.0068	3.937008	0.1705	0.53247	1458	58	1341	65	29.7	6.5
34	21.3	0.94	8.41	0.49	0.226	0.019	3.389831	0.1609	0.5528	1665	69	1413	88	46	10
35	26.5	1	9.87	0.56	0.1798	0.0091	3.571429	0.1276	0.17978	1588	53	1432	57	33	6.6
36	27.3	1.3	8.79	0.35	0.226	0.013	3.496503	0.1467	0.38868	1619	61	1374	71	47.1	7.7
37	10.82	0.48	2.27	0.13	0.3	0.021	3.08642	0.1715	0.46428	1805	89	1390	110	69	11
38	61.2	4.8	34.9	2.8	0.1383	0.0045	3.846154	0.1775	0.29148	1488	61	1406	67	27.6	7
39	26.9	1.5	12.59	0.79	0.172	0.012	3.584229	0.1927	0.41871	1586	76	1449	89	31.1	9.2

2131386

Sample	U ppm	±	Th ppm	±	^{207}Pb-^{206}Pb	±	^{238}U-^{206}Pb	±	Error Correlation	^{206}Pb-^{238}U age	±	^{207}Pb corrected ^{206}Pb-^{238}U age	±	Discordance %	±
4	11.73	0.69	1.03	0.13	0.184	0.018	3.703704	0.2743	0.40292	1540	100	1380	120	38.5	8.9
5	20.9	1.4	2.42	0.21	0.164	0.012	3.558719	0.228	0.20979	1592	88	1468	98	32.6	7.1
6	11.3	0.63	0.84	0.11	0.254	0.031	3.30033	0.1634	0.23184	1704	74	1390	110	57	12
8	17.73	0.94	1.58	0.19	0.228	0.015	3.267974	0.2029	0.30316	1716	93	1460	110	48.8	6.7
9	19.5	1.2	2.11	0.24	0.195	0.015	3.597122	0.1682	0.21888	1579	63	1392	74	41.5	6.7
10	21.33	0.87	1.71	0.14	0.213	0.019	3.610108	0.2085	0.22466	1573	78	1355	96	50	11
11	31.2	2	5.29	0.28	0.173	0.015	3.484321	0.17	-0.38123	1626	72	1479	70	33.5	7.3
14	12.04	0.69	1.07	0.15	0.175	0.021	3.802281	0.3036	0.38527	1500	110	1360	130	38	10
15	18.75	0.97	1.71	0.15	0.187	0.016	3.663004	0.2013	-0.055122	1556	74	1384	78	39.8	7.9
16	17.69	0.98	0.704	0.099	0.184	0.017	3.496503	0.2201	0.47552	1621	88	1460	110	34.7	8.1
18	8.75	0.55	0.8	0.13	0.223	0.024	3.571429	0.1786	-0.006785	1589	71	1346	86	52	10
19	4.85	0.22	0.166	0.044	0.328	0.042	2.898551	0.3193	0.39941	1900	180	1430	240	65	15
20	19	1.6	1.69	0.21	0.171	0.013	3.816794	0.2622	0.054881	1496	89	1345	95	33.6	5.6
21	7.2	0.5	0.626	0.085	0.262	0.025	3.30033	0.2396	0.21302	1700	110	1380	120	59	11
23	10.71	0.37	0.99	0.1	0.206	0.02	3.623188	0.2363	-0.048409	1567	92	1360	96	45.4	8.4
24	29.8	3.3	1.83	0.29	0.166	0.014	4.065041	0.2479	0.72528	1416	78	1291	92	37	7.9
25	17	1.4	0.44	0.076	0.214	0.017	3.546099	0.2766	-0.082958	1600	110	1370	110	49.2	7.8
26	20.05	0.84	1.28	0.12	0.184	0.016	3.610108	0.1825	0.42491	1577	71	1397	89	41	11
27	12.96	0.74	1.58	0.22	0.183	0.018	3.623188	0.1838	0.5103	1568	69	1408	89	40.6	7.3
28	15.19	0.91	2.17	0.17	0.21	0.02	3.787879	0.2296	0.46186	1508	80	1300	100	46.7	8.4
29	33.1	1.7	700	110	0.65	0.039	1.203369	0.1057	-0.60191	3870	260	1370	190	30.4	8.6
32	17.35	0.93	0.896	0.088	0.205	0.02	3.521127	0.1984	0.52313	1608	82	1410	110	40.9	8.5
33	10.58	0.46	0.617	0.078	0.217	0.023	3.484321	0.2671	0.066615	1620	110	1390	120	47	11
36	16.63	0.92	1.22	0.13	0.19	0.025	3.597122	0.2588	0.40819	1575	99	1410	120	37	10
37	12.23	0.62	1.08	0.14	0.22	0.021	3.533569	0.2123	-0.033615	1605	87	1370	100	45	8
38	16.2	1.2	1.1	0.14	0.22	0.023	3.460208	0.2275	0.24547	1633	94	1359	87	44.5	8.4
39	32.3	2	2.4	0.22	0.178	0.016	3.90625	0.2289	0.62812	1466	79	1319	95	39.3	9.9

2131380

Sample	U ppm	±	Th ppm	±	^{207}Pb-^{206}Pb	±	^{238}U-^{206}Pb	±	Error Correlation	^{206}Pb-^{238}U age	±	^{207}Pb corrected ^{206}Pb-^{238}U age	±	Discordance %	±
2	16.6	1.4	18.2	1.1	0.254	0.015	3.676471	0.1757	-0.21078	1547	66	1228	70	60.8	5.6
3	30.5	3.2	33.5	3.6	0.254	0.014	3.584229	0.1413	0.30654	1584	57	1259	62	59.5	5.5
4	19.05	0.99	14.58	0.85	0.578	0.028	1.70068	0.162	-0.31887	2960	230	1150	130	67	13
5	18.46	0.9	24.9	1.2	0.288	0.016	3.424658	0.1759	0.45577	1647	73	1245	83	66.7	6.7
6	17.2	0.92	19.7	1.4	0.293	0.02	3.344482	0.1566	0.53448	1686	72	1267	90	66.5	8.2
7	3.95	0.22	13.3	0.73	0.422	0.034	2.544529	0.1424	0.42686	2130	100	1280	150	78	11
8	9.82	0.35	1.45	0.15	0.428	0.017	2.475248	0.1164	0.46071	2184	88	1281	87	76.5	7.7
10	8.9	0.47	3.71	0.24	0.388	0.026	2.475248	0.1777	0.14219	2180	130	1410	140	67	6.9
12	22.4	1.1	67.4	2.6	0.299	0.013	3.267974	0.1388	-0.49584	1721	66	1273	53	65.3	4.8
13	16.34	0.71	23.2	1.3	0.317	0.015	2.985075	0.1871	0.28614	1860	100	1316	81	68.2	5.7
14	12.41	0.44	11.53	0.52	0.324	0.019	3.164557	0.1302	0.21602	1766	66	1255	78	66.9	5.2
15	18.91	0.8	14.6	1.3	0.293	0.011	3.10559	0.164	0.6333	1794	84	1355	90	61	5.9
17	13.87	0.69	10.92	0.68	0.302	0.015	3.003003	0.2164	-0.024549	1850	120	1380	110	64.2	8.1

2131373

Sample	U ppm	±	Th ppm	±	^{207}Pb-^{206}Pb	±	^{238}U-^{206}Pb	±	Error Correlation	^{206}Pb-^{238}U age	±	^{207}Pb corrected ^{206}Pb-^{238}U age	±	Discordance %	±
1	10.37	0.33	7.74	0.24	0.295	0.023	2.824859	0.1516	0.45172	1950	89	1600	110	55.6	8.6
2	13.19	0.53	9.22	0.39	0.268	0.019	3.08642	0.181	0.28621	1807	94	1510	100	54.1	7.2
3	13.27	0.68	9.16	0.5	0.264	0.013	2.994012	0.1793	0.42976	1853	94	1560	110	53.2	7.2
5	11.08	0.5	7.29	0.34	0.275	0.018	2.932551	0.1548	0.6311	1887	87	1580	100	53.6	7.5
9	12.14	0.56	8.52	0.49	0.297	0.017	2.785515	0.1474	0.15279	1975	88	1608	95	56.2	6.1
10	16.38	0.82	5.63	0.37	0.215	0.015	3.10559	0.1543	0.73043	1796	77	1590	100	41.9	7.9
11	23	1	11.38	0.6	0.1954	0.0082	2.949853	0.1044	0.20391	1880	56	1722	61	30.5	3.5
12	10.66	0.52	7.31	0.41	0.296	0.02	2.680965	0.1294	0.22001	2038	85	1670	100	52.4	6.9
13	38.4	2.2	8.18	0.36	0.1335	0.0079	3.460208	0.1556	0.59178	1633	65	1576	73	16.4	3.8
14	14.2	0.64	5.15	0.39	0.24	0.015	2.832861	0.1445	0.57894	1946	86	1700	100	40.9	6.5
15	11.12	0.55	6.63	0.32	0.276	0.018	2.610966	0.15	0.6674	2090	100	1770	130	45.4	7.9
16	17.51	0.61	5.39	0.21	0.219	0.013	3.115265	0.1359	0.28844	1795	66	1591	75	39.9	5.1
17	17.6	1	5.95	0.37	0.208	0.01	3.08642	0.1429	0.42916	1805	72	1623	82	36	4.8
18	17.6	0.79	11.97	0.6	0.219	0.012	3.058104	0.1309	0.43345	1822	68	1620	81	38.8	5.2
19	15.21	0.56	5.46	0.29	0.238	0.011	3.076923	0.1325	0.36425	1813	67	1574	77	44.5	4.8
20	12.08	0.75	8.27	0.46	0.268	0.019	2.915452	0.1445	0.38812	1899	81	1600	100	49.3	7
21	12.56	0.58	9.21	0.48	0.296	0.016	2.531646	0.1538	0.67222	2140	110	1770	130	46.1	7.4
22	2.25	0.15	0.526	0.073	0.568	0.04	1.72117	0.1126	0.24173	3010	190	1620	190	58.4	9.9
23	14.8	1.2	5.21	0.4	0.245	0.018	3.003003	0.1713	-0.2709	1852	92	1596	91	43.1	5.5
24	12.76	0.34	4.52	0.26	0.25	0.018	2.770083	0.1611	-0.020198	1983	99	1710	110	39.9	6.3
25	10.06	0.72	6.7	0.45	0.311	0.029	2.380952	0.1247	-0.47935	2257	99	1828	95	43.6	6
26	12.48	0.5	4.51	0.25	0.256	0.023	2.967359	0.1585	-0.077501	1869	84	1590	100	45.3	7.2
27	9.11	0.74	5.54	0.63	0.298	0.022	2.666667	0.128	-0.10022	2052	83	1672	85	49.2	6.1
28	11.79	0.62	7.68	0.41	0.269	0.022	2.777778	0.1466	0.41483	1977	91	1670	120	45.1	7.9
29	16.4	0.56	10.04	0.4	0.217	0.015	2.86533	0.1806	0.65863	1970	130	1730	130	32.6	6.9
30	15.29	0.77	10.35	0.51	0.223	0.011	2.857143	0.1388	0.20693	1933	81	1723	91	34.1	4.6
31	10.14	0.43	7.07	0.35	0.305	0.017	2.65252	0.1618	0.12024	2060	110	1670	120	52	7.1
32	11.65	0.45	7.06	0.49	0.234	0.016	2.747253	0.2038	0.47734	1990	130	1770	150	36	7.6
33	16.19	0.65	11.6	0.52	0.2054	0.0098	2.762431	0.1526	0.52067	1990	93	1820	110	28.2	5.1
34	12.4	0.66	4.7	0.29	0.226	0.015	3.067485	0.1506	0.41332	1816	77	1601	92	40.2	6.4
35	11.91	0.55	9.25	0.44	0.269	0.017	2.747253	0.1585	0.38851	1995	99	1690	120	45.6	7
36	12.38	0.87	5.14	0.36	0.236	0.019	2.857143	0.1959	0.72061	1930	120	1710	140	39.2	8.9
37	45.6	3.1	12.68	0.92	0.1419	0.0079	3.378378	0.1598	0.60761	1672	72	1608	85	16.7	4.7
39	11.64	0.63	4.29	0.26	0.313	0.032	2.57732	0.3056	-0.13491	2170	160	1690	190	51	10
40	22.3	1.6	10.39	0.62	0.194	0.011	2.985075	0.1337	0.37146	1861	74	1707	87	29.4	5.1
41	11.68	0.69	7.22	0.38	0.262	0.024	2.724796	0.1708	0.64006	2050	140	1710	140	43.8	9
42	19.39	0.67	10.61	0.52	0.2	0.012	2.747253	0.1208	0.41618	1998	75	1838	94	26.7	5.2
43	30.9	2.1	11.21	0.67	0.186	0.014	2.95858	0.105	-0.03787	1878	58	1737	66	26	4.9

2131374

Sample	U ppm	±	Th ppm	±	^{207}Pb-^{206}Pb	±	^{238}U-^{206}Pb	±	Error Correlation	^{206}Pb-^{238}U age	±	^{207}Pb corrected ^{206}Pb-^{238}U age	±	Discordance %	±
1	14.37	0.72	0.97	0.11	0.349	0.02	2.673797	0.1573	0.51415	2040	110	1310	130	64.6	7.9
4	26.3	2	22	1.2	0.252	0.014	3.401361	0.2545	0.393	1660	110	1280	110	56.4	7
5	25.3	1.9	2.7	0.22	0.256	0.013	3.215434	0.2068	0.23617	1743	99	1340	100	53.6	6.5
6	18.98	0.69	2.68	0.21	0.3	0.017	3.04878	0.1208	0.27754	1830	61	1312	98	63.7	5
9	33.1	2.5	0.96	0.12	0.227	0.018	3.355705	0.4054	0.56656	1670	170	1300	150	49.6	8.6

2131367

Sample	U ppm	±	Th ppm	±	^{207}Pb-^{206}Pb	±	^{238}U-^{206}Pb	±	Error Correlation	^{206}Pb-^{238}U age	±	^{207}Pb corrected ^{206}Pb-^{238}U age	±	Discordance %	±
1	3.69	0.3	11.9	1	0.489	0.055	1.872659	0.2876	-0.47613	2720	310	1430	210	60	11
2	4.54	0.18	25.3	1.1	0.327	0.023	2.785515	0.1785	0.35947	1970	110	1430	120	59.6	9.5
3	10.83	0.52	40.8	1.7	0.186	0.017	3.676471	0.2298	0.070677	1546	88	1370	100	36.9	7.3
5	9.13	0.43	40.8	1.8	0.223	0.018	3.448276	0.1902	0.3514	1641	80	1390	100	46.2	7.5
6	6.49	0.39	31.4	2	0.245	0.03	3.322259	0.2539	0.081731	1690	110	1390	130	50	10
7	3.95	0.2	13.54	0.64	0.374	0.03	2.724796	0.2227	0.019393	2010	140	1280	230	76	14
8	3.69	0.36	16	1.8	0.431	0.032	2.145923	0.1566	0.45071	2460	150	1510	200	63	11
10	4.22	0.34	18.3	2.3	0.197	0.028	3.424658	0.1994	-0.015934	1650	83	1447	99	37	9.2
11	2.62	0.19	8.9	0.8	0.467	0.042	2.398082	0.1725	0.42613	2240	140	1250	180	79	12
12	3.55	0.22	7.56	0.42	0.301	0.023	2.832861	0.2006	-0.051847	1940	120	1450	140	55.5	7.5
13	18.18	0.93	112.6	4.9	0.22	0.012	3.246753	0.1476	0.1492	1729	67	1473	74	42.2	4.8
14	9.31	0.32	75.2	2.4	0.314	0.024	3.125	0.2246	0.34669	1780	110	1300	140	68	11
15	4.04	0.25	15.22	0.79	0.217	0.03	3.30033	0.2178	0.080085	1700	99	1460	130	41	11
16	9.42	0.56	54.7	3.4	0.275	0.026	3.144654	0.1681	0.46532	1779	82	1400	110	55.5	9
17	3.93	0.27	16.98	0.97	0.259	0.032	3.067485	0.2635	0.1439	1810	130	1440	180	53	14
18	11.75	0.34	50.8	2.2	0.198	0.011	3.636364	0.1587	-0.030108	1563	59	1362	62	40.2	4.3
19	5.94	0.35	20.8	1.4	0.226	0.021	3.546099	0.2138	0.39811	1599	83	1320	110	47.2	8
20	9.25	0.44	81.7	3.2	0.236	0.02	3.225806	0.1769	0.13817	1739	84	1450	100	45.7	7.3
21	7.31	0.39	17.32	0.79	0.286	0.017	2.906977	0.1268	-0.19292	1905	72	1473	77	53.1	5.2
22	6.93	0.31	25.9	1.1	0.304	0.03	2.857143	0.1469	-0.16023	1930	86	1450	100	56.1	7.7
23	4.85	0.39	23.6	1.9	0.397	0.023	2.358491	0.1446	0.27599	2270	120	1470	140	63.3	7.8
24	8.68	0.38	61.6	2.6	0.274	0.023	3.236246	0.1257	0.64706	1734	61	1390	120	55.4	8.4
25	5.65	0.27	24.4	1.2	0.321	0.026	2.994012	0.1703	0.40975	1852	91	1350	110	64	8.6
26	9.62	0.63	47.2	2	0.268	0.018	3.115265	0.1844	0.61521	1793	95	1430	120	52.9	7.9
27	6.22	0.41	49.8	3.1	0.352	0.021	2.666667	0.1564	0.13909	2050	100	1400	130	65.3	8.3
28	4.88	0.25	19.63	0.99	0.256	0.017	3.115265	0.1747	-0.15074	1794	87	1451	93	49.4	6.2
29	5.31	0.38	37.2	2.2	0.36	0.035	2.898551	0.252	0.41	1900	140	1310	160	71	12
30	6.67	0.25	37	1.6	0.246	0.026	3.246753	0.1687	0.41068	1728	76	1420	110	48.5	9.3
32	2.79	0.17	7.7	0.38	0.475	0.035	1.858736	0.1486	0.54966	2760	180	1570	220	57	12
33	10.43	0.5	63.4	3.1	0.17	0.013	3.508772	0.1477	0.53626	1615	60	1473	79	29.1	6
34	8.75	0.56	45.6	2.7	0.262	0.021	2.97619	0.186	0.51012	1860	100	1510	130	49.5	8.5
35	8.22	0.46	61.2	3.1	0.292	0.017	2.985075	0.1426	0.4092	1861	79	1427	95	57.6	6.6
36	2.89	0.14	7.78	0.38	0.365	0.044	2.538071	0.2255	0.42489	2130	160	1480	210	63	14
37	6.54	0.4	32	1.7	0.278	0.029	3.215434	0.2171	0.47445	1740	100	1360	130	58	10
38	10.02	0.34	50	4.2	0.219	0.02	3.472222	0.1567	0.31055	1629	67	1383	87	45.2	7.1
39	9	0.48	45.2	2.4	0.257	0.022	3.30033	0.1634	0.67474	1702	73	1370	100	54.1	8.4
40	11.38	0.57	44.4	2	0.244	0.014	3.344482	0.1454	0.14844	1683	65	1362	75	52.9	6
41	8.93	0.51	31.2	1.4	0.266	0.028	2.985075	0.2406	0.60737	1860	130	1450	150	50	11

2131371

Sample	U ppm	±	Th ppm	±	^{207}Pb-^{206}Pb	±	^{238}U-^{206}Pb	±	Error Correlation	^{206}Pb-^{238}U age	±	^{207}Pb corrected ^{206}Pb-^{238}U age	±	Discordance %	±
1	14.96	0.77	23.8	1.7	0.361	0.017	2.55102	0.1497	-0.26665	2120	110	1515	89	74.8	6.5
2	22.7	1.7	73.1	5.1	0.268	0.022	3.058104	0.2244	0.028717	1820	110	1490	130	62.5	8.8
3	19.5	1	48.1	2.5	0.345	0.031	2.898551	0.2604	0.19064	1900	150	1390	150	79	12
4	13.84	0.58	31.9	2.1	0.282	0.035	3.04878	0.1673	-0.35972	1823	90	1450	110	64	11
5	11.82	0.8	150	9.7	0.415	0.035	2.583979	0.2404	-0.15131	2100	160	1380	170	82	13
6	23.9	1.1	108.5	5.5	0.357	0.023	2.915452	0.1955	-0.13993	1900	110	1350	100	80.7	7.9
7	8.53	0.33	31.1	1.3	0.264	0.037	3.012048	0.2087	-0.39441	1880	130	1500	130	58	12
8	8.92	0.46	50.4	2.9	0.339	0.05	3.076923	0.2178	0.22958	1810	110	1390	180	76	16
9	18.5	1.1	81.2	4.9	0.243	0.025	3.311258	0.1974	-0.50182	1697	86	1415	88	56	8.3
10	25.8	1.8	52.9	3.4	0.268	0.018	3.184713	0.213	-0.12649	1750	100	1430	110	61.9	7.5
11	27.7	1.1	76.5	4.5	0.218	0.021	3.424658	0.2228	0.077289	1648	96	1400	120	48.5	9
12	11.02	0.75	35.7	2.5	0.345	0.031	2.583979	0.1669	0.014294	2100	110	1510	140	63.7	8.9
13	16.92	0.98	15.34	0.96	0.414	0.029	2.688172	0.1951	0.25878	2030	130	1320	140	83	11
14	7.13	0.48	15.98	0.87	0.531	0.051	2.096436	0.2417	0.39342	2490	230	1420	300	82	18
15	10.5	0.59	50.6	2.7	0.375	0.034	2.873563	0.2642	0.14643	1910	150	1340	170	81	12
17	21.7	1.2	10.61	0.79	0.278	0.02	3.278689	0.172	-0.071346	1712	78	1365	90	62.2	7
18	9.29	0.41	8.17	0.53	0.38	0.03	2.673797	0.2002	0.10985	2040	130	1380	160	76	12
19	28	1.7	81.6	4.5	0.282	0.018	3.095975	0.1438	-0.24328	1800	75	1430	80	59.3	6
20	10.71	0.58	34.2	2.4	0.362	0.04	2.5	0.1313	-0.31989	2164	99	1540	130	62.8	8.6
21	15.38	0.87	74	4.1	0.31	0.025	2.73224	0.209	-0.34569	2000	130	1540	130	55.4	7.4
22	20.9	1.1	74.5	3.9	0.291	0.029	3.184713	0.213	-0.22415	1760	100	1400	110	58.1	8.1

1039420

Sample	U ppm	±	Th ppm	±	^{207}Pb-^{206}Pb	±	^{238}U-^{206}Pb	±	Error Correlation	^{206}Pb-^{238}U age	±	^{207}Pb corrected ^{206}Pb-^{238}U age	±	Discordance %	±
2	20.14	0.87	0.584	0.074	0.278	0.015	2.994012	0.1165	0.58961	1854	64	1445	81	54.2	5.8
4	8.79	0.37	0.173	0.033	0.395	0.024	2.444988	0.1076	0.45371	2206	83	1390	110	65.6	8.3
5	10.42	0.49	0.02	0.014	0.378	0.017	2.48139	0.1478	0.10109	2180	110	1440	100	64.6	6.2
7	19.6	1.1	1.23	0.1	0.289	0.015	3.11042	0.088	0.16254	1796	44	1364	57	59.9	4.7
11	12.45	0.83	0.019	0.014	0.304	0.015	3.067485	0.16	0.70963	1817	85	1330	110	62.2	6.2
13	6.58	0.64	0.077	0.024	0.383	0.022	2.28833	0.1623	0.51157	2330	140	1510	170	57.6	8.2
14	16.97	0.74	0.019	0.013	0.301	0.012	2.95858	0.1313	0.35419	1874	75	1403	76	59.6	4.9
16	15.03	0.84	0.008	0.012	0.341	0.015	2.631579	0.1039	0.25527	2075	71	1461	82	60.9	5.2
18	3.68	0.21	0.037	0.015	0.54	0.034	1.808318	0.121	0.56343	2830	150	1310	190	63	11

1039423

Sample	U ppm	±	Th ppm	±	^{207}Pb-^{206}Pb	±	^{238}U-^{206}Pb	±	Error Correlation	^{206}Pb-^{238}U age	±	^{207}Pb corrected ^{206}Pb-^{238}U age	±	Discordance %	±
1	11.75	0.66	29	1.8	0.299	0.023	2.898551	0.21	0.66195	1900	120	1450	150	57	11
2	11.79	0.51	27	1.3	0.288	0.022	3.021148	0.1825	0.61267	1838	97	1410	130	53.2	9
3	6.06	0.67	14.4	1.2	0.352	0.029	2.597403	0.1956	0.30423	2150	180	1440	160	58	11
5	29.7	3.3	64.3	7.7	0.18	0.018	3.533569	0.2123	0.62395	1602	84	1440	110	33.2	8.7
6	21.2	3	51.5	7.4	0.226	0.02	3.205128	0.3595	0.23913	1740	170	1420	140	45.4	9.3
7	21	1.6	38.4	3.1	0.234	0.013	3.058104	0.1309	0.28498	1824	69	1525	82	43.3	5.3
8	39.5	2.6	76.2	4.1	0.166	0.012	3.623188	0.1838	0.43739	1569	69	1431	83	29.8	6.5
9	38.1	2.6	96.9	5.3	0.179	0.011	3.412969	0.1864	0.76593	1653	81	1481	95	31.2	6
10	34.4	2.3	87.6	4.4	0.1771	0.0074	3.460208	0.1437	0.040016	1636	61	1471	64	32.2	4.6
11	33.1	1.1	86.7	3.8	0.165	0.012	3.367003	0.2041	0.21717	1676	90	1540	100	25.9	6.3
12	10.68	0.43	22.67	0.9	0.321	0.019	2.65252	0.1478	0.23253	2058	98	1510	120	59.6	7.8
13	12.43	0.73	48.9	2.7	0.296	0.024	2.747253	0.1887	0.56572	1990	120	1530	160	56	10
14	66.9	4.3	203.2	9.4	0.1516	0.0071	3.623188	0.1575	0.029919	1570	63	1459	66	26.2	4.1

1039419

Sample	U ppm	±	Th ppm	±	^{207}Pb-^{206}Pb	±	^{238}U-^{206}Pb	±	Error Correlation	^{206}Pb-^{238}U age	±	^{207}Pb corrected ^{206}Pb-^{238}U age	±	Discordance %	±
1	10.9	0.48	1.08	0.1	0.428	0.027	2.320186	0.1507	0.59471	2300	130	1630	150	70.4	9.8
2	5.48	0.25	2.8	0.19	0.543	0.029	1.869159	0.1293	0.5142	2750	160	1620	180	72	11
3	19.5	1	0.018	0.035	0.258	0.014	3.095975	0.1629	0.43112	1799	84	1536	96	51.2	6.9
4	6.74	0.32	0.41	0.069	0.471	0.032	2.197802	0.1787	0.2517	2410	170	1600	170	71	11
5	8.26	0.47	0.647	0.079	0.392	0.03	2.610966	0.1704	0.37635	2080	120	1530	130	70.3	8.9
6	26.3	2	2.98	0.28	0.223	0.013	3.205128	0.1849	0.44534	1749	90	1550	100	42.6	6.5
7	5.03	0.49	0.061	0.058	0.486	0.029	1.926782	0.1225	0.38147	2690	140	1740	180	61.2	9.2
8	3.91	0.23	0	0	0.497	0.041	2.141328	0.1376	0.41662	2460	130	1580	180	75	12
9	3.97	0.24	1.13	0.12	0.597	0.032	1.855288	0.1446	0.2663	2770	170	1500	160	75.2	9.6
10	10.23	0.44	0.044	0.045	0.383	0.024	2.645503	0.196	0.53334	2060	130	1530	150	71.5	9.8
11	13.27	0.48	1.57	0.15	0.389	0.024	2.590674	0.1544	0.55208	2100	100	1550	120	69.4	8.4
12	8.49	0.44	0.68	0.12	0.411	0.023	2.293578	0.121	0.4136	2330	100	1680	120	63.9	8.1
13	8.27	0.48	1.71	0.15	0.465	0.038	2.257336	0.158	0.78728	2350	140	1590	180	72	12
14	3.26	0.2	0.054	0.055	0.627	0.06	1.811594	0.151	0.41076	2820	190	1470	260	74	16
15	2.68	0.13	0.007	0.048	0.638	0.072	1.748252	0.1498	0.52671	2890	210	1490	280	67	14
16	18.88	0.9	0.002	0.03	0.323	0.019	2.816901	0.1904	0.72202	1950	110	1560	130	60.4	9.2
17	5.08	0.32	0.69	0.11	0.505	0.034	2.123142	0.1713	0.43637	2470	170	1570	190	73	12
18	20.5	2.5	2.01	0.27	0.292	0.027	3.021148	0.3012	0.19309	1830	160	1520	170	56	11
19	4.36	0.22	0.94	0.11	0.682	0.05	1.72117	0.1333	0.64374	2930	190	1370	250	75	15
20	15.49	0.72	0.74	0.12	0.367	0.027	2.793296	0.1873	0.5081	1960	120	1480	130	68.2	9.6
21	11.95	0.7	0.92	0.15	0.408	0.036	2.45098	0.1502	0.47158	2200	120	1590	160	62	11
22	3.41	0.22	1.05	0.15	0.677	0.066	1.402525	0.1377	0.3372	3440	260	1660	360	51	17
23	7.56	0.38	2.32	0.19	0.52	0.042	2.252252	0.1522	0.59523	2360	130	1460	180	79	13
24	9.26	0.59	1.24	0.11	0.416	0.031	2.525253	0.1275	0.21837	2145	93	1510	110	67.3	9.9
25	7.26	0.53	0.016	0.067	0.411	0.039	2.645503	0.203	0.49931	2060	130	1480	180	70	12
26	15.2	1.2	1.72	0.24	0.381	0.026	2.659574	0.1698	0.15361	2050	110	1520	110	65.1	9
27	6.27	0.45	0.379	0.085	0.539	0.055	2.237136	0.1652	0.32413	2370	150	1400	190	80	14
28	19.9	1.3	2.28	0.26	0.322	0.028	2.890173	0.1921	0.69269	1910	110	1530	140	59	11
29	10.34	0.64	1.28	0.2	0.417	0.033	2.469136	0.1585	0.24498	2190	120	1560	140	63	9.9
30	13.32	0.88	0.53	0.12	0.391	0.025	2.80112	0.1962	0.033654	1960	120	1420	110	69.7	8.5

307

Sample	U ppm	±	Th ppm	±	^{207}Pb-^{206}Pb	±	^{238}U-^{206}Pb	±	Error Correlation	^{206}Pb-^{238}U age	±	^{207}Pb corrected ^{206}Pb-^{238}U age	±	Discordance %	±
1	6.9	1.6	38.3	7	0.425	0.046	2.427184	0.218	0.43045	2210	170	1500	210	73	19
2	5.58	0.6	18.4	2.5	0.384	0.029	2.544529	0.2719	0.10025	2120	190	1520	200	71	13
4	6.69	0.56	7.15	0.61	0.384	0.037	2.557545	0.2289	0.75512	2120	160	1530	190	68	14
6	15.9	1.3	62.7	5.5	0.213	0.018	3.174603	0.2016	0.045434	1761	95	1560	100	44.6	8.8
7	2.36	0.26	12.4	1.1	0.639	0.053	1.451379	0.1475	0.4211	3350	270	1560	320	57	21
9	11.05	0.76	56.2	4	0.287	0.034	2.941176	0.2768	0.52588	1880	150	1540	200	61	14
11	2.16	0.36	7.4	1.1	0.641	0.091	1.449275	0.21	0.038208	3310	400	1290	450	68	24
12	2.72	0.29	5.4	1.3	0.54	0.063	1.547988	0.1941	0.28058	3170	310	1680	380	64	20
13	17.4	2.9	96	15	0.276	0.029	2.666667	0.2133	-0.14859	2040	140	1660	150	56	14
14	2.96	0.19	13.97	0.81	0.643	0.063	1.445087	0.1671	0.28558	3360	300	1420	300	63	19
15	4.32	0.48	15.3	2.1	0.429	0.042	2.024291	0.2008	0.5662	2570	210	1790	270	62	19
16	9.71	0.49	29.8	1.7	0.305	0.033	2.898551	0.2268	0.69062	1910	130	1520	170	62	10
17	1.73	0.21	6.01	0.91	0.638	0.068	1.075269	0.185	0.43453	4130	500	1730	420	41	17
20	21.2	2.8	75	8.4	0.215	0.019	3.508772	0.2462	0.41482	1610	100	1470	150	50	12
22	13.3	1.6	64.6	6.1	0.248	0.018	2.747253	0.2113	0.73489	1990	130	1720	160	50	11
23	10.47	0.87	52	5.2	0.278	0.022	2.898551	0.1932	-0.19907	1910	110	1560	120	66.4	8.5
24	16.3	1.1	115.8	7.8	0.237	0.019	2.967359	0.2113	0.15454	1870	110	1610	120	49	11
26	8.49	0.75	34.5	3.6	0.313	0.029	2.73224	0.321	0.5685	2000	200	1610	240	62	16
27	6.26	0.5	32.6	2.9	0.407	0.029	2.398082	0.1553	0.20301	2240	120	1540	130	77	14
29	28.9	2.6	81.9	7	0.175	0.014	3.164557	0.2804	-0.2888	1760	140	1640	140	33.5	8.1
30	1.36	0.14	3.75	0.41	0.658	0.083	1.180638	0.1324	0.30244	3910	330	1510	460	48	18
32	9.6	1.3	32.7	4.6	0.301	0.039	2.673797	0.1501	-0.18191	2046	98	1630	120	62.6	7.6

501

Sample	U ppm	±	Th ppm	±	^{207}Pb-^{206}Pb	±	^{238}U-^{206}Pb	±	Error Correlation	^{206}Pb-^{238}U age	±	^{207}Pb corrected ^{206}Pb-^{238}U age	±	Discordance %	±
1	11.1	1.1	5.33	0.63	0.362	0.028	2.512563	0.1957	0.64791	2150	140	1620	130	73	13
2	4.71	0.32	2.1	0.29	0.565	0.047	1.626016	0.1771	-0.2062	3060	260	1660	290	64	17
4	7.32	0.68	3.81	0.47	0.442	0.042	2.217295	0.1967	0.61218	2390	180	1540	260	82	20
6	2.05	0.28	0.99	0.19	0.688	0.075	1.010101	0.153	0.2725	4360	470	1470	420	49	21
8	2.71	0.46	1.27	0.27	0.651	0.08	1.234568	0.1524	0.35404	3770	360	1480	470	58	21

2131395

Sample	U ppm	±	Th ppm	±	^{207}Pb-^{206}Pb	±	^{238}U-^{206}Pb	±	Error Correlation	^{206}Pb-^{238}U age	±	^{207}Pb corrected ^{206}Pb-^{238}U age	±	Discordance %	±
2	10.96	0.56	0.467	0.079	0.283	0.029	2.145923	0.1151	-0.6148	2460	110	2180	120	39	17
3	16.78	0.85	0.622	0.078	0.273	0.027	2.5	0.1563	-0.45692	2170	110	1930	100	52	27
4	25.6	2.8	6.82	0.85	0.207	0.014	2.525253	0.1913	-0.26696	2140	140	2030	150	59	35
5	6.4	0.26	0.004	0.019	0.46	0.031	2.04499	0.1798	-0.58572	2550	180	1940	130	66	28
7	57.3	5.8	13.7	1.3	0.201	0.013	2.631579	0.1108	-0.17301	2075	73	1958	78	43	22
8	17.2	1.2	0.99	0.12	0.234	0.022	2.427184	0.1591	-0.41197	2220	120	2050	120	38	19
9	14.54	0.75	1.85	0.14	0.205	0.021	2.604167	0.1221	0.1713	2091	84	1970	110	38	23
10	23.1	1.5	2.33	0.19	0.1826	0.009	2.659574	0.1061	-0.14037	2056	69	1968	79	28.5	9.6
11	3.91	0.19	0	0	0.368	0.055	2.421308	0.1935	0.35549	2220	150	1840	200	47	20
12	19.1	2	0.121	0.042	0.161	0.016	2.570694	0.1388	-0.003706	2116	99	2070	110	33	13
13	7.05	0.32	0	0.018	0.358	0.029	2.386635	0.1709	0.14183	2250	140	1870	160	53	23
14	37	2.2	5.43	0.6	0.1823	0.0092	2.680965	0.1294	0.11564	2040	83	1953	93	36	12
16	16.75	0.8	1.02	0.1	0.28	0.025	2.304147	0.1115	-0.50024	2319	96	2071	99	62	37

2016111

Sample	U ppm	±	Th ppm	±	^{207}Pb-^{206}Pb	±	^{238}U-^{206}Pb	±	Error Correlation	^{206}Pb-^{238}U age	±	^{207}Pb corrected ^{206}Pb-^{238}U age	±	Discordance %	±
3	69.5	6.7	556	55	0.1462	0.0064	3.378378	0.2967	0.30821	1670	130	1600	140	26.9	9.2
4	13.2	1.6	246	48	0.24	0.026	3.246753	0.2635	0.025113	1730	130	1440	130	59	14
6	31.8	6.8	233	53	0.223	0.015	2.849003	0.2435	-0.10442	1930	140	1670	140	40	13
8	2.94	0.31	13.4	1	0.563	0.067	1.669449	0.2146	0.38632	2990	310	1240	340	71	21
9	80	6.8	781	69	0.1481	0.0079	3.558719	0.3926	0.48241	1590	150	1500	170	34	10
10	43	5	393	47	0.183	0.011	3.144654	0.2571	0.4307	1780	130	1620	140	40	14
11	10.3	2.2	23.8	2.8	0.382	0.047	2.469136	0.2683	0.12276	2180	200	1470	190	72	16
13	20.8	1.8	158	11	0.371	0.08	2.525253	0.2933	-0.17528	2130	210	1490	320	78	24
16	31.3	3.1	256	23	0.204	0.018	2.898551	0.2436	-0.010474	1900	140	1700	160	35	11
18	8.64	0.78	53.6	3.6	0.383	0.026	2.109705	0.2047	0.54389	2490	200	1750	240	60	16
19	41.9	4.8	368	35	0.201	0.017	2.967359	0.273	0.48823	1860	150	1680	180	40	12
20	2.84	0.32	14.9	1.5	0.482	0.056	1.776199	0.1924	0.44091	2850	260	1680	320	75	25
21	2.86	0.24	11.47	0.94	0.559	0.063	1.351351	0.2009	0.33345	3510	410	1600	380	62	24

2017952

Sample	U ppm	±	Th ppm	±	^{207}Pb-^{206}Pb	±	^{238}U-^{206}Pb	±	Error Correlation	^{206}Pb-^{238}U age	±	^{207}Pb corrected ^{206}Pb-^{238}U age	±	Discordance %	±
1	8.66	0.74	127.8	9.6	0.322	0.034	2.493766	0.2301	0.63592	2160	170	1640	230	55	16
2	16.1	1.2	194	14	0.243	0.025	2.808989	0.1973	0.22607	1960	120	1670	140	38.3	8.9
3	5.89	0.53	47.9	4.3	0.401	0.052	2.34192	0.2687	0.52709	2270	220	1570	260	64	18
4	6.65	0.6	72.3	7.4	0.329	0.04	2.427184	0.2474	0.3253	2210	200	1710	240	52	14
5	2.07	0.25	17.5	1.9	0.623	0.096	1.461988	0.2095	0.32747	3310	380	1220	530	60	23
6	6.5	0.73	52.1	6.5	0.368	0.057	2.512563	0.2336	0.41989	2150	170	1550	240	62	17
7	3.59	0.41	32.9	4	0.552	0.067	1.980198	0.3568	0.27527	2580	370	1260	340	80	21
8	4.4	0.49	34.3	4.9	0.446	0.04	2.028398	0.2098	0.73885	2570	220	1500	250	58	12
9	3.74	0.38	33.3	3	0.462	0.079	1.996008	0.2271	0.53077	2590	250	1500	350	65	20
10	9.28	0.62	86.8	5.5	0.353	0.048	2.347418	0.1433	0.46374	2280	120	1690	210	54	14
11	4.13	0.48	37.9	4.1	0.503	0.069	2.227171	0.2282	0.48497	2380	210	1340	300	79	18
12	6.62	0.62	51.5	4.2	0.379	0.061	2.816901	0.3253	0.28029	1950	200	1360	240	74	18
13	4.04	0.39	34.3	2.6	0.464	0.053	1.908397	0.2003	0.5875	2690	230	1640	310	60	17
14	2.57	0.29	26	2.2	0.546	0.054	1.436782	0.1755	0.38105	3370	320	1860	360	44	17
15	6.02	0.73	54.4	7.8	0.367	0.058	2.28833	0.2828	0.494	2310	240	1580	310	61	17
16	7.7	1	79	11	0.428	0.045	2.604167	0.3662	0.17802	2180	320	1400	250	76	18
17	9.9	1.1	99	11	0.321	0.035	2.666667	0.1991	0.32809	2040	130	1560	150	59	10
18	8.01	0.61	74.8	5.4	0.305	0.029	2.710027	0.3305	0.56409	2010	210	1600	250	59	14
19	11.46	0.97	135	12	0.301	0.045	3.012048	0.2722	0.2598	1840	140	1440	190	62	13
20	11.5	1	51.2	3.9	0.273	0.044	2.890173	0.3007	0.58695	1900	170	1580	210	52	17
22	8.24	0.7	92.5	8.9	0.297	0.035	3.184713	0.355	0.7341	1750	170	1380	200	66	15
23	3.91	0.39	49.1	5	0.448	0.067	1.964637	0.2161	0.40203	2630	240	1680	290	53	14
24	2.41	0.37	21.5	3.5	0.495	0.088	1.594896	0.2442	0.093447	3080	390	1590	400	45	17
25	13.02	0.99	143	11	0.322	0.042	2.857143	0.2694	0.31794	1920	160	1470	210	65	14
26	8.95	0.95	60.7	6.2	0.343	0.063	2.824859	0.3352	0.52461	1940	200	1370	220	71	19
27	3.25	0.58	31.9	4.7	0.5	0.075	1.988072	0.1739	0.1573	2610	180	1480	320	69	17
28	12.9	1.5	140	14	0.305	0.028	2.793296	0.2731	0.59573	1960	160	1550	220	62	12
29	5.95	0.59	52.6	5.2	0.437	0.061	2.267574	0.2571	0.046529	2440	290	1570	310	69	18
30	13.43	0.98	125.3	8.2	0.336	0.039	2.717391	0.192	-0.07597	2010	120	1490	160	65	11
31	7.2	0.64	66.7	5.6	0.368	0.038	2.320186	0.2584	0.59116	2290	210	1600	230	65	14
32	3.72	0.28	30.1	2.6	0.503	0.082	1.923077	0.2256	0.61153	2680	250	1430	340	73	21
33	2.1	0.3	16.4	1.7	0.53	0.12	1.923077	0.4438	0.88325	2590	510	1240	550	93	40
34	2.21	0.3	12.3	1.6	0.58	0.12	1.538462	0.2604	0.6415	3180	430	1290	470	74	28

1472758

Sample	U ppm	±	Th ppm	±	^{207}Pb-^{206}Pb	±	^{238}U-^{206}Pb	±	Error Correlation	^{206}Pb-^{238}U age	±	^{207}Pb corrected ^{206}Pb-^{238}U age	±	Discordance %	±
1	2.38	0.19	0.62	0.12	0.582	0.079	1.821494	0.1493	0.70471	2810	190	1400	320	69	19
2	2.57	0.18	0.481	0.094	0.572	0.056	2	0.144	0.62862	2600	160	1330	240	74	16
3	1.56	0.19	0.167	0.056	0.7	0.13	1.782531	0.2383	0.81079	2830	310	1080	450	76	24
4	6.75	0.48	3.1	0.31	0.393	0.047	2.95858	0.2976	0.3822	1870	160	1300	170	78	14
6	5.93	0.54	2.46	0.34	0.405	0.067	2.631579	0.2839	0.53291	2060	190	1470	280	72	20
8	9.36	0.87	16.7	1.8	0.339	0.045	3.125	0.2832	0.61011	1780	140	1360	180	68	14
9	18.1	1.7	18.5	1.7	0.222	0.023	3.367003	0.3401	0.29172	1670	150	1470	170	43	10
10	6.67	0.57	3.44	0.33	0.385	0.047	2.659574	0.2546	0.75575	2040	170	1480	210	69	16
11	9.16	0.44	15	1.2	0.34	0.037	2.785515	0.2173	0.18435	1970	130	1490	150	63	11
12	3.15	0.25	1.17	0.19	0.538	0.08	2.040816	0.2582	0.76955	2540	260	1430	340	78	25
13	5.21	0.49	1.26	0.18	0.422	0.042	2.531646	0.2692	0.37938	2130	190	1450	210	76	14
14	6.8	0.57	1.84	0.25	0.368	0.043	2.849003	0.1948	0.61163	1980	140	1390	160	70	13
15	3.16	0.44	1.27	0.25	0.597	0.082	2.192982	0.2405	0.59379	2400	220	1220	310	92	23
16	3.71	0.42	1.26	0.19	0.538	0.068	2.304147	0.2867	0.13354	2300	250	1200	360	93	22
17	4.95	0.35	3.37	0.39	0.389	0.048	2.724796	0.2673	0.49475	2000	170	1430	210	76	16
18	5.5	0.48	1.92	0.21	0.386	0.041	2.659574	0.2122	0.61342	2050	140	1470	190	71	15
19	5.03	0.48	4.67	0.73	0.5	0.065	1.754386	0.3693	-0.256	2820	440	1580	290	64	17
20	8.05	0.85	22.4	2.7	0.36	0.046	3.076923	0.2462	0.42996	1810	130	1330	170	77	14
21	4.31	0.34	1.58	0.2	0.382	0.051	2.469136	0.2439	0.88052	2180	190	1550	280	62	16
22	3.72	0.27	1.06	0.13	0.452	0.06	2.083333	0.2214	0.25309	2510	220	1670	290	64	17
23	8.09	0.84	9.9	1.1	0.37	0.037	2.967359	0.2642	0.50474	1860	140	1290	140	76	13
24	9.51	0.79	25.4	2.1	0.279	0.025	3.04878	0.2138	-0.046717	1820	110	1490	110	55.4	7.9
25	3.13	0.29	3.2	0.57	0.554	0.076	2.178649	0.2183	0.62628	2420	200	1330	290	87	21
26	6.37	0.56	4.44	0.46	0.323	0.031	2.544529	0.2137	0.56612	2130	150	1690	200	56	12
27	4.83	0.5	2.17	0.26	0.419	0.063	2.475248	0.3063	0.65869	2170	230	1540	310	77	21
28	8.12	0.66	1.85	0.23	0.298	0.035	2.873563	0.2312	0.46677	1920	130	1550	170	58	12
30	7.69	0.57	2.47	0.32	0.314	0.05	2.967359	0.3258	0.1933	1860	180	1400	140	67	11
31	2.8	0.31	0.94	0.15	0.465	0.051	1.960784	0.1423	0.55744	2650	160	1730	280	62	14
32	1.65	0.16	0.125	0.047	0.65	0.11	1.474926	0.1958	0.77603	3290	360	1390	520	67	29
33	5.87	0.63	2.82	0.39	0.336	0.031	2.48139	0.2217	0.31589	2170	170	1690	190	58	12
34	20.5	1.5	21.1	3.1	0.188	0.016	3.676471	0.2703	0.18938	1548	98	1400	110	39.7	7.6
35	10.36	0.74	3.04	0.48	0.274	0.029	3.257329	0.2546	0.65561	1770	150	1470	180	59	13
36	5.39	0.69	4.13	0.49	0.384	0.054	2.680965	0.2803	0.72187	2030	180	1490	250	76	20
37	3.67	0.33	1.08	0.17	0.44	0.075	2.380952	0.3401	0.48481	2230	270	1520	310	77	22
38	9.4	1.4	5.5	1.1	0.254	0.041	3.355705	0.3378	-0.075868	1670	150	1410	170	55	12
40	3.32	0.3	0.78	0.12	0.413	0.05	2.380952	0.2381	0.44333	2240	190	1570	240	72	14
41	24.1	2.1	36.6	4.5	0.169	0.016	3.787879	0.33	0.43579	1500	120	1390	130	36.2	8.8

1472763

Sample	U ppm	±	Th ppm	±	^{207}Pb-^{206}Pb	±	^{238}U-^{206}Pb	±	Error Correlation	^{206}Pb-^{238}U age	±	^{207}Pb corrected ^{206}Pb-^{238}U age	±	Discordance %	±
1	25.6	1.7	0.023	0.051	0.259	0.022	2.949853	0.2698	-0.19912	1870	150	1520	140	50	10
2	25.8	3.1	0.17	0.13	0.265	0.024	3.030303	0.303	0.74257	1830	150	1430	150	60	11
5	35.1	3	0.122	0.076	0.218	0.014	3.076923	0.3314	0.10941	1800	170	1570	190	45.2	9.6
7	25.5	1.8	0.011	0.051	0.229	0.012	3.039514	0.2402	-0.15297	1830	130	1540	140	47.7	8.2
9	17.2	1.6	0.087	0.042	0.281	0.018	2.570694	0.1652	-0.16081	2110	120	1680	110	48.5	9.4
10	30.1	3	1.48	0.2	0.196	0.017	3.04878	0.2138	0.52918	1820	110	1640	140	36.6	9.2
11	25.2	2.3	0.027	0.051	0.228	0.018	2.97619	0.2392	-0.091828	1860	130	1560	150	49	11
12	16.5	1.6	0.032	0.042	0.292	0.028	2.724796	0.2302	-0.29992	2010	140	1490	130	59.4	9.5
13	19.1	1.3	0.007	0.047	0.349	0.053	2.34192	0.2687	0.34606	2270	220	1610	240	56	12
14	26.2	2.3	0.212	0.059	0.227	0.018	3.076923	0.1515	0.13695	1810	79	1530	100	48.6	6.8
15	24.9	2.7	0.012	0.053	0.26	0.018	2.680965	0.2228	0.65889	2040	150	1690	180	50	11
17	20.9	2.3	0.038	0.048	0.341	0.023	2.347418	0.2755	0.6036	2270	230	1680	230	61	16
18	13.2	1.1	0.89	0.14	0.303	0.025	2.57732	0.2657	0.43508	2100	180	1560	160	60	12
19	22.2	2.3	0.078	0.051	0.243	0.014	2.873563	0.2973	0.12787	1990	220	1610	180	48	10
20	24.8	3.3	0.023	0.036	0.243	0.018	2.724796	0.2747	0.58341	2000	180	1720	210	47	13
21	21.9	1.9	0.008	0.033	0.264	0.019	2.824859	0.2075	0.1786	2000	160	1640	180	54	11
22	25.8	2.1	0.074	0.047	0.314	0.019	2.439024	0.2142	0.30877	2210	160	1680	180	56	11
23	29	2.7	0.24	0.074	0.225	0.018	2.857143	0.2122	-0.26239	1930	120	1650	110	43.4	7.7
24	25.2	2.6	0.018	0.047	0.294	0.023	2.557545	0.1635	0.066272	2120	120	1660	140	57.8	8.6
25	19.9	1.7	0	0.038	0.286	0.016	2.666667	0.2631	0.13785	2040	170	1620	170	55.9	9.5
26	25.9	2.2	0.084	0.06	0.236	0.015	2.915452	0.289	-0.1926	1890	170	1600	170	47.7	8.4
27	33.2	3.1	0.037	0.052	0.221	0.014	3.10559	0.2508	0.18319	1790	120	1540	130	51.4	7.2
28	25.3	2.2	0.016	0.041	0.231	0.017	3.039514	0.194	0.002616	1830	100	1550	120	47.4	7.7
29	4	0.38	0.029	0.045	0.537	0.053	1.587302	0.1512	0.29979	3130	230	1490	280	60	16

2017972

Sample	U ppm	±	Th ppm	±	^{207}Pb-^{206}Pb	±	^{238}U-^{206}Pb	±	Error Correlation	^{206}Pb-^{238}U age	±	^{207}Pb corrected ^{206}Pb-^{238}U age	±	Discordance %	±
1	6.15	0.78	42.3	5.2	0.427	0.06	1.968504	0.2364	0.43594	2620	250	1520	280	70	24
3	23	1.4	266	16	0.211	0.012	3.058104	0.187	0.34961	1821	99	1590	110	44	12
4	4.06	0.56	25.6	3.8	0.632	0.069	1.426534	0.1465	0.18848	3400	270	1160	400	66	23
6	4.42	0.54	24	2.3	0.534	0.049	1.342282	0.1676	0.56413	3540	330	1630	400	45	16
7	24.8	2.3	209	21	0.23	0.018	3.154574	0.2786	0.21368	1770	130	1500	150	60	24
8	31.1	2.5	261	24	0.188	0.017	3.401361	0.3471	0.61918	1650	150	1490	160	44	13
10	6.9	0.65	35.3	3.8	0.398	0.049	2.118644	0.2469	0.30178	2470	230	1610	290	73	22
11	17.5	3.3	191	36	0.264	0.019	2.57732	0.2657	-0.1165	2100	180	1740	200	56	21
12	11.13	0.88	86	6.8	0.353	0.032	2.304147	0.2389	0.55539	2310	200	1610	220	68	20
13	7.54	0.79	37.9	5.7	0.435	0.039	2.114165	0.1922	0.3573	2480	190	1480	280	80	23
17	14.7	2.3	123	20	0.343	0.032	2.155172	0.3066	0.16143	2420	290	1750	280	63	30
19	13.7	2.4	128	23	0.308	0.038	2.375297	0.1862	0.46674	2260	150	1770	200	59	23
20	11.2	1.4	15	2.3	0.361	0.038	2.364066	0.2291	0.2604	2260	180	1610	240	73	29
21	12.31	0.65	85.8	3.8	0.361	0.027	2.232143	0.1794	0.36691	2380	170	1690	200	67	30
22	14.6	3.1	127	29	0.299	0.027	2.392344	0.2347	-0.04099	2240	180	1750	170	48	15
23	4.66	0.71	39.7	7.1	0.501	0.061	1.751313	0.2116	-0.036983	2880	280	1490	360	71	27
24	32.7	3.9	335	36	0.209	0.013	2.923977	0.2565	0.66347	1890	140	1680	180	40	15
25	28.5	2.6	292	25	0.261	0.021	3.067485	0.2541	0.095484	1810	130	1470	150	65	21
26	3.76	0.74	35.5	7.3	0.56	0.086	1.519757	0.2148	0.38136	3210	370	1440	480	65	31
27	15	1.9	156	17	0.331	0.035	2.659574	0.3254	0.31223	2040	210	1530	260	75	30
28	8.2	1.3	42.5	6.9	0.383	0.041	2.123142	0.2074	0.32881	2470	210	1650	250	68	30
29	7.6	1.2	73	12	0.415	0.034	1.862197	0.215	0.67504	2750	260	1710	310	58	22
30	25.8	3.8	249	33	0.215	0.026	2.857143	0.3592	0.50956	1920	210	1730	260	45	14

2016116

Sample	U ppm	±	Th ppm	±	^{207}Pb-^{206}Pb	±	^{238}U-^{206}Pb	±	Error Correlation	^{206}Pb-^{238}U age	±	^{207}Pb corrected ^{206}Pb-^{238}U age	±	Discordance %	±
1	35.8	6.4	55	11	0.456	0.063	1.77305	0.2326	-0.1782	2980	390	1730	250	45	20
2	26.9	3.6	40.8	4.9	0.248	0.025	2.487562	0.229	0.33225	2170	170	1880	220	38	13
5	9.6	1.1	10.6	1.2	0.375	0.036	2.188184	0.2394	0.3682	2410	210	1540	190	45	22
6	28.4	3.5	22.8	3.3	0.209	0.018	2.890173	0.2673	0.065005	1900	150	1700	180	44	21
8	13.9	2	8	1.1	0.3	0.035	2.403846	0.208	-0.006994	2230	160	1770	210	40	17
9	25.1	2.9	24.6	3	0.244	0.018	2.898551	0.1512	0.40458	1937	67	1600	110	48	20
11	23.6	3.1	13.1	2.1	0.283	0.027	2.65252	0.1829	0.59422	2060	120	1630	150	42	19
12	27.4	2.2	26.4	2.5	0.239	0.019	2.816901	0.2539	-0.32209	1950	150	1660	170	34	12
13	13.4	1.4	8.17	0.9	0.343	0.036	2.347418	0.27	-0.21668	2270	220	1710	240	45	17
14	61.1	7.6	104	10	0.18	0.011	3.205128	0.2465	-0.37827	1740	120	1590	130	38	16
15	27.9	2.1	18.2	1.5	0.268	0.024	2.680965	0.2731	0.090449	2030	180	1680	210	54	27
16	8.8	1	13.5	1.5	0.471	0.05	1.949318	0.1862	0.30972	2650	210	1590	290	52	29
17	43.5	4.5	47.6	5.3	0.215	0.01	2.857143	0.2041	0.32294	1930	120	1680	130	40	16
18	12.5	1.2	7.03	0.82	0.385	0.035	2.136752	0.1963	0.39443	2460	190	1640	310	68	33
19	20.2	3.5	17.2	2.8	0.309	0.019	2.680965	0.23	0.38043	2040	150	1550	140	54	26
21	20.3	2.2	15.6	2.1	0.304	0.037	2.403846	0.1849	-0.63535	2230	150	1820	210	44	18
22	18.5	2.2	13.7	1.3	0.317	0.029	2.197802	0.2222	-0.004021	2400	200	1870	210	51	22
25	48.9	6	56.6	6.7	0.222	0.018	2.881844	0.3073	0.5988	1910	180	1680	210	88	47
26	74.7	5.9	125.5	8.7	0.238	0.014	2.57732	0.2591	-0.29675	2100	180	1800	200	36	17
27	31.6	3.5	25.9	2.7	0.302	0.023	2.375297	0.2595	0.17501	2250	210	1780	230	63	29

TAR

Sample	U ppm	±	Th ppm	±	^{207}Pb-^{206}Pb	±	^{238}U-^{206}Pb	±	Error Correlation	^{206}Pb-^{238}U age	±	^{207}Pb corrected ^{206}Pb-^{238}U age	±	Discordance %	±
1	8.74	0.76	46	10	0.403	0.015	2.427184	0.1002	-0.001997	2218	79	1504	82	68.2	4.8
2	15.3	1	37.9	2.1	0.33	0.011	2.680965	0.0863	0.15141	2053	62	1547	64	61	4.3
3	12.16	0.83	45.6	9	0.465	0.042	1.795332	0.2675	-0.80723	2990	390	1600	120	54.5	6.6
4	2.23	0.15	0.462	0.038	0.688	0.024	1.18624	0.0605	0.34303	3920	140	1440	170	35	5.7
5	8.76	0.36	28.8	1	0.437	0.014	2.105263	0.1152	-0.267	2490	110	1579	80	63.6	4.9
6	11.15	0.51	35.1	1.2	0.407	0.013	2.272727	0.0775	0.17422	2345	69	1578	70	64.2	4.4
7	10.91	0.41	23.8	0.86	0.353	0.011	2.583979	0.1068	-0.070578	2104	72	1529	67	63.5	3.9
8	10.22	0.48	33.4	1.3	0.39	0.011	2.358491	0.0834	0.27401	2272	68	1569	61	62.8	3.3
9	6.59	0.41	19.1	1.1	0.437	0.015	2.262443	0.087	0.27641	2352	78	1494	81	69.1	5.4
10	11.37	0.45	35.3	1.1	0.362	0.011	2.463054	0.0789	0.21074	2190	60	1576	60	61.9	3.8
11	28.8	1.6	34.8	1.3	0.246	0.011	3.039514	0.1201	-0.29063	1844	65	1550	57	46.4	3.1
12	10.42	0.55	30.2	1.3	0.404	0.012	2.364066	0.0894	0.30253	2267	70	1527	73	67.4	4.4
13	14.56	0.53	27.85	0.85	0.3191	0.0093	2.666667	0.0853	0.11723	2049	56	1567	55	58.1	3.3
14	2.53	0.1	0.561	0.049	0.588	0.019	1.519757	0.0739	0.35391	3240	120	1490	130	52.4	6.7
15	9.42	0.35	23.8	0.58	0.365	0.012	2.427184	0.0825	0.28783	2218	62	1595	66	60.3	3.7
16	9.8	1.1	22.3	4	0.364	0.018	2.512563	0.1136	-0.068629	2155	82	1544	81	63.2	5.3
17	5.68	0.33	12.39	0.34	0.517	0.022	1.814882	0.0758	0.16804	2822	94	1570	100	61.4	6.1
18	17.92	0.91	37.7	1.3	0.277	0.01	2.95858	0.1225	-0.000914	1870	70	1504	67	55	4
19	2.84	0.19	0.61	0.045	0.591	0.019	1.490313	0.08	0.27014	3290	140	1550	130	51.1	7.1
20	14.3	0.59	33.63	0.99	0.324	0.011	2.747253	0.1057	-0.043974	1995	65	1507	60	61.3	3.7
21	15.7	2	65	11	0.338	0.02	2.544529	0.123	-0.52613	2130	87	1576	69	56.9	4.4
22	17.55	0.94	51.6	3.1	0.2893	0.0094	2.890173	0.1002	-0.009753	1910	57	1515	54	56.2	3.3
23	6.29	0.23	18.6	0.59	0.505	0.015	1.805054	0.0652	0.35119	2834	84	1607	86	58.5	5.4
24	4.4	0.18	12.8	0.47	0.537	0.02	1.73913	0.0635	0.26378	2938	91	1570	110	59.1	5.8
25	21.75	0.84	55.8	2.5	0.2435	0.0094	3.194888	0.1123	-0.049397	1752	54	1467	54	50.2	3.5
28	6.75	0.33	22.6	1.8	0.463	0.017	2.114165	0.0849	0.33474	2491	82	1499	81	67.5	5.5
29	8.32	0.27	19.63	0.56	0.382	0.011	2.380952	0.0907	0.12205	2254	74	1576	69	63.4	4.3
30	7.6	0.33	23.55	0.78	0.409	0.013	2.375297	0.1016	0.20497	2277	74	1489	72	68.6	4.9
32	2.37	0.16	0.589	0.075	0.653	0.028	1.090513	0.0678	0.19527	4160	190	1560	180	31.6	5.2
33	7.93	0.43	24.15	0.93	0.406	0.012	2.242152	0.1106	0.28282	2370	96	1591	89	63.3	5.4
34	3.3	0.15	0.72	0.05	0.577	0.025	1.602564	0.0796	0.047059	3110	120	1520	140	56.8	7.1
35	5.68	0.33	13.37	0.87	0.515	0.018	1.960784	0.0846	-0.04456	2649	92	1439	90	70	5.4
36	11.39	0.5	28.95	0.85	0.384	0.012	2.538071	0.0902	0.25084	2135	65	1476	66	69.2	4.3
37	2.34	0.13	0.562	0.047	0.637	0.026	1.396648	0.08	0.12556	3460	150	1430	150	49.5	7.3
38	12.13	0.85	30.4	1.2	0.337	0.017	2.590674	0.1141	-0.19265	2097	79	1560	73	58.7	4.3
39	2.93	0.13	0.698	0.05	0.595	0.021	1.54321	0.0643	0.23747	3230	110	1520	120	53.7	6.3
40	9.98	0.48	29.1	1.3	0.395	0.016	2.557545	0.085	0.17555	2124	61	1434	68	72.1	4.6

2017967

Sample	U ppm	±	Th ppm	±	^{207}Pb-^{206}Pb	±	^{238}U-^{206}Pb	±	Error Correlation	^{206}Pb-^{238}U age	±	^{207}Pb corrected ^{206}Pb-^{238}U age	±	Discordance %	±
1	5.18	0.32	5.98	0.64	0.477	0.039	2.283105	0.1616	0.54548	2330	140	1610	190	84	14
2	7.25	0.63	14.5	1.4	0.44	0.034	2.538071	0.1546	0.36917	2130	110	1510	130	81	10
3	9.98	0.58	5.35	0.45	0.353	0.026	2.610966	0.1227	0.22654	2086	86	1630	92	63.5	8.6
4	44.2	4.9	53	5.7	0.172	0.011	3.311258	0.1974	0.27423	1698	88	1595	97	28.3	5.1
5	17.1	1.4	44.9	5	0.24	0.023	3.08642	0.2096	-0.25163	1800	100	1590	110	46.6	8
6	5.93	0.42	4.8	0.58	0.439	0.053	2.475248	0.2451	0.4478	2170	180	1570	220	79	17
7	9.21	0.74	4.99	0.5	0.365	0.031	2.710027	0.2056	0.17935	2020	130	1560	130	70	10
8	38.3	4.4	55	7.8	0.179	0.014	3.460208	0.1556	0.13742	1632	64	1517	70	33.5	4.9
9	27.8	3.5	58.4	7.3	0.23	0.017	2.80112	0.2275	0.043975	1960	140	1770	160	38.9	9
10	2.09	0.2	2.88	0.29	0.586	0.078	2.024291	0.2827	0.72586	2660	350	1380	400	95	28
11	6.82	0.52	5.74	0.54	0.421	0.041	2.57732	0.2192	0.59533	2110	150	1480	160	79	13
12	6.45	0.39	2.6	0.3	0.435	0.037	2.475248	0.2573	0.30882	2170	190	1560	180	80	13
13	7.68	0.77	1.82	0.27	0.324	0.03	2.518892	0.2157	0.3748	2150	160	1770	180	56	11
14	3.66	0.38	1.96	0.28	0.459	0.063	2.008032	0.2016	0.73683	2590	210	1860	320	66	20
15	4.26	0.28	4.73	0.42	0.498	0.05	2.232143	0.1893	0.54012	2380	170	1600	220	84	16
16	6.24	0.52	4.6	0.63	0.419	0.045	2.283105	0.1981	0.095944	2330	170	1730	210	69	14
17	7.12	0.8	0.85	0.18	0.344	0.04	2.590674	0.2215	0.52544	2090	160	1700	200	64	14
18	11.3	1.4	20.2	2.7	0.307	0.022	2.710027	0.235	0.14528	2020	150	1680	160	59	10
19	9.42	0.8	2.09	0.28	0.337	0.028	2.583979	0.2604	0.21102	2090	180	1670	200	66	13
20	2.85	0.22	2.47	0.32	0.56	0.062	1.77305	0.1792	0.49101	2860	230	1730	260	70	16
21	5.44	0.43	0.85	0.14	0.381	0.049	2.421308	0.258	0.2873	2210	200	1740	260	68	16
22	8.99	0.82	6.9	0.71	0.355	0.023	2.673797	0.1787	-0.027729	2040	110	1600	120	70.2	8.1
23	7.7	0.48	4.66	0.46	0.341	0.028	2.857143	0.2367	0.65343	1930	140	1540	170	72	12
24	11.09	0.94	14.4	1.3	0.306	0.028	2.777778	0.2932	0.4987	1970	180	1650	200	62	12
25	12.4	1.1	12.4	1.4	0.264	0.031	2.906977	0.2282	0.17289	1900	130	1650	140	56	12
26	3.22	0.43	1.24	0.59	0.5	0.062	2.109705	0.2314	0.068056	2480	220	1670	260	79	16
27	5.38	0.48	3	0.28	0.408	0.04	2.309469	0.256	0.34396	2300	210	1660	190	72	14
28	8.17	0.64	4.56	0.39	0.332	0.035	2.762431	0.2137	0.49183	1980	130	1610	170	68	13
29	9.7	1.4	8.9	1.5	0.285	0.03	2.785515	0.1707	0.2155	1970	100	1670	120	55.2	9.5
30	6.67	0.58	5.69	0.55	0.383	0.031	2.159827	0.1819	0.27473	2440	170	1910	200	60	12
31	12.4	1.6	9.79	0.75	0.28	0.021	2.570694	0.1718	0.42371	2110	120	1820	140	50.3	8.7
32	8.71	0.73	6.91	0.74	0.361	0.034	2.493766	0.2736	0.53093	2160	200	1730	240	69	15
33	12.8	1.1	4.5	0.49	0.304	0.021	2.898551	0.3109	0.56642	1900	180	1580	180	67	10
34	12.69	0.66	2.34	0.26	0.278	0.026	2.724796	0.1485	0.099753	2010	91	1720	120	53.9	8.2
35	11.82	0.92	7.25	0.67	0.299	0.028	2.638522	0.2297	0.33096	2060	150	1740	180	60	12

SB12-10

Sample	U ppm	±	Th ppm	±	^{207}Pb-^{206}Pb	±	^{238}U-^{206}Pb	±	Error Correlation	^{206}Pb-^{238}U age	±	^{207}Pb corrected ^{206}Pb-^{238}U age	±	Discordance %	±
1	13.52	0.68	27.7	1.5	0.2922	0.007	1.876173	0.0563	0.36189	2750	66	2362	81	25.2	3.2
3	7.75	0.4	7.43	0.44	0.357	0.014	1.736111	0.0633	0.64052	2924	88	2340	120	32.2	5.5
4	4.31	0.29	1.5	0.12	0.402	0.014	1.547988	0.0695	0.14609	3200	110	2370	140	29.3	5.2
5	12.27	0.57	41.8	1.8	0.3048	0.0087	1.876173	0.0634	0.34083	2749	76	2329	90	27	3.5
7	9.5	0.36	11.62	0.44	0.358	0.01	1.686341	0.0483	0.25104	2998	68	2363	76	28	3.5
9	3.82	0.2	3.37	0.15	0.515	0.027	1.283697	0.0676	0.32629	3690	140	2230	160	29.9	6
10	6.1	0.33	7.04	0.4	0.417	0.012	1.515152	0.0574	0.041523	3258	96	2380	130	29.7	4.7
11	4.88	0.22	4.93	0.23	0.479	0.015	1.414427	0.06	0.11341	3440	110	2300	120	29.4	4.3
13	3.72	0.36	3.64	0.46	0.531	0.022	1.261034	0.0541	0.17314	3780	130	2270	170	25.8	5.5
14	7.15	0.31	7.59	0.47	0.387	0.015	1.689189	0.0742	0.18859	2990	100	2245	95	34.1	4.2
16	3.74	0.63	1.88	0.36	0.537	0.028	1.121076	0.088	-0.4114	4100	240	2340	160	24.2	4.5
17	11.68	0.4	16.77	0.59	0.3006	0.0071	1.869159	0.0629	0.27543	2758	76	2390	110	26.6	3.5
18	6.7	0.63	7.14	0.88	0.399	0.016	1.623377	0.0632	-0.23667	3085	95	2323	99	30.7	3.9
19	9.29	0.29	11.06	0.35	0.3204	0.0096	1.883239	0.0603	0.15278	2741	74	2286	92	30.6	3.8
21	21.3	1.2	42.7	2.1	0.253	0.0055	2.079002	0.0648	0.2272	2528	67	2275	87	24.5	2.9
22	16.4	1.2	36.8	2.5	0.2785	0.0092	1.988072	0.0593	0.04338	2620	66	2271	77	27.1	3
23	11.66	0.53	23.9	1.2	0.3307	0.0099	1.901141	0.0651	0.041568	2718	78	2230	95	34	4
24	4.05	0.3	3.62	0.2	0.471	0.018	1.466276	0.058	0.13761	3340	110	2240	130	32.7	4.9
25	6.16	0.24	6.82	0.25	0.43	0.013	1.545595	0.0549	0.36877	3207	89	2320	120	32.4	4.8
26	5.37	0.31	6.05	0.26	0.451	0.015	1.574803	0.0595	0.28734	3158	97	2220	120	37.1	5.3
27	2.39	0.15	1.39	0.097	0.598	0.024	1.092896	0.0502	0.035771	4170	140	2260	170	20.4	4.8
28	7.42	0.25	7.31	0.23	0.373	0.012	1.709402	0.0614	0.62537	2962	87	2340	110	32.2	4.3
31	5.76	0.26	7.03	0.31	0.433	0.014	1.572327	0.0569	0.21997	3163	89	2300	120	33.7	4.6
32	4.12	0.2	3.78	0.16	0.533	0.017	1.30719	0.0581	0.30148	3670	130	2250	140	29.5	5.4
35	9.24	0.45	10.76	0.38	0.3485	0.0094	1.77305	0.0597	0.060192	2895	82	2313	89	30.6	3.6
36	5.15	0.28	4.89	0.25	0.395	0.016	1.626016	0.074	0.19883	3080	110	2310	120	31.6	4.7
38	13.27	0.51	21.6	0.52	0.2964	0.0078	1.872659	0.0596	0.036508	2753	70	2352	83	26.3	3.2
40	12.71	0.41	15.8	0.42	0.305	0.01	1.926782	0.0668	0.21214	2689	76	2247	86	31.8	3.9
41	15.3	0.58	31.53	0.92	0.307	0.017	1.919386	0.0737	-0.037279	2695	82	2216	85	33.8	4.1
42	7.71	0.37	9.33	0.47	0.413	0.016	1.663894	0.0775	-0.18605	3020	110	2230	110	36.6	4.9

Chapter 2; Apatite U-Pb data.

2131358

Sample	U ppm	±	Th ppm	±	^{207}Pb-^{206}Pb	±	^{238}U-^{206}Pb	±	Error Correlation	^{206}Pb-^{238}U age	±	^{207}Pb corrected ^{206}Pb-^{238}U age	±	Discordance %	±
1	19.8	1.9	1.23	0.33	0.198	0.017	2.932551	0.1118	0.21278	1889	65	1672	86	29.2	6.2
2	30.8	1.5	0.475	0.096	0.1931	0.0072	2.985075	0.098	0.060009	1861	53	1645	60	29.9	3.5
3	39.1	2.4	0.816	0.061	0.1253	0.0074	3.267974	0.1495	0.53089	1717	68	1674	84	10.5	3.1
4	37.5	2.2	0.65	0.051	0.1659	0.0066	3.134796	0.1376	-0.18039	1780	68	1640	71	22.3	2.9
5	47.8	4.3	0.84	0.06	0.1876	0.0068	2.985075	0.1604	0.29948	1861	88	1670	100	27.3	4.4
6	42.6	2.3	0.863	0.084	0.1749	0.0086	3.04878	0.1022	0.34482	1828	53	1668	65	24	3.9
7	38.2	3.2	0.733	0.076	0.213	0.011	3.021148	0.1552	0.2169	1840	80	1585	92	35.8	4.9
8	46	2.6	0.99	0.067	0.168	0.0055	3.115265	0.165	0.55015	1794	84	1654	98	23	4
9	30.2	1.7	0.364	0.047	0.1182	0.0083	3.401361	0.162	0.56508	1658	68	1627	85	10.3	3.9
10	62.5	3.2	1.57	0.11	0.167	0.01	2.985075	0.1515	0.32393	1858	82	1720	100	20.3	4.9
11	21.4	1.5	0.161	0.022	0.174	0.011	3.154574	0.1891	0.13937	1772	94	1620	110	25.5	5.1
12	37.9	1.8	0.648	0.064	0.1534	0.0072	3.205128	0.1541	0.36369	1751	72	1634	86	18.3	3.8
13	52.1	3.8	1.49	0.26	0.1532	0.0059	3.154574	0.1194	0.26159	1774	60	1666	69	17.9	3.2
14	38.9	2.4	1.2	0.36	0.198	0.011	3.04878	0.1394	0.27095	1828	75	1612	90	31.5	5
15	53.5	3.4	1.256	0.078	0.1698	0.0051	3.134796	0.1179	0.49647	1783	58	1633	64	23.7	2.9
16	35.5	1.8	0.875	0.063	0.1894	0.0081	3.030303	0.1194	-0.030257	1834	65	1637	73	28.6	3.5
17	45.8	3.3	0.635	0.084	0.1846	0.0088	2.923977	0.1111	0.31525	1895	61	1713	76	25	4
18	55.8	2.6	1.215	0.075	0.1681	0.0071	3.095975	0.1054	0.14616	1805	54	1660	62	22.3	3.2
19	22.6	1.9	0.163	0.048	0.2046	0.0088	2.890173	0.1504	0.23193	1915	87	1682	99	30.8	4.6
20	33.4	2.4	0.146	0.03	0.191	0.0097	3.04878	0.1115	0.1869	1848	71	1648	81	28.6	4.2
21	24.7	1.6	0.343	0.041	0.182	0.009	3.225806	0.1457	0.10418	1741	67	1561	76	29.2	4.1
22	47.1	2.8	1.233	0.089	0.1766	0.0059	3.039514	0.1571	0.3721	1830	84	1670	97	24.6	4
23	35.6	1.8	0.557	0.064	0.1512	0.009	3.333333	0.1667	0.46888	1690	75	1574	90	19.6	4.1
24	40.1	3.5	0.274	0.042	0.1469	0.0085	3.10559	0.1929	0.60377	1793	97	1710	120	16.3	4.8

2111462

Sample	U ppm	±	Th ppm	±	^{207}Pb-^{206}Pb	±	^{238}U-^{206}Pb	±	Error Correlation	^{206}Pb-^{238}U age	±	^{207}Pb corrected ^{206}Pb-^{238}U age	±	Discordance %	±
2	50.5	5.1	197	15	0.0987	0.0069	3.533569	0.2123	0.63062	1605	87	1620	110	9.8	3
3	7.84	0.63	50.3	3.5	0.093	0.022	3.623188	0.2757	0.081376	1570	110	1590	150	22	11
4	9.6	1.1	51.9	4.4	0.137	0.016	3.436426	0.2952	0.37195	1640	120	1510	120	23	6.3
5	4.64	0.31	30.1	2.3	0.122	0.027	3.436426	0.4133	0.40449	1640	170	1480	170	29.8	7.8
6	87.7	7.1	695	52	0.1012	0.0067	3.636364	0.2248	0.46851	1563	85	1560	100	9.9	3.1
7	59.5	4.9	506	21	0.0962	0.0089	3.731343	0.2506	0.33744	1525	93	1530	110	11.2	3.5
8	5.39	0.79	28.6	4.5	0.103	0.022	3.546099	0.4401	0.43698	1590	180	1600	240	22.5	7.1
10	45	5.4	209	30	0.0967	0.0073	3.676471	0.1622	0.45069	1550	62	1520	100	10.4	3.5
12	53	4.9	302	32	0.0982	0.009	3.703704	0.2881	0.21708	1540	100	1540	120	8.3	3.1
13	71.5	4.4	572	35	0.0974	0.0062	3.584229	0.2055	0.34848	1581	80	1590	100	9.1	2.6
14	28.8	2.2	332	36	0.097	0.013	3.584229	0.2184	0.24469	1584	88	1600	110	14.3	5.6
15	72.2	5.2	521	41	0.1015	0.006	3.717472	0.2488	0.46852	1533	90	1530	110	9.9	3.4
16	12.44	0.9	62.6	4.2	0.098	0.018	3.584229	0.2826	-0.27215	1580	110	1590	140	15.5	4.6
17	10.13	0.63	49.1	2.7	0.087	0.016	3.448276	0.3092	0.24052	1630	130	1680	180	22.3	7.4
18	31.9	3.7	235	24	0.1	0.011	3.546099	0.3521	0.38279	1590	140	1630	200	15.4	4.9
19	74.5	5.6	642	52	0.096	0.0063	3.676471	0.2163	0.31528	1548	82	1556	99	9.2	2.5
20	55.6	4.3	515	40	0.0936	0.007	3.759398	0.2544	0.21035	1516	92	1530	110	9.6	2.7
21	21.4	1.4	146.2	8.8	0.106	0.014	3.703704	0.2743	0.1056	1540	100	1520	120	16.3	5.4
22	6.25	0.26	40.8	1.8	0.124	0.028	3.759398	0.4664	0.54196	1510	160	1490	230	31	12
24	9.65	0.69	56.1	4.1	0.097	0.013	3.663004	0.322	0.067274	1550	120	1540	150	15.6	5
25	7.53	0.73	41.4	3.7	0.134	0.035	3.496503	0.379	0.62624	1670	190	1580	240	32	13
26	52.3	4.4	425	30	0.1027	0.0093	3.690037	0.2723	0.1534	1540	99	1530	120	10.9	4.5
28	85.6	6.8	637	46	0.0916	0.0076	3.731343	0.2506	0.51547	1529	93	1540	110	9.7	2.8
29	56.2	4.7	485	38	0.0986	0.0088	3.816794	0.3059	0.48817	1490	110	1490	130	14	3.7

2117350

Sample	U ppm	±	Th ppm	±	^{207}Pb-^{206}Pb	±	^{238}U-^{206}Pb	±	Error Correlation	^{206}Pb-^{238}U age	±	^{207}Pb corrected ^{206}Pb-^{238}U age	±	Discordance %	±
1	28.8	2.1	4.46	0.49	0.222	0.018	2.785515	0.1397	0.025394	1973	87	1770	100	31.4	7.9
4	9.28	0.74	1.95	0.27	0.325	0.042	2.695418	0.2616	0.50772	2020	170	1620	200	33	11
5	7.48	0.58	1.4	0.2	0.341	0.031	2.336449	0.1256	0.25844	2290	110	1800	130	36	11
7	31	3.1	8.37	0.68	0.223	0.015	3.164557	0.2704	0.49179	1760	130	1560	150	38	13
9	20.1	1.4	0.51	0.11	0.191	0.016	3.311258	0.1974	0.307	1697	89	1547	97	36	11
10	10.04	0.89	1.69	0.2	0.183	0.019	3.205128	0.2568	0.23808	1740	120	1570	110	37	10
11	5.93	0.45	0.88	0.13	0.412	0.037	2.369668	0.1909	0.39624	2260	160	1610	180	144	35
12	7.88	0.44	1.08	0.12	0.367	0.032	2.739726	0.1801	0.52922	2000	110	1490	140	175	44
13	13.4	0.87	3.02	0.29	0.312	0.022	2.873563	0.1982	0.43015	1920	120	1530	140	174	49
15	10.51	0.72	0.48	0.11	0.276	0.019	2.80112	0.2118	0.001308	1960	130	1640	140	151	45
18	4.02	0.34	0.7	0.12	0.567	0.071	2	0.176	0.62651	2600	190	1470	270	152	50
21	6.16	0.46	0.76	0.13	0.441	0.042	2.10084	0.181	0.4439	2500	180	1680	210	58	21
23	8.92	0.73	1.86	0.27	0.312	0.029	2.808989	0.2052	0.38218	1960	120	1570	150	58	30
24	24	2.2	0.73	0.12	0.15	0.013	3.412969	0.3029	0.61425	1650	130	1570	150	40	16
25	14.8	1	3.11	0.34	0.153	0.018	3.246753	0.2003	0.50611	1726	94	1650	120	42	11
26	3.59	0.38	0.42	0.11	0.54	0.064	1.872659	0.1648	0.46224	2740	200	1640	270	61	31
27	14.81	0.83	2.83	0.14	0.263	0.019	2.717391	0.1403	0.80445	2017	88	1750	120	43.6	7.8
28	13.6	0.49	0.833	0.07	0.269	0.019	2.80112	0.1334	0.50357	1964	83	1680	100	47	7.3

2131356

Sample	U ppm	±	Th ppm	±	^{207}Pb-^{206}Pb	±	^{238}U-^{206}Pb	±	Error Correlation	^{206}Pb-^{238}U age	±	^{207}Pb corrected ^{206}Pb-^{238}U age	±	Discordance %	±
1	27.7	2.4	16	1.1	0.2	0.011	2.702703	0.1826	0.32757	2020	120	1830	140	26	6.5
2	16.3	1.4	6.24	0.62	0.233	0.012	2.538071	0.1804	0.52606	2130	130	1860	150	31.6	7
3	16.4	1.6	5.74	0.61	0.243	0.023	2.222222	0.1728	0.75979	2380	160	2080	230	30	9.5
4	22.2	3.9	11.3	1.9	0.206	0.013	2.747253	0.2642	0.18653	2060	200	1790	190	28.1	8.3
5	16.2	1.4	7.06	0.7	0.258	0.019	2.217295	0.1622	0.70342	2390	150	2070	200	30.2	9.2
7	58	6.1	9.5	1.1	0.1412	0.0098	3.012048	0.245	0.69936	1840	130	1800	170	16.2	5.7
8	25.8	2.1	12.2	1.1	0.203	0.013	2.840909	0.2018	0.31521	1940	120	1690	110	30	7.6
9	18.2	1.5	9.35	0.77	0.236	0.018	2.80112	0.1962	0.31656	1960	120	1670	150	38.8	8.8
10	10.51	0.98	5.87	0.48	0.26	0.019	2.597403	0.2361	0.52561	2090	170	1750	190	42	10
11	9.1	0.5	6.54	0.34	0.357	0.032	2.242152	0.1609	0.49381	2370	140	1640	170	57	10
12	29.7	2.2	14.8	1.1	0.179	0.012	2.967359	0.2025	0.50935	1920	140	1720	130	26	7.2
13	18.8	2.8	280	150	0.211	0.014	2.666667	0.2916	0.59705	2040	190	1840	260	34.1	9.5
14	67	11	48.6	8	0.1401	0.0073	2.881844	0.191	0.33632	1920	110	1860	130	11.9	3.1
15	20.8	2.3	16.3	1.5	0.226	0.013	2.631579	0.187	0.15466	2070	130	1750	120	38.8	7.9
17	13.5	1.1	8.64	0.79	0.247	0.025	2.557545	0.1962	0.12626	2120	140	1800	170	38.9	9.3
18	49.1	5.3	37.8	3.6	0.1628	0.009	2.610966	0.2181	0.56926	2080	150	2020	200	16.9	4.9
19	29.8	2.8	21.2	2	0.1717	0.0095	2.816901	0.1904	-0.000905	1950	120	1830	130	21.4	5.8
20	17	2.3	11.4	1.8	0.218	0.02	2.531646	0.1538	0.3792	2140	110	1900	150	27.9	7.4
21	6.5	1	3.07	0.47	0.403	0.031	1.915709	0.1908	0.50614	2690	220	1820	240	50	14
22	13.29	0.91	4.08	0.37	0.272	0.014	2.325581	0.1406	0.21769	2300	120	1890	130	36.9	5.6
23	12.54	0.91	7.99	0.79	0.247	0.023	2.493766	0.1493	0.35936	2170	110	1850	150	38.4	8.5
24	23.1	2.7	15.4	2.2	0.216	0.015	2.808989	0.1736	0.1524	1960	100	1720	120	35.4	6.7
25	16.7	1.5	0.73	0.16	0.26	0.017	2.463054	0.1699	0.17393	2190	130	1830	150	40.8	8
26	16.6	1.5	8.82	0.88	0.247	0.018	2.525253	0.1658	0.7587	2140	120	1830	160	38	10
27	33.4	2.4	14.5	1.1	0.1961	0.0093	2.777778	0.1929	0.011435	1980	120	1790	130	28	6.2
28	18.1	1.8	6.9	0.76	0.254	0.016	2.518892	0.2411	0.54364	2140	170	1760	190	41.9	8.9
29	7.88	0.53	4.76	0.41	0.353	0.031	2.079002	0.1556	0.47507	2520	160	1850	210	53	11
30	21.2	2.7	7.5	1	0.242	0.014	2.369668	0.219	0.23942	2260	180	1910	180	31.9	8.6
31	16.83	0.93	9.7	0.66	0.233	0.013	2.710027	0.1469	0.27191	2021	94	1730	110	40.6	6.5
33	24	1.5	14.28	0.99	0.198	0.014	2.754821	0.1366	0.46076	1993	86	1800	110	29.6	7.7
34	16.5	1.2	7.11	0.66	0.242	0.016	2.518892	0.1586	0.61253	2150	120	1850	160	35.9	7.7
35	30.2	2.1	15.6	1.2	0.182	0.01	2.832861	0.1685	0.51693	1944	96	1790	120	25.1	6.9
36	25.4	1.6	7.5	0.51	0.222	0.026	2.512563	0.2083	0.47061	2150	150	1930	230	33.5	9.3
37	23.1	1.6	8.79	0.9	0.261	0.018	2.415459	0.1459	0.51642	2230	110	1870	160	40.3	8.9
38	23.5	1.9	12	1.1	0.203	0.015	2.631579	0.1593	0.37423	2070	110	1870	130	27.6	8
39	16.1	1.2	7.5	0.8	0.239	0.022	2.610966	0.1977	0.71261	2090	140	1800	180	38	11
40	13.94	0.73	3.69	0.21	0.308	0.017	2.347418	0.1102	0.30174	2284	89	1790	110	43.9	6.1
41	24.2	1.1	12.21	0.45	0.237	0.014	2.617801	0.1439	0.47977	2078	98	1800	120	34	6.5
42	18	0.84	9.14	0.36	0.254	0.016	2.493766	0.1493	0.5021	2210	130	1840	140	35	6.9
43	12.2	0.58	4.75	0.23	0.274	0.021	2.352941	0.1384	0.58187	2280	110	1910	160	36.2	8.4

2131355

Sample	U ppm	±	Th ppm	±	^{207}Pb-^{206}Pb	±	^{238}U-^{206}Pb	±	Error Correlation	^{206}Pb-^{238}U age	±	^{207}Pb corrected ^{206}Pb-^{238}U age	±	Discordance %	±
1	18.9	3.3	62.3	7.4	0.219	0.023	3.367003	0.3628	0.17788	1670	160	1360	170	50	10
2	8.08	0.46	69.9	4	0.243	0.028	2.849003	0.2435	0.18552	1930	140	1560	200	46	12
3	6.96	0.77	29.4	2.8	0.234	0.036	3.205128	0.339	0.70162	1740	160	1390	240	55	18
5	6.69	0.53	30.3	2.3	0.266	0.039	2.597403	0.3036	0.78906	2080	210	1590	250	51	14
6	9.29	0.63	40.8	2.5	0.21	0.021	3.125	0.2148	0.46626	1780	110	1510	140	41	10
8	11.14	0.68	43.3	1.7	0.234	0.023	2.873563	0.2312	0.31362	1920	130	1560	170	44.9	9.1
9	6.88	0.67	54.9	5	0.28	0.026	2.86533	0.2381	0.40481	1920	140	1420	170	58	12
10	7.92	0.71	75	7.5	0.258	0.037	2.932551	0.1978	0.26039	1890	110	1470	190	54	14
11	5	0.47	26.1	1.6	0.327	0.046	2.590674	0.2483	0.715	2090	180	1460	270	62	16
12	11.24	0.81	50	3.5	0.204	0.021	3.095975	0.2205	0.19754	1800	110	1530	130	38.4	8.5
13	12.07	0.92	92.3	5.3	0.221	0.018	3.257329	0.1804	0.30435	1724	83	1410	110	48.1	8
14	7.36	0.8	52.2	4.8	0.244	0.035	3.154574	0.2886	0.60178	1770	140	1410	200	53	13
17	7.63	0.61	60.8	4.6	0.233	0.033	3.030303	0.2755	0.4199	1830	140	1500	210	47	13
18	6.53	0.55	54.8	4	0.259	0.031	2.86533	0.2627	0.78819	1920	150	1520	210	52	14
19	7.17	0.64	58.7	4.5	0.315	0.039	2.369668	0.2583	-0.53288	2250	210	1520	160	47.4	8.3
21	9.02	0.65	63.9	5.6	0.218	0.025	3.076923	0.2367	0.49936	1810	120	1510	160	44	12
22	12.63	0.88	58.7	4.2	0.189	0.015	3.115265	0.2814	0.51689	1780	140	1580	180	32.1	8.5
23	7.55	0.75	59.7	5.3	0.231	0.03	2.86533	0.3038	0.36937	1920	180	1590	210	44	12
24	6.01	0.43	48.9	2.7	0.282	0.034	2.777778	0.216	0.20239	1980	130	1460	180	53	12
25	8.92	0.76	68	3.8	0.267	0.025	2.702703	0.1388	0.7442	2024	88	1550	150	44.1	9.3
26	10.42	0.8	72.6	4.4	0.244	0.02	2.824859	0.1436	0.5165	1952	86	1550	120	40.5	7.7
27	9.24	0.66	71.7	4.2	0.252	0.014	2.816901	0.119	0.17468	1957	73	1521	89	42.7	5.1
28	8.01	0.58	60.4	3	0.303	0.025	2.544529	0.1748	0.32389	2130	120	1510	150	49.3	9.3
29	12.2	1	55.2	2.2	0.223	0.019	2.906977	0.169	0.15541	1904	94	1570	120	36.3	6.9
30	8.59	0.54	65.8	2.3	0.267	0.022	2.717391	0.1477	-0.090063	2018	96	1520	110	43.9	6.9
31	6.1	1.6	49	11	0.311	0.037	2.336449	0.1965	0.45419	2280	160	1600	230	46	12

1831646 + 1831650

Sample	U ppm	±	Th ppm	±	^{207}Pb-^{206}Pb	±	^{238}U-^{206}Pb	±	Error Correlation	^{206}Pb-^{238}U age	±	^{207}Pb corrected ^{206}Pb-^{238}U age	±	Discordance %	±
1	31.1	3	0.75	0.092	0.227	0.011	2.590674	0.094	0.031463	2102	67	1853	74	30.3	3.8
2	20.7	1.6	0.185	0.096	0.349	0.023	2.155172	0.1254	0.071342	2450	120	1850	130	45.8	6.9
3	36.2	7.5	0.243	0.081	0.216	0.02	2.770083	0.1918	-0.046924	1980	120	1760	130	31.2	6.5
4	27.3	1.6	0.318	0.027	0.217	0.013	2.45098	0.1021	0.37353	2203	77	1990	100	24.2	5.4
5	33.9	2.2	0.426	0.05	0.229	0.011	2.544529	0.0971	0.032626	2134	69	1883	82	29.7	4
6	37.8	3.1	1.5	0.38	0.211	0.011	2.531646	0.1025	0.29263	2141	75	1939	88	24.4	4.4
7	33.6	1.7	2.48	0.14	0.214	0.014	2.673797	0.1573	0.54845	2040	100	1840	130	29.3	6.6
8	17.9	1.2	0.069	0.014	0.266	0.02	2.564103	0.1381	0.32233	2116	97	1740	110	40.6	7
9	44	7.4	0.52	0.14	0.209	0.011	2.80112	0.2275	-0.006141	1960	140	1760	140	30.1	5.6
10	32.8	4.4	0.0224	0.0089	0.2321	0.009	2.439024	0.1785	-0.14645	2210	140	1930	130	27.8	5
11	30.6	2	0.067	0.018	0.231	0.012	2.564103	0.1512	0.36396	2120	110	1870	130	31	5.9
12	31.8	1.5	0.0144	0.0082	0.223	0.011	2.710027	0.0955	0.34766	2022	60	1784	74	32.2	4.3
13	31.5	3	0.134	0.027	0.316	0.017	2.057613	0.1397	0.19889	2540	140	1960	120	36.9	6.2
14	34	2.1	0.063	0.017	0.218	0.013	2.617801	0.1096	0.43122	2083	74	1863	94	28.7	5.1
15	27.5	1.4	0.218	0.035	0.234	0.015	2.597403	0.1552	0.55046	2090	110	1800	120	33.5	6.4
16	7.16	0.35	0.255	0.032	0.411	0.029	1.988072	0.1186	0.47489	2620	130	1810	170	51.4	9.5
17	35.5	2.7	0.274	0.036	0.18	0.011	2.73224	0.1269	0.58716	2009	80	1870	100	21.4	4.3
18	34.1	2.8	0.045	0.02	0.202	0.011	2.873563	0.1817	0.13033	1950	90	1740	120	29.5	5.7
19	44.4	2.5	3.54	0.24	0.202	0.011	2.770083	0.1228	0.37189	1986	77	1802	91	27.1	5.2
20	14.96	0.79	0.035	0.01	0.274	0.017	2.544529	0.123	0.17528	2133	91	1760	110	43.2	7.2
21	12.53	0.76	0.0108	0.0065	0.316	0.027	2.304147	0.154	0.27727	2310	130	1840	170	44.7	8.8
22	38.4	2.8	1.53	0.12	0.208	0.013	2.785515	0.1474	0.63915	1972	89	1780	110	29.6	6.4
23	41.9	1.7	8.73	0.35	0.1724	0.0092	2.724796	0.1633	0.57512	2010	100	1910	130	18.4	5
24	24.74	0.84	11.38	0.35	0.194	0.013	2.673797	0.1144	0.55622	2045	76	1890	100	23.7	5.2
25	109.5	5	36.2	1.2	0.1409	0.0042	2.857143	0.1061	0.5197	1934	62	1893	79	9.6	2.6
26	25.9	1.1	8.37	0.31	0.197	0.012	2.538071	0.1482	0.60839	2130	110	1950	120	23	5.1
27	91.3	5.8	33.6	2.1	0.1444	0.0053	2.793296	0.1326	0.38472	1968	82	1918	98	10.6	3.4
28	38.1	2.3	11.5	0.65	0.1784	0.0098	2.680965	0.115	0.19085	2038	73	1918	86	18.2	4
29	16.4	0.82	4.98	0.26	0.251	0.013	2.427184	0.106	0.029525	2223	81	1933	99	32.8	5.4
30	23.3	1.3	7.1	0.39	0.207	0.012	2.65252	0.1196	0.1122	2057	78	1861	95	27.5	5.3

31	13.39	0.56	5.89	0.27	0.282	0.02	2.304147	0.1221	0.34953	2320	100	1960	140	37.1	7.5
32	114.7	6	44.1	1.7	0.1357	0.0069	2.857143	0.1224	0.1501	1934	72	1902	87	9.5	2.5
33	6.41	0.43	1.388	0.093	0.413	0.031	2.004008	0.1205	0.37373	2600	130	1820	170	51.7	9.6
34	13.01	0.56	4.59	0.2	0.27	0.024	2.583979	0.1402	0.54898	2105	99	1780	130	41.8	8.7
35	28.4	2.7	5.64	0.54	0.184	0.01	2.695418	0.138	0.33254	2031	91	1864	88	21.8	4.1
36	10.96	0.69	10.73	0.89	0.336	0.027	1.972387	0.1167	0.52602	2640	130	2080	180	37.3	8.7
37	22.12	0.67	6.41	0.28	0.224	0.013	2.624672	0.1309	0.4648	2076	90	1860	110	31.1	5.5
38	29.6	1.6	5.55	0.31	0.188	0.014	2.710027	0.1616	0.51273	2020	100	1890	130	21	5.1
39	31	1.2	8.19	0.38	0.184	0.014	2.739726	0.1126	0.56679	2003	73	1863	97	22.6	5.6
40	20.21	0.86	5.7	0.21	0.218	0.011	2.48139	0.1047	0.35756	2178	76	1974	98	25.5	5
41	15.56	0.88	3.96	0.23	0.275	0.016	2.325581	0.119	0.67876	2301	99	1940	140	35.2	6.6
42	17.69	0.83	5.2	0.22	0.238	0.022	2.538071	0.1417	0.52263	2130	100	1890	150	34	7.7
43	18.6	1.1	0.045	0.015	0.237	0.017	2.570694	0.1454	0.49727	2110	100	1870	130	33	7.4
44	30.6	2.3	10.22	0.68	0.197	0.013	2.645503	0.098	-0.37597	2064	66	1899	79	23.2	4.9
45	33.3	1.9	9.32	0.38	0.197	0.013	2.463054	0.1395	0.55566	2190	100	2060	150	22.2	4.7
46	112.4	9.9	31.4	2.3	0.1371	0.0059	2.638522	0.1392	0.30243	2068	93	2020	100	8.4	2.5
47	23.5	1.1	9.38	0.38	0.215	0.013	2.531646	0.1154	0.30563	2144	81	1950	110	26.5	4.9

2131360

Sample	U ppm	±	Th ppm	±	^{207}Pb-^{206}Pb	±	^{238}U-^{206}Pb	±	Error Correlation	^{206}Pb-^{238}U age	±	^{207}Pb corrected ^{206}Pb-^{238}U age	±	Discordance %	±
1	35	3.3	27.1	2.3	0.194	0.016	2.785515	0.1474	0.3604	1973	93	1800	110	30.8	6.9
2	34.3	5.8	25.9	3.8	0.2	0.015	2.666667	0.1991	0.52109	2040	130	1880	170	28.4	7.9
3	37.4	3.6	26.8	3.2	0.186	0.011	2.932551	0.215	0.47956	1890	120	1740	140	30.2	6.4
4	59	14	52	13	0.175	0.018	2.840909	0.1776	0.32474	1940	110	1820	130	23.6	8.6
5	24.2	2.3	17.9	1.6	0.219	0.017	2.538071	0.1546	0.45853	2140	110	1920	150	31.2	8.2
6	19.5	1.8	16.8	1.6	0.222	0.016	2.816901	0.1746	0.4767	1960	110	1720	130	39.3	7.5
7	20	1.2	13.91	0.98	0.286	0.022	2.469136	0.2256	0.10639	2180	170	1780	180	46	11
8	16.5	1.2	11.6	1.1	0.247	0.017	2.610966	0.1772	0.57119	2080	120	1740	120	43.7	7.4
9	25.8	3.7	17.2	2.3	0.244	0.025	2.739726	0.1576	0.43929	2000	97	1710	140	46	10
10	25.3	2.2	17.2	1.9	0.215	0.013	2.702703	0.1826	0.76309	2020	120	1800	150	32.1	7.9
11	11.9	1.4	11.7	1.4	0.294	0.021	2.409639	0.209	0.29612	2220	160	1750	160	47	11
12	20.9	1.6	17.3	1.8	0.242	0.018	2.45098	0.1862	0.7643	2200	140	1930	190	36.4	8.7
13	8.2	0.56	6.73	0.61	0.38	0.034	2.217295	0.2606	0.58708	2380	230	1570	190	59	12
14	24.1	2.1	17.6	1.5	0.219	0.012	2.57732	0.1793	0.38106	2110	130	1890	140	33.9	7
15	27.7	2.1	19.2	1.4	0.227	0.015	2.777778	0.216	0.51063	1980	130	1740	160	44	7.9
16	10.25	0.93	6.23	0.63	0.35	0.031	2.150538	0.2359	0.595	2440	230	1800	250	52	12
17	7.41	0.52	6.5	1.3	0.35	0.025	2.178649	0.1566	0.20367	2430	140	1820	180	53.4	9.8
18	19.8	1.4	10.82	0.95	0.244	0.018	2.932551	0.2322	0.2674	1890	130	1600	140	52.3	8.2
19	21.2	1.9	14.1	1.2	0.21	0.017	2.610966	0.2795	0.56511	2080	190	1910	240	29.9	9.5
20	28.4	2.1	22.4	1.6	0.227	0.018	2.890173	0.1754	0.14998	1910	100	1621	89	44.7	6.4
21	16.4	2.3	12	1.6	0.268	0.02	2.564103	0.2367	0.37218	2110	160	1710	160	43	11
22	24.7	2.1	23.3	1.7	0.179	0.015	2.941176	0.2422	0.72729	1880	140	1740	170	31.2	8.5
23	4.63	0.49	2.62	0.5	0.496	0.043	1.733102	0.2163	0.65217	2900	300	1800	350	61	20
24	19.1	1.3	12.35	0.62	0.278	0.027	2.604167	0.1967	0.6449	2090	130	1730	170	47	13
25	16.1	1.9	11.2	1.6	0.258	0.025	2.531646	0.2179	0.4339	2140	160	1760	160	41	12
26	23.5	2.8	15.8	1.7	0.238	0.018	2.487562	0.1733	-0.022251	2170	130	1900	150	36.1	8.7
27	37.5	4.1	31.1	3.6	0.177	0.011	2.881844	0.1578	0.52312	1916	91	1790	120	27.8	6.9
28	6.89	0.65	4.29	0.38	0.433	0.049	1.879699	0.1731	0.69431	2730	200	1780	290	63	15
29	30.3	2.2	22.9	1.6	0.205	0.013	2.724796	0.1485	0.34877	2010	95	1820	120	35.5	7
30	14.4	2.1	10.2	1.6	0.262	0.021	2.475248	0.1716	0.23289	2180	130	1840	160	46	9.7
31	39.8	3	33.3	2.2	0.171	0.012	2.949853	0.2088	0.47292	1880	120	1760	140	26.8	7.3
32	12.12	0.83	7.42	0.45	0.324	0.021	2.325581	0.1028	0.26696	2301	86	1800	120	46.5	7
33	16	1.7	9.91	0.98	0.272	0.016	2.512563	0.1578	0.42321	2190	130	1800	140	39.2	7.4
34	7.02	0.36	4.33	0.2	0.396	0.024	2.03666	0.1244	0.3239	2570	130	1820	150	50.2	8.1
35	3.9	0.27	2.79	0.19	0.526	0.048	1.508296	0.1365	0.51031	3250	230	1810	300	45	13
36	31.2	2.2	23.8	1.5	0.199	0.013	2.932551	0.1462	0.13137	1887	80	1710	100	29.4	5.9
37	2.69	0.15	0.952	0.062	0.616	0.045	1.222494	0.0867	0.49025	3830	210	1760	310	32	11

Chapter 2; Muscovite Ar-Ar data.

2111462

Incremental Heating			36Ar(a) [V]	37Ar(ca) [V]	38Ar(cl) [V]	39Ar(k) [V]	40Ar(r) [V]	Age ± 2σ (Ma)	40Ar(r) (%)	39Ar(k) (%)	K/Ca ± 2σ
6M42390D	63 °C		0.0000059	0.0000468	0.0000024	0.0000358	0.1388974	6766.44 ±905.56	101.28	0.10	0.4 ±0.8
6M42391D	64 °C		0.0000034	0.0000667	0.0000000	0.0000345	0.0701374	5635.01 ±982.84	101.49	0.09	0.3 ±0.4
6M42392D	67 °C		0.0000074	0.0001504	0.0000000	0.0054044	0.7394436	1621.02 ±11.73	100.30	14.47	18.7 ±13.8
6M42394D	71 °C		0.0000042	0.0001445	0.0000003	0.0066566	0.7996328	1485.44 ±7.77	100.16	17.82	24.0 ±19.3
6M42395D	75 °C	4	0.0000017	0.0002053	0.0000000	0.0065818	0.8316634	1537.24 ±9.12	100.06	17.62	16.7 ±8.2
6M42396D	88 °C	4	0.0000044	0.0003229	0.0000278	0.0186349	2.3367252	1529.34 ±9.61	100.06	49.90	30.0 ±11.3

2111462

Incremental Heating			36Ar(a) [V]	37Ar(ca) [V]	38Ar(cl) [V]	39Ar(k) [V]	40Ar(r) [V]	Age ± 2σ (Ma)	40Ar(r) (%)	39Ar(k) (%)	K/Ca ± 2σ
6M42966D	61 °C		0.0000051	0.0000455	0.0000046	0.0000820	0.0416351	3352.26 ±363.56	103.80	0.35	0.9 ±8.0
6M42967D	61 °C		0.0000031	0.0000750	0.0000031	0.0002183	0.0872088	2993.97 ±152.65	98.95	0.92	1.5 ±8.3
6M42969D	61 °C		0.0000025	0.0000061	0.0000014	0.0002309	0.0196306	1162.27 ±168.60	104.03	0.98	19.7 ±1323.2
6M42970D	61 °C		0.0000006	0.0000221	0.0000036	0.0011394	0.2121132	1970.90 ±32.26	100.09	4.82	26.8 ±474.5
6M42971D	61 °C		0.0000061	0.0000283	0.0000045	0.0005569	0.0640149	1441.23 ±62.39	97.24	2.35	10.2 ±148.8
6M42972D	61 °C		0.0000014	0.0000573	0.0000000	0.0008708	0.2780739	2673.49 ±53.49	99.85	3.68	7.9 ±58.2
6M42975D	61 °C		0.0000028	0.0000583	0.0000000	0.0004683	0.0438808	1247.55 ±92.14	98.13	1.98	4.2 ±32.3
6M42976D	61 °C		0.0000040	0.0000173	0.0000000	0.0008437	0.0814779	1274.98 ±52.39	101.50	3.57	25.3 ±592.7
6M42977D	62 °C		0.0000022	0.0000940	0.0000000	0.0004662	0.0475501	1325.73 ±85.68	101.42	1.97	2.6 ±11.4
6M42978D	62 °C		0.0000005	0.0000668	0.0000000	0.0018307	0.1911028	1347.61 ±33.51	100.08	7.74	14.3 ±89.0
6M42980D	62 °C	4	0.0000001	0.0000187	0.0000023	0.0015661	0.1726595	1400.18 ±28.92	100.01	6.62	43.5 ±945.7
6M42981D	63 °C	4	0.0000009	0.0000041	0.0000037	0.0034995	0.3816568	1389.62 ±13.55	99.93	14.80	440.8 ±42472.0
6M42982D	64 °C	4	0.0000026	0.0000331	0.0000042	0.0048323	0.5265085	1388.70 ±14.60	99.85	20.43	75.9 ±968.9
6M42983D	67 °C	4	0.0000002	0.0000183	0.0000038	0.0070431	0.7563674	1374.73 ±10.27	99.99	29.78	200.4 ±4438.1

2131358

Incremental Heating		36Ar(a) [V]	37Ar(ca) [V]	38Ar(cl) [V]	39Ar(k) [V]	40Ar(r) [V]	Age ± 2σ (Ma)	40Ar(r) (%)	39Ar(k) (%)	K/Ca ± 2σ
6M42370D	61 °C	0.0000038	0.0000018	0.0000063	0.0019040	0.135399	995.88 ±22.63	99.18	1.43	543.9 ±31495.4
6M42372D	61 °C	0.0000121	0.0001564	0.0000000	0.0155444	1.317851	1137.37 ±6.37	99.73	11.69	51.7 ±43.7
6M42373D	62 °C	0.0000114	0.0000770	0.0000000	0.0163012	1.499399	1207.69 ±5.94	99.77	12.26	110.1 ±158.7
6M42374D	62 °C	0.0000092	0.0001425	0.0000000	0.0109363	0.873998	1088.29 ±9.72	99.69	8.23	39.9 ±29.4
6M42376D	62 °C	0.0000086	0.0000393	0.0000014	0.0093139	0.667523	1001.87 ±5.11	99.62	7.01	123.2 ±334.4
6M42377D	62 °C	0.0000087	0.0001788	0.0000000	0.0173897	1.188254	965.68 ±5.77	99.78	13.08	50.6 ±33.2
6M42378D	63 °C	0.0000154	0.0002984	0.0000255	0.0198020	1.344563	960.96 ±3.58	99.66	14.89	34.5 ±12.7
6M42379D	64 °C	0.0000268	0.0002809	0.0000038	0.0134025	0.993611	1028.15 ±7.71	99.20	10.08	24.8 ±10.6
6M42381D	65 °C	0.0000145	0.0001677	0.0000102	0.0074959	0.618678	1114.88 ±12.04	99.30	5.64	23.2 ±14.2
6M42382D	70 °C	0.0000171	0.0004744	0.0000037	0.0126880	1.039730	1108.93 ±3.84	99.51	9.54	13.9 ±3.4
6M42384D	75 °C	0.0000207	0.0001497	0.0000063	0.0081695	0.709267	1157.56 ±9.21	99.13	6.14	28.4 ±21.5

2111462

Incremental Heating		36Ar(a) [V]	37Ar(ca) [V]	38Ar(cl) [V]	39Ar(k) [V]	40Ar(r) [V]	Age ± 2σ (Ma)	40Ar(r) (%)	39Ar(k) (%)	K/Ca ± 2σ
6M42348D	61 °C	0.0000249	0.0000567	0.0000033	0.0001596	0.3156258	5586.91 ±223.94	97.70	0.13	1.5 ±2.4
6M42349D	61 °C	0.0000360	0.0000365	0.0000095	0.0003218	0.6344069	5581.47 ±159.23	98.33	0.27	4.6 ±13.6
6M42351D	61 °C	0.0002233	0.0015828	0.0000397	0.0176851	3.5819550	2073.52 ±14.76	98.17	14.86	5.8 ±0.6
6M42352D	61 °C	0.0000055	0.0005029	0.0000000	0.0049106	0.1961209	638.56 ±12.59	99.17	4.13	5.1 ±1.0
6M42353D	62 °C	0.0000077	0.0001113	0.0000000	0.0057817	0.2469822	675.62 ±11.14	99.07	4.86	27.0 ±25.2
6M42354D	62 °C	0.0000178	0.0001291	0.0000082	0.0062075	0.3051335	758.64 ±12.16	98.28	5.22	25.0 ±16.6
6M42356D	62 °C	0.0000259	0.0003101	0.0000014	0.0114060	0.5736301	772.91 ±7.67	98.67	9.58	19.1 ±6.8
6M42357D	62 °C	0.0000314	0.0002068	0.0000112	0.0126060	0.6699309	808.23 ±5.63	98.62	10.59	31.7 ±18.2
6M42358D	63 °C	0.0000311	0.0001694	0.0000119	0.0170497	0.8904803	796.97 ±6.73	98.97	14.33	52.3 ±31.9
6M42359D	64 °C	0.0000311	0.0000501	0.0000044	0.0147272	0.7989262	821.72 ±8.67	98.85	12.37	152.7 ±285.7
6M42361D	65 °C	0.0000081	0.0000199	0.0000126	0.0039341	0.2131608	820.93 ±18.62	98.88	3.31	102.8 ±505.6
6M42362D	72 °C	0.0000062	0.0000354	0.0000010	0.0026080	0.1411002	819.96 ±21.34	98.70	2.19	38.3 ±98.9
6M42363D	75 °C	0.0000324	0.0000625	0.0000000	0.0140663	0.7708588	828.45 ±7.54	98.76	11.82	117.0 ±154.3
6M42364D	88 °C	0.0000232	0.0000052	0.0000133	0.0075550	0.4661139	910.18 ±11.05	98.54	6.35	758.5 ±15186.5

2111462

Incremental Heating			36Ar(a) [V]	37Ar(ca) [V]	38Ar(cl) [V]	39Ar(k) [V]	40Ar(r) [V]	Age ± 2σ (Ma)	40Ar(r) (%)	39Ar(k) (%)	K/ Ca ± 2σ
6M42930D	61 °C		0.0000081	0.0003469	0.0000261	0.0004873	0.6914177	5018.74 ±82.05	99.65	0.60	0.7 ±0.4
6M42932D	61 °C		0.0000118	0.0005686	0.0000468	0.0059938	1.8268864	2608.75 ±12.16	99.81	7.42	5.5 ±1.9
6M42933D	61 °C		0.0000109	0.0005308	0.0000131	0.0035380	0.3670883	1341.84 ±15.89	99.12	4.38	3.5 ±0.9
6M42934D	62 °C		0.0000037	0.0007366	0.0000090	0.0063662	0.4635577	1034.69 ±11.70	99.76	7.88	4.5 ±1.5
6M42935D	62 °C		0.0000062	0.0006505	0.0000058	0.0036587	0.2658078	1032.91 ±17.78	99.31	4.53	2.9 ±1.0
6M42937D	62 °C		0.0000042	0.0004182	0.0000063	0.0021712	0.1881873	1178.77 ±24.38	99.34	2.69	2.7 ±1.6
6M42938D	62 °C		0.0000127	0.0004920	0.0000166	0.0059375	0.5655207	1262.42 ±13.71	99.34	7.35	6.3 ±3.2
6M42939D	63 °C		0.0000150	0.0006828	0.0000409	0.0174850	1.5834459	1217.17 ±4.22	99.72	21.65	13.3 ±4.4
6M42940D	64 °C		0.0000203	0.0011562	0.0000430	0.0351345	2.7752616	1100.29 ±3.42	99.78	43.50	15.8 ±2.7

2131362

Incremental Heating			36Ar(a) [V]	37Ar(ca) [V]	38Ar(cl) [V]	39Ar(k) [V]	40Ar(r) [V]	Age ± 2σ (Ma)	40Ar(r) (%)	39Ar(k) (%)	K/ Ca ± 2σ
6M42334D	63 °C		0.0000032	0.0000142	0.0000000	0.0000327	0.0409666	4807.42 ±1261.00	97.74	1.30	1.2 ±9.5
6M42337D	72 °C		0.0000019	0.0000738	0.0000027	0.0000782	0.0640985	4107.67 ±432.30	100.87	3.11	0.6 ±0.8
6M42338D	75 °C	4	0.0000023	0.0000662	0.0000057	0.0011837	0.0410080	565.81 ±58.66	98.38	47.10	9.3 ±14.3
6M42339D	88 °C	4	0.0000052	0.0000020	0.0000000	0.0012186	0.0476583	627.34 ±49.86	96.87	48.49	324.2 ±15642.5

2131362

Incremental Heating			36Ar(a) [V]	37Ar(ca) [V]	38Ar(cl) [V]	39Ar(k) [V]	40Ar(r) [V]	Age ± 2σ (Ma)	40Ar(r) (%)	39Ar(k) (%)	K/ Ca ± 2σ
6M42918D	62 °C		0.0003653	0.0000758	0.0000580	0.0056327	3.362249	3601.91 ±13.77	96.86	2.91	38.7 ±196.0
6M42919D	62 °C		0.0002298	0.0002707	0.0000242	0.0186983	2.689218	1674.97 ±6.12	97.51	9.67	35.9 ±52.8
6M42920D	63 °C		0.0000158	0.0000173	0.0000000	0.0057604	0.673878	1458.76 ±9.60	99.30	2.98	172.9 ±4066.1
6M42922D	63 °C		0.0000119	0.0000874	0.0000067	0.0058753	0.599483	1326.05 ±13.10	99.41	3.04	35.0 ±154.4
6M42923D	64 °C		0.0000266	0.0001373	0.0000015	0.0101105	0.788498	1089.81 ±8.31	99.00	5.23	38.3 ±107.4
6M42924D	65 °C		0.0000440	0.0003441	0.0000173	0.0189227	1.503784	1105.29 ±3.95	99.13	9.79	28.6 ±34.1
6M42925D	67 °C		0.0001351	0.0004876	0.0000448	0.0395543	3.619434	1226.39 ±4.47	98.90	20.46	42.2 ±33.9
6M42927D	72 °C		0.0001086	0.0004132	0.0000267	0.0254745	2.531503	1301.39 ±8.30	98.73	13.17	32.1 ±30.5
6M42928D	77 °C		0.0003010	0.0013759	0.0000426	0.0633325	5.988779	1255.88 ±3.00	98.52	32.75	23.9 ±7.1

Chapter 2; apatite fission track data.

2131358

Sample	U ppm	RF	Sandard Deviation	Ns	rho s			±
					Area		Age (Ma)	
SHD1_B1	33.5241	5.677	1.903198	101	1600	6312500	343.7311	39.378
SHD1_B2	19.3773	8.004	1.550897	95	2500	3800000	357.5972	46.532
SHD1_B3	29.0874	6.603	1.92055	105	1600	6562500	409.7263	48.277
SHD1_B6	23.0246	5.506	1.267821	42	1600	2625000	210.2992	34.454
SHD1_C7	29.5818	6.003	1.775863	103	2500	4120000	255.9916	29.536
SHD1_BI11	38.8974	5.31	2.065357	126	1600	7875000	368.8505	38.254
SHD1_F11	35.5547	6.243	2.219844	118	2500	4720000	244.2284	27.166
SHD1_H5	43.796	6.374	2.79177	107	1600	6687500	280.1321	32.439
SHD1_B8	26.0777	5.23	1.363756	77	1600	4812500	337.0561	42.262
SHD1_B7	53.4187	7.155	3.822288	68	900	7555556	259.8923	36.594
SHD1_F6	20.6072	6.995	1.441489	259	4900	5285714	463.8425	43.399
SHD1_F5	38.2844	8.195	3.137503	57	900	6333333	302.9494	47.186
SHD1_E2	38.8639	6.467	2.513348	314	4900	6408163	301.9809	25.919
SHD1_D7	27.9396	5.532	1.545675	107	2500	4280000	281.0139	31.3
SHD1_C3	40.693	6.015	2.447794	111	1600	6937500	311.9862	35.058
SHD1_C4	31.6736	6.374	2.018859	178	2500	7120000	408.2823	40.171
SHD1_DA	47.9363	5.632	2.699631	100	1600	6250000	239.9452	27.538
SHD1_I7	31.533	5.987	1.887844	155	3600	4305556	251.0631	25.151
SHD1_E9	23.3343	6.333	1.477833	105	1600	6562500	506.8667	58.969
SHD1_K1	33.817	4.951	1.674434	88	2500	3520000	192.2731	22.6
SHD1_J9	43.4119	6.489	2.817155	158	2500	6320000	267.3471	27.447
SHD1_J6	17.4237	6.465	1.126506	83	1600	5187500	535.3818	68.202
SHD1_E1	28.7452	6.193	1.780213	200	2500	8000000	501.7842	47.166
SHD1_J8	19.266	5.514	1.062411	86	2500	3440000	326.385	39.53
SHD1_J11	41.6345	6.295	2.620745	245	2500	9800000	426.8911	38.287
SHD1_D4	28.2647	7.036	1.988588	89	1600	5562500	358.8282	45.651
SHD1_I2	34.8788	7.49	2.612476	66	900	7333333	382.6401	55.134

2111462

Sample	U ppm	RF	Sandard Deviation	Ns	rho s			±
					Area		Age (Ma)	
BLANCH1_D4	8.38995	6.029	0.50581	142	10000	1420000	309.7822	32.009
BLANCH1_F7	9.576	6.052	0.579549	23	900	2555556	481.9152	104.63
Blanch 1_1	21.9	1.8	8.219178	59	1170	5042735	445.1391	68.535
Blanch 1_2	51	3	5.882353	21	265	7924528	303.7291	68.645
Blanch 1_3	8.49	0.48	5.65371	30	2310	1298701	299.1172	57.17
Blanch 1_4	10.86	0.96	8.839779	22	1210	1818182	326.6717	75.396
Blanch 1_5	5.91	0.39	6.598985	12	816	1470588	479.7314	142.06
Blanch 1_6	109.4	9.9	9.04936	105	1040	10096154	182.1143	24.238
Blanch 1_7	60	3.2	5.333333	52	940	5531915	181.9431	27.033
Blanch 1_8	6.11	0.67	10.96563	15	278	5395683	1562.003	438.17
Blanch 1_9	15.9	1.4	8.805031	33	882	3741497	454.5698	88.677
Blanch 1_10	63.9	6.3	9.859155	37	1790	2067039	64.42144	12.349
Blanch 1_11	10.9	1.7	15.59633	67	1800	3722222	649.6267	128.7
Blanch 1_12	58	5.6	9.655172	85	2790	3046595	104.2854	15.144
Blanch 1_13	83.2	6.1	7.331731	101	1690	5976331	142.1894	17.574
Blanch 1_14	35.1	2.8	7.977208	25	1470	1700680	96.25507	20.726
Blanch 1_15	78.6	7	8.905852	83	1310	6335878	159.3529	22.524
Blanch 1_16	14	1.2	8.571429	37	1430	2587413	359.683	66.686
Blanch 1_17	9.72	0.75	7.716049	74	2540	2913386	573.6153	80.034
Blanch 1_18	36.3	4.2	11.57025	53	1970	2690355	146.6587	26.339
Blanch 1_19	76.5	5.8	7.581699	136	2480	5483871	141.903	16.242
Blanch 1_20	55.9	6.4	11.44902	75	746	10053619	350.2778	56.958
Blanch 1_21	21.1	1.7	8.056872	25	2310	1082251	101.8509	21.961
Blanch 1_22	5.92	0.42	7.094595	24	3470	691642.7	229.6964	49.638
Blanch 1_23	6.93	0.75	10.82251	23	2470	931174.1	263.4793	61.899
Blanch 1_24	9.57	0.71	7.419018	15	1420	1056338	217.2239	58.356
Blanch 1_25	7.02	0.63	8.974359	18	559	3220036	858.3118	216.47
Blanch 1_26	40.6	3.3	8.128079	98	3470	2824207	137.7453	17.859
Blanch 1_27	103.9	8.7	8.373436	80	1210	6611570	126.1212	17.617
Blanch 1_28	79.5	5.8	7.295597	145	2350	6170213	153.4994	16.968
Blanch 1_29	56.9	4.2	7.381371	42	714	5882353	203.6642	34.837

2131363 + 2131364

Sample	U ppm	RF	Sandard Deviation	Ns	rho s			±
					Area		Age (Ma)	
RED324_A3	6.23606	5.53	0.344845	100	2500	4000000	1102.752	126.01
RED324_K1	5.51464	6.334	0.349308	7	900	777777.8	259.1689	99.323
RED324_E2	6.98914	5.518	0.385675	12	900	1333333	348.1287	102.32
RED324_B2	11.3135	5.968	0.675213	19	900	2111111	340.7141	80.767
R323_A1	6.17163	12.41	0.765761	97	2500	3880000	1082.577	173.57
R323_A9	5.43097	18.15	0.985459	30	900	3333333	1058.885	272.56
R323_C3	10.082	10.93	1.102142	121	4900	2469388	443.6272	63.075
R323_E8	6.03949	29.44	1.77831	98	2500	3920000	1114.799	347.03
R323_F6	3.6378	15.58	0.566823	69	3600	1916667	919.1411	180.98
R323_E6	3.58325	11.7	0.419342	18	1600	1125000	563.3335	148.24
R323_B3	4.07222	9.574	0.38986	72	8100	888888.9	396.8119	60.251
R323_H4	5.9584	14.94	0.890387	11	1600	687500	212.7941	71.608
R323_A3	15.4126	9.887	1.523906	117	3600	3250000	383.7264	51.942
R323_F5	7.18971	14.4	1.03541	57	2500	2280000	568.7585	111.28
R323_E4	6.70023	13.79	0.924196	109	2500	4360000	1117.421	187.65
R323_C4	5.39677	7.568	0.408453	41	2500	1640000	545.9994	94.756
R323_C10	5.14511	8.959	0.460964	81	2500	3240000	1084.227	154.75
R323_G8	6.52192	6.726	0.438639	34	900	3777778	1003.727	184.9
R323_I3	3.4686	8.65	0.300019	68	3600	1888889	947.8439	141.19
R323_H1	5.79534	11.47	0.664487	72	4900	1469388	458.6898	75.42

2131356

Sample	U ppm	RF	Sandard Deviation	Ns	rho s			±
					Area		Age (Ma)	
ODO4_B2	9.47529	5.351	0.507015	99	4900	2020408	387.8992	44.166
ODO4_H7	10.3033	6.664	0.686644	48	2500	1920000	340.264	54.095
AS1 ODO4_1	24.7	2.2	8.906883	39	1570	2484076	198.2114	36.319
AS1 ODO4_4	8.26	0.74	8.958838	29	3620	801105	191.2518	39.432
AS1 ODO4_5	6.95	0.63	9.064748	21	2170	967741.9	272.8389	64.471
AS1 ODO4_6	3.19	0.36	11.28527	21	2550	823529.4	497.0413	122.11
AS1 ODO4_7	26.4	3.3	12.5	23	977	2354145	176.0516	42.8
AS1 ODO4_10	9.8	1.1	11.22449	44	3860	1139896	228.7005	42.985
AS1 ODO4_11	5.69	0.53	9.314587	43	6230	690208.7	238.3252	42.588
AS1 ODO4_12	7.83	0.58	7.407407	32	2900	1103448	276.0656	52.913

AS1 ODO4_13	13.98	0.99	7.081545	26	2010	1293532	182.5828	38.07
AS1 ODO4_15	12.3	1.4	11.38211	15	2050	731707.3	117.9795	33.291
AS1 ODO4_18	4.01	0.39	9.725686	14	2940	476190.5	233.4022	66.381
AS1 ODO4_19	2.51	0.44	17.52988	8	2030	394088.7	306.8302	121.08
AS1 ODO4_21	6.52	0.69	10.58282	17	1440	1180556	352.5838	93.3
AS1 ODO4_23	8.17	0.69	8.445532	9	1040	865384.6	208.5913	71.727
AS1 ODO4_24	19.8	2.2	11.11111	48	1620	2962963	292.7632	53.327
AS1 ODO4_25	15.3	1.4	9.150327	43	3080	1396104	180.0944	32.029
AS1 ODO4_26	3.41	0.37	10.85044	23	1170	1965812	1061.443	249.5

2131355

Sample	U ppm	RF	Sandard Deviation	Ns	rho s			±
					Area		Age (Ma)	
ASD1 L8	9.25292	7.686	0.711197	22	900	2444444	477.2332	108.16
ASD1 K1	15.8095	7.809	1.234612	63	1600	3937500	450.8501	66.829
ASD1 J3	13.058	8.139	1.062836	23	900	2555556	356.8903	79.885
ASD1 G8	8.40266	7.695	0.646552	31	1600	1937500	418.4627	81.765
ASD1_1	25.2	1.9	7.539683	38	1440	2638889	206.257	36.897
ASD1_2	17.45	0.99	5.673352	75	3530	2124646	239.2011	30.774
ASD1_3	16.4	1.5	9.146341	27	1740	1551724	186.6477	39.771
ASD1_5	16.6	1.3	7.831325	37	2250	1644444	195.2858	35.561
ASD1_7	64.1	4.9	7.644306	90	1510	5960265	183.4709	23.89
ASD1_8	29.9	2.1	7.023411	48	1690	2840237	187.3746	30.077
ASD1_9	22.3	2	8.96861	62	2570	2412451	212.9681	33.111
ASD1_10	13.5	1.3	9.62963	38	1820	2087912	302.349	57.038
ASD1_11	8.82	0.6	6.802721	24	2410	995850.6	222.1144	47.79
ASD1_12	34.8	2.8	8.045977	78	2120	3679245	208.21	28.921
ASD1_13	20.3	2.2	10.83744	28	1440	1944444	188.9186	41.156
ASD1_15	22.4	2.3	10.26786	28	1660	1686747	148.9801	32.042
ASD1_16	16.5	1.3	7.878788	51	1630	3128834	368.7834	59.253
ASD1_17	16.3	1.5	9.202454	32	1900	1684211	203.5581	40.568
ASD1_21	6.21	0.58	9.339775	11	720	1527778	474.5055	149.78
ASD1_22	13.21	0.67	5.071915	25	1780	1404494	209.3631	43.198
ASD1_25	17.3	1.4	8.092486	26	1030	2524272	285.6195	60.596
ASD1_26	18	1.6	8.888889	13	807	1610905	176.6797	51.457
ASD1_27	31.9	2.3	7.210031	29	911	3183315	196.6984	39.183
ASD1_28	18.2	1.8	9.89011	10	370	2702703	290.5739	96.277
ASD1_29	8.01	0.58	7.240949	8	1000	800000	196.8628	71.046

ASD1_32	10.78	0.71	6.586271	15	1310	1145038	209.1659	55.736
ASD1_33	24.6	1.8	7.317073	24	939	2555911	204.6692	44.381
ASD1_34	16.8	1.3	7.738095	36	1820	1978022	231.4497	42.53
ASD1_35	32.2	2.5	7.763975	52	1720	3023256	185.2333	29.439
ASD1_36	22.2	1.7	7.657658	17	670	2537313	224.7923	57.173
ASD1_37	19.4	1.5	7.731959	10	499	2004008	203.5068	66.25
ASD1_38	23.5	1.8	7.659574	20	828	2415459	202.5102	47.866
ASD1_39	15.5	1.4	9.032258	33	939	3514377	438.5458	86.006

2131357

Sample	U ppm	RF	Sandard Deviation	Ns	rho s			±
					Area		Age (Ma)	
PSC_B8	21.8175	5.54	1.208766	84	2500	3360000	282.4807	34.567
PSC_D2	14.9223	5.197	0.775522	185	4900	3775510	457.755	41.214
PSC_C4	34.0278	6.814	2.318544	143	2500	5720000	307.7228	33.194
PSC_D6	16.5301	12.51	2.068331	91	2500	3640000	400.2033	65.327
PSC_F5	16.2044	7.654	1.240276	288	6400	4500000	500.7356	48.368
PSC_1	15.3	1.4	9.150327	14	289.9	4829251	602.6756	170.25
PSC_2	27.1	2	7.380074	58	1564	3708440	268.2315	40.402
PSC_3	5.23	0.76	14.53155	72	1934	3722854	1287.206	240.83

1831646 and 1831650

Sample	U ppm	RF	Sandard Deviation	Ns	rho s			±
					Area		Age (Ma)	
646 A6	17.3366	7.778	1.348423	44	900	4888889	508.1817	86.207
646 A10	10.8145	7.374	0.797474	112	4900	2285714	384.5917	46.097
646 B9	20.3481	10.19	2.073197	136	2500	5440000	482.7441	64.286
646 C16	26.0181	8.666	2.254623	95	1600	5937500	414.2872	55.637
646 H17	19.1102	7.978	1.524684	76	2500	3040000	291.5772	40.741
646 G7	21.6983	8.277	1.796074	149	2500	5960000	495.4815	57.704
646 C2	23.1264	9.411	2.176417	106	2500	4240000	334.9131	45.295
646 E1	19.6521	9.539	1.87453	59	1600	3687500	342.5601	55.287
646 H13	11.1143	8.95	0.994688	69	2500	2760000	449.5711	67.439
646 B13	22.352	9.889	2.210304	62	1600	3875000	317.1264	51.044
646 G8	16.847	9.201	1.550062	139	3600	3861111	416.0122	52.059

646 H9	19.7083	9.51	1.874212	48	1600	3000000	279.2763	48.273
646 J7	19.0738	9.9	1.888383	87	2500	3480000	333.3263	48.643
646 J9	16.8367	10.06	1.693735	61	1600	3812500	411.1812	66.952
646 J13	22.8477	9.694	2.214764	44	900	4888889	389.2197	69.76
646 J14	16.5289	9.55	1.578563	70	1600	4375000	478.1154	73.148
646 F1	4.42234	10.91	0.48233	40	3600	1111111	454.678	87.336
646 F2	22.8739	10.15	2.322186	69	1600	4312500	344.1504	54.196
646 A14	21.4836	10.12	2.173427	53	1600	3312500	282.8081	48.246
646 F6	30.2503	10.31	3.118935	45	900	5000000	302.6975	54.865
646 B4	10.261	9.996	1.025659	80	3600	2222222	393.7938	59.058
646 H2	9.11426	10.37	0.944887	58	2500	2320000	460.4352	77.031
646 G13	28.9586	10.34	2.993171	41	900	4555556	288.4145	54.014
650 A3	25.7043	11.11	2.855609	102	2500	4080000	290.9513	43.298
650 B2	16.6729	11	1.833217	42	1600	2625000	288.645	54.69
650 C7	67.9527	12	8.15133	226	2500	9040000	244.7348	33.569
650 J4	16.6294	11.95	1.987561	71	1600	4437500	481.8727	81.163
650 J7	65.4245	12.65	8.279088	76	900	8444444	237.5786	40.578
650 J8	24.4133	12.06	2.943022	70	1600	4375000	327.5487	55.604
650 I7	11.3712	12.16	1.382922	148	4900	3020408	479.7381	70.421
650 H7	14.4865	11.78	1.70665	67	1600	4187500	520.4128	88.324
650 H8	8.8812	11.75	1.043788	11	900	1222222	253.0068	81.875
650 E7	71.5258	12.26	8.770521	86	900	9555556	245.7498	40.129
650 E5	4.19885	13.97	0.586556	35	4900	714285.7	311.3265	68.269
650 E4	9.14181	12.97	1.185825	40	2500	1600000	320.0849	65.462
650 C5	22.7764	13.54	3.082786	57	1600	3562500	286.7987	54.313
650 B1	7.04623	12.31	0.867701	45	2500	1800000	462.0232	89.335
650 A8	15.242	12.23	1.864846	63	2500	2520000	302.7782	53.174
650 A12	14.8326	12.3	1.824285	29	1600	1812500	225.1437	50.147
650 A14	21.0324	12.53	2.634967	88	2500	3520000	306.4051	50.403
650 B10	12.802	12.2	1.562408	104	4900	2122449	303.5971	47.53
650 B9	9.57673	12.01	1.149943	48	1600	3000000	562.1281	105.54
650 J5	11.2135	12.21	1.368727	100	3600	2777778	448.5039	70.771
650 D3	13.2564	12.92	1.712721	61	1600	3812500	517.8782	94.2
650 G3	21.035	12.83	2.698092	110	2500	4400000	380.7376	60.85
650 F3	18.5617	13.52	2.510077	36	900	4000000	391.9021	84.113
650 G1	63.1996	13.3	8.402629	27	400	6750000	197.2121	46.13
650 J1	14.3206	12.65	1.812012	36	1600	2250000	288.0617	60.279

2131360

Sample	U ppm	RF	Sandard Deviation	Ns	rho s			±
					Area		Age (Ma)	
NHD1 K3	6.58456	7.604	0.500671	23	1200	1916667	557.764	123.79
NHD1 H1	6.20488	7.689	0.47712	35	2500	1400000	436.479	81.054
NHD1 A3	9.31068	7.123	0.663243	28	1600	1750000	365.6259	73.843
NHD1 B5	4.35103	7.069	0.307585	27	2500	1080000	478.592	98.122
NHD1 B2	18.473	6.64	1.226544	17	900	1888889	201.4745	50.663
NHD1 A5	1.96723	19.75	0.388561	19	3600	527777.8	515.7754	156.14
NHD1_1	27.5	2.5	9.090909	87	1461	5954825	419.4545	58.961
NHD1_2	29.8	5	16.77852	86	1727	4979734	326.0726	65.035
NHD1_3	32.1	3.3	10.28037	57	2039	2795488	171.989	28.837
NHD1_5	23.2	2.2	9.482759	46	1559	2950609	249.6556	43.766
NHD1_6	19.7	2.3	11.67513	66	2835	2328042	232.2902	39.409
NHD1_7	20.7	1.8	8.695652	34	1344	2529762	240.0776	46.163
NHD1_8	15.3	1.3	8.496732	21	1325	1584906	204.0677	47.788
NHD1_9	19.8	2.7	13.63636	41	1518	2700922	267.4009	55.44
NHD1_10	20.7	1.7	8.21256	31	1373	2257830	214.6956	42.4
NHD1_11	10.65	0.94	8.826291	27	2414	1118476	206.8451	43.794
NHD1_12	19.1	1.7	8.900524	17	709.5	2396054	246.3168	63.636
NHD1_13	7.83	0.53	6.768838	17	2895	587219.3	148.3833	37.364
NHD1_14	21.1	1.9	9.004739	31	1412	2195467	204.9635	41.18
NHD1_15	28.4	2.5	8.802817	36	1476	2439024	169.6389	31.974
NHD1_16	10.2	1.1	10.78431	53	4746	1116730	215.4882	37.632
NHD1_17	7.78	0.81	10.41131	16	2332	686106.3	174.1355	47.158
NHD1_18	16.6	1	6.024096	52	1786	2911534	341.8244	51.682
NHD1_19	20.3	2.1	10.34483	67	1085	6175115	581.7801	93.134
NHD1_20	26.9	2.3	8.550186	65	3127	2078670	152.8372	23.025
NHD1_21	9.84	0.88	8.943089	73	2386	3059514	594.0821	87.507
NHD1_22	14.9	1.5	10.06711	22	968.1	2272493	298.2533	70.32
NHD1_23	23.8	2	8.403361	34	1613	2107874	174.8712	33.397
NHD1_24	4.61	0.6	13.01518	15	2423	619067.3	263.3244	76.14
NHD1_25	15.1	1.2	7.94702	36	1956	1840491	239.453	44.213
NHD1_27	2.73	0.27	9.89011	8	1178	679117.1	479.602	176.07
NHD1_30	1.74	0.23	13.21839	13	1592	816582.9	876.8666	269.41
NHD1_32	33.6	2.7	8.035714	65	1466	4433834	258.8487	38.255
NHD1_33	6.97	0.76	10.90387	8	285.8	2799160	757.501	280.26
NHD1_34	26.7	2.1	7.865169	19	653.9	2905643	214.2149	51.952
NHD1_35	11.8	1.5	12.71186	21	841.9	2494358	409.7836	103.49
NHD1_36	37.3	3.3	8.847185	37	999.7	3701110	195.6015	36.517

Chapter 3; apatite fission track data.

1039419

Sample	U ppm	RF	Sandard Deviation	Ns	rho s			±
					Area		Age (Ma)	
419_1.D	7.82	0.48	6.138107	20	1476	1355014	337.8024	78.329
419_2.D	3.92	0.18	4.591837	15	1869	802568.2	397.2823	104.19
419_3.D	14.87	0.9	6.052455	51	3022	1687624	223.2429	34.055
419_4.D	5.6	0.38	6.785714	14	2130	657277	230.7381	63.624
419_5.D	7.04	0.48	6.818182	29	2755	1052632	292.5278	57.867
419_6.D	20.5	1.8	8.780488	139	4315	3221321	307.0786	37.489
419_7.D	3.82	0.22	5.759162	22	3372	652431.8	333.0871	73.56
419_8.D	3.11	0.16	5.144695	11	2423	453982.7	285.741	87.399
419_9.D	3.61	0.31	8.587258	6	1522	394218.1	214.943	89.67
419_10.D	7.98	0.46	5.764411	78	4090	1907090	461.4106	58.625
419_11.D	9.94	0.44	4.426559	29	1673	1733413	339.9146	64.889
419_12.D	6.11	0.28	4.582651	45	3609	1246883	396.032	61.764
419_13.D	6.07	0.36	5.930807	36	3278	1098231	352.3201	62.327
419_14.D	2.62	0.16	6.10687	17	2027	838677.8	610.8162	152.77
419_15.D	2.22	0.17	7.657658	15	3004	499334.2	435.1629	117.2
419_16.D	13.26	0.94	7.088989	97	4151	2336786	343.4084	42.525
419_17.D	4.5	0.42	9.333333	20	2544	786163.5	340.5134	82.508
419_19.D	3.38	0.3	8.87574	17	1956	869120.7	495.1447	127.88
419_20.D	11.24	0.88	7.829181	79	5102	1548412	269.9905	37.007
419_21.D	7.91	0.5	6.321113	11	1427	770847.9	192.1577	59.197
419_22.D	2.36	0.19	8.050847	16	1576	1015228	808.1629	212.26
419_23.D	5.47	0.29	5.301645	21	2675	785046.7	281.0357	63.111
419_24.D	6.4	0.4	6.25	18	2327	773528.1	237.4797	57.909
419_25.D	5.39	0.36	6.679035	34	3021	1125455	404.9322	74.526
419_27.D	4.32	0.33	7.638889	14	2569	544959.1	247.6654	68.842
419_28.D	13.02	0.89	6.835637	53	2928	1810109	272.4203	41.797
419_29.D	7.67	0.56	7.301173	19	2242	847457.6	217.4364	52.349
419_30.D	9.92	0.76	7.66129	41	2055	1995134	390.4768	67.925

1039420

Sample	U ppm	RF	Sandard Deviation	Ns	rho s			±
					Area		Age (Ma)	
420_1	15.3145	3.067	0.469659	61	2760	2210145	282.5657	37.202
420_3	7.0181	4.109	0.288392	43	3029	1419610	392.6546	62.015
420_4	8.33345	3.445	0.287055	55	3863	1423764	333.1927	46.37
420_6	15.8342	3.231	0.511637	56	2435	2299795	284.3376	39.091
420_10	12.2322	3.246	0.397077	48	3021	1588878	254.8744	37.707
420_12	6.05469	3.697	0.22382	32	2086	1534036	488.148	88.16
420_13	14.626	3.424	0.500818	64	2359	2713014	360.9651	46.783
420_14	8.76902	4.181	0.366657	39	1985	1964736	433.5331	71.749
420_15	13.2762	3.599	0.477873	68	3314	2051901	302.1474	38.221
420_16	10.7301	4.588	0.492302	14	892.1	1569331	286.2764	77.63
420_17	3.3594	3.808	0.127914	11	2417	455109.6	265.6017	80.718
420_18	10.7204	3.283	0.352004	43	2215	1941309	352.6193	55.006

2131371

Sample	U ppm	RF	Sandard Deviation	Ns	rho s			±
					Area		Age (Ma)	
KDDL1.D	11.5	0.55	4.782609	99	4436	2231740	377.1668	41.98
KDDL2.D	16.9	1.3	7.692308	105	3292	3189550	367.0905	45.615
KDDL3.D	16.1	1.4	8.695652	58	1874	3094984	373.7125	58.856
KDDL4.D	12.8	0.7	5.46875	88	3456	2546296	386.3442	46.288
KDDL5.D	10.26	0.87	8.479532	62	2633	2354728	443.7264	67.76
KDDL6.D	18.51	0.93	5.024311	137	3803	3602419	378.2159	37.487
KDDL7.D	6.76	0.4	5.91716	37	2577	1435778	411.6745	71.929
KDDL8.D	7.07	0.48	6.78925	58	3455	1678726	458.5403	67.781
KDDL9.D	14.2	1	7.042254	71	3378	2101835	289.6486	39.971
KDDL11.D	19.2	1.2	6.25	61	2741	2225465	227.9156	32.473
KDDL12.D	8.49	0.61	7.184923	60	3511	1708915	390.7843	57.737
KDDL13.D	12.33	0.98	7.948094	71	3239	2192035	346.3535	49.471
KDDL14.D	5.73	0.4	6.980803	43	3294	1305404	440.5746	73.892
KDDL15.D	8.34	0.45	5.395683	52	3677	1414196	330.7569	49.217
KDDL17.D	21.2	1.9	8.962264	65	1734	3748558	344.5289	52.722
KDDL18.D	9.61	0.84	8.740895	73	4658	1567196	318.4085	46.513
KDDL19.D	22.3	1.2	5.381166	101	3328	3034856	266.7902	30.18
KDDL20.D	8.49	0.5	5.889282	23	1690	1360947	313.1108	67.842

KDDL21.D	9.5	0.63	6.631579	73	4480	1629464	334.4724	44.994
KDDL22.D	16	1.1	6.875	171	5779	2958989	359.9132	37.011

1039423

Sample	U ppm	RF	Sandard Deviation	Ns	rho s			±
					Area		Age (Ma)	
423_1.D	12.35	0.7	5.668016	54	2515	2147117	338.9044	49.96
423_2.D	11.5	0.64	5.565217	76	4178	1819052	309.0647	39.404
423_3.D	6.19	0.56	9.04685	35	3104	1127577	354.6572	67.994
423_4.D	7.46	0.95	12.73458	34	2815	1207815	316.1713	67.537
423_5.D	34	1.9	5.588235	94	2490	3775100	218.486	25.63
423_7.D	19.7	1.4	7.106599	81	1973	4105423	404.1668	53.307
423_8.D	38.6	2.5	7.106599	68	2509	2710243	269.6386	37.9
423_9.D	34.8	2.6	6.476684	32	1349	2372128	121.8413	22.939
423_10.D	35.1	1.9	7.471264	31	1209	2564103	145.8108	28.364
423_11.D	34.7	1.9	5.413105	37	1262	2931854	165.051	28.567
423_12.D	8.81	0.4	5.475504	47	2060	2281553	130.2747	20.297
423_13.D	10.4	0.68	4.540295	19	1181	1608806	355.51	83.141
423_14.D	57.6	2.7	6.538462	37	861.1	4296830	778.0324	137.65
423_15.D	11.59	0.89	4.6875	24	1341	1789709	61.89107	12.962
423_16.D	18.7	1.1	7.679034	35	1604	2182045	366.2185	67.991

2131373

Sample	U ppm	RF	Sandard Deviation	Ns	rho s			±
					Area		Age (Ma)	
AMPB_1	8.42211	3.608	0.30388	47	2555	1839530	422.975	63.557
AMPB_2	10.6011	3.751	0.397671	65	3821	1701125	313.4284	40.615
AMPB_3	11.2154	3.553	0.398535	42	2508	1674641	292.134	46.257
AMPB_4	10.2604	5.141	0.527516	71	4445	1597300	304.2898	39.356
AMPB_5	9.25193	3.792	0.350804	37	2430	1522634	321.256	54.201
AMPB_6	12.6411	4.498	0.568612	97	2776	3494236	530.7854	58.945
AMPB_7	12.4234	3.852	0.478508	71	2655	2674200	417.0457	52.036
AMPB_8	42.8215	3.773	1.61551	190	3074	6180872	282.6104	23.109
AMPB_9	9.58176	3.231	0.309572	41	2673	1533857	312.6932	49.869
AMPB_10	12.4223	3.992	0.495874	84	3212	2615193	408.1626	47.421

AMPB_11	18.0944	3.546	0.641619	97	2625	3695238	396.3091	42.622
AMPB_12	8.83967	4.01	0.35447	65	2882	2255378	491.4489	64.063
AMPB_13	33.2104	3.873	1.286187	120	2420	4958678	292.1248	28.968
AMPB_14	11.904	3.785	0.450585	70	3206	2183406	357.0385	44.763
AMPB_15	8.32654	4.121	0.343142	25	1617	1546073	361.32	73.782
AMPB_16	14.6545	3.501	0.513019	60	3130	1916933	256.635	34.328
AMPB_17	14.749	3.46	0.510325	115	4315	2665122	351.8867	35
AMPB_18	15.0646	4.044	0.609241	67	3633	1844206	240.4812	30.947
AMPB_19	13.5192	3.842	0.519353	81	3555	2278481	328.7966	38.655
AMPB_20	11.7022	3.781	0.442412	88	6186	1422567	238.8297	27.013
AMPB_21	10.0594	4.114	0.413832	62	3943	1572407	305.5038	40.784
AMPB_23	15.3425	3.868	0.593455	78	3389	2301564	293.4669	35.114
AMPB_24	12.0914	3.892	0.470585	83	4521	1835877	296.9486	34.583
AMPB_25	8.7235	3.952	0.344763	36	2535	1420118	317.8608	54.446
AMPB_26	11.3363	3.801	0.430848	52	2328	2233677	382.7784	55.039
AMPB_27	7.66629	6.063	0.464827	108	6263	1724413	435.1801	49.495
AMPB_28	10.7528	3.804	0.409007	46	3011	1527732	278.2735	42.373
AMPB_29	14.2697	5.023	0.716706	113	5055	2235410	306.1556	32.649
AMPB_30	13.6758	4.009	0.548215	101	4132	2444337	348.1634	37.349
AMPB_31	8.28756	4.7	0.389489	57	2973	1917255	447.155	62.845
AMPB_32	10.6141	4.521	0.479871	54	2686	2010424	368.3773	52.824
AMPB_33	13.8125	3.855	0.532477	58	2069	2803287	393.9234	53.908
AMPB_34	11.9028	4.365	0.519523	51	2405	2120582	347.0693	50.906
AMPB_35	10.0315	4.231	0.424423	34	1618	2101360	406.1943	71.75
AMPB_36	11.1547	4.471	0.498689	52	2524	2060222	359.4559	52.374
AMPB_37	37.9202	4.352	1.650221	78	1772	4401806	228.2463	27.687
AMPB_38	49.5742	3.852	1.909574	168	2670	6292135	249.1593	21.486
AMPB_39	10.4413	4.233	0.44194	42	2381	1763965	329.5647	52.731
AMPB_40	18.7041	4.423	0.827342	86	3054	2815979	294.5031	34.325
AMPB_41	10.3966	4.213	0.437967	42	2248	1868327	350.0049	55.983
AMPB_42	17.0645	4.397	0.750406	98	2867	3418207	388.947	42.851
AMPB_43	26.3818	4.067	1.073045	135	2894	4664824	344.5309	32.797

2131376

Sample	U ppm	RF	Sandard Deviation	Ns	rho s		±
					Area	Age (Ma)	
KAR_1.D	38.6	2.4	6.217617	175	4002	4372814	222.8435	21.812
KAR_2.D	37.7	2.9	7.692308	79	1546	5109961	265.735	36.217

KAR_3.D	20.3	1.9	9.359606	36	1332	2702703	261.1147	49.912
KAR_4.D	59.6	5.6	9.395973	170	2867	5929543	196.1131	23.786
KAR_5.D	5.96	0.5	8.389262	17	1367	1243599	404.6564	103.85
KAR_6.D	12.81	0.93	7.259953	53	2852	1858345	284.0075	44.125
KAR_7.D	13.06	0.67	5.130168	43	2898	1483782	223.4765	35.957
KAR_8.D	41.3	1.8	4.358354	158	2862	5520615	262.1391	23.779

2131380

Sample	U ppm	RF	Sandard Deviation	Ns	rho s			±
					Area		Age (Ma)	
OBD8_1	26.742	12.61	3.371887	63	1769	3561334	261.1837	46.555
OBD8_2	14.5713	9.085	1.323757	14	429.9	3256571	432.4825	122.08
OBD8_3	28.319	9.289	2.630651	30	1108	2707581	188.578	38.63
OBD8_4	18.0678	9.145	1.652368	35	739.2	4734848	504.2645	96.912
OBD8_5	18.4723	9.307	1.719273	79	2867	2755494	291.8529	42.615
OBD8_6	15.7889	9.587	1.513619	73	2550	2862745	353.0524	53.414
OBD8_7	3.9644	9.544	0.378345	29	819	3540904	1577.824	329.42
OBD8_8	9.88537	9.516	0.940667	43	1798	2391546	466.8938	83.925
OBD8_10	7.82133	9.764	0.763692	37	2543	1454974	361.9752	69.213
OBD8_11	11.1312	9.964	1.109157	36	1711	2104033	367.6386	71.389
OBD8_12	19.4178	10.09	1.959096	89	1265	7035573	687.2268	100.57
OBD8_13	15.5688	10.18	1.584149	40	2108	1897533	239.4416	45.021
OBD8_14	11.926	10.12	1.206328	75	3500	2142857	349.9553	53.721
OBD8_15	15.7491	10.23	1.611667	55	1643	3347535	411.9773	69.738
OBD8_17	11.2879	10.46	1.181076	53	1087	4875805	811.2848	140.09
OBD8_19	13.3007	11.54	1.534711	45	1337	3365744	487.5677	91.912

2131386

Sample	U ppm	RF	Sandard Deviation	Ns	rho s			±
					Area		Age (Ma)	
OBD1_1.D	12.6	1.2	9.52381	65	2351	2764781	424.8683	66.441
OBD1_2.D	36.3	1.9	5.23416	81	1786	4535274	245.3359	30.133
OBD1_4.D	10.95	0.63	5.753425	52	1539	3378817	589.7759	88.547
OBD1_5.D	19.8	1.2	6.060606	85	1949	4361211	426.4349	52.984
OBD1_6.D	10.09	0.5	4.955401	63	2924	2154583	413.8208	56.024

OBD1_8.D	15.16	0.99	6.530343	46	1461	3148528	402.831	64.959
OBD1_9.D	17.9	0.93	5.195531	88	1979	4446690	478.9658	56.799
OBD1_10.D	19.1	1.1	5.759162	68	2666	2550638	261.8896	35.158
OBD1_11.D	25.1	1.9	7.569721	56	1263	4433888	344.2066	52.864
OBD1_14.D	11.44	0.75	6.555944	34	1459	2330363	395.3367	72.585
OBD1_15.D	19.9	1.2	6.030151	97	2606	3722180	363.9008	42.974
OBD1_16.D	17.7	1.1	6.214689	39	1465	2662116	294.2117	50.535
OBD1_18.D	10.29	0.76	7.385811	75	3076	2438231	457.623	62.727
OBD1_19.D	5.91	0.39	6.598985	43	3338	1288197	422.1355	70.144
OBD1_20.D	22.4	1.5	6.696429	82	2383	3441041	300.3581	38.791
OBD1_21.D	8.31	0.42	5.054152	57	2023	2817598	645.2329	91.474
OBD1_23.D	12.43	0.61	4.907482	52	2340	2222222	348.2469	51.228
OBD1_25.D	17.6	1.2	6.818182	29	951.2	3048780	337.7089	66.805
OBD1_26.D	21.2	1.3	6.132075	63	1667	3779244	347.2747	48.66
OBD1_27.D	16.8	1.3	7.738095	37	1666	2220888	259.3033	47.115
OBD1_28.D	17.2	1.2	6.976744	44	1411	3118356	353.0252	58.643
OBD1_31.D	28.5	1.1	3.859649	46	933.5	4927691	337.0922	51.376
OBD1_32.D	16.27	0.84	5.162876	36	1088	3308824	394.7089	68.869
OBD1_33.D	11.02	0.7	6.352087	20	990	2020202	356.8548	82.952
OBD1_36.D	16.5	1.2	7.272727	35	1172	2986348	352.4398	64.853
OBD1_37.D	12.56	0.71	5.652866	38	1156	3287197	503.6342	86.519
OBD1_38.D	15	1.2	8	32	1069	2993452	387.5394	75.197
OBD1_39.D	25.7	1.5	5.836576	47	1147	4097646	311.4738	48.935

2131379

Sample	U ppm	RF	Sandard Deviation	Ns	rho s			±
					Area		Age (Ma)	
OBD7_1.D	42.6	1.9	4.460094	245	3806	6437204	295.5617	23.029
OBD7_2.D	38	1.7	4.473684	152	2811	5407328	278.6967	25.816
OBD7_3.D	14.5	0.74	5.103448	132	4577	2883985	386.2804	38.975
OBD7_4.D	18.5	1	5.405405	129	4237	3044607	321.2533	33.19
OBD7_5.D	30.9	1.4	4.530744	219	4427	4946917	312.7188	25.442
OBD7_6.D	14.37	0.79	5.497564	87	3439	2529805	343.0657	41.334
OBD7_7.D	13.26	0.4	3.016591	104	9183	1132527	168.719	17.309
OBD7_8.D	21.9	1	4.56621	215	5882	3655219	325.6917	26.731
OBD7_9.D	41.5	2.2	5.301205	241	3894	6189009	291.7841	24.342
OBD7_10.D	39.1	2.3	5.882353	228	3493	6527340	325.7576	28.855
OBD7_11.D	22.5	1.1	4.888889	259	6000	4316667	372.9888	29.49

OBD7_12.D	10.7	0.43	4.018692	111	4070	2727273	490.9711	50.606
OBD7_13.D	3.78	0.2	5.291005	53	4877	1086734	551.1722	81.132
OBD7_14.D	12.72	0.61	4.795597	104	3010	3455150	521.9555	56.975
OBD7_15.D	12.06	0.68	5.638474	221	6835	3233358	515.4452	45.242
OBD7_16.D	15	0.72	4.8	136	4921	2763666	358.6024	35.24
OBD7_17.D	27	1.7	6.296296	223	3829	5823975	417.8859	38.411
OBD7_18.D	33.9	2.4	7.079646	234	3411	6860158	392.8165	37.853
OBD7_19.D	33.7	1.7	5.04451	170	3629	4684486	272.3824	25.004
OBD7_20.D	18.56	0.86	4.633621	175	4585	3816794	398.9935	35.376
OBD7_21.D	19.67	0.9	4.575496	161	4070	3955774	390.4478	35.582
OBD7_22.D	25.9	1.9	7.335907	199	5501	3617524	273.6624	27.917
OBD7_23.D	23.7	1.1	4.64135	203	4754	4270088	350.8889	29.525
OBD7_24.D	34	2	5.882353	266	6455	4120837	238.1304	20.234
OBD7_25.D	43.5	2.7	6.206897	331	5029	6581825	295.9407	24.536
OBD7_26.D	22.29	0.99	4.441454	166	4984	3330658	292.341	26.142
OBD7_27.D	30.9	1.7	5.501618	191	3907	4888661	309.1231	28.099
OBD7_28.D	22.6	1.2	5.309735	155	3207	4833177	414.4233	39.903
OBD7_29.D	33.9	1.9	5.60472	225	4543	4952674	285.9736	24.907
OBD7_30.D	29.1	1.6	5.498282	179	3886	4606279	309.2801	28.698
OBD7_31.D	46.6	1.9	4.077253	265	4078	6498283	273.2316	20.145
OBD7_32.D	41.3	2.3	5.569007	234	3925	5961783	282.6346	24.272
OBD7_33.D	35.1	2.1	5.982906	152	2024	7509881	414.6097	41.788
OBD7_34.D	46.5	2.4	5.16129	494	7622	6481239	273.1037	18.699
OBD7_35.D	22.9	1.3	5.676856	132	3697	3570463	304.7457	31.668
OBD7_36.D	22.7	1.2	5.286344	154	3840	4010417	344.2473	33.177
OBD7_37.D	24.58	0.98	3.986981	80	2795	2862254	228.9526	27.177
OBD7_38.D	10.58	0.6	5.671078	71	2967	2392990	437.5107	57.547
OBD7_39.D	58	3.1	5.344828	269	3358	8010721	270.6752	21.947
OBD7_40.D	26.8	1.9	7.089552	186	4879	3812257	278.6014	28.415

2131385

Sample	U ppm	RF	Sandard Deviation	Ns	rho s		±
					Area	Age (Ma)	
BD12_1.D	8.82	0.49	5.555556	111	2096	5295802	1101.968	121.19
BD12_2.D	10.83	0.6	5.540166	87	1930	4507772	783.4821	94.55
BD12_3.D	12.68	0.58	4.574132	74	1700	4352941	652.8897	81.561
BD12_4.D	15.7	1	6.369427	69	1501	4596935	560.9085	76.394
BD12_5.D	32.5	1.6	4.923077	96	1570	6114650	365.9792	41.471

BD12_6.D	13.47	0.84	6.23608	78	1812	4304636	609.844	78.831
BD12_7.D	24.5	2	8.163265	27	427.9	6309885	495.9047	103.67
BD12_8.D	10.44	0.73	6.992337	49	1353	3621582	659.403	104.88
BD12_9.D	18.5	1.3	7.027027	65	1022	6360078	653.787	93.202
BD12_10.D	11.16	0.74	6.630824	59	1192	4949664	831.6683	121.51
BD12_11.D	9.45	0.5	5.291005	53	1307	4055088	806.2704	118.68
OBD12_2nd_1	12.01	0.7	5.828476	45	1594	2823087	454.098	72.683
OBD12_2nd_2	13.03	0.82	6.29317	46	1122	4099822	600.866	96.325
OBD12_2nd_4	6.06	0.41	6.765677	34	2706	1256467	402.1752	74.146

2131367

Sample	U ppm	RF	Sandard Deviation	Ns	rho s			±
					Area		Age (Ma)	
DD_1	3.55806	4.808	0.17107	22	1837	1197605	640.7554	140.04
DD_2	4.48441	4.377	0.196288	30	3348	896057.3	388.0153	72.849
DD_3	9.44551	4.637	0.437952	49	1499	3268846	657.9201	98.815
DD_4	6.55649	4.569	0.299592	25	1697	1473188	434.7258	89.186
DD_5	8.306	4.35	0.361275	15	860.3	1743578	407.0249	106.57
DD_6	5.64221	5.1	0.287748	15	1050	1428571	487.8329	128.39
DD_7	3.6143	4.335	0.156698	16	1805	886426.6	473.0855	120.04
DD_8	2.955	4.841	0.143055	15	1226	1223491	779.6004	204.8
DD_11	2.8052	4.864	0.136433	16	1230	1300813	867.1024	220.84
DD_12	3.33805	4.772	0.159275	14	1350	1037037	593.6175	161.16
DD_13	16.4773	4.48	0.738155	43	1013	4244817	496.0336	78.841
DD_14	8.0197	4.761	0.381791	60	2380	2521008	600.3318	82.604
DD_16	9.55767	4.418	0.422284	27	2021	1335972	273.8684	54.077
DD_17	3.90007	4.897	0.191001	53	3865	1371281	667.9065	97.401
DD_18	10.7897	4.51	0.486627	52	2577	2017850	363.8496	53.058
DD_19	5.83966	4.937	0.288295	26	1139	2282704	738.4234	149.33
DD_20	9.04109	4.861	0.439458	12	994.9	1206151	261.6331	76.59
DD_21	6.23272	4.736	0.295183	17	1046	1625239	501.8562	124.02
DD_22	5.86633	4.686	0.274891	56	1802	3107658	981.6047	139
DD_23	3.83616	5.091	0.195306	23	1000	2300000	1100.496	236.21
DD_24	8.53832	4.908	0.419073	29	1133	2559576	573.6963	110.19
DD_26	8.55903	4.986	0.426766	27	2060	1310680	299.434	59.529
DD_27	5.92792	5.608	0.33244	41	2044	2005871	643.9934	106.86
DD_28	4.63577	4.995	0.231563	14	1430	979021	409.412	111.31
DD_29	5.73597	5.696	0.326709	37	3211	1152289	390.0356	67.861

DD_30	6.84432	5.675	0.388399	42	2620	1603053	452.5221	74.398
DD_31	8.95383	5.023	0.449718	33	1727	1910828	413.5814	74.932
DD_32	2.55679	5.404	0.138158	17	2402	707743.5	531.5061	132.07
DD_33	9.42562	5.134	0.483893	34	1892	1797040	370.7274	66.367
DD_34	8.37823	5.268	0.441367	26	1739	1495112	347.6268	70.592
DD_35	7.4816	5.181	0.3876	25	1963	1273561	332.0077	68.593
DD_36	2.73016	5.455	0.148932	14	1318	1062215	735.1579	200.53
DD_37	5.36667	6.132	0.32907	28	1527	1833661	649.9662	129.14
DD_38	9.11354	5.168	0.471006	32	2255	1419069	304.3534	56.055
DD_39	9.60636	5.658	0.54352	40	2614	1530222	311.1897	52.259
DD_40	10.4515	5.228	0.546365	30	1610	1863354	347.3105	65.958
DD_41	7.70501	5.821	0.448512	39	1651	2362205	586.1445	99.868

650666

Sample	U ppm	RF	Sandard Deviation	Ns	rho s			±
					Area		Age (Ma)	
666_2	7.54758	5.918	0.446655	51	2402	2123231	539.8011	82.06
666_3	2.01768	5.965	0.120359	19	1284	1479751	1322.461	313.48
666_4	6.96641	6.045	0.42114	11	553	1989150	547.5672	168.38
666_5	4.60667	5.728	0.263859	11	701.4	1568292	647.728	198.79
666_6	10.8438	6.682	0.724579	45	3782	1189847	215.958	35.279
666_8	7.62214	5.778	0.440393	18	1325	1358491	347.2052	84.26
666_9	4.74843	5.725	0.271827	13	583.4	2228317	876.8214	248.31
666_10	6.38455	6.164	0.393571	47	1737	2705815	796.8969	126.19
666_11	1.82237	7.194	0.1311	10	1524	656168	683.1522	221.55
666_12	1.33545	7.663	0.102337	10	1658	603136.3	845.9297	275.25
666_14	3.3976	6.374	0.216555	9	830.7	1083424	608.5819	206.54
666_15	8.36736	6.899	0.577297	27	1513	1784534	413.3268	84.502
666_19	4.68771	6.905	0.323675	18	3470	518732	217.7613	53.484
666_20	3.85127	6.829	0.262997	45	3994	1126690	560.453	91.896

501

Sample	U ppm	RF	Sandard Deviation	Ns	rho s			±
					Area		Age (Ma)	
501_1	9.02	0.81	8.980044	11	387.1	2841643	601.583	189.26
501_2	3.3	0.34	10.30303	9	804.4	1118846	645.2025	225.11
501_3	1.19	0.12	10.08403	5	2272	220070.4	359.9062	165
501_4	6.14	0.66	10.74919	13	1016	1279528	404.1574	120.22
501_6	1.83	0.29	15.84699	14	1511	926538.7	941.19	292.44
501_8	2.22	0.29	13.06306	4	920.5	434546.4	380.3323	196.55

2131395

Sample	U ppm	RF	Sandard Deviation	Ns	rho s			±
					Area		Age (Ma)	
CH1_1	12.1253	8.494	1.029875	190	3478	5462910	844.0066	94.277
CH1_2	10.3389	7.997	0.826849	66	3099	2129719	399.6424	58.664
CH1_3	15.1786	8.405	1.275795	81	1854	4368932	551.7954	76.877
CH1_4	21.881	8.807	1.92703	29	1026	2826511	253.4963	52.099
CH1_5	5.99564	8.292	0.497177	47	2149	2187064	691.631	116.05
CH1_6	22.7545	8.507	1.935715	68	1143	5949256	503.1433	74.531
CH1_7	48.3975	8.127	3.933441	35	685.5	5105762	207.766	38.968
CH1_8	15.6738	8.481	1.329257	40	1412	2832861	351.9613	63.15
CH1_10	13.1737	7.976	1.050736	72	2765	2603978	383.9597	54.639
CH1_11	22.0823	8.382	1.850967	56	1170	4786325	419.8488	66.229
CH1_12	3.71821	8.413	0.312806	28	1952	1434426	729.2911	150.86
CH1_13	15.0128	8.576	1.287519	37	1016	3641732	468.0988	86.797
CH1_14	5.57661	8.544	0.476486	35	1438	2433936	819.229	155.16
CH1_15	30.2045	8.608	2.599891	36	1272	2830189	184.8657	34.677
CH1_16	12.6336	8.614	1.088266	223	4119	5413935	805.256	87.86
CH1_17	14.1819	8.683	1.231347	52	1407	3695807	501.5616	82.062

307

Sample	U ppm	RF	Sandard Deviation	Ns	rho s			±
					Area		Age (Ma)	
307_1	6.95	0.96	13.81295	13	1455	893470.8	252.3036	78.175
307_2	6.13	0.68	11.09299	17	914.5	1858939	580.0606	154.7
307_4	7.22	0.7	9.695291	31	3705	836707.2	227.8727	46.509
307_6	16.7	1.4	8.383234	33	1584	2083333	244.9733	47.332
307_7	2.47	0.27	10.93117	6	1571	381922.3	302.2807	127.75
307_9	12.07	0.97	8.036454	6	441.5	1359003	221.5057	92.165
307_10	1.06	0.24	22.64151	3	1353	221729.5	405.6361	251.56
307_11	1.94	0.37	19.07216	22	3108	707850.7	691.8033	197.9
307_12	2.22	0.3	13.51351	13	2311	562527	488.1982	150.62
307_14	2.63	0.34	12.92776	34	2032	1673228	1162.044	249.57
307_15	3.93	0.5	12.72265	13	2426	535861.5	267.2882	81.56
307_16	8.44	0.64	7.582938	20	2458	813669.7	190.1253	44.891
307_19	1.18	0.21	17.79661	21	6188	339366.5	551.3615	155.26
307_20	19.2	1.3	6.770833	67	2655	2523540	257.8394	36.014
307_22	11.3	1.1	9.734513	21	582.2	3607008	609.1742	145.56
307_23	7.6	1	13.15789	25	3394	736594	191.124	45.755
307_24	19.9	3.5	17.58794	23	1691	1360142	135.3685	36.927
307_25	9.6	1.1	11.45833	9	946.9	950470	195.1778	68.796
307_26	8.21	0.84	10.23143	52	2551	2038416	478.717	82.499
307_27	5.39	0.41	7.606679	36	1881	1913876	674.1739	123.51
307_29	24.5	1.7	6.938776	14	887.2	1577998	127.6404	35.244
307_31	1.34	0.14	10.44776	8	3505	228245.4	332.2103	122.48

2131381

Sample	U ppm	RF	Sandard Deviation	Ns	rho s			±
					Area		Age (Ma)	
DDH2.D	11.2	1.1	9.821429	31	918.1	3376539	576.8108	118.08
DDH5.D	7.6	1.2	15.78947	19	1104	1721014	438.0134	121.99
DDH9.D	6.01	0.36	5.990017	41	2118	1935788	614.4354	102.77
DDH13.D	6.14	0.73	11.88925	16	1363	1173881	371.7306	102.91

1472758

Sample	U ppm	RF	Sandard Deviation	Ns	rho s			±
					Area		Age (Ma)	
Tal 9_1	2.29	0.18	7.860262	18	2640	681818.2	569.9633	141.61
Tal 9_2	2.55	0.25	9.803922	20	2120	943396.2	700.9438	171.14
Tal 9_3	1.7	0.21	12.35294	18	3100	580645.2	649.7492	172.91
Tal 9_4	6.77	0.7	10.33973	22	2900	758620.7	220.4666	52.24
Tal 9_5	1.86	0.2	10.75269	16	3160	506329.1	523.0421	142.34
Tal 9_6	6.02	0.55	9.136213	21	975	2153846	679.0446	160.64
Tal 9_7	1.029	0.088	8.551992	10	3420	292397.7	545.0347	178.55
Tal 9_8	9.1	0.98	10.76923	23	2270	1013216	219.0858	51.416
Tal 9_9	18.2	1.6	8.791209	20	617	3241491	346.9668	83.365
Tal 9_10	6.56	0.53	8.079268	24	1610	1490683	439.4887	96.482
Tal 9_11	8.23	0.52	6.318348	37	3790	976253.3	233.1523	41.063
Tal 9_12	3.01	0.26	8.637874	20	2800	714285.7	458.2804	109.85
Tal 9_13	4.72	0.41	8.686441	48	3720	1290323	525.1705	88.47
Tal 9_14	6.31	0.58	9.191759	24	1930	1243523	382.8417	85.705
Tal 9_15	3.08	0.26	8.441558	40	3260	1226994	751.7565	134.74
Tal 9_16	3.55	0.46	12.95775	39	3430	1137026	611.1494	125.89
Tal 9_17	4.96	0.37	7.459677	18	2750	654545.5	258.8593	63.997
Tal 9_18	5.6	0.46	8.214286	29	2420	1198347	414.6732	84.2
Tal 9_20	7.91	0.58	7.332491	125	4290	2913753	698.0777	80.738
Tal 9_21	3.68	0.21	5.706522	45	4300	1046512	545.4412	87.064
Tal 9_22	3.86	0.41	10.62176	32	2420	1322314	651.581	134.38
Tal 9_23	7.23	0.66	9.128631	21	1660	1265060	341.0274	80.667
Tal 9_24	9.15	0.69	7.540984	26	1550	1677419	356.8607	74.982
Tal 9_25	2.9	0.14	4.827586	27	2930	921501.7	606.5422	120.35
Tal 9_26	6.13	0.59	9.624796	7	3750	186666.7	60.66186	23.66
Tal 9_27	4.43	0.5	11.28668	40	3140	1273885	551.2881	107.1
Tal 9_29	8.49	0.69	8.127208	17	1070	1588785	364.0746	93.127
Tal 9_31	2.3	0.19	8.26087	20	5540	361010.8	306.742	73.121
Tal 9_32	1.49	0.13	8.724832	21	3460	606936.4	767.7055	180.42
Tal 9_33	5.44	0.51	9.375	14	1100	1272727	452.0381	128.03
Tal 9_35	10.58	0.85	8.034026	16	1670	958083.8	178.7464	46.937
Tal 9_36	5.43	0.62	11.41805	16	2180	733945	265.0091	72.835
Tal 9_37	3.74	0.39	10.42781	24	2810	854092.5	441.5985	101.22
Tal 9_39	8.36	0.83	9.92823	64	2970	2154882	496.3026	79.225
Tal 9_40	3.6	0.2	5.555556	23	3650	630137	341.1494	73.616
Tal 9_41	25.2	2.7	10.71429	32	1080	2962963	231.1378	47.779

1472763

Sample	U ppm	RF	Sandard Deviation	Ns	rho s			±
					Area		Age (Ma)	
Tal65_1	21.4	1.7	7.943925	96	1129	8503100	749.9153	96.989
Tal65_2	20.2	1.7	8.415842	83	946.5	8769149	815.1067	112.74
Tal65_3	7.43	0.85	11.44011	35	4087	856373.9	226.6583	46.262
Tal65_4	11.8	1.2	10.16949	58	1190	4873950	777.8371	129.18
Tal65_5	29	2.4	8.275862	40	357.3	11195074	729.7434	130.23
Tal65_7	23.1	2.3	9.95671	27	427.3	6318746	525.4755	113.86
Tal65_9	17.1	1.4	8.187135	46	808	5693069	634.1172	106.94
Tal65_10	27.5	2	7.272727	42	545.7	7696537	537.1524	91.629
Tal65_11	23.4	1.9	8.119658	48	655.9	7318189	597.3976	98.934
Tal65_12	14.2	1.2	8.450704	42	875.2	4798903	643.2222	113.16
Tal65_13	14.8	1.3	8.783784	21	286.1	7340091	923.2581	217.18
Tal65_14	24.5	2.2	8.979592	80	1094	7312614	571.3132	81.926
Tal65_15	20.9	2.1	10.04785	34	556.3	6111810	560.2345	111.36
Tal65_16	23.2	2.6	11.2069	38	555.6	6839453	564.5871	111.32
Tal65_17	21.1	2.3	10.90047	27	471	5732484	522.0487	115.46
Tal65_18	11.8	1.6	13.55932	36	584	6164384	968.9768	208.19
Tal65_19	21.8	2.6	11.92661	50	636.9	7850526	683.2478	126.4
Tal65_20	22.1	2.8	12.66968	71	765.2	9278620	789.8898	137.12
Tal65_21	19.5	2.2	11.28205	7	119.5	5857741	574.8345	226.74
Tal65_22	20.4	1.7	8.333333	42	638.3	6579978	615.2603	107.9
Tal65_23	27.5	2	7.272727	55	687.7	7997673	557.2859	85.378
Tal65_24	22.1	1.7	7.692308	57	713.2	7992148	685.9832	105.07
Tal65_25	23.3	2	8.583691	33	476.3	6928406	569.2658	110.49
Tal65_26	23.4	2.4	10.25641	57	898.3	6345319	521.0994	87.295
Tal65_27	29.8	3	10.06711	63	779.6	8081067	521.1165	84.04
Tal65_28	23	1.4	6.086957	38	513.5	7400195	613.804	106.35

1472783

Sample	U ppm	RF	Sandard Deviation	Ns	rho s			±
					Area		Age (Ma)	
Bac28_1	8.9	0.7	7.865169	26	910.4	2855888	612.2364	129.37
Bac28_2	4.86	0.41	8.436214	9	1056	852272.7	341.7696	117.52
Bac28_3	5.06	0.47	9.288538	5	327.9	1524855	576.5878	263.36
Bac28_4	3.81	0.29	7.611549	9	763	1179554	591.6506	202.29

Chapter 4; Apatite U-Pb data.

WR 16

Sample	^{207}Pb-	±	^{238}U-^{206}Pb	±	Error Correlation	^{206}Pb-^{238}U age	±	^{207}Pb correcte	±	Discordance %	±
16_1.d	0.672	0.033	5.089059	0.204598	0.13992	1155	43	N/A	N/A	167.3	6.5
16_3.d	0.374	0.024	3.412969	0.256264	-0.37256	1640	110	N/A	N/A	84.9	5.7
16_4.d	0.267	0.018	4.541326	0.179426	-0.27314	1281	46	N/A	N/A	71.4	5
16_5.d	0.223	0.011	4.757374	0.199167	-0.15476	1228	47	N/A	N/A	60.1	3.9
16_6.d	0.2326	0.008	2.475248	0.11641	0.29367	2181	86	N/A	N/A	29.8	3.9
16_7.d	0.295	0.012	2.375297	0.107199	0.11625	2258	87	N/A	N/A	42.8	4.6
16_8.d	0.358	0.062	3.636364	0.528926	-0.79597	1530	200	N/A	N/A	70	10

WR 17

Sample	^{207}Pb-	±	^{238}U-^{206}Pb	±	Error Correlation	^{206}Pb-^{238}U age	±	^{207}Pb correcte	±	Discordance %	±
17_9.d	0.215	0.011	4.539265	0.135993	-0.46995	1282	35	N/A	N/A	55.8	3.5
17_13.d	0.697	0.031	1.538462	0.094675	0.47662	3200	150	N/A	N/A	67.4	9.8
17_14.d	0.229	0.024	6.21118	0.424366	-0.23142	956	60	N/A	N/A	67.5	7.3
17_17.d	0.1536	0.005	3.265839	0.087459	0.33173	1720	41	N/A	N/A	20.6	2.6
17_19.d	0.267	0.02	4.424779	0.254523	0.13638	1309	67	N/A	N/A	70.4	6.7
17_20.d	0.309	0.013	3.777862	0.134159	0.1777	1513	48	N/A	N/A	77.1	4.8
17_22.d	0.367	0.017	3.802281	0.144573	-0.18854	1505	52	N/A	N/A	90.7	4.1
17_23.d	0.2628	0.009	3.91696	0.150357	-0.20938	1464	51	N/A	N/A	64.8	2.9
17_24.d	0.288	0.015	4.1841	0.280107	0.50938	1377	81	N/A	N/A	74.1	6.6
17_25.d	0.33	0.013	3.533569	0.137347	0.12432	1602	58	N/A	N/A	77.6	4.3
17_26.d	0.249	0.011	4.631774	0.1609	-0.071702	1258	39	N/A	N/A	66.3	2.8
17_27.d	0.316	0.019	3.003003	0.13527	-0.048519	1847	71	N/A	N/A	64	5.7
17_28.d	0.292	0.015	3.90625	0.183106	0.00952	1468	62	N/A	N/A	72.5	4.5
17_29.d	0.438	0.032	4	0.24	0.23124	1435	75	N/A	N/A	111.1	9.6
17_30.d	0.242	0.016	5.350455	0.27196	0.10856	1102	51	N/A	N/A	69.7	5.7
17_31.d	0.485	0.02	3.496503	0.122255	0.38389	1620	53	N/A	N/A	113.3	5.6
17_32.d	0.1641	0.006	4.805382	0.161642	0.23362	1217	37	N/A	N/A	39.8	2.8
17_33.d	0.25	0.01	2.638522	0.104427	-0.047329	2067	69	N/A	N/A	38.5	3.7
17_34.d	0.334	0.023	2.283105	0.140739	-0.41575	2330	120	N/A	N/A	47.6	4.7
17_35.d	0.363	0.014	4.098361	0.218355	0.12506	1402	67	N/A	N/A	94.9	4.2
17_36.d	0.166	0.012	6.65336	0.301017	-0.16721	901	38	N/A	N/A	49.6	5.2
17_38.d	0.1521	0.006	3.889537	0.127079	0.28681	1473	43	N/A	N/A	27.4	2.8
17_40.d	0.237	0.017	6.535948	0.328933	-0.1961	916	43	N/A	N/A	73.1	5.3
17_41.d	0.571	0.023	2.232143	0.094667	0.033735	2381	84	N/A	N/A	90.5	5.9
17_44.d	0.464	0.036	2.309469	0.138675	0.23295	2330	120	N/A	N/A	73.5	9.2
17_45.d	0.515	0.02	2.631579	0.124654	0.47753	2086	88	N/A	N/A	96.2	6.7
17_47.d	0.2515	0.009	3.773585	0.142399	0.16303	1521	56	N/A	N/A	59.4	3.6
17_48.d	0.127	0.005	4.612546	0.127654	0.19369	1272	35	N/A	N/A	22.7	2.5
17_50.d	0.327	0.016	3.571429	0.140306	0.043157	1588	58	N/A	N/A	77.5	4.7
17_51.d	0.2634	0.01	4.098361	0.201559	0.074944	1405	61	N/A	N/A	67	3.7
17_52.d	0.254	0.011	3.484321	0.103194	-0.19617	1625	43	N/A	N/A	55.8	3.5
17_53.d	0.1618	0.005	3.827019	0.128885	0.19213	1494	45	N/A	N/A	30	2.8
17_54.d	0.495	0.022	2.754821	0.098658	0.20794	1991	62	N/A	N/A	96	5.3
17_55.d	0.403	0.013	3.215434	0.124068	0.07739	1742	59	N/A	N/A	88.6	4.1
17_56.d	0.352	0.016	2.247191	0.121197	0.20405	2360	110	N/A	N/A	50	5.5
17_58.d	0.1524	0.006	5.847953	0.24281	0.3442	1016	39	N/A	N/A	40.7	3.1
17_60.d	0.1555	0.008	2.985075	0.124749	0.23264	1861	66	N/A	N/A	17.3	3.4

17_61.d	0.153	0.006	3.685957	0.118201	0.16357	1545	44	N/A	N/A	25.5	2.8
17_62.d	0.1358	0.004	6.6357	0.193743	0.31693	904	25	N/A	N/A	36.8	2.2
17i_7.d	0.251	0.01	4.030633	0.142965	-0.29489	1427	46	N/A	N/A	63.3	3.3
17i_8.d	0.747	0.03	1.190476	0.075113	0.24627	3930	190	N/A	N/A	42.7	7.6
17i_10.d	0.218	0.01	5.988024	0.229481	-0.089299	1001	33	N/A	N/A	65.8	3.6
17i_11.d	0.628	0.04	1.494768	0.109482	0.12717	3270	180	N/A	N/A	55.4	9.2
17i_13.d	0.381	0.019	2.808989	0.142028	0.11839	1975	79	N/A	N/A	75.3	6.8
17i_14.d	0.735	0.03	1.057082	0.065928	0.27557	4250	190	N/A	N/A	31.4	7.3
17i_15.d	0.293	0.01	4.826255	0.191	0.14618	1212	44	N/A	N/A	82.3	3.5
17i_16.d	0.439	0.021	4.444444	0.25679	0.21201	1301	70	N/A	N/A	115.2	5.9
17i_17.d	0.1743	0.008	2.857143	0.081633	0.18501	1932	48	N/A	N/A	20.4	2.9
17i_18.d	0.48	0.022	2.469136	0.140223	0.30279	2180	100	N/A	N/A	83.5	7.7
17i_19.d	0.444	0.018	3.021148	0.13691	0.02915	1852	67	N/A	N/A	93.6	5
17i_20.d	0.399	0.018	3.10559	0.125381	0.30241	1797	65	N/A	N/A	86	5.6

WR 24

Sample	^{207}Pb-	±	^{238}U-^{206}Pb	±	Error Correlation	^{206}Pb-^{238}U age	±	^{207}Pb correcte	±	Discordance %	±
24_1.d	0.51	0.022	10.42753	0.532793	0.26745	590	29	252	25	145.1	4.2
24_2.d	0.376	0.018	14.14427	0.460139	0.17067	440	14	262	15	115.6	3.7
24_3.d	0.389	0.018	14.74926	0.652622	0.25852	423	18	244	16	117.9	3.6
24_6.d	0.452	0.02	12.0048	0.47558	0.043278	515	19	255	17	133.1	4

WR 25

Sample	^{207}Pb-	±	^{238}U-^{206}Pb	±	Error Correlation	^{206}Pb-^{238}U age	±	^{207}Pb correcte	±	Discordance %	±
1	0.652	0.027	2.079002	0.099412	0.27529	2520	100	N/A	N/A	96.7	7.6
2	0.533	0.026	10.48218	0.362591	0.45418	587	19	N/A	N/A	149.9	4.7
3	0.631	0.024	7.052186	0.25364	0.062833	854	28	N/A	N/A	169.5	4.9
4	0.431	0.019	12.77139	0.58719	-0.001125	485	21	N/A	N/A	128.1	3.8
5	0.564	0.025	9.049774	0.51596	0.42475	674	37	N/A	N/A	155.7	4.5
6	0.451	0.022	13.1406	0.535294	0.21049	473	19	N/A	N/A	131.6	4.3
7	0.721	0.014	1.468429	0.077626	0.008452	3330	140	N/A	N/A	63	6.9
8	0.708	0.017	1.972387	0.042793	0.36982	2641	49	N/A	N/A	97.2	4.2
9	0.3058	0.007	4.205214	0.047746	0.27928	1375	14	N/A	N/A	80.6	2.2
10	0.495	0.011	3.181674	0.068837	0.40389	1760	33	N/A	N/A	108.4	3.2
11	0.493	0.011	3.032141	0.057002	0.10013	1836	30	N/A	N/A	104.2	2.7

WR 26

Sample	^{207}Pb-	±	^{238}U-^{206}Pb	±	Error Correlation	^{206}Pb-^{238}U age	±	^{207}Pb correcte	±	Discordance %	±
1	0.1746	0.006	4.201681	0.164183	0.016254	1374	48	N/A	N/A	39	2.9
2	0.2328	0.007	4.251701	0.168116	0.13109	1359	49	N/A	N/A	59.4	3.1
3	0.1788	0.004	4.712535	0.122144	0.432	1240	30	N/A	N/A	45.8	2.4
4	0.1815	0.005	4.677268	0.144387	-0.01029	1248	35	N/A	N/A	46.1	2.5
5	0.367	0.027	4.545455	0.289256	0.36152	1276	73	N/A	N/A	97.7	8.1
6	0.667	0.024	1.485884	0.101561	-0.25368	3280	180	N/A	N/A	59	8.2
7	0.658	0.027	1.540832	0.08547	0.58067	3200	140	N/A	N/A	63.8	7.7
8	0.293	0.016	3.802281	0.144573	0.1788	1503	53	N/A	N/A	71.5	5.2
9	0.572	0.022	2.028398	0.098746	0.35314	2570	100	N/A	N/A	81.3	7.2
10	0.628	0.025	1.605136	0.100482	0.25919	3100	150	N/A	N/A	63.8	8.8
11	0.2219	0.007	5.324814	0.19564	-0.016853	1108	38	N/A	N/A	63.8	2.9
12	0.2197	0.009	5.099439	0.18203	-0.00494	1153	38	N/A	N/A	61.8	3.1
13	0.406	0.023	3.257329	0.222814	-0.31542	1710	100	N/A	N/A	88.6	4.9
14	0.304	0.011	4.035513	0.13354	-0.12628	1425	42	N/A	N/A	77.9	3
15	0.416	0.019	3.039514	0.129341	-0.30667	1828	66	N/A	N/A	86.9	3.9
16	0.499	0.017	2.645503	0.10498	0.015983	2062	70	N/A	N/A	94.1	4.6
17	0.1274	0.004	4.882812	0.143051	0.079435	1200	32	N/A	N/A	24.7	2.1
18	0.2263	0.008	4.27899	0.159295	0.14378	1352	45	N/A	N/A	57.5	3
19	0.2776	0.006	4.159734	0.055371	0.58664	1388	17	N/A	N/A	72.3	2.2
20	0.771	0.033	1.226994	0.091836	0.11369	3840	230	N/A	N/A	50	9.9
21	0.562	0.017	2.34192	0.087753	-0.006936	2302	77	N/A	N/A	93.3	4.9

WR 29

Sample	^{207}Pb-	±	^{238}U-^{206}Pb	±	Error Correlation	^{206}Pb-^{238}U age	±	^{207}Pb correcte	±	Discordance %	±
29_1.d	0.562	0.028	7.686395	0.384024	-0.64344	787	37	N/A	N/A	155.7	5.7
29_2.d	0.554	0.022	8.688097	0.377415	0.2212	701	29	N/A	N/A	154.8	4.4
29_3.d	0.551	0.025	8.598452	0.436207	0.40001	708	34	N/A	N/A	153.9	4.9
29_4.d	0.683	0.032	4.926108	0.213546	0.13278	1189	47	N/A	N/A	168.6	6.4
29_5.d	0.723	0.036	4.524887	0.198604	0.31334	1285	51	N/A	N/A	171.2	7.5
29i_1 - 1.d	0.448	0.01	2.854696	0.057045	0.32445	1935	34	N/A	N/A	90.2	3
29i_2 - 1.d	0.42	0.012	3.113325	0.065911	-0.097062	1794	33	N/A	N/A	91	2.8
29i_3 - 1.d	0.564	0.016	1.531394	0.042213	0.17758	3235	71	N/A	N/A	47.3	4.3
29i_5 - 1.d	0.829	0.023	0.692042	0.035919	0.35424	5760	210	N/A	N/A	27.2	4.4
29i_7 - 1.d	0.0815	0.009	7.342144	0.2318	-0.12565	822	25	N/A	N/A	20.8	3.4
29i_8 - 1.d	0.093	0.007	7.127584	0.177809	0.31041	846	20	N/A	N/A	19.5	3.1
29i_9 - 1.d	0.123	0.011	6.684492	0.232349	-0.31664	898	29	N/A	N/A	30.7	4.6
29iii - 3.d	0.1556	0.009	5.055612	0.089457	-0.69629	1163	19	N/A	N/A	37.4	3.1
29iii - 4.d	0.1736	0.009	4.545455	0.206612	-0.85181	1280	53	N/A	N/A	41.1	1.9
29iii - 5.d	0.0867	0.009	7.283321	0.259929	0.059144	829	27	N/A	N/A	20.9	3.6
29iii - 6.d	0.131	0.011	6.868132	0.193402	-0.017731	876	23	N/A	N/A	33.4	5.3
29iii - 7.d	0.479	0.014	2.941176	0.057958	0.7768	1886	33	N/A	N/A	99	3.5
29iii - 11.d	0.442	0.017	3.30033	0.130706	-0.79086	1700	61	N/A	N/A	99.1	2.3
29iii - 13.d	0.3397	0.007	3.526093	0.07087	0.33805	1608	28	N/A	N/A	80.5	2.3
29iii - 14.d	0.1575	0.006	3.608805	0.053396	-0.38843	1576	21	N/A	N/A	25.9	2.1
29iii - 20.d	0.457	0.015	3.209243	0.086514	0.033525	1755	43	N/A	N/A	100.5	3.8
29iii - 21.d	0.1957	0.009	3.134796	0.147404	-0.64433	1780	72	N/A	N/A	32.9	2.1

WR 34

Sample	^{207}Pb-	±	^{238}U-^{206}Pb	±	Error Correlation	^{206}Pb-^{238}U age	±	^{207}Pb correcte	±	Discordance %	±
34_1.d	0.342	0.019	13.73626	0.641529	-0.11433	452	21	286	14	108.2	4.5
34_2.d	0.297	0.014	15.84786	0.77858	0.26054	394	19	272	18	96.6	3.4
34_3.d	0.1891	0.007	18.58736	0.587333	0.29771	338	10	280	10	67.2	2.3
34_4.d	0.1634	0.009	19.53125	0.610352	0.25797	321.5	9.7	274.7	9.8	59	2.8
34_5.d	0.158	0.01	18.34862	0.84168	0.26468	342	15	298	13	56.1	3.3
34_6.d	0.224	0.022	16.77852	1.35129	-0.69372	372	29	281	14	76	6.4
34_7.d	0.315	0.015	14.77105	0.610915	0.43239	422	17	288	18	101.4	3.4
34_8.d	0.1802	0.007	19.37984	0.600925	0.37506	324.4	9.6	272.5	9.5	64.3	2.3
34_9.d	0.316	0.011	14.64129	0.514482	0.19742	425	14	285	13	102.2	2.7
34_10.d	0.269	0.01	16.47446	0.569957	0.31173	380	13	277	12	89.9	2.6
34_11.d	0.322	0.013	15.08296	0.477741	0.34471	414	13	272	13	104	3.1
34_12.d	0.466	0.031	8	1.472	-0.59833	770	130	324	50	129.8	5.6
34_13.d	0.278	0.022	15.87302	0.730663	-0.42873	393	17	279	13	91.1	5.8
34_14.d	0.266	0.011	16.83502	0.651861	0.1415	375	13	275	11	89	2.8

WR 38

Sample	^{207}Pb-	±	^{238}U-^{206}Pb	±	Error Correlation	^{206}Pb-^{238}U age	±	^{207}Pb correcte	±	Discordance %	±
1	0.439	0.02	13.02083	0.542535	0.40796	477	19	244	18	129.3	3.8
2	0.689	0.038	6.451613	0.332987	0.53538	927	45	187	55	176.5	7.4
3	0.678	0.038	5.77034	0.309661	0.21936	1027	50	214	60	171.7	7.5
4	0.449	0.021	11.27396	0.851584	-0.12635	546	40	265	28	131.5	4.6
5	0.468	0.02	11.72333	0.577233	0.16374	527	25	249	21	136.3	4
6	0.426	0.02	11.76471	0.608997	0.079011	525	26	274	19	127.3	4.4
7	0.512	0.021	11.29944	0.44687	0.035447	546	21	226	18	145.4	4
8	0.416	0.02	14.70588	0.58391	0.40777	424	16	229	17	123.3	3.8
9	0.323	0.013	16.63894	0.636765	0.22957	376	14	250	13	102.7	2.8
10	0.2068	0.008	21.97802	0.917764	0.037848	287	12	230	10	72.7	2.3
11	0.265	0.013	17.69912	0.53254	0.33929	354	11	259	11	88.2	3.4
12	0.334	0.014	15.77287	0.59708	0.019673	396	14	254	13	106.3	3.4
13	0.489	0.017	11.48106	0.434988	-0.025604	538	20	238	15	141.1	3.4
14	0.596	0.035	8.375209	0.498023	-0.011021	725	40	215	38	161.3	6.5
15	0.6	0.033	18.55288	1.170311	0.10248	338	21	97	17	149.8	5
16	0.494	0.021	12.34568	0.442006	0.21621	502	17	220	17	141	3.9
17	0.581	0.027	7.770008	0.392425	-0.1403	788	41	257	29	158.9	5
18	0.57	0.025	10.01001	0.410821	0.24091	613	24	211	26	156.8	4.5
19	0.53	0.023	10.2145	0.417344	0.48797	602	24	239	23	149.5	4.1
20	0.562	0.027	9.29368	0.423225	0.3465	658	28	234	28	155.8	5
21	0.2232	0.009	20.24291	0.696619	0.13067	310	10	240.5	8.4	77.6	2.3
22	0.417	0.016	9.149131	0.334826	0.25013	668	23	358	19	127.3	3.3

Chapter 4; apatite fission track data.

WR 16

Sample	U ppm	RF	Sandard Deviation	Ns	rho s			±
					Area		Age (Ma)	
16_1.d	10.19	0.6	5.888126	16	1570	1019108	197.1258	50.63
16_2.d	2.85	0.24	8.421053	6	478	1255230	826.2358	344.41
16_5.d	17.24	0.98	5.684455	10	566.9	1763980	201.6053	64.775
16_6.d	13.93	0.78	5.599426	9	620.5	1450443	205.1052	69.326
16_7.d	10.42	0.7	6.71785	19	754.2	2519226	466.5967	111.54

WR 17

Sample	U ppm	RF	Sandard Deviation	Ns	rho s			±
					Area		Age (Ma)	
17_4.d	38.6	5.6	14.50777	23	391.2	5879346	297.868	75.664
17_7.d	9	1.3	14.44444	9	710.5	1266714	275.7209	100.16
17_10.d	22.4	2	8.928571	12	360.6	3327787	290.6921	87.838
17_11.d	125.2	9.3	7.428115	37	255	14509804	227.8835	41.111
17_12.d	2.17	0.26	11.98157	8	1291	619674.7	547.6224	204.43
17_13.d	2.15	0.16	7.44186	6	634.4	945775.5	825.2919	342.48
17_15.d	31.8	2.6	8.176101	66	2012	3280318	203.2262	30.031
17_16.d	27.9	7.4	26.5233	11	272.4	4038179	283.3711	113.79
17_17.d	64.2	3.5	5.451713	44	342.8	12835473	388.2292	62.237
17_19.d	5.04	0.38	7.539683	9	308.8	2914508	1064.483	363.79
17_20.d	26.5	2.9	10.9434	10	276.2	3620565	267.8134	89.618
17_21.d	12.7	2.2	17.32283	15	585.9	2560164	391.3534	121.68
17_22.d	12.49	0.59	4.723779	17	397.3	4278882	651.6104	161.01
17_24.d	21.8	1.4	6.422018	15	233.4	6426735	564.5877	150.22
17_25.d	29.6	1.5	5.067568	16	321.8	4972032	327.7257	83.598
17_26.d	213	14	6.57277	30	676.9	4431969	41.51189	8.0552
17_27.d	14.67	0.94	6.407635	35	1854	1887810	252.5502	45.653
17_28.d	20.8	1.8	8.653846	12	646.6	1855861	176.1528	53.087
17_29.d	3.07	0.21	6.840391	21	898.6	2336969	1367.68	312.77
17_30.d	13.8	1.1	7.971014	5	378.3	1321702	188.8993	85.81
17_31.d	10.66	0.54	5.065666	14	1374	1018923	188.5266	51.283
17_32.d	50.2	2.6	5.179283	37	526.6	7026206	274.2216	47.266
17_33.d	24.8	1.7	6.854839	58	922.2	6289308	488.5889	72.371

17_34.d	20	1.1	5.5	69	1019	6771344	644.3385	85.281
17_35.d	15.35	0.86	5.602606	8	367.7	2175687	277.6241	99.38
17_36.d	12.17	0.57	4.683648	21	988.2	2125076	340.348	75.961
17_37.d	11.29	0.72	6.377325	21	1449	1449275	251.94	57.277
17_38.d	46.1	2.1	4.555315	80	2088	3831418	164.2362	19.828
17_39.d	3.87	0.37	9.560724	23	1087	2115915	1010.763	231.86
17_40.d	8.48	0.48	5.660377	7	789.8	886300.3	205.8669	78.678
17_41.d	8.22	0.52	6.326034	24	893.7	2685465	622.8077	133.1
17_43.d	40	2.5	6.25	20	521.8	3832886	188.9899	43.879
17_44.d	2.15	0.16	7.44186	7	645	1085271	938.5467	361.55
17_45.d	6.55	0.36	5.496183	12	950.8	1262095	374.5648	110.07
17_46.d	7.88	0.83	10.53299	9	912.1	986733.9	245.8779	85.954
17_47.d	22.5	1.3	5.777778	18	674.3	2669435	233.1914	56.591
17_50.d	11.89	0.76	6.391926	17	1280	1328125	219.7795	55.124
17_51.d	24.6	1.7	6.910569	38	1219	3117309	248.7669	43.864
17_53.d	34.1	1.6	4.692082	36	997.4	3609384	208.4456	36.091
17_54.d	5.55	0.31	5.585586	5	1077	464252.6	165.2861	74.492
17_55.d	12.11	0.74	6.110652	23	1530	1503268	243.7861	52.971
17_56.d	8.07	0.62	7.682776	29	1998	1451451	350.2922	70.395
17_61.d	39.9	2	5.012531	90	2286	3937008	194.5265	22.705
17_62.d	113	6.7	5.929204	33	458.6	7195813	126.2111	23.21
17i_1.d	3.84	0.21	5.46875	10	1233	811030	409.4445	131.4
17i_2.d	13.4	3	22.38806	27	1132	2385159	346.7639	102.37
17i_3.d	2.4	1.1	45.83333	8	1387	576784.4	463.9126	268.54
17i_7.d	25.2	1.7	6.746032	29	644.7	4498216	347.7192	68.699
17i_8.d	2.16	0.14	6.481481	4	1190	336134.5	304.1776	153.36
17i_11.d	43	3.9	9.069767	52	607.3	7739173	350.5255	60.207
17i_14.d	14.58	0.94	6.447188	41	1497	1469606	198.6502	44.246
17i_17.d	9.5	0.86	9.052632	48	1135	3171806	635.8335	120.6
17i_18.d	28.1	1.8	6.405694	19	1425	3368421	235.5674	37.199
17i_19.d	22.5	1.5	6.666667	26	663.1	2865330	249.9763	59.721
17i_20.d	7.82	0.38	4.859335	24	773.5	3361345	807.5589	163.16
17i_21.d	8.61	0.5	5.807201	19	1270	1889764	424.9764	90.19

Sample	U ppm	RF	Sandard Deviation	Ns	rho s			±
					Area		Age (Ma)	
24_1.d	22.2	1.2	5.405405	17	1426	1192146	106.5946	26.487
24_2.d	34.8	1.6	4.597701	24	1376	1744186	99.54297	20.828
24_3.d	38.9	2.1	5.398458	26	1384	1878613	95.94146	19.516
24_6.d	27.7	1.6	5.776173	29	1710	1695906	121.3895	23.607

WR 25

Sample	U ppm	RF	Sandard Deviation	Ns	rho s			±
					Area		Age (Ma)	
25_1	3.87	0.24	6.20155	10	971.8	1029018	511.3609	164.79
25_2	18.44	0.98	5.314534	8	534.4	1497006	160.4724	57.373
25_4	2.25	0.77	34.22222	6	850.1	705799.3	599.1223	319.16
25i_2	35.3	1.6	4.532578	9	721.4	1247574	70.35163	23.666
25i_3	28.4	2.2	7.746479	13	1176	1105442	77.43922	22.3
25i_4	27	1.3	4.814815	23	1348	1706231	125.2571	26.805
25ii_3 - 1.d	6	0.19	3.166667	20	1033	1936108	615.5091	139.01
25ii_4 - 1.d	6.53	0.14	2.143951	17	875.5	1941748	569.2685	138.61
25iii - 2.d	54.7	1.3	2.3766	62	1001	6193806	222.741	28.779
25iii - 4.d	11.03	0.21	1.903898	28	1472	1902174	336.2433	63.866
25iii - 5.d	12.74	0.2	1.569859	24	1289	1861908	286.0694	58.566

WR 26

Sample	U ppm	RF	Sandard Deviation	Ns	rho s			±
					Area		Age (Ma)	
26_1.d	53.2	2.2	4.135338	34	894.2	3802281	141.4857	24.96
26_2.d	29	1.9	6.551724	48	1120	4285714	289.2021	45.842
26_3.d	72	2.4	3.333333	72	948	7594937	207.7445	25.443
26_4.d	66.4	2.5	3.76506	110	1408	7812500	231.2927	23.71
26_5.d	2.7	0.15	5.555556	22	2412	912106.1	642.9798	141.66
26_6.d	5.01	0.34	6.786427	13	1658	784077.2	305.8664	87.335
26_7.d	4.48	0.3	6.696429	18	1740	1034483	446.3521	109.37
26_8.d	5.14	0.24	4.669261	13	2079	625300.6	239.0036	67.22

26_9.d	5.46	0.35	6.410256	36	2419	1488218	523.6834	93.514
26_10.d	4.77	0.25	5.24109	14	2766	506146.1	208.9557	56.909
26i_1	44.6	2.6	5.829596	60	1108	5415162	238.5453	33.79
26i_2	40.7	2.5	6.142506	141	1725	8173913	389.9321	40.645
26i_3	16.7	1.6	9.580838	24	1308	1834862	216.2405	48.76
26i_4	23.1	1.2	5.194805	35	998.8	3504205	296.6878	52.464
26i_5	12.3	1.1	8.943089	17	1004	1693227	269.8016	69.743
26i_6	8.58	0.52	6.060606	23	1343	1712584	387.6117	84.167
26i_7	138.2	7.3	5.2822	34	300	11333333	162.0813	29.085
26i_8	38.9	2.1	5.398458	31	764.7	4053877	205.278	38.498
26ii_1 - 1.d	24.35	0.39	1.601643	45	1432	3142458	253.2597	37.971
26ii_2 - 1.d	1.37	0.11	8.029197	12	3695	324763.2	457.8129	137.18
26ii_8 - 1.d	3.56	0.17	4.775281	21	3924	535168.2	294.0704	65.69

WR 29

Sample	U ppm	RF	Sandard Deviation	Ns	rho s			±
					Area		Age (Ma)	
29_1.d	47.4	3.1	6.540084	18	811.4	2218388	92.99877	22.748
29_2.d	22.3	1.3	5.829596	16	1653	967937.1	86.2952	22.153
29_3.d	20.6	1.1	5.339806	24	1745	1375358	132.2635	27.907
29_4.d	7.89	0.39	4.942966	13	1117	1163832	288.6738	81.325
29_5.d	7.05	0.47	6.666667	5	1283	389711.6	109.7004	49.602
29i_1 - 1.d	11.29	0.29	2.568645	29	2029	1429276	248.5294	46.59
29i_2 - 1.d	11.92	0.24	2.013423	16	875.4	1827736	299.8149	75.196
29i_3 - 1.d	4.67	0.12	2.569593	5	501.2	997605.7	413.9778	185.44
29i_5 - 1.d	0.967	0.047	4.860393	4	1310	305343.5	602.9059	302.87
29i_7 - 1.d	4.79	0.13	2.713987	14	829.2	1688374	669.4851	179.85
29i_8 - 1.d	11.18	0.2	1.788909	50	1967	2541942	439.7258	62.682
29i_9 - 1.d	10.5	0.41	3.904762	16	937.9	1705939	317.2476	80.273
29iii - 3.d	62.2	4.9	7.877814	37	324.8	11391626	356.5209	64.994
29iii - 4.d	80.7	4.4	5.452292	33	335.3	9841933	239.5884	43.705
29iii - 5.d	7.46	0.18	2.412869	10	600.3	1665834	432.1254	137.05
29iii - 6.d	7.1	0.14	1.971831	11	589.2	1866938	505.9097	152.86
29iii - 7.d	7.59	0.15	1.976285	13	1281	1014832	262.2071	72.908
29iii - 11.d	23.22	0.39	1.679587	20	642.9	3110904	262.7235	58.912
29iii - 13.d	21.35	0.42	1.967213	20	476.5	4197272	381.9395	85.734
29iii - 14.d	45.22	0.69	1.525874	49	1223	4006541	174.9393	25.133
29iii - 20.d	8.94	0.19	2.12528	17	1389	1223902	268.3447	65.333

29iii - 21.d	24.79	0.59	2.379992	18	538.1	3345103	264.5726	62.677

WR 34

Sample	U ppm	RF	Sandard Deviation	Ns	rho s			±
					Area		Age (Ma)	
34_1.d	38.4	3.1	8.072917	21	799.5	2626642	135.473	31.521
34_2.d	42.4	2.4	5.660377	25	817.4	3058478	142.7827	29.678
34_3.d	85.6	4.2	4.906542	32	497	6438632	148.8167	27.302
34_4.d	103	5.6	5.436893	52	773.1	6726167	129.3954	19.274
34_7.d	35.4	2.2	6.214689	31	613.9	5049682	279.3643	53.094
34_8.d	85	3.6	4.235294	61	1348	4525223	105.6843	14.253
34_9.d	46.9	2.5	5.33049	17	397.2	4279960	180.111	44.726
34_10.d	58.3	3.7	6.346484	30	791.9	3788357	128.7633	24.889
34_11.d	51.7	2.9	5.609284	38	1296	2932099	112.5244	19.314
34_12.d	26.6	2.2	8.270677	12	758.5	1582070	117.9557	35.421
34_14.d	84.5	5.2	6.153846	25	575.8	4341785	102.0293	21.35
34_15.d	35	35	100	25	803.4	3111775	175.5368	179.01

WR 38

Sample	U ppm	RF	Sandard Deviation	Ns	rho s			±
					Area		Age (Ma)	
38_1	31	1.6	5.16129	43	2126	2022578	129.2813	20.814
38_2	7.34	0.45	6.13079	11	2111	521080.1	140.5465	43.244
38_3	6.11	0.37	6.055646	19	3048	623359.6	201.0308	47.699
38_4	39.9	1.9	4.761905	17	1065	1596244	79.57882	19.669
38_5	29.8	1.4	4.697987	17	1378	1233672	82.33067	20.339
38_6	38.1	1.8	4.724409	45	2156	2087199	108.7241	17.002
38_7	22.3	1.1	4.932735	25	1753	1426127	126.7451	26.109
38_8	32.1	1.6	4.984424	10	902.2	1108402	68.74307	22.007
38_9	50.3	2.5	4.970179	11	1031	1066925	42.315	12.931
38_10	112	5.9	5.267857	24	425.6	5639098	99.99388	21.08
38_11	79	4.7	5.949367	43	898.7	4784689	120.0962	19.659
38_12	44.5	2.9	6.516854	26	855.2	3040225	135.3113	27.963
38_13	24.6	1.3	5.284553	17	2233	761307.7	61.6455	15.302
38_14	15.5	1.3	8.387097	15	1975	759493.7	97.33389	26.424

38_15	31.2	2.1	6.730769	11	1895	580474.9	37.1306	11.471
38_16	26.7	1.4	5.243446	22	1384	1589595	118.0719	25.923
38_17	10	1	10	20	1843	1085187	213.6207	52.326
38_18	17.38	0.92	5.293441	21	2596	808936.8	92.49111	20.769
38_19	36	12	33.33333	11	769.5	1429500	78.99007	35.503
38_20	18.8	1	5.319149	24	2332	1029160	108.6462	22.918
38_21	17.8	1.1	6.179775	4	1095	365296.8	40.94495	20.628
38_22	123.7	5.4	4.3654	42	1026	4093567	65.89691	10.567
38_23	5.17	0.9	17.40812	3	878.8	341374.6	130.822	78.889
38_24	24.7	1.4	5.668016	17	1261	1348136	108.3271	26.981

7571 + 7582

Sample	U ppm	RF	Sandard Deviation	Ns	Area	rho s	Age (Ma)	±
7571 A8	8.40703	0.876	0.073624	38	2100	1809524	417.0166	67.748
7571 B4	11.7197	0.832	0.097465	17	1600	1062500	178.947	43.427
7571 B6	6.17633	1.033	0.063821	11	900	1222222	384.3813	115.96
7571 C3	3.82137	1.276	0.048771	21	2000	1050000	527.7477	115.36
7571 C4	2.04438	1.172	0.023964	18	2400	750000	695.377	164.1
7571 D7	4.05819	1.154	0.046815	33	2800	1178571	556.54	97.094
7571 E3	4.35829	0.985	0.042936	36	4500	800000	357.3033	59.654
7571 E4	3.45868	0.981	0.033936	21	2400	875000	487.4489	106.48
7571 E6	2.25381	1.379	0.031082	8	1800	444444.4	383.0776	135.54
7571 G1	5.60283	1.686	0.094452	42	3000	1400000	481.6691	74.765
7571 G9	3.461	1.111	0.038436	26	3500	742857.1	415.8854	81.693
7571 H3	3.89586	1.025	0.039939	49	6400	765625	381.8063	54.684
7571 H13	2.80431	1.197	0.033578	24	3600	666666.7	459.0726	93.869
7571 I11	2.79834	1.45	0.040569	13	2800	464285.7	323.8071	89.931
7571 I13	3.90363	1.239	0.048374	26	5600	464285.7	233.7615	45.936
7582 B6i	24.1788	0.596	0.144208	70	2000	3500000	283.4043	33.915
7582 B6ii	24.5574	2.511	0.61665	52	1600	3250000	259.5862	36.584
7582 D4	17.35	7.244	1.256817	44	1500	2933333	329.8073	55.162

9508

Sample	U ppm	RF	Sandard Deviation	Ns	Area	rho s	Age (Ma)	±
9508 I1	7.01943	1.387	0.097366	21	1200	1750000	480.6182	105.09
9508 K3	12.8018	0.887	0.113549	43	1600	2687500	407.0496	62.179
9508 K7	8.7343	4.383	0.382828	35	1800	1944444	430.8515	75.236
9508 L3	11.5758	6.29	0.728165	48	2000	2400000	402.1604	63.32
9508 L7	10.1409	5.965	0.604911	23	1200	1916667	367.6069	79.726

9528

Sample	U ppm	RF	Sandard Deviation	Ns		rho s		±
					Area		Age (Ma)	
9528 C2i	24.5933	0.647	0.159069	56	2100	2666667	213.4498	28.557
9528 C7	5.2715	3.243	0.170972	24	2400	1000000	368.9215	76.25
9528 C9	9.11459	1.816	0.165492	32	2400	1333333	286.3355	50.884
9528 H6	3.59708	1.599	0.057531	13	1800	722222.2	389.8319	108.3
9528 B9	3.09148	2.065	0.063842	13	2000	650000	407.6584	113.38
9528 D7	5.00419	4.168	0.208594	5	600	833333.3	324.9724	145.96
9528 D12	6.28949	1.19	0.074828	10	1000	1000000	310.6231	98.297
9528 E7	8.7295	1.098	0.095868	8	1200	666666.7	151.069	53.437
9528 E8	4.39983	4.152	0.182682	9	800	1125000	492.4664	165.42
9528 J1	27.8831	0.74	0.206279	45	2100	2142857	152.0116	22.688
9528 A5	8.03283	1.161	0.093261	11	900	1222222	297.5599	89.784
9528 A7	10.1792	1.181	0.120259	15	1400	1071429	207.3015	53.581
9528 A9	5.89662	1.137	0.067059	11	1200	916666.7	303.8692	91.685
9528 C2ii	12.1791	0.981	0.119446	41	2100	1952381	313.1212	48.998

9582

Sample	U ppm	RF	Sandard Deviation	Ns		rho s		±
					Area		Age (Ma)	
9582 A3	1.80065	1.773	0.031921	20	3000	666666.7	701.4431	157.34
9582 B2	9.18871	1.043	0.095817	38	2800	1357143	289.0366	46.985
9582 B7	11.7439	6.732	0.790576	28	1800	1555556	259.8048	52.12
9582 C7	4.05635	1.101	0.044646	24	1500	1600000	744.7506	152.24
9582 C9	5.76421	1.03	0.059398	11	1600	687500	234.4055	70.717
9582 E9	6.42347	0.972	0.062421	34	3000	1133333	343.8032	59.056
9582 F4	5.30108	1.481	0.078498	13	1200	1083333	396.5747	110.15
9582 H5	4.83809	1.888	0.091345	24	2400	1000000	400.9626	82.196
9582 H9	3.52166	1.115	0.039257	17	2000	850000	465.8428	113.1
9582 I9	3.50359	1.091	0.038234	21	2500	840000	462.846	101.13

9594

Sample	U ppm	RF	Sandard Deviation	Ns		rho s		±
					Area		Age (Ma)	
9594 A5	5.0676	1.283	0.064995	34	3000	1133333	432.7631	74.426
9594 A8	2.82731	1.263	0.035714	20	1800	1111111	742.1613	166.22
9594 B6	5.36281	1.586	0.085077	25	2400	1041667	377.4967	75.736
9594 B7	3.36616	1.807	0.06083	14	1600	875000	500.3389	134.03
9594 B11	4.93479	1.235	0.060934	28	2100	1333333	519.2959	98.347
9594 C1	5.39293	0.756	0.040765	31	2100	1476190	525.8232	94.524
9594 C7	4.82544	2.87	0.138507	29	2000	1450000	575.0067	108.04
9594 D1	4.47914	0.695	0.031126	75	5600	1339286	572.2853	66.201
9594 D4	2.95771	0.946	0.02798	22	3500	628571.4	411.912	87.906
9594 D9	5.43829	0.968	0.052631	41	4000	1025000	366.6129	57.365
9594 E9	4.12527	1.277	0.052678	19	2400	791666.7	373.0921	85.726
9594 E14	4.30444	0.719	0.030936	7	900	777777.8	351.8738	133.02
9594 F11	8.95537	1.249	0.111822	56	5000	1120000	245.5786	32.96
9594 G10	5.58283	0.884	0.049358	23	2800	821428.6	287.9613	60.098
9594 H4	7.13299	0.497	0.035487	33	2500	1320000	360.1381	62.718
9594 H5	6.1038	0.603	0.036785	32	3000	1066667	340.6109	60.247
9594 I5	3.17656	0.836	0.026544	16	3500	457142.9	281.7883	70.486
9594 I6	7.50912	0.637	0.04785	33	1800	1833333	471.0246	82.05

2017960

Sample	U ppm	RF	Sandard Deviation	Ns		rho s		±
					Area		Age (Ma)	
60 A1	9.69099	3.078	0.298242	36	2800	1285714	260.2172	44.103
60 B1	4.88124	1.148	0.05603	38	4800	791666.7	316.7049	51.505
60 B4	4.41312	0.903	0.039832	87	7200	1208333	525.9665	56.589
60 B9	4.7098	3.101	0.146052	36	3600	1000000	411.5435	69.768
60 C1	4.06961	1.124	0.045734	23	2000	1150000	542.1383	113.21
60 C3	4.4704	1.098	0.049084	46	4000	1150000	495.3515	73.238
60 C4	2.51988	2.809	0.07078	25	3000	833333.3	630.081	127.25
60 C9	2.98287	1.113	0.033196	35	6000	583333.3	379.9916	64.369
60 C10	11.475	1.226	0.140648	82	4500	1822222	310.249	34.472
60 C11	18.2592	4.998	0.91267	50	1500	3333333	355.4052	53.309
60 D3	11.7993	1.049	0.123798	36	2100	1714286	284.4225	47.498
60 D6	7.82076	2.913	0.227835	50	3000	1666667	413.0167	59.636

60 D9	11.4134	4.113	0.469401	21	1800	1166667	201.4107	44.725
60 D11	3.99447	1.283	0.05125	46	5000	920000	445.2447	65.896

2017962

Sample	U ppm	RF	Sandard Deviation	Ns		rho s		±
					Area		Age (Ma)	
62 E3	12.2912	1.631	0.200419	38	5000	760000	122.5853	19.986
62 E10	9.22691	0.729	0.067233	31	3500	885714.3	189.321	34.031
62 F6	3.52388	1.009	0.035551	48	8100	592592.6	328.0882	47.471
62 F10	8.11492	1.817	0.147453	24	3600	666666.7	162.3671	33.274
62 H5	5.04626	1.194	0.06027	29	6000	483333.3	188.909	35.152
62 J5	3.51964	1.2	0.042238	56	10000	560000	310.8359	41.704
62 J11	10.0505	1.732	0.174031	61	6300	968254	189.995	24.548
62K3	8.64766	6.812	0.589073	79	5600	1410714	318.5091	41.891
62 K4	7.6623	0.831	0.06366	54	3500	1542857	390.9187	53.296
62 K7	17.1821	1.051	0.180585	107	5600	1910714	218.8174	21.279
62 K8	3.28411	1.021	0.033523	41	5400	759259.3	446.8762	69.939
62 K10	5.38575	0.996	0.053636	31	3600	861111.1	312.3232	56.181
62 L1	2.1011	1.53	0.03215	32	6300	507936.5	466.5592	82.785
62 L4	21.285	0.568	0.120989	171	6000	2850000	262.5737	20.135
62 L5	8.0658	1.211	0.097717	64	3500	1828571	438.4951	55.069
62 L6	6.69911	0.826	0.055351	75	6000	1250000	363.0451	42.028
62 L8	7.04552	1.718	0.121039	45	2800	1607143	441.1151	66.193
62 L10	11.9768	1.564	0.18728	70	7200	972222.2	160.4588	19.342
62 L11	15.8229	1.085	0.171644	59	3000	1966667	244.0902	31.888

Chapter 5; Titanite U-Pb data.

9583

Sample	^{207}Pb-^{235}U	±	^{206}Pb-^{238}U	±	Rho	Discordance %
9583_K2	2.2963	0.204	0.09711	0.00223	0.25807	24
9583_C1	1.46918	0.13	0.08868	0.00203	0.258624	28
9583_B4	1.60534	0.143	0.0882	0.002	0.254526	26
9583_A8	2.62646	0.249	0.0961	0.00233	0.255959	21
9583_H10	2.84473	0.24	0.09974	0.00223	0.26499	22
9583_J11	1.45643	0.17	0.09046	0.00245	0.232471	28

9583_C7	1.7619	0.163	0.08716	0.00212	0.262253	23
9583_D11	1.6824	0.128	0.08679	0.00184	0.277809	24
9583_J10	1.71079	0.156	0.0922	0.00212	0.252241	27
9583_B6	1.75815	0.148	0.08713	0.00198	0.27076	23
9583_A9	1.81607	0.158	0.08836	0.00206	0.267277	24
9583_E11	1.64588	0.187	0.08227	0.00221	0.236003	24
9583_I2	4.95712	0.461	0.12179	0.00281	0.248114	22
9583_J2	1.76212	0.128	0.09139	0.00191	0.287601	25
9583_H4	1.44202	0.13	0.0872	0.0021	0.267197	25
9583_E7	1.58295	0.15	0.08716	0.00209	0.253353	26
9583_K8	1.72961	0.19	0.09104	0.00235	0.235314	26
9583_D2	2.68771	0.212	0.09863	0.00219	0.281914	21
9583_I11	1.56321	0.148	0.08936	0.00208	0.245671	28